Fakultät Georessourcen Materialtechnik | RWTH AACHEN UNIVERSITY

"New insights into thorium and uranium oxo-arsenic (III/V) and oxo-phosphates (V) crystal chemistry"

Von der Fakultät für Georessourcen und Materialtechnik
der Rheinisch-Westfälischen Techenischen Hochschule Aachen

zur Erlangung des akademischen Grades eines

Doktors der Naturwissenschaften

Genehmigte Dissertation

vorgelegt von **Master**

Na Yu

aus Sichuan

Berichter: Prof. Dr. rer. nat. Evgeny V. Alekseev
Univ. -Prof. Dr. rer. nat. Dirk Bosbach
Prof. Dr. Thorsten M. Gesing
Univ. -Prof. Dr. rer. nat. Georg Roth

Tag der mündlichen Prüfung: 11. Dezember 2015

Diese Dissertation ist auf den Internetseiten der Hochschulbibliothek online verfügbar

NEW INSIGHTS INTO THORIUM AND URANIUM OXO-ARSENIC (III/ V) AND OXO-PHOSPHATES (V) CRYSTAL CHEMISTRY

Abstract

The fundamental chemistry of actinides is of great interest owing to the diverse number of valence states and complex coordination chemistry of the actinides. The phases based on actinides and oxo-salt fragments have been under thorough investigation in the last decades. These compounds can be widely found in nature and they affect the migration process of actinides in nature. A better understanding of the fundamental coordination chemistry of actinide compounds with oxo-salts of group V elements is not only important for understanding the actinides behavior within the migration process but can also be used to understand actinide properties in phosphate ceramics. Concerning the radioactive issues, the less radioactive early actinides (i.e. U, Th) can be taken as modeling elements to study the crystal chemistry of the transuranic elements (Np, Pu) without the major handling problems. This can be done as Th(IV) has a very similar coordination chemistry with An(IV) and U(VI) can be chosen as a modeling element for transuranic elements in higher valence states. Therefore, a systematic research on the actinides (U, Th) bearing phases with tetrahedral oxo-anions such as phosphates and arsenates have been performed in this work. High temperature (HT) solid state reaction, High pressure high temperature (HP-HT) solid state reaction and the hydrothermal method were the methods of choice for synthesizing actinide bearing oxo-arsenic(III/V) and oxo- phosphorus(V) phases in the past three years. As a result, numerous novel compounds containing actinides were obtained. The structures of all compounds were determined using single crystal X-ray diffraction data. Raman spectroscopy, EDS, DSC and high temperature powder X-ray diffraction (HT-PXRD) measurements were implemented to characterize the chemical and physical properties of the obtained compounds.

The core of this dissertation is a fundamental study of the crystal chemistry of actinides (Th, U) oxo-arsenic (III/V) and oxo-phosphate(V) phases that were derived from the before mentioned methods. They can be separated into several main parts according to the structural features: layers in U(VI) phases (chapter 3); cations driving structural diversity of thorium arsenates and phosphates (chapter 4 and 5); uranium metaphosphate with $(PO_3)_n^{n-}$ polymeric chains (chapter 6); mixed-valent arsenic(III/V) Th compounds obtained under extreme pressure (chapter 7); series of compounds adopting the typical structure type of $KTh_2(AsO_4)_3$ and presented by $ATh_2(AsO_4)_3$(A= K, Rb, Cs, Ag), $LiTh_2(PO_4)_3$ and $BU^{IV}_2(PO_4)_3$ (B= Rb, Cs); tri-phosphate and tri-arsenate $\boldsymbol{T}_3O_{10}$ units in the $ATh(\boldsymbol{T}_3O_{10})$ (A= Rb, Cs; ***T***= P, As) family (chapter 7).

CONTENTS

FIGURES v

TABLES x

ACKNOWLEDGMENTS i

Chapter 1 INTRODUCTION 1

1.1 Overview 1

1.2 Background I: Structural Chemistry of Uranium and Thorium 2

1.2.1 Oxidation States of Uranium and Thorium 2

1.2.2 Coordination Numbers and Coordination Polyhedra of Uranium and Thorium 3

1.3 Background II: Structural Chemistry of Phosphates/Phosphites and Arsenate/ Arsenites 5

1.4 Background III: Overview of some known Uranium and Thorium bearing Phosphates/Phosphites and Arsenates/Arsenites 7

1.5 References 8

Chapter 2 SYNTHETIC METHODS AND CHARACTERIZATION TECHNIQUES 11

2.1 Synthetic Methods 11

2.1.1 Hydrothermal Synthetic Method 11

2.1.2 High Temperature (**HT**) Solid State Synthesis 11

2.1.3 High-Temperature High-Pressure (**HTHP**) Synthetic Method 12

2.2 Systematic Synthesis of Thorium and Uranium bearing Phosphates and Arsenates 14

2.3 Characterization Techniques 17

2.3.1 Single Crystal X-ray Diffraction 18

2.3.2 Powder X-ray Diffraction 20

2.3.3 Raman and IR Spectroscopy 21

2.3.4 Element analysis 22

2.3.5 TG-DCS Experiment 23

2.4 Structure Determination from Single Crystals 24

2.5 Bond Valence Analysis 25

2.6 References 26

Chapter 3 TOPOLOGICALLY IDENTICAL, BUT GEOMETRICALLY ISOMERIC LAYERS IN ANHYDROUS $Rb[UO_2(AsO_3OH)(AsO_2(OH)_2)]$ AND HYDROUS α- and β-$Rb[UO_2(AsO_3OH)(AsO_2(OH)_2)]\cdot H_2O$ 27

3.1 Abstract 27

3.2 Introduction 27

3.3 Synthesis 28

3.4 Single Crystal X-ray Diffraction 30

3.5 Chemical Composition 32

3.6 Bond Valence Analysis 33

3.7 Structure Description 37

3.8 Graph Representation of Structure Topology, Geometric Isomerism and Topotactic Dehydration Reactions 43

3.9 Raman Spectroscopy 47

3. 10 Conclusions 49

3.11 References 50

Chapter 4 MORPHOTROPY AND TEMPERATURE DRIVEN POLYMORPHISM IN $\mathbf{A}_2Th(AsO_4)_2$ (**A**= Li, Na, K, Rb, Cs) SERIES 52

4.1 Abstract 52

4.2 Introduction 52

4.3 Synthesis 53

4.4 Single Crystal X-ray Diffraction 54

4.5 Chemical Compositions 55

4.6 Pure Powder Samples Preparation and Powder X-ray Diffraction 57

4.7 Bond Valence Analysis 62

4.8 Crystal Structure Description 65

4.9 Properties and Topology 70

4.9.1 TG-DCS Experiment 70

4.9.2 High-temperature (**HT**) Powder XRD and Phase Transition 71

4.9.3 Topological Studies 77

4. 10 Raman and IR Spectroscopy 78

4.11 Conclusions 81

4.12 References 83

Chapter 5 STRUCTURAL EVOLUTION OF THORIUM PHOSPHATE FAMILY $A_2Th(PO_4)_2$ (A= Li, Na, K, Rb, Cs) 85
5.1 Abstract 85
5.3 Synthesis 86
5.4 Single Crystal X-ray Diffraction 87
5.5 Bond Valence Analysis 90
5.6 Crystal Structures Description 93
5.7 Conclusions 97
5.8 References 99
Chapter 6 FURTHER INSIGHT INTO U AND Th METAPHOSPHATE CRYSTAL CHEMISTRY AND EFFECT OF Nd^{3+} INCORPORATION INTO U^{4+} METAPHOSPHATE 100
6.1 Abstract 100
6.2 Introduction 100
6.3 Synthesis 101
6.4 Single Crystal X-ray Diffraction 102
6.5 Chemical Compositions 105
6.6 Structure Description 106
6.7 Analysis of Structures and Systematization of the Polymorphs 110
6.8 Raman Spectroscopy 114
6.9 Conclusions 115
6.10 References 116
Chapter 7 SOME OTHER RESULTS FROM EXPLORING THE Th/U- A^{I}/ A^{II}- P/As SYSTEM 118
7.1 $Th(As^{III}_4As^{V}_4O_{18})$: A Mixed- valent oxo- As(III)/As(V) Actinide Compound obtained under Extreme Conditions 118
7.1.1 Abstract 118
7.1.2 Introduction 118
7.1.3 Synthesis 118
7.1.4 Single Crystal X-ray Diffraction 119
7.1.5 Chemical Compositions 120
7.1.6 Structure Description 121
7.1.7 Raman Spectroscopy 124

7.1.8 Conclusions....126

7.2 $ATh_2(AsO_4)_3$(A= K, Rb, Cs, Ag), $LiTh_2(PO_4)_3$ and $BU^{IV}_2(PO_4)_3$ (B= Rb, Cs): Formation, Structures and Properties....127

7.2.1 Introduction....127

7.2.2 Synthesis....127

7.2.3 Single Crystal X-ray Diffraction....128

7.2.4 Bond Valence Analysis....129

7.2.3 Results and Discussion....132

7.2.4 Conclusions....134

7.3 $ATh(As_3O_{10})$ (A= Rb, Cs) and $RbTh(P_3O_{10})$: Formation, Structures....134

7.3.1 Introduction....134

7.3.2 Synthesis....134

7.3.3 Single Crystal X-ray Diffraction....136

7.3.4 Bond Valence Analysis....136

7.3.5 Results and Discussion....138

7.3.6 Conclusions....139

7.4 References....140

Chapter 8 CONCLUSIONS AND OUTLOOK....142

Appendix: PAPERS AND CONFERENCES....144

FIGURES

Figure 1.1: Common coordination environment of the **An**O_X(X= 6, 7, 8, 9, 10) (**An** = U^{IV}, Th^{IV}) polyhedra, (a) 6-coordinated: tetragonal bipyramid; (b) 7-coordinated: pentagonal bipyramid; (c) 8-coordinated: square antiprism; (d) 9-coordinated: monocapped square antiprism; (e) 10-coordinated: bicapped square antiprism. Uranium and Thorium polyhedra are shown in green, O atoms are red. 4
Figure 1.2: Some examples of the coordination modes between the actinide polyhedra and the bridging group (in this dissertation, i.e. PO_4 and AsO_4), (a) Monodentate; (b) Bidentate-chelating; (c) Bidentate-bridging; (d) Tridentate-bridging. Actinide (U^{IV}, Th^{IV}) polyhedra are shown in green, PO_4 and AsO_4 in magenta. 4
Figure 1.3: Basic coordination polyhedra of phosphate and arsenate, (a) **T**O_4 single tetrahedron; (b) $\mathbf{T}_2O_7$ dimer; (c) $\mathbf{T}_3O_{10}$ trimer; (d) Infinite polymeric **T**O_3 chain; (e) Cyclic tetramer-phosphate/ arsenate anion $\mathbf{T}_4O_{12}$. (**T** = P and As) phosphate and arsenate polyhedra are magenta or green. 6
Figure 2.1: The experimental procedure for the hydrothermal method 11
Figure 2.2: The experimental processes of the **HT** method..... 12
Figure 2.3: The combined piston cylinder/ multi anvil press installed at IEK-6, Forschungszentrum Jülich (Voggenreiter LP 1000-540/50) 14
Figure 2.4: Interaction of X-Rays with a crystal lattice. 18
Figure 2.5: The inside chamber of the SuperNova (Agilent) diffractometer. 1) Sources of radiation - Copper X-ray tube (high intensity, large absorption by heavy atoms; suitable for organic compounds); Molybdenum X-ray tube (low intensity, low absorption by heavy atoms; suitable for actinide compounds). 2) Detector - CCD area detector. 3) Temperature control system - temperature ranges from 100 K (liquid nitrogen) to 500 K. 4) Camera. 19
Figure 2.6: (a) left: the needle used to pick a crystal; right: pin and glass fiber attached with a single crystal, (b) holder of the pin. 20
Figure 2.7: (a) Bruker D4 Endeavor diffractometer; (b) the sample holder; (c) the inside chamber of the diffractometer. 21
Figure 2.8: (a) Horiba LabRAM HR spectrometer for Raman experiments; (b) Bruker Equinox spectrometer for IR experiments 22
Figure 2.9: Scanning electron microscopy for element analysis..... 23
Figure 2.10: Netzsch STA 449C Jupiter apparatus for TG- DCS experiment 24
Figure 2.11: The process of the crystal structure solution and refinement. CIF file contains all necessary data on crystal structure model, e.g. unit cell parameters, symmetry, atomic coordination, experiment details. The R1 value is usual reference to experiment quality and reflects difference between calculated and experimental intensities. 25
Figure 3.1: The tempering profile of the furnace. 29
Figure 3.2: Electronic-microscopic image of a crystal of **RbUAs- 1**, **2**, and **3** 33
Figure 3.3: Structural fragments of (a) **RbUAs-1**, (b) **RbUAs-2** and (c) **RbUAs-3** with unit cells outlined and different layer isomers indicated by capital letters, see text for more details. U and

As polyhedra are shown in yellow or green, respectively; Rb atoms are in blue and H_2O molecules are shown in magenta. O atoms are omitted for clarity. 37
Figure 3.4: The coordination environments of Rb atoms in (a) **RbUAs-1**, (b) **RbUAs-2** and (c,d,e,f) **RbUAs-3**. 39
Figure 3.5: Ball-and stick models of two layers and the interlayer space in (a) **RbUAs-1**, (b) **RbUAs-2** and (c) **RbUAs-3**. U, As, O and Rb atoms are shown as yellow, green, red and blue spheres, respectively, whereas water molecules are shown in magenta. Possible hydrogen bonds are shown as blue dashed lines. Only interlayer hydrogen bonds are marked, interlayer hydrogen bonds are omitted for clarity. 40
Figure 3.6: (a) Schematic representation of layers A in **RbUAs-1** and **RbUAs-3**; (b) layer B in **RbUAs-2** and (c) layer C in **RbUAs-3**. Two different coordination environments of U polyhedra are observed within the layers, viz. types I and II, which are shown schematically on the top. See text for discussion of type I and II. U polyhedra are shown in yellow, “up” and “down” pointing As tetrahedra are shown in green or red, respectively. 44
Figure 3.7: (a) Black-and-white graph of the $[UO_2(AsO_3OH)(AsO_2(OH)_2)]^-$ layer. Colored graph of (b) A-layers, (c) B-layer and (c) C-layer. U sites are black circles, As sites are white circles on (a). Green circles are “up” and red are “down” As tetrahedra sites (see text for details). During the topotactic dehydration of **RbUAs-1** and **RbUAs-2,** the marked As tetrahedra in layers B and C have to change their orientation. 46
Figure 3.8: The changes of Rb coordinations via dehydration process, ... 46
Figure 3.9: The Raman spectra of (a)**RbUAs- 1**, (b)**RbUAs- 2** and (c)**RbUAs- 3** 47
Figure 4.1: Electronic-microscopic image of $Li_2Th(AsO_4)_2$ (a), $Na_2Th(AsO_4)_2$ (b), $K_2Th(AsO_4)_2$ (c), $Rb_2Th(AsO_4)_2$ (d), and $Cs_2Th(AsO_4)_2$ (e). 56
Figure 4.2: The powder X-ray diffraction patterns of the pure phase powder of $Li_2Th(AsO_4)_2$ and the theoretical simulations from single crystal structures. (up is theoretical data, down is experimental data) 58
Figure 4.3: The powder X-ray diffraction patterns of the pure phase powder of $Na_2Th(AsO_4)_2$ and the theoretical simulations from single crystal structures. (up is theoretical data, down is experimental data) 59
Figure 4.4: The powder X-ray diffraction patterns of the pure phase powder of $K_2Th(AsO_4)_2$ and the theoretical simulations from single crystal structures. (up is theoretical data, down is experimental data) 60
Figure 4.5: The powder X-ray diffraction patterns of the pure phase powder of $Rb_2Th(AsO_4)_2$ and the theoretical simulations from single crystal structures. (up is theoretical data, down is experimental data) 61
Figure 4.6: The powder X-ray diffraction patterns of the pure phase powder of $Cs_2Th(AsO_4)_2$ and the theoretical simulations from single crystal structures. (up is theoretical data, down is experimental data) 62

Figure 4.7: Polyhedra representation of the crystal structures of $Li_2Th(AsO_4)_2$ (a), $Na_2Th(AsO_4)_2$ (b), $K_2Th(AsO_4)_2$ (c), and $Cs_2Th(AsO_4)_2$ (d). $Rb_2Th(AsO_4)_2$ is isostructural with $K_2Th(AsO_4)_2$. Th and As polyhedra are shown in yellow and green, respectively, alkaline atoms as colored spheres. 66
Figure 4.8: Coordination types of arsenate-anions in the crystal structures of $A_2Th(AsO_4)_2$ (A = Li, K, Rb, and Cs). 66
Figure 4.9: Second neighbor coordination of Th atoms in the crystal structures of $Na_2Th(AsO_4)_2$ (a), $A_2Th(AsO_4)_2$ (A = K, Rb) (b), and $Cs_2Th(AsO_4)_2$ (c). Th polyhedra are shown in yellow, As and O atoms are green and red, respectively. 67
Figure 4.10: Comparison of the crystal structures of $Na_2Th(PO_4)_2$ (c) and $A_2Th(AsO_4)_2$ (A = Na, K) (a, b, respectively) along [100]. Th and As polyhedra are shown in yellow and green, respectively. 69
Figure 4.11: The DSC and TA curves of $K_2Th(AsO_4)_2$ and $Rb_2Th(AsO_4)_2$. The peaks are marked with the corresponding onset temperatures. 71
Figure 4.12: 2D plot of the temperature-dependent powder pattern of $K_2Th(AsO_4)_2$ (left) and $Rb_2Th(AsO_4)_2$ (right). 72
Figure 4.13: Temperature-dependent development of the autocorrelation parameter of $K_2Th(AsO_4)_2$ (left) and $Rb_2Th(AsO_4)_2$ (right) together with the respective evaluation of transition temperatures. 73
Figure 4.14: Temperature-dependent metric parameters and thermal expansion coefficients (TEC, inset top) together with the respective DEA fit results and single energy term contribution (insert bottom) for the X-ray powder data of room-temperature phases of $K_2Th(AsO_4)_2$ (left) and $Rb_2Th(AsO_4)_2$ (right). 74
Figure 4.15: View on underlying net of $Cs_2Th(AsO_4)_2$ (**ant** topological type[41]) along [100] (up) and [010] (right). Black and white sphere corresponds to Th and As atoms, respectively. 77
Figure 4.16: Raman spectra of $A_2Th(AsO_4)_2$ (A = Li, Na, K, Rb, Cs). 79
Figure 4.17: IR spectra of $Li_2Th(AsO_4)_2$, $Na_2Th(AsO_4)_2$, $K_2Th(AsO_4)_2$, $Rb_2Th(AsO_4)_2$, and $Cs_2Th(AsO_4)_2$. 81
Figure 5.1: Polyhedra representation of the crystal structures of $A_2Th(PO_4)_2$ (A= Li, Na, K, Rb, Cs). $Rb_2Th(PO_4)_2$ is isostructural with $Cs_2Th(PO_4)_2$. Th and P polyhedra are shown in yellow and green, respectively, alkaline atoms as blue spheres. 93
Figure 5.2: Coordination types of phosphate-anions in the crystal structures of $A_2Th(PO_4)_2$ (A = Li, Na, K, Rb, and Cs). 94
Figure 5.3: The coordination of Th atoms in the crystal structures of $A_2Th(PO_4)_2$ (A = Na, K, Rb, and Cs). (a) cis-position, (b) cis- and trans- position, (c) trans- position. Th polyhedra are shown in yellow, P and O atoms are green and red, respectively. 95
Figure 5.4: (a) A fragment of the structure of $K_2Th(PO_4)_2$ along the direction shown in the picture. (b) A fragment of the structure of $Na_2Th(PO_4)_2$ along [001]. The yellow and purple polyhedra of thorium adopted the cis- position and cis- and trans- position, respectively; the black and white sphere corresponds to Th and P atoms, respectively. 96

Figure 5.5: Structural evolution in $\mathbf{A_2Th(TO_4)_2}$ (**A**= **Li**, **Na**, **K**, **Rb**, **Cs**; **T**= **P** and **As**) family. The color assignment of all pictures is the same with above picture. **P** stands for $\mathbf{A_2Th(PO_4)_2}$, and **As** stands for $\mathbf{A_2Th(AsO_4)_2}$. 97
Figure 6.1: Electronic-microscopic image of tetragonal $U(PO_3)_4$ (a), $(U_{0.62}Nd_{0.38})(PO_3)_4$ (b), $Th(P_4O_{12})$ (c), and $U(P_4O_{12})$ (d). 105
Figure 6.2: Crystal structure of tetragonal $U(PO_3)_4$ (a), "$(U_{0.62}Nd_{0.38})(PO_3)_4$" (b), and $Th(P_4O_{12})$ (c). $Th(P_4O_{12})$ and $U(P_4O_{12})$ are isostructural. U, U/Nd, and Th sites are yellow. PO_4 polyhedra are green (a and b) or purple. Green or purple (c) PO_4 tetrahedra are to show plain and distorted P_4O_{12} groups, respectively. O atoms omitted for clarity. 107
Figure 6.3: Metal atoms coordination polyhedra in $U(PO_3)_4$ (a and b for U1 and U2, respectively), "$(U_{0.62}Nd_{0.38})(PO_3)_4$" (c), and $Th(P_4O_{12})$ (d and e for Th1 and Th2, respectively). 107
Figure 6.4: Polyphosphate chains in crystal structures of the tetragonal $U(PO_3)_4$, "$(U_{0.62}Nd_{0.38})(PO_3)_4$", and β-$U(PO_3)_4$[12]. 108
Figure 6.5: View on two different conformational types of tetraphosphate anions in crystal structure of $Th(P_4O_{12})$. One of them contains two bridging O atoms above and two below plane of P atoms (a) and another one – three above and one below the plane built using any of three P atoms of this anion (b). 110
Figure 6.6: Schloegel projections of metal atom Voronoi-Dirichlet polyhedra in metal sublattice in β-$U(PO_3)_4$ (a), tetragonal $U(PO_3)_4$ (b), "$(U_{0.62}Nd_{0.38})(PO_3)_4$" (c). 111
Figure 6.7: The VDP of the U atoms in U-sublattice in the crystal structures of β -$U(PO_3)_4$ (a), tetragonal $U(PO_3)_4$ (b), $(U_{0.62}Nd_{0.38})H_{0.38}(PO_3)_4$ (c). In the latter, only U atoms that form direct contacts are shown. 112
Figure 6.8: The Raman spectra of Raman spectrum of $Th(P_4O_{12})$. 114
Figure 7.1: Electronic-microscopic image of a crystal of $Th(As^{III}_4As^{V}_4O_{18})$. 120
Figure 7.2: A view of the crystal structure of $Th(As^{III}_4As^{V}_4O_{18})$. ThO_8, AsO_4, and AsO_3 coordination polyhedra are yellow, green, and magenta, respectively, and O atoms are red. $[As^{III}_4As^{V}_4O_{18}]^{4-}$ layer is marked with blue. 121
Figure 7.3: The simplification procedure applied to the $(As^{III}_4As^{V}_4O_{18})^{4-}$ layers. O, As^{III} and As^{V} atoms are red, green, and magenta, respectively. In graph representation, As^{III} and As^{V} nodes are black and grey, respectively. 123
Figure 7.4: The arsenic layers (a–c) and their graph representation (d–f) in the crystal structures of monoclinic-As_2O_3, $As^{III}_2As^{V}O_5(OH)$, and $Th(As^{III}_4As^{V}_4O_{18})$. The color scheme is the same as in Fig. 7.3. Blue and red transparent circles marks nodes and corresponding AsO_4 tetrahedra and $As^{III}_2As^{V}_2O_9$ ring fragments that are implemented in the edges of initial As_2O_3 layer on each step in the (d) – (e) – (f) series. 124
Figure 7.5: The Raman spectra of Raman spectrum of $Th(As^{III}_4As^{V}_4O_{18})$. 125
Figure 7.6: The comparison of the structure of (a) $LiTh_2(PO_4)_3$ (b) $ATh_2(AsO_4)_3$(A= K, Rb, Cs, Ag) and $BU^{IV}_2(PO_4)_3$ (B= Rb, Cs). ThO_8, As(P)O_4 coordination polyhedra are yellow and green, respectively, and O atoms are red; black dot is U atom, white dot is As(P) atom. 133

Figure 7.7: The comparison of the structure of (a) $RbTh(P_3O_{10})$ (b) $ATh(As_3O_{10})$ (A= Rb, Cs). ThO_8, $As(P)O_4$ coordination polyhedra are yellow and green, respectively, and O atoms are red; black dot is U atom, white dot is As(P) atom. 138

TABLES

Table 1.1: Oxidation states of actinides (most stable forms are highlighted) 3
Table 1.2: Bond length of U(IV)–O 5
Table 1.3: Bond length of Th(IV)–O 5
Table 1.4: Average <***T*** –O> bond length in the $(\boldsymbol{T}^{q+}O_m)^{n-}$ group (m = 3, 4; q = 3, 5; ***T*** = As, P) 6
Table 2.1: New thorium and uranium bearing phosphate and arsenate compounds obtained in this work. 15
Table 2.2: Cell parameters for all thorium and uranium bearing phosphates and arsenates (without the e.s.d) obtained within this work 16
Table 3.1: The Experimental Reactants used in this chapter 29
Table 3.2: Synthesis data and crystal profile of **RbUAs-1**, **2**, and **3** 29
Table 3.3: Crystallographic Data for **RbUAs- 1**, **2**, and **3** 31
Table 3.4: Selected interatomic distances /Å in the structure **RbUAs-1**, **2**, and **3** 32
Table 3.5: EDX elemental analysis and stoichiometry for **RbUAs- 1**, **2**, and **3** 33
Table 3.6: Bond-valence analysis for **RbUAs- 1** 34
Table 3.7: Bond-valence analysis for **RbUAs- 2** 34
Table 3.8: Bond-valence analysis for **RbUAs- 3** 35
Table 3.9: Coordination environment of rubidium atoms in the structures of **RbUAs-1**, **2** and **3,** i) Compound coordination center layer, ii) A in **RbUAs-1**, iii) Layer B in **RbUAs-2**, iv) Layer A, C in **RbUAs-3**, v) Layer above, vi) Interlayer Space, vii) Layer below, r is distance of Rb-O, Å 41
Table 3.10: Possible hydrogen bonds in **RbUAs-1**, **2** and **3**, and distances [Å] between supposed donor and acceptor oxygens. # denotes intralayer hydrogen bonds. 42
Table 3.11: Raman band positions in **RbUAs- 1**, **2**, and **3** 48
Table 4.1: The Experimental Reactants used in this chapter 54
Table 4.2: Synthesis data and crystal profile of $A_2Th(AsO_4)_2$ (A = Li, Na, K, Rb, Cs) 54
Table 4.3: Crystallographic data for $A_2Th(AsO_4)_2$ (A=Li, Na, K, Rb, Cs) 55
Table 4.4: EDX elemental analysis and stoichiometry for $A_2Th(AsO_4)_2$ A = (Li, Na, K, Rb, and Cs). 57
Table 4.5: Bond-valence analysis for $Li_2Th(AsO_4)_2$ 63
Table 4.6: Bond-valence analysis for $Na_2Th(AsO_4)_2$ 63
Table 4.7: Bond-valence analysis for $K_2Th(AsO_4)_2$ 64
Table 4.8: Bond-valence analysis for $Rb_2Th(AsO_4)_2$ 64
Table 4.9: Bond-valence analysis for $Cs_2Th(AsO_4)_2$ 65
Table 4.10: Values resulting from the fitting of the temperature-dependent metric parameters 76
Table 4.11: Assignment of selected Raman bands corresponding to AsO_4 vibrational modes, a) the data of this study; b) the data of known Ref; c) assignment; d) Ref. Nr. 80
Table 5.1: The Experimental Reactants used in this chapter 87
Table 5.2: Synthesis data and crystal profile of $A_2Th(PO_4)_2$ (A = Li, Na, K, Rb, Cs) 87
Table 5.3: Crystallographic data for $\mathbf{A}_2Th(PO_4)_2$ (**A** = Li, Na, K, Rb, Cs) 88

Table 5.4: Selected interatomic distances /Å in the structure $\mathbf{A}_2Th(PO_4)_2$ (**A** = Li, Na, K, Rb, Cs) 88
Table 5.5: Bond-valence analysis for $Li_2Th(PO_4)_2$ 90
Table 5.6: Bond-valence analysis for $Na_2Th(PO_4)_2$ 91
Table 5.7: Bond-valence analysis for $K_2Th(PO_4)_2$ 92
Table 5.8: Bond-valence analysis for $Rb_2Th(PO_4)_2$ 92
Table 5.9: Bond-valence analysis for $Cs_2Th(PO_4)_2$ 92
Table 5.10: The distances between alkaline cation within the cages in $\mathbf{A}_2Th(\boldsymbol{T}O_4)_2$ (**A**= **Na**, **K**, **Rb**, **Cs**; ***T***= **P** and **As**) 97
Table 6.1: Crystallographic data for tetragonal $U(PO_3)_4$, "$(U_{0.62}Nd_{0.38})(PO_3)_4$", $Th(P_4O_{12})$, and $U(P_4O_{12})$ 103
Table 6.2: Bond distances in the crystal structures of tetragonal $U(PO_3)_4$, "$(U_{0.62}Nd_{0.38})(PO_3)_4$", and $Th(P_4O_{12})$. 104
Table 6.3: Quantitate amounts of Th, U, Nd, and P (found by EDS and calculated according to formula) in the crystal of tetragonal $U(PO_3)_4$, $(U_{0.62}Nd_{0.38})(PO_3)_4$, $Th(P_4O_{12})$, and $U(P_4O_{12})$ 106
Table 6.4: Polymorphic modifications of U(IV) and Th metaphosphates 113
Table 6.5: Determined Raman Bands (cm^{-1}) for $Th(P_4O_{12})$ 115
Table 7.1: The Experimental Reactants used in this chapter 119
Table 7.2: Crystallographic data for $Th(As^{III}_4As^{V}_4O_{18})$ 120
Table 7.3: EDX elemental analysis and stoichiometry for $Th(As^{III}_4As^{V}_4O_{18})$ 120
Table 7.4: Assignment of selected Raman bands corresponding to AsO_3 and AsO_4 vibrational modes 126
Table 7.5: The experimental reactants used in this chapter 127
Table 7.6: Synthesis data and crystal profile of $ATh_2(AsO_4)_3$(A= K, Rb, Cs, Ag) and $LiTh_2(PO_4)_3$ 128
Table 7.7: Synthesis data and crystal profile of $BU^{IV}_2(PO_4)_3$ (B= Rb, Cs) 128
Table 7.8: Crystallographic data for the titled structures 129
Table 7.9: Bond-valence analysis for $KTh_2(AsO_4)_3$ 129
Table 7.10: Bond-valence analysis for $RbTh_2(AsO_4)_3$ 130
Table 7.11: Bond-valence analysis for $CsTh_2(AsO_4)_3$ 130
Table 7.12: Bond-valence analysis for $AgTh_2(AsO_4)_3$ 131
Table 7.13: Bond-valence analysis for $RbU^{IV}_2(PO_4)_3$ 131
Table 7.14: Bond-valence analysis for $CsU^{IV}_2(PO_4)_3$ 132
Table 7.15: The Experimental Reactants used in this chapter 135
Table 7.16: Synthesis data and crystal profile of $RbTh(\boldsymbol{T}_3O_{10})$ (***T***= P, As) 135
Table 7.17: Synthesis data and crystal profile of $CsTh(As_3O_{10})$ 135
Table 7.18: Crystallographic data for the titled structures 136
Table 7.19: Bond-valence analysis for $RbTh(P_3O_{10})$ 137
Table 7.20: Bond-valence analysis for $RbTh_2(AsO_4)_3$ 137
Table 7.21: Bond-valence analysis for $CsTh_2(AsO_4)_3$ 137

ACKNOWLEDGMENTS

First of all, I want to thank my parents who created and nurtured me and always gave me unconditional support.

I would like to thank my supervisor, Prof. Dr. Evgeny V. Alekseev, who offered me great help, both for study and life. He is such a generous mentor that navigated me through all the challenges and problems I encountered in every experiment. This has not only helped me lay a solid foundation in my study of solid state inorganic chemistry, but also widened my horizons in a very inspiring way.

My sincere gratitude goes to Prof. Dr. Dirk Bosbach without whom I would not have a chance to perform my PhD work in IEK-6.

Dr. Vladislav Klepov is another person I would like to say thank you. Together, we have produced many exciting results and I really appreciate the opportunity of working with him.

I want to thank Prof. Dr. Thorsten M. Gesing, who helped me with high temperature PXRD measurements.

I also want to thank Prof. Ning Ye, my supervisor of my postgraduate study, who enlightened me and from whom I learned a lot.

I'd also like to thank: Dr. Philip Kegler, Bin Xiao, Yucheng Hao, Eike Langer, Ralf König, Dr. Giuseppe Modolo, Dr. Hartmut Schlenz, Jakob Dellen, Dr. Sabrina Labs, Simone Weigelt, Dr. Martina Klinkenberg, Dr. Stefan Neumeier and all those who have kindly offered their help to me and especially a good friend of mine, Emily Sun.

Finally, I want to thank my defense committee members: Jun. -Prof. Dr. Evgeny V. Alekseev, Prof. Dr. Drik Bosbach, Prof. Thorsten M. Gesing and Prof. Dr. Georg Roth for their great help in my research and insightful suggestion for this dissertation.

Chapter 1 INTRODUCTION

1.1 Overview

In recent decades, the potential of phosphate actinide compounds as nuclear waste disposal hosts have been studied thoroughly[1], therefore many actinide phosphates were synthesized and characterized in the lab. In nature, phosphates (P^V) are commonly observed in phosphorus based minerals, and they are mainly responsible for the mobility of actinides not only in most groundwater but also in soils and sediments that are contaminated by actinides.[2, 3] Understanding the chemistry and behavior of the actinide phosphates is important for predicting actinide migration in nature and also for aspects of nuclear waste management.

In the past few decades, the chemistry of actinide elements is a matter of fundamental science and applied research. It is well known, that thorium and uranium are constantly found in the earth's crust and natural waters. However, the majority of transuranic elements are generated by nuclear reactors for commercial use.[4] Actinides are the only elements showing 5f electrons and it rises the interest to study their chemistry from a fundamental point of view. One of the interesting fields here is the inorganic chemistry of actinides, for example the structural diversity, new synthetic methods, and the chemical behavior of actinides in natural environments. However, very little data is available concerning the behavior of transuranic elements in nature, owing to their high radioactive toxicity.[5] So the less radioactive uranium and thorium were taken as the surrogate for studying the behavior of transuranic elements.[6-9] The coordination chemistry of Th(IV) and U(IV), for instance, is very similar to Np(IV) and Pu(IV).[10] And all the crystal chemistry of An(VI) is dominated by the layered motif, owing to their common tendency to form the liner $An(VI)O_2^{2+}$ group.[10]

The synthetic and structural chemistry of thorium and uranium are of great interest in respect to their geochemical behavior in nature. Thorium and uranium are concentrated in the earth's crust in an average Th/U ratio of about 3.5.[11] Th and U can also be found in the hydrosphere (sea water and fresh water), the biosphere (ore deposits), and the atmosphere.[12] The geochemistry of actinides will influence the formation of actinide bearing phases as well as the mobilization and transport of the actinides in natural environment.[13] Thorium commonly fixed in insoluble Th(IV) minerals, like monazite ($(REE,Th)PO_4$), thorianite (ThO_2), allanite ($(REE,Th)_2(Al,Fe^{+3})_3(SiO_4)_3(OH)$), zircon ($(REE,Th,Zr)SiO4$) et cetera. Uranium can either be transported in solution (as U(VI)) or in the solution-dissolution processes of minerals. Uranium is found in hundreds of minerals, the common known ones are uraninite (UO_2), carnotite($K_2(UO_2)_2(VO_4)_2 \cdot 3H_2O$), autunite ($Ca(UO_2)_2(PO_4)_2 \cdot 10\text{-}12H_2O$), uranophane

($Ca(UO_2)_2[HSiO_4]_2{\cdot}5H_2O$), torbernite ($Cu(UO_2)_2(PO_4)_2{\cdot}8\text{-}12H_2O$), and coffinite ($U(SiO_4)_{1-x}(OH)_{4x}$). Both Th and U are in the +4 oxidation state in the primary rocks, but uranium can be oxidized to the higher valence states +5 and +6 to form the soluble and highly mobile uranyl ions UO_2^{2+}. It has been reported in many studies that in the natural environment the mobility and solubility of actinides is decreased under reducing aqueous conditions, which could be beneficial for the long term stability of nuclear waste disposal.[14] There is a large number of phosphate or arsenate actinides(Th, U) minerals in the natural environment. For example, there are around 60 U bearing phosphates (althupite, autunite, bassetite, bergenite, 'cheralite-(Ce)', chernikovite, coconinoite etc.), 38 U bearing arsenates (abernathyite, arsenovanmeersscheite, arsenuranospathite, arsenuranylite, asselbornite, chadwickite etc.), 14 Th bearing phosphates (althupite, brockite, cheralite, eylettersite, grayite, monazite etc.) and only 1 Th bearing arsenate (vicanite-(Ce)). Among them, one of the well-known phosphate actinide mineral, monazite, was proposed as a potential nuclear waste form, because of its outstanding advantages including lower solubility and higher resistance to corrosion.[15]

Uranium shows diverse coordination chemistry, owing to the oxidation state ranges from +2 to +6. Till now, there are many studies have been reported regarding the synthesis and the relationship between structure and chemical or physical properties of the uranium oxo-phosphorus (III/V) phases. However, uranium oxo-arsenic (III/V) phases have barely been studied, which should exhibit common properties with phosphate analogues. Comparing to the uranium, the lower oxidation state Th has larger coordination numbers, which will increase their structural complexity.

Obviously, the study of the structures and behavior of uranium and thorium-bearing oxo-phosphorus (III/V) and oxo-arsenic (III/V) phases would be of great significance since they offer the possibility to predict the long term behavior of actinide-bearing phases.

1.2 Background I: Structural Chemistry of Uranium and Thorium

Structural chemistry of uranium and thorium is rich owing to the variety of oxidation states (from +2 to +6 for U and from +2 to +4 for Th) and, therefore also a large diversity of their coordination geometries.

1.2.1 Oxidation States of Uranium and Thorium

The maximum value of the oxidation state of early actinides corresponds to the number of electrons within the 'outer shell'.[16] Therefore, chemical forms presented by thorium is limited to a large extent to the +2, +3 and +4 state, however, uranium's oxidation states varies in +2, +3, +4, +5 and +6.

Among all the oxidation states of uranium, which range from +2 to +6, the most important ones are uranium(IV) and uranium(VI). In nature, there are some uranium oxides

such as diuranium pentoxide (U_2O_5) and uranium peroxide ($UO_4 \cdot 2H_2O$), while the most common forms of the uranium oxide are triuranium octoxide (U_3O_8) and uranium dioxide (UO_2).[17] U_3O_8 is, to some extent and subject to conditions, the most stable form of uranium in natural conditions.[18] UO_2, on the other hand, is the form of uranium that is frequently used as a fuel in a nuclear reactor. UO_2 would slowly convert into U_30_8 at ambient temperature on air. Since uranium oxides are very stable forms, they have been seen as priority forms to store or dispose nuclear waste.[19] Uranium compounds show mostly yellow and green color when it is in oxidation states VI and IV, respectively.

For thorium, +4 is referred as the most significant oxidation state, whilst existing in oxo-compounds. Because the 6d and 5f orbitals of thorium(IV) lack electrons, there is no color presented in tetravalent thorium compounds.[20]

Table 1.1: Oxidation states of actinides (most stable forms are highlighted)

	Oxidation States	Known oxides and hydroxides
U	2 3 <u>4</u> 5 <u>6</u>	$UO_4 \cdot 2H_2O$; U_2O_5; <u>U_3O_8</u>; <u>UO_2</u>; UO_3
Th	2 3 <u>4</u>	<u>ThO_2</u>; $Th(OH)_4$

Th(IV), as the only stable oxidation state, dominates the structural chemistry of thorium. For the U(VI), which commonly forms the near-linear uranyl ion UO_2^{2+}, the U═O bond distances is around 1.78 Å. The sum valence unit for the O atom is 2 v.u., while the average valence unit of the O atom in the uranyl ion is around 1.6 to 1.7 v.u., which means there are only 0.4 to 0.3 v.u. left for the uranyl O atom to be bonded to other donor ligands. It is obvious that the uranyl O atom lacks sufficient bond valence to be bonded to other donor ligands. Therefore, crystal chemistry of uranium (VI) is dominated by sheet of polymerized polyhedrals.[21] The number of U(V) crystal structures are comparatively limited in the Inorganic Crystal Structure Database (ICSD).

1.2.2 Coordination Numbers and Coordination Polyhedra of Uranium and Thorium

Usually, U(VI) forms the linear uranyl group (UO_2^{2+}) with variable numbers of bonding partners in the equatorial plane, most commonly four, five or six, which gives rise to the formation of square, pentagonal or hexagonal bipyramids.[10, 22] The coordination environment of U(IV) shares the similarity to that of Th(IV), which presents a variable amount of coordination numbers. (Fig. 1.1) This ranges from six-coordinate to twelve-coordinate, of which the eight and nine are the most common. The actinide polyhedra build isolated clusters in the form of 1D chains, 2D sheets and 3D frameworks by linking each other by corners and edges or by bridging groups. Fig. 1.2 illustrates some typical coordination modes between actinide polyhedra and a bridging group, which is quite normal to be observed in all compounds mentioned in this dissertation. [10]

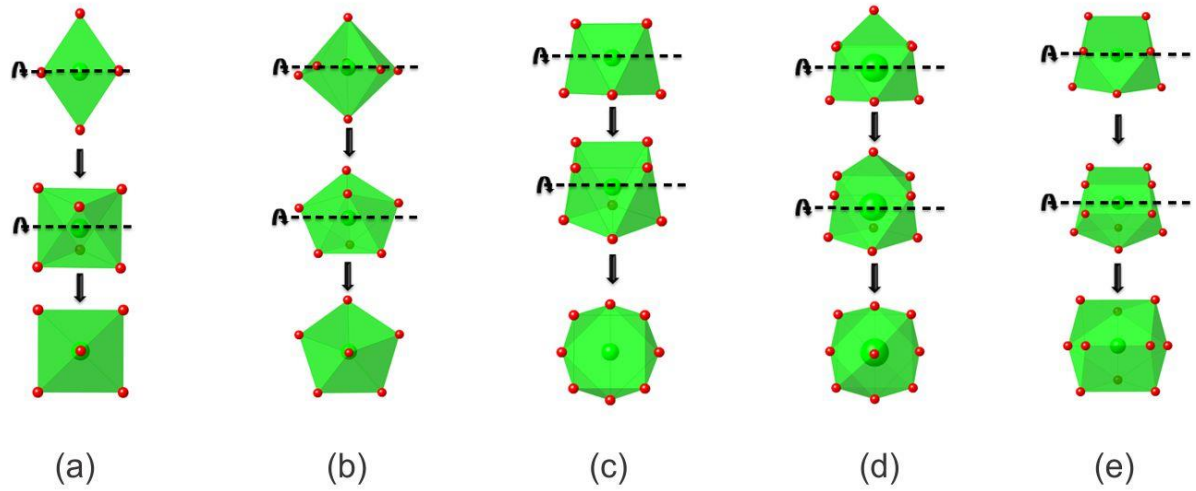

***Figure 1.1**: Common coordination environment of the **An**O_X(X= 6, 7, 8, 9, 10) (**An** = U^{IV}, Th^{IV}) polyhedra, (a) 6-coordinated: tetragonal bipyramid; (b) 7-coordinated: pentagonal bipyramid; (c) 8-coordinated: square antiprism; (d) 9-coordinated: monocapped square antiprism; (e) 10-coordinated: bicapped square antiprism. Uranium and Thorium polyhedra are shown in green, O atoms are red.*

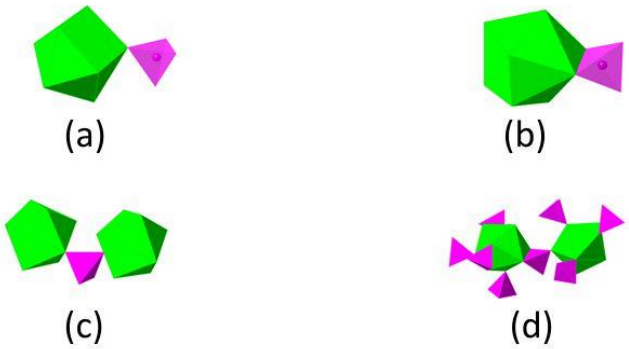

***Figure 1.2:** Some examples of the coordination modes between the actinide polyhedra and the bridging group (in this dissertation, i.e. PO_4 and AsO_4), (a) Monodentate; (b) Bidentate-chelating; (c) Bidentate-bridging; (d) Tridentate-bridging. Actinide (U^{IV}, Th^{IV}) polyhedra are shown in green, PO_4 and AsO_4 in magenta.*

The bond length for U–O is listed in Table 1.2, the data were concluded from this work. For Th–O the same is shown in Table 1.3, accordingly.

Table 1.2: Bond length of U(IV)–O

Coordination number	Bond length [Å]	
	range	mean
8	2.24-2.55	2.38
9	2.29-2.61	2.44

Table 1.3: Bond length of Th(IV)–O

Coordination number	Bond length [Å]	
	range	mean
8	2.32-2.55	2.43
9	2.32-2.69	2.48
10	2.34-3.00	2.58

1.3 Background II: Structural Chemistry of Phosphates/Phosphites and Arsenate/ Arsenites

Phosphates are being actively investigated owing to their potential as nuclear waste storage hosts.[15, 23] In particular, the phosphate minerals and glasses display a remarkably low solubility, a slow dissolution rate, a high resistance to corrosion and great resistance to radiation damage.[24] From a structural chemical point of view, phosphorus atoms can adopt a rich coordination environment which results in diversity of their structural chemistry (Fig. 1.3). Phosphorus bonds to oxygen atoms not only in three-fold (triangle, $P^{III}O_3$) coordination, but also in four-fold coordination (tetrahedron, $P^{V}O_4$) depending on its oxidations state. Larger polyphosphate anions, like the P_2O_7 dimer, the P_3O_{10} trimer, the P_4O_{10} tetramer or the infinite polymeric PO_3 chain [25-30] are formed by corner sharing PO_4 groups. These groups, including PO_4, can be taken as the Fundamental Building Blocks (FBBs).[31, 32]

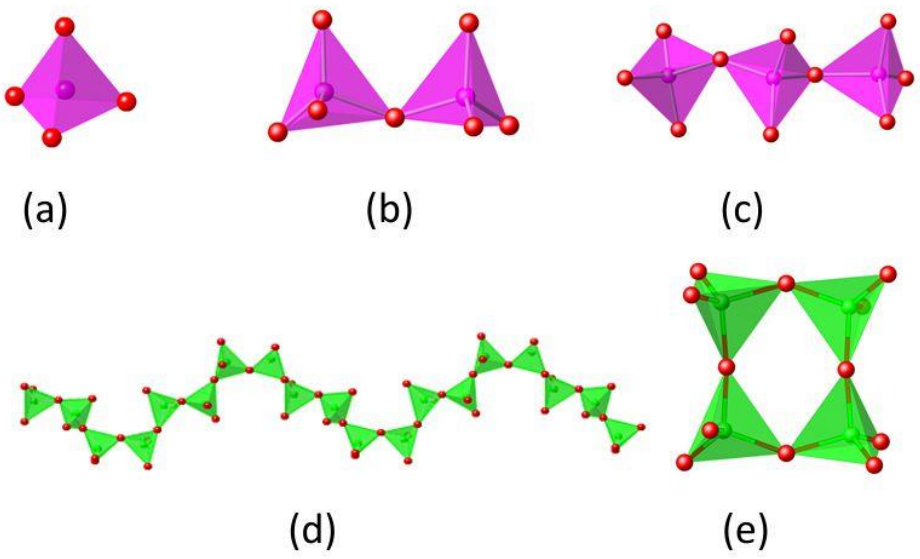

***Figure 1.3**: Basic coordination polyhedra of phosphate and arsenate, (a) **T**O_4 single tetrahedron; (b) $\boldsymbol{T_2O_7}$ dimer; (c) $\boldsymbol{T_3O_{10}}$ trimer; (d) Infinite polymeric **T**O_3 chain; (e) Cyclic tetramer-phosphate/ arsenate anion $\boldsymbol{T_4O_{12}}$. (**T** = P and As) phosphate and arsenate polyhedra are magenta or green.*

The coordination chemistry of As^{V} is similar to that of P^{V}. As^{V} is also connected to four O atoms and forms a tetragonal polyhedron. For P^{III} and As^{III} however, the coordination chemistry is different. Conceptually, the phosphite anion is made up of the $[PO_4]^{3-}$ group. The tetrahedral $[HPO_3]^{2-}$ phosphite anion can be formed via changing P^{V} to P^{III} in the $[PO_4]^{3-}$ group and exchanging the position of one of the oxygen atoms by a hydrogen atom. However, the structure is different, when it comes to the arsenic analog $[HAs^{III}O_3]^{2-}$.[33] Here, two oxygen atoms and one $(OH)^{-}$ group are bonded to As^{III} with the formation of a trigonal-pyramidal coordination.[22]

The average bond length of the ***T*** –O (***T*** = As and P) is listed in Table 1.4. The data were concluded by Sergey V. Krivovichev.[10]

Table 1.4: Average <***T*** –O> bond length in the $(\boldsymbol{T}^{q+}O_m)^{n-}$ group (m = 3, 4; q = 3, 5; ***T*** = As, P)

m	T	q	<***T*** –O> [Å]	Reference
4	P	5+	1.537	Huminicki and Hawthorne 2002
	As	5+	1.682	Baur 1981
3	P	3+	1.496	Villa and Albrecht- Schimit 2012
	As	3+	1.788	Krivovichev 2007

1.4 Background III: Overview of some known Uranium and Thorium bearing Phosphates/Phosphites and Arsenates/Arsenites

There are many synthetic methods for synthesizing phosphate/phosphite and arsenate/arsenite compounds. The most important ones are hydrothermal methods, high temperature solid state fluxes and room temperature slow evaporation methods.

A large number of different structure types of uranium and thorium phosphates and arsenates has been reported[27, 30, 34-39]. It includes well-known structure types of eulytine[40-43], kosnarite[44-46], $Zr_2O(PO_4)_2$[47-49], $UPO_4Cl(H_2O)_2$[50], scheelite[51, 52], zircon[53-56], rhabdophane[57-59], $KTh_2(PO_4)_3$[6, 54, 60-66], monazite[67, 68], ZrP_2O_7[36], $Th_4(PO_4)_4P_2O_7$[24, 69], $U_2PO_4(P_3O_{10})$[70-72], $Zr(PO_3)_4$[38, 39], autunite[73-76], phosphuranylite[77-79] et cetera. As mentioned, the O atom in the uranyl group does not have enough valence units to link up with other donor ligands, therefore uranyl orthophosphate and orthoarsenates are mainly dominated by the layered structure, among which autunite-type sheets are the most commonly seen, with general stoichiometry: $A_n[(UO_2)(\boldsymbol{T}O_4)]_n(H_2O)_m$ [80], where A = monovalent, divalent or trivalent cations, and ***T*** = P or As.[10]

According to the Inorganic Crystal Structure Database (ICSD) and other literature, numerous researches have been reported in the field of uranium phosphate and arsenate structural chemistry. However, when it comes to the thorium phosphates and arsenates, the data for thorium bearing phosphates is very limited and data for thorium arsenates is even more limited. This dissertation is aims at a deep study of synthetic and structural chemistry of uranium (IV) and thorium (IV) phosphates and arsenates.

1.5 References

1. C. Rodney; Wang, L. M., *Rev. Miner. Geochem.,* **2002,** *48* 673-699.
2. T. Murakami; T. Ohnuki; H. Isobe; T. Tsutomu, *Am. Mineral.,* **1997,** *82*, 888.
3. R. Finch; T. Murakami, *Rev. Mineral.,* **1999,** *38*, 91.
4. Dozol, M.; Hagemann, R., Radionuclide migration in groundwaters: Review of the behaviour of actinides (Technical Report). In *Pure and Applied Chemistry*, 1993; Vol. 65, p 1081.
5. Allard, B.; Olofsson, U.; Torstenfelt, B., *Inorganica Chimica Acta* **1984,** *94*, 205-221.
6. V. Brandel; N. Dacheux, *J. Solid. State. Chem.,* **2004,** *177*, 4755-4767.
7. R. Philippe E.; J. Regis; B. Daniel; M.K. Rudy; G. Thorsten; P. Claudiu C.; R. Jean; P. Karin, *Phys. Chem. Miner.,* **2008,** *35*, 603-609.
8. E.M. Villa; S. Wang; E.V. Alekseev; W. Depmeier; T.E. Albrecht-Schmitt, *Eur. J. Inorg. Chem.,* **2011,** *2011*, 3749-3754.
9. W. Gilles; B. Damien; P. Karin; R. Philippe E.; A. Christos; L-R. Patric; Konings; J.M. Rudy; Popa; F. Aurelian, *European Journal of Inorganic Chemistry,* **2011,** *2011*, 110-115.
10. S.V. Krivovichev; P.C. Burns; I.G. Tananaev, *Structural Chemistry of Inorganic Actinide Compounds*. Elsevier: Amsterdam, 2007.
11. Rogers;, J.; Adams;, J., *Handbook of geochemistry*. Springer Berlin: KH Wedepohl 1969.
12. Adams, J. A. S.; Osmond, J. K.; Rogers, J. J. W., *Physics and Chemistry of the Earth* **1959,** *3*, 298-348.
13. Gascoyne, M.; Ivanovich, M.; Harmon, R. S., *Geochemistry of the actinides and their daughters*. Clarendon Press: United Kingdom, 1992.
14. Grambow, B., *Journal of Contaminant Hydrology* **2008,** *102*, 180-186.
15. E.H. Oelkers; J.M. Montel, *Mineral. Soc. America,* **2008,** *4*, 113-116.
16. K. L. Ziegelgruber; K. E. Knope; M. Frisch; C. L.Cahill, *J. Solid State Chem,* **2008,** *181*, 373.
17. Seaborg; Glenn T., *The Encyclopedia of the Chemical Elements. Skokie, Illinois: Reinhold Book Corporation*. Reinhold Book Corporation: Skokie, Illinois, 1968.
18. S.M. Thein; P.J. Bereolos, Thermal Stabilization of 233UO2, 233UO3, and 233U3O8. In OAK RIDGE NATIONAL LABORATORY: Oak Ridge, Tennessee 37831-6285, 2000.
19. Davidovits, J., *Concrete International* **1994,** *16*, 53-58.
20. Hoffman, D. C.; Lawrence, F. O.; Mewherter, J. L.; Rourke, F. M., *Nature,* **1971,** *234*, 132–134.
21. Burns, P. C., *Am. Mineral.* **1999,** *84*, 1661-1673.
22. N. Yu; V.V. Klepov; E.M. Villa; D. Bosbach; E.V. Suleimanov; W. Depmeier; T.E. Albrecht-Schmitt ; Alekseev, E. V., *J.Solid State Chem.* **2014,** *215*, 152-159.
23. R.C. Ewing; L.M. Wang, *Mineral. Soc. America,* **2002,** *48*, 673-699.
24. N. Dacheux; R. Podor; V. Brandel; M. Genet, *J. Nucl. Mater.,* **1998,** *252*, 179.

25. E.V. Alekseev; S.V. Krivovichev; W. Depmeier; K. Knorr, *Z. Anorg. Allg. Chem.,* **2008,** *634*, 1527-1532.
26. N.C. Justin; E.M. Villa; S. Wang; J. Diwu; M.J. Polinski; T.E. Albrecht-Schmitt, *Inorg. Chem.,* **2012,** *51*, 8419-8424.
27. E.V. Alekseev; S.V. Krivovichev; W. Depmeier, *Z. Anorg. Allg. Chem.,* **2007,** *633*, 1125-1126.
28. E.V. Alekseev ; S.V. Krivovichev ; W. Depmeier, *J. Mater. Chem.,* **2009,** *19*, 2583-2587.
29. E.V. Alekseev; S.V. Krivovichev; W. Depmeier, *Cryst. Growth Des.,* **2011,** *11*, 3295-3300.
30. E.V. Alekseev ; S.V. Krivovichev ; W. Depmeier, *J. Solid State Chem.,* **2009,** *182*, 2977-2984.
31. P.C. Burns; J.D. Grice; F.C. Hawthorne, *Can. Mineral.,* **1995,** *33*, 1131.
32. J.D. Grice; P.C. Burns; F.C. Hawthorne, *Can. Mineral.,* **1999,** *37*, 731-762.
33. V. Brandel; N. Dacheux; M. Genet, *Radiochem.,* **2001,** *43*, 16-23.
34. E.V. Alekseev; S.V. Krivovichev; T. Malcherek; W. Depmeier, *J. Solid State Chem.,* **2008,** *181*, 3010-3015.
35. E.V. Alekseev ; S.V. Krivovichev ; W. Depmeier, *J. Solid State Chem.,* **2009,** *182*, 2074-2080.
36. A. Cabeza; M.A.G. Aranda; F.M. Cantero; D. Lozano; M. Martínez-Lara; S. Bruque, *J.Solid State Chem.,* **1996,** *123*, 181.
37. Z. Ruzic Toros; B. Kojic-Prodic; R. Liminga; S. Popovic, *Inorg. Chim. Acta,* **1974,** *8*, 273.
38. G. Masse, *Bull. Soc. Fr. Mineral. Cristallogr.,* **1972,** *95*, 136.
39. S.A. Linde; Yu.E. Gorbunova; V.V. Ilyukhin; A.V. Lavrov; V.G. Kuznetsov, *Zh.Neorg. Khim.,* **1979,** *24*, 1786.
40. Sheldrick, G. M., *Acta Crystallogr. A* **2007,** *64*, 112.
41. Farrugia, L. J., *J. Appl. Crystallogr.* **2012,** *45*, 849.
42. Blatov, V. A.; Shevchenko, A. P.; Serezhkin, V. N., *J. Appl. Crystallogr.* **2000,** *33*, 1193.
43. Blatov, V. A.; Serezhkin, V. N., *Russ. J. Inorg. Chem.,* **2000,** *45*, S105.
44. E.R. Gobechiya; Yu. K. Kabalov; S.V. Tomilin; A.N. Lukinykh; A.A. Lizin; A.I.Orlova, *Cryst. Rep.,* **2005,** *50*, 374.
45. A.A. Burnaeva; Yu. F. Volkov; A.I. Kryokuva; I.A. Korshunov; O.V. Skiba, *Sov.Radiochem.,* **1992,** *34*, 528.
46. Yu.F. Volkov; S.V. Tomilin; A.I. Orlova; A.A. Lizin; Vi. Spiryakov; A.N. Lukinykh, *Radiochem.,* **2003,** *45*, 319.
47. V. Brandel; N. Dacheux, *J. Solid State Chem.,* **2004,** *177*, 4755.
48. J.H. Albering; W. Jeitschko, *Z. Krist.,* **1995,** *210*, 878.
49. P. Bénard; D. Louër; N. Dacheux; V. Brandel; M. Genet, *Anales Quim. Int. Ed.,* **1996,** *92*, 79.

50. P. Bénard-Rocherullé; M. Louër; D. Louër; N. Dacheux; Brandel, V.; M. Genet, *J. Solid State Chem.,* **1997,** *132*, 315.
51. M.A. Nabar; S. Mangaonkar, *J. Mater. Sci. Lett.,* **1994,** *13*, 225.
52. M.A. Nabar; R.R. Sakhardande, *J. Less-Common Metals,* **1985** *110*, 415.
53. M.A. Nabar; R.R. Sakhardande, *J. Crystallogr. Spectrosc. Res.,* **1985** *15*, 263.
54. M. Pagès; W. Freundlich, *Plutonium 1975 and other Actinides,* **1976**, 205.
55. W. Freundlich; A. Erb; M. Pagès, *Rev. Chim. Miner.,* **1974** *11*, 598.
56. Y. Dusausoy; N.E. Ghermani; R. Podor; M. Cuney, *Eur. J. Mineral.,* **1996,** *8*, 667.
57. F.G. Fisher; R. Meyrowitz, *Am. Mineral.,* **1962,** *47*, 1346.
58. D. Atkin; I. R. Basham; J. F. W. Bowles, *Mineral. Mag.,* **1983,** *47*, 393.
59. C.W. Bjorklund, *J. Am. Chem. Soc.,* **1958,** *79*, 6347.
60. B. Matkovic; B. Prodic; Sljukic, M., *Croat. Chem. Acta,* **1968,** *40*, 147.
61. J. Keester, *Ferroelectrics,* **1974,** *8*, 657.
62. A. Guesdon; J. Provost; B. Raveau, *J. Mater. Chem.,* **1999,** *9*, 2583.
63. B. Matkovic; B. Kojic-Prodic; M. Sljukic; M. Topic; R.D. Willett; F. Pullen, *Inorg. Chim. Acta,* **1970,** *4*, 571.
64. M. Laügt, *J. Appl. Crystallogr.,* **1973,** *6*, 299.
65. H.T. Hawkins; D.R. Spearing; D.K. Veirs; J.A. Danis; D.M. Smith; C.D. Tait; W.H. Runde, *Chem. Mater.,* **1999,** *11*, 2851.
66. R.M. Hazen; L.W. Finger; J.W.E. Mariathasan, *J. Phys. Chem. Solids,* **1985,** *46*, 253.
67. D.B. Kitaev; Yu. F. Volkov; A.I. Orlova, *Radiochem.,* **2004,** *46*, 211.
68. J.-M. Montel; J.-L. Devidal; D. Avignant, *Chem. Geol.,* **2002,** *191*, 89.
69. P. Bénard; V. Brandel; N. Dacheux; S. Jaulmes; S. Launay; C. Lindecker; M. Genet; D. Louër; M. Quarton, *Chem. Mater.,* **1996,** *8*, 181-188.
70. A. Burdese; M.L. Borlera, *Ann. Chim. (Rome),* **1963,** *53*, 344.
71. R. Podor; M. François; N. Dacheux, *J. Solid State Chem.,* **2003,** *172*, 66.
72. G. Le Flem; J. Lamic; P. Hagenmuller, *Bull. Soc. Chim. Fr.,* **1966,** *6*, 1880.
73. A.J. Locock; P.C. Burns; M.J.M. Duke; T.M. Flynn, *Can. Mineral.,* **2004,** *42*, 973.
74. B. Morosin, *Acta Cryst.,* **1978,** *B34*, 3732.
75. A.N. Fitch; B.E.F. Fender; A.F. Wright, *Acta Cryst.,* **1982,** *B38*, 1108.
76. M. Ross; H.T. Evans, *Amer. Mineral.,* **1964,** *49*, 1578.
77. P. Piret; M. Deliens; J. Piret-Meunier, *Bull. Minéral.,* **1988,** *111*, 443.
78. P. Piret; J.-P. Declercq, *Bull. Minéral.,* **1983,** *106*, 383.
79. L.I. Belova; Zap.Vses., *Mineral. Obsch.,* **1958,** *87*, 598.
80. A.J. Locock; P. C. Burns; M.J.M. Duke; T.M. Flynn, *Can. Miner.,* **2004,** *42*, 973-996.

Chapter 2 SYNTHETIC METHODS AND CHARACTERIZATION TECHNIQUES

2.1 Synthetic Methods

2.1.1 Hydrothermal Synthetic Method

Hydrothermal synthesis is commonly used to synthesize single crystals, whose solubility is higher under high pressure and high temperature and low under ambient conditions. Karl Emil von Schafhäutl (1803-1890), the German geologist, was the first to publish the result of growing crystals through the hydrothermal method.[1] Hereby, an autoclave, a container composed of a steel pressure vessel, is applied. Together with choosing the reactants and a certain amount of water, sometimes pH needs to be adjusted to achieve the desired conditions.

In this dissertation, the reactants were mixed in their appropriate ratios and loaded into a 23 mL PTFE-lined autoclave together with appropriate distilled water. After sealing, the autoclave was placed into a programmable box furnace. The furnace was ramped up to an aimed temperature, held there for a certain time and then slowly cooled down to room temperature at a certain rate.[2] Fig. 2.1 depicts the experimental procedure for the hydrothermal method applied in this dissertation.

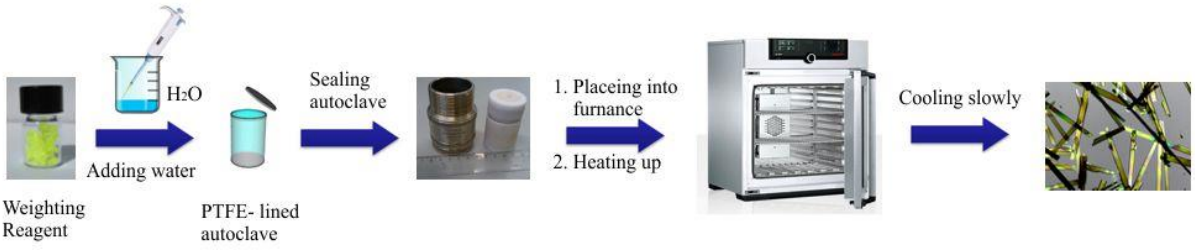

***Figure 2.1**: The experimental procedure for the hydrothermal method*

2.1.2 High Temperature (**HT**) Solid State Synthesis

When preparing polycrystalline solids from a bundle of solid starting materials, the most commonly applied method is the solid-state reaction. **HT** reaction is the most common method for synthesizing the polycrystalline compounds from the solid reactants. As solids tend to not react with each other at normal temperature in reasonable experiment times, it is essential to provide them with higher temperatures, usually ranging from 450 to 1500 °C, to perform the reaction.[3]

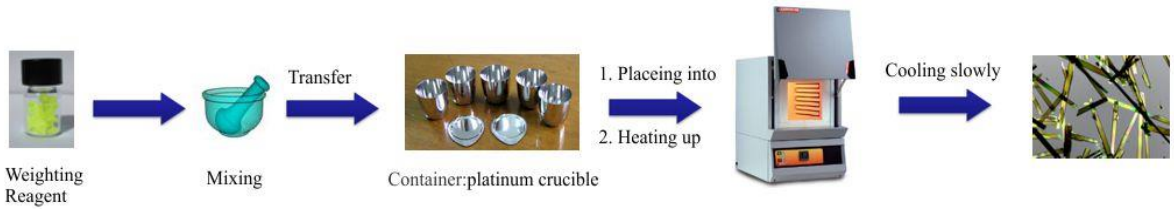

***Figure 2.2**: The experimental processes of the **HT** method*

Ref. [3, 4] elaborate some factors that play an important role during the solid state reaction, such as reaction conditions, reactant structures, surface area of the materials, reactivity among solids and the thermodynamic free energy change. The procedure of the experiment is shown in Fig. 2.2. After weighting the reactants with their appropriate ratio, the reactants are mixed fully. It is noteworthy, that mixing fully is of upmost importance, because enlarging the surface area enhances the reaction. There the details of mixing are also expressed. When mixing reactants in small quantities, a manual mixing method is applied. Here, an agate mortar and pestle is used for grinding and mixing at the same time. When the procedure goes on, some volatile organic liquid as acetone or alcohol is added to the solids by sufficient amount to achieve aimed homogenization. This process continues until the mixture forms a paste. The organic liquid would normally evaporate thoroughly 10 to 15 minutes after the process started. For large quantities far beyond ~20 g, mechanical mixing is employed with a ball mill which may take several hours. In this dissertation, only small quantities of reactants were needed. Considering the appropriate container material is critical when the reaction taking place under high temperatures. Therefore, the container should be made of chemically inert materials for the reactants. Taking this into consideration, in this dissertation, platinum crucibles were applied to conduct the synthesis of single crystals.

As Fig. 2.2 shows, in this dissertation, the reactants were thoroughly ground together with their appropriate ratios and loaded into a platinum crucible. The reaction mixture was then placed into a program-controlled furnace (CARBOLITE CWF 1300) and heated to the aimed temperature by heating with a certain rate. The homogenized melt solution was then cooled slowly with a certain rate to the final crystallization temperature and then allowed to cool down to the room-temperature by powering off the furnace.

2.1.3 High-Temperature High-Pressure (**HTHP**) Synthetic Method

When given a high external pressure, polymorphic phase transformation and reactions of different materials may occur, creating new phase or novel materials. Normally, when this high pressure is relieved, most of the structures and properties of the materials that have

been changed under the high pressure would reversibly return to their previous forms and status. Therefore, studying the materials under high pressure environment may help people to gain a better knowledge of the physical phenomena and characteristics of the materials and, at the same time, some new features of the materials that may not emerge under normal conditions.

Various devices can be used in a high-pressure experiment, when the pressure is between 0.1 and 500 GPa, for instance, Piston-cylinder and Belt-apparatus, the former capable of reaching a pressure of 3 GPa, while the latter 10 GPa. Comparatively, the cap of pressure of a Walker-type multi anvil module is 25 GPa.

In this dissertation, the piston cylinder module of a Voggenreiter LP 1000-540/50 (Forschungszentrum Jülich, IEK-6) was applied, to synthesize single crystals at high temperatures and high pressures (up to 2000^{o}C and 25 GPa) was applied. Philip Kegler helped the author to carry out the HTHP experiments. As in our publication[5] described that, "the reactants were mixed together and finely grounded with the proper ratio. Then, the mixture was filled into a Platinum capsule (outer diameter: 4mm, wall thickness: 0.2 mm, length: 7 mm). The capsule was sealed on both sides with an impulse micro welding device (Lampert PUK U4) and placed into the center of a ½-inch piston cylinder talc-pyrex assembly. Therefore the capsule was inserted into a 6 mm diameter MgO spacer and positioned in the center of a tapered graphite furnace. The graphite furnace was contained in sleeves of pyrex glass and pyrophyllite pressure medium. Pressure calibration of the piston cylinder apparatus was accomplished using the reactions MgO +H2O = $Mg(OH)_2$ (850°C, 1.05 GPa) and $NaAlSi_2O_6$ + SiO_2 = $NaAlSi_3O_8$ (600°C, 1.6 GPa). A pressure correction of 15% is required based on the calibrations. The temperature of the charge was measured and controlled using a C - Type thermocouple. The uncertainties in temperature and pressure determination are assumed to be ±5 °C and ±0.05 GPa, respectively. The experiments were performed with the 'cold piston in' method: the piston cylinder assembly was pressurized cold to about 90 % of the desired pressure in a period of 20 minutes. The temperature was then raised to the aimed temperature at a proper rate (°C/min). During the heating period the assembly was pressurized to the final pressure. Temperature and pressure were automatically controlled over the period of the experiment. After heating the temperature was kept a certain time. After that, the sample was slowly cooled down to 300°C in a certain rate (°C/min). When the final temperature of 300°C was reached the sample was quenched to room temperature automatically by switching off the heating. The time which is needed to quench the experiment to a temperature less than 100°C is about 5 seconds. After quenching the decompression of the assembly was done within 20 minutes."

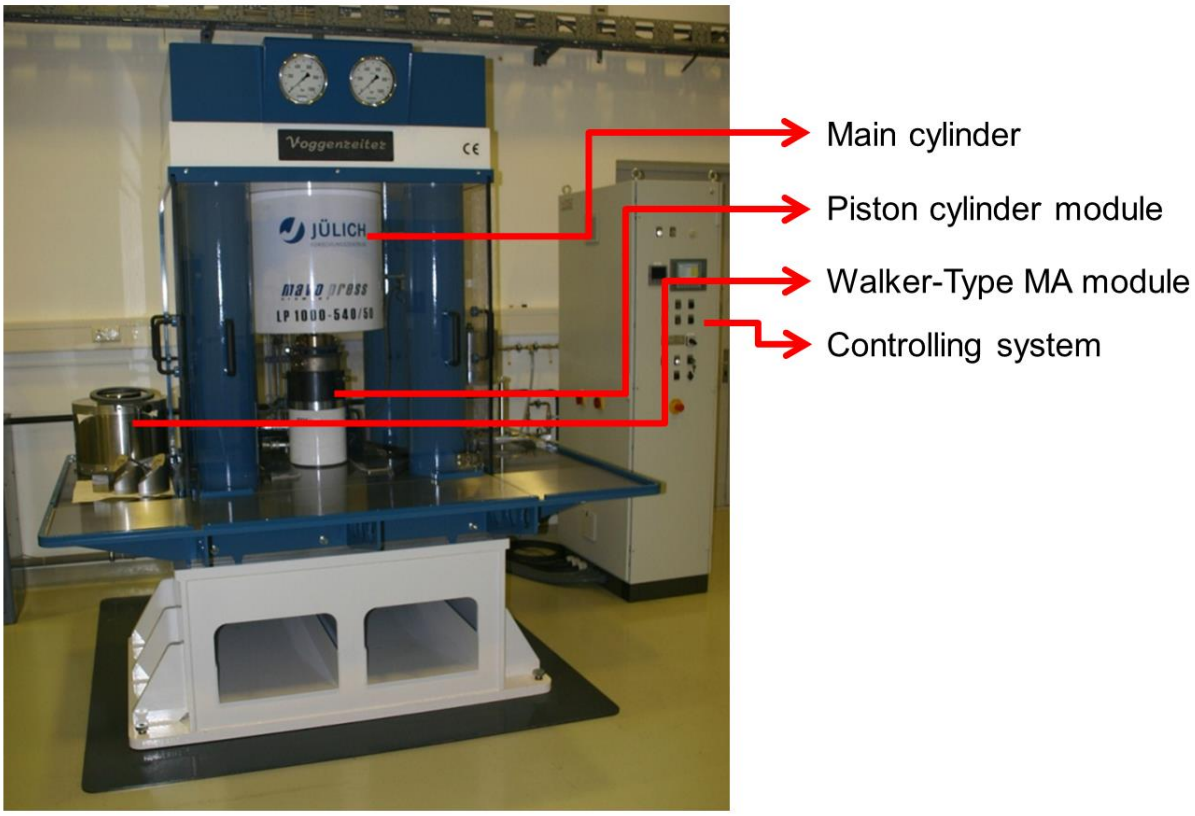

Figure 2.3: *The combined piston cylinder/ multi anvil press installed at IEK-6, Forschungszentrum Jülich (Voggenreiter LP 1000-540/50)*

2.2 Systematic Synthesis of Thorium and Uranium bearing Phosphates and Arsenates

In this dissertation, all three techniques mentioned above are utilized to synthesize a series of novel thorium and uranium bearing phosphates and arsenate compounds. All new compounds are summarized and the unit cell parameter information is listed in Table 2.1 and Table 2.2. In total, 44 new Th and U phosphates/arsenates/mixed-valent oxoarsenic(III)/arsenic(V) phases were obtained. Only a part of them are systematically investigated in this dissertation.

Table 2.1: New thorium and uranium bearing phosphate and arsenate compounds obtained in this work.

Compound Name	Space Group	Formula	
RbUAsO-1	*P*2$_1$/*n*	Rb[$UO_2(AsO_3OH)(AsO_2(OH)_2)$]	Chapter 3
RbUAsO-2	*P*2$_1$/*n*	α- Rb[$UO_2(AsO_3OH)(AsO_2(OH)_2)$]·$H_2O$	
RbUAsO-3	*P*2$_1$/*n*	β- Rb[$UO_2(AsO_3OH)(AsO_2(OH)_2)$]·$H_2O$	
LiThAsO-1	*P*2$_1$/*a*	$Li_2Th(AsO_4)_2$	$A_2Th(AsO_4)_2$ family Chapter 4
NaThAsO-1	*Fddd*	$Na_2Th(AsO_4)_2$	
KThAsO-1	*P*2$_1$/*n*	$K_2Th(AsO_4)_2$	
RbThAsO-1	*P*2$_1$/*n*	$Rb_2Th(AsO_4)_2$	
CsThAsO-1	*I*4$_1$/*amd*	$Cs_2Th(AsO_4)_2$	
LiThPO-1	*P*2$_1$/*a*	$Li_2Th(PO_4)_2$	$A_2Th(PO_4)_2$ family Chapter 5
NaThPO-1	*P*2$_1$/*a*	$Na_2Th(PO_4)_2$	
KThPO-1	*P*2$_1$/*n*	$K_2Th(PO_4)_2$	
RbThPO-1	*I*4$_1$/*amd*	$Rb_2Th(PO_4)_2$	
CsThPO-1	*I*4$_1$/*amd*	$Cs_2Th(PO_4)_2$	
ThPO-1	*P*-1	$Th(P_4O_{12})$	Polyphosphate family Chapter 6
UPO-1	*I*422	$U(PO_3)_4$	
UPO-2	*P*-1	$U(P_4O_{12})$	
UNdPO-1	*C*2/*c*	"$(U_{0.62}Nd_{0.38})(PO_3)_4$"	
ThAsO-1	*C*2/*c*	$Th(As_4As_4O_{18})$	Chapter 7.1
KThAsO-2	*C*2/*c*	$KTh_2(AsO_4)_3$	$KTh_2(AsO_4)_3$ structure type Chapter 7.2
RbThAsO-2	*C*2/*c*	$RbTh_2(AsO_4)_3$	
CsThAsO-2	*C*2/*c*	$CsTh_2(AsO_4)_3$	
AgThAsO-1	*C*2/*c*	$AgTh_2(AsO_4)_3$	
LiThPO-2	*P*2$_1$/*a*	$LiTh_2(PO_4)_3$	
RbUPO-1	*C*2/*c*	$RbU^{IV}_2(PO_4)_3$	
CsUPO-1	*C*2/*c*	$CsU^{IV}_2(PO_4)_3$	
CsThAsO-3	*Fddd*	$CsTh(As_3O_{10})$	Chapter 7.3
RbThAsO-3	*Fddd*	$RbTh(As_3O_{10})$	
RbThPO-2	*P*2$_1$2$_1$2$_1$	$RbTh(P_3O_{10})$	
Additional phases which are not presented with detailed descriptions in this work.			
LiThAsO-2	*P*-1	$Li_2Th_2(AsO_4)_2(As_2O_7)$	
LiThAsO-3	*P*2$_1$/*n*	$Li_4Th(As_2O_7)_2$	
NaThAsO-2	*P*4/*ncc*	$Na_4Th(As_2O_7)_2$	
NaThAsO-3	*C*2/*c*	$Na_5Th_4(AsO_4)_7$	

NaThAsO-4	$P2_1/a$	$Na_5Th(AsO_4)_3$
SrUPO-1	$P2_1/c$	$Sr_2(UO_2)(PO_4)_2$
SrUPO-2	*Aba*2	$SrU^{IV}(PO_4)_2$
CsThPO-2	$P2_1/c$	$Cs_4Th_4(P_2O_7)_5$
CsThAsO-4	*C*2	$Cs_2Th_2(As_2O_7)_3H_2$
ThPO-2	$Pna2_1$	$Th(P_2O_7)$
LiCsThPO-1	$P2_1/a$	$LiCsTh(PO_4)_2$
CaUPO-1	*I*-42*m*	$Ca_5(UO_2)_4(PO_4)_6$
UPO-1	*C*2/*c*	$U_2(PO_4H)_3{\cdot}H2O$
CsUAsO-1	$Pmn2_1$	$Cs_2[(UO_2)(As_2O_7)]$
CsUAsO-2	*P*-1	$Cs[(UO_2)(HAs_2O_7)]$
CsUAsO-3	*P*-1	$Cs[(UO_2)(HAs_2O_7)]{\cdot}0.17H_2O$

Table 2.2: Cell parameters for all thorium and uranium bearing phosphates and arsenates (without the e.s.d) obtained within this work

Compound Name	a(Å)	b(Å)	c(Å)	α(deg)	β(deg)	γ(deg)	Space Group
RbUAsO-1	6.72	12.06	11.55	90.00	94.73	90.00	$P2_1/n$
RbUAsO-2	8.39	11.97	10.01	90.00	90. 13	90.00	$P2_1/n$
RbUAsO-3	12.92	12.05	26.60	90.00	98.65	90.00	$P2_1/n$
LiThAsO-1	5.64	13.77	9.19	90.00	106.44	90.00	$P2_1/a$
NaThAsO-1	7.04	12.33	18.22	90.00	90.00	90.00	*Fd d d*
KThAsO-1	7.75	11.36	9.49	90.00	110.79	90.00	$P2_1/n$
RbThAsO-1	8.04	11.45	9.67	90.00	111.14	90.00	$P2_1/n$
CsThAsO-1	7.32	7.32	18.62	90.00	90.00	90.00	$I4_1/amd$
LiThPO-1	5.44	13.55	8.87	90.00	105.97	90.00	$P2_1/a$
NaThPO-1	7.06	21.70	9.11	90.00	111.60	90.00	$P2_1/a$
KThPO-1	7.71	10.96	9.20	90.00	111.44	90.00	$P2_1/n$
RbThPO-1	7.05	7.05	17.68	90.00	90.00	90.00	$I4_1/amd$
CsThPO-1	7.18	7.18	17.64	90.00	90.00	90.00	$I4_1/amd$
ThPO-1	8.24	8.79	14.65	78.54	74.70	62.70	*P*-1
UPO-1	11.31	11.31	14.93	90.00	90.00	90.00	*I*422
UPO-2	8.18	8.71	14.47	78.72	74.14	62.04	*P*-1
UNdPO-1	16.32	7.11	9.54	90.00	125.61	90.00	*C*2/*c*
ThAsO-1	18.21	5.19	17.35	90.00	99.12	90.00	*C*2/*c*
KThAsO-2	18.23	7.06	8.22	90.00	100.34	90.00	*C*2/*c*

RbThAsO-2	18.38	7.09	8.24	90.00	100.95	90.00	*C*2/*c*
CsThAsO-2	18.54	7.14	8.26	90.00	101.68	90.00	*C*2/*c*
AgThAsO-1	18.03	7.02	8.24	90.00	99.38	90.00	*C*2/*c*
LiThPO-2	17.38	6.80	8.13	90.00	101.08	90.00	$P2_1/a$
RbUPO-1	17.59	6.80	8.05	90.00	102.56	90.00	*C*2/*c*
CsUPO-1	17.59	6.80	8.05	90.00	102.51	90.00	*C*2/*c*
CsThAsO-3	9.38	19.91	20.40	90.00	90.00	90.00	*Fddd*
RbThAsO-3	9.33	19.81	20.31	90.00	90.00	90.00	*Fddd*
RbThPO-2	8.30	10.02	10.31	90.00	90.00	90.00	$P2_12_12_1$
LiThAsO-2	6.78	9.52	9.93	96.63	106.78	98.64	*P*-1
LiThAsO-3	4.72	12.98	17.13	90.00	97.24	90.00	$P2_1/n$
NaThAsO-2	10.93	10.93	10.33	90.00	90.00	90.00	*P*4/*ncc*
NaThAsO-3	18.40	7.05	20.75	90.00	107.14	90.00	*C*2/*c*
NaThAsO-4	14.46	16.52	20.71	90.00	110.45	90.00	$P2_1/a$
SrUPO-1	9.81	8.32	13.02	90.00	101.58	90.00	$P2_1/c$
SrUPO-2	13.32	8.97	10.54	90.00	90.00	90.00	*Aba*2
CsThPO-2	12.54	20.08	15.59	90.00	153.89	90.00	$P2_1/c$
CsThAsO-4	9.80	10.63	9.39	90.00	100.00	90.00	*C*2
ThPO-2	11.70	12.94	7.18	90.00	90.00	90.00	$Pna2_1$
LiCsThPO-1	10.28	8.61	10.36	90.00	117.63	90.00	$P2_1/a$
CaUPO-1	10.01	10.01	13.02	90.00	90.00	90.00	*I*-42*m*
UPO-1	17.53	6.78	8.03	90.00	102.29	90.00	*C*2/*c*
CsUAsO-1	13.01	6.18	13.26	90.00	90.00	90.00	$Pmn2_1$
CsUAsO-2	6.84	9.88	13.75	72.36	88.88	83.83	*P*-1
CsUAsO-3	6.80	9.85	20.60	77.49	82.15	84.03	*P*-1

2.3 Characterization Techniques

After the actinide bearing compounds are synthesized, characterization then ensues. Single Crystal X-ray Diffraction is utilized to determine crystal structures of actinide bearing compounds. Powder X-ray Diffraction is employed to examine the purity and numbers of phases in the reaction products. Raman and Infrared Spectroscopy are used to observe vibrational, rotational, and other low- frequency modes in a system. Scanning electron microscopy combined with energy-dispersive spectroscopy (SEM/EDS) is used to analyze the chemical composition. Thermo gravimetric Analysis was used to provide information on thermal stability of studied materials.

2.3.1 Single Crystal X-ray Diffraction

The single crystal X-ray diffraction (SC XRD) starts its history with the pioneer experiments of Max von Laue in 1912. This method was first only able to determine crystal structures of simple compounds (e.g. NaCl, NaBr, NaI) and then was significantly developed during the 20th century. Nowadays, SC XRD is employed to evaluate crystal structures of huge molecules, such as proteins. Among more than 1 million studied and deposited in international databases crystal structures, over 95% were studied by SC XRD.

The fundamental characteristic of crystals is that their atomic structures are periodic.[6] When X-rays are diffracted by crystals, those coherent scattered waves that boast the same wavelength as the incident beam would have constructive interferences with the latter.[7] And the interferences would reinforce itself in a specific direction, which would lead to diffraction rays. The direction of diffraction is determined by the atomic structures of crystals (space group) and their basic specifications (unit cell parameters and interplanar distance). While the intensity of diffraction is subject to the types of atom elements within the crystals and their arrangement coordinates. X-ray diffraction it the most powerful way to study the crystal structure.

Understanding Bragg's Law[8] is the basic knowledge of crystallographic chemistry. The constructive interferences should obey Bragg's Law,

$$n \cdot \lambda = 2 \cdot d \cdot \sin\theta$$

which can be elaborated as the following Fig. 2.4. Two beams with identical wavelength and phase approach a crystalline solid and are scattered off two different atoms within it. The lower beam traverses an extra length of 2dsinθ. Constructive interference occurs when this length is equal to an integer multiple of the wavelength of the radiation.

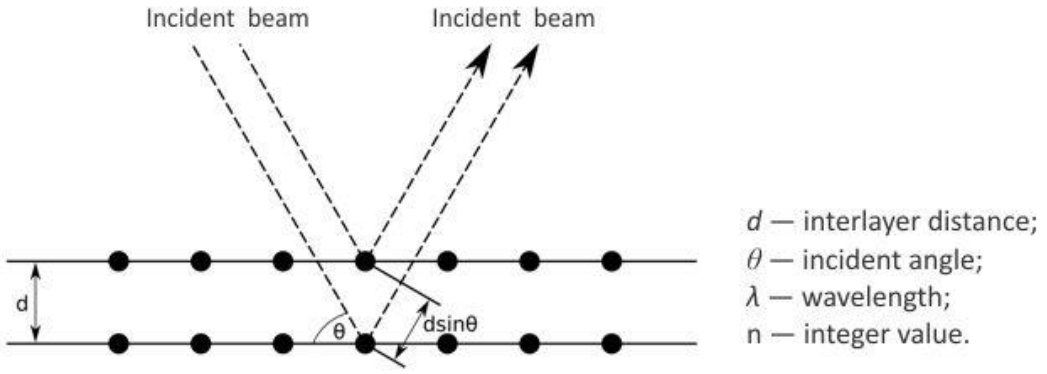

***Figure 2.4**: Interaction of X-Rays with a crystal lattice.*

According to Bragg's equation, the X-ray diffraction of crystals can be referred to as 'reflection'. The reason why the terminology of 'reflection' in optics is borrowed here is

because when diffraction occurs, the incident wave, the diffraction wave and the normal of crystal surface are abiding by the law of the visible light when reflected by a mirror. However, this 'reflection' does not exist by all angle of incidence. Only those obey the Bragg's equation can lead to the 'reflection'. Therefore, it is also called 'selective reflection'. Given this, the crystal face's orientation of crystal plane can be immediately pictured whenever a diffraction ray is detected. Consequently, the inter-plane distance can be calculated by using the Bragg's equation with diffraction angle θn (with known experimental incident wavelength).

In this dissertation, single crystal X-ray diffraction data were collected at room and elevated temperature on a SuperNova (Agilent) diffractometer using MoKα radiation (λ = 0.71073 Å). (Fig. 2.5)

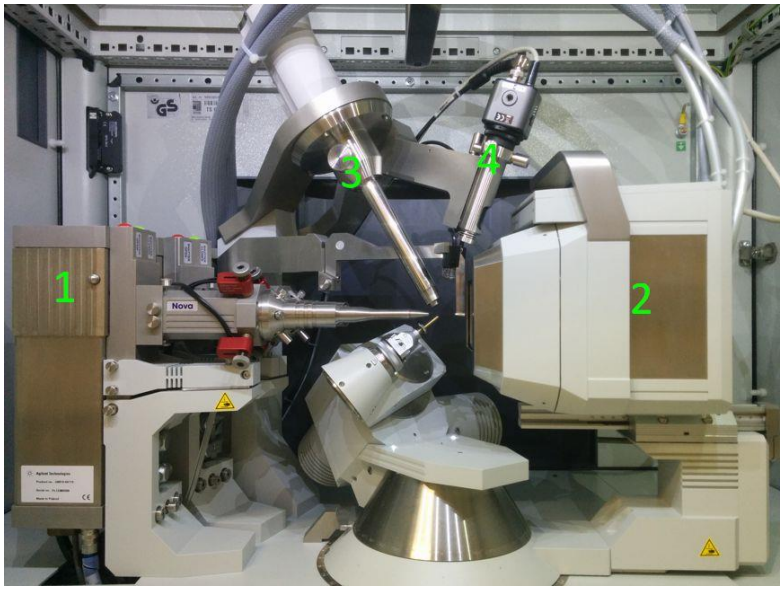

Figure 2.5: *The inside chamber of the SuperNova (Agilent) diffractometer. 1) Sources of radiation - Copper X-ray tube (high intensity, large absorption by heavy atoms; suitable for organic compounds); Molybdenum X-ray tube (low intensity, low absorption by heavy atoms; suitable for actinide compounds). 2) Detector - CCD area detector. 3) Temperature control system - temperature ranges from 100 K (liquid nitrogen) to 500 K. 4) Camera.*

In this dissertation, as our publications [2, 5, 9] described that, all single crystals were picked in the air and mounted on a glass fiber with epoxy glue. The specific procedure is that, the single crystal was picked under the microscope owing to the small size of the crystal then the isolated crystal will be attached to a glass fiber with epoxy glue. For some unstable crystals, oil is preferred to cover them and protect them from exposure to air. The glass fiber was previously mounted onto a metal pin which is now placed into the goniometer head. Here the crystal position is adjusted by micrometer screws to ensure that the crystal is in

position for the incident X-ray beam. The pin and holder are shown in Fig. 2.6. Then the data collection and data processing software CrysAlisPro™ will start to collect the diffraction data.

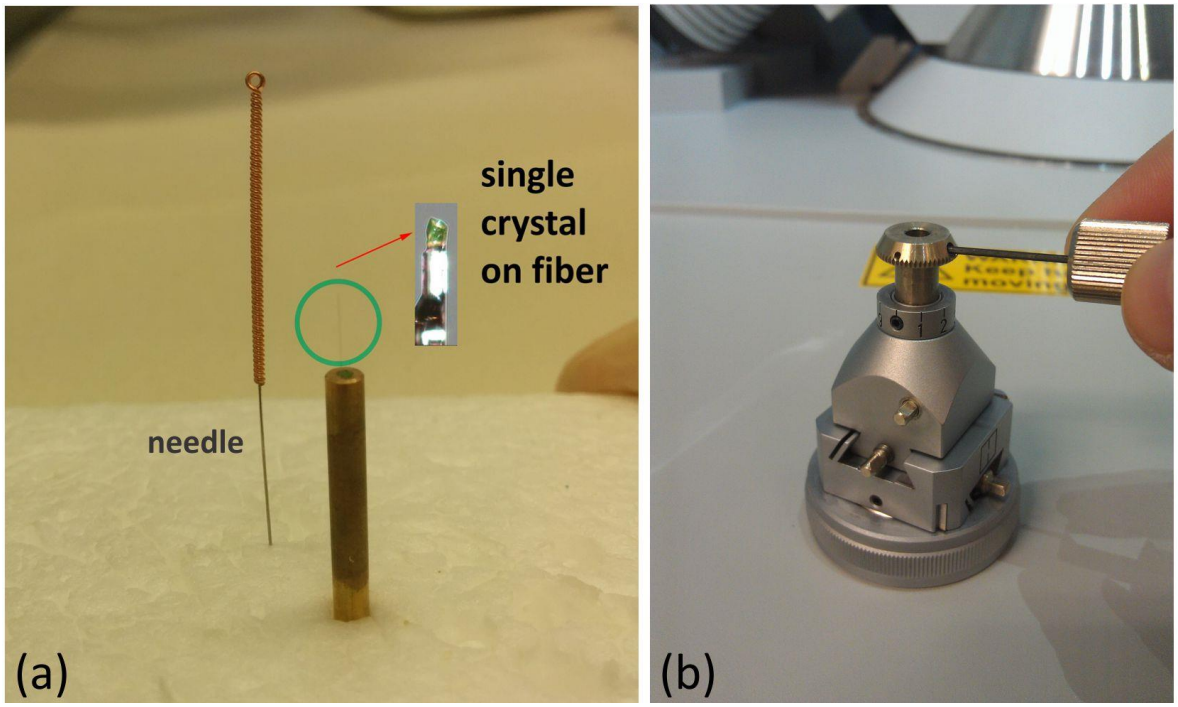

Figure 2.6*: (a) left: the needle used to pick a crystal; right: pin and glass fiber attached with a single crystal, (b) holder of the pin.*

2.3.2 Powder X-ray Diffraction

Powder diffraction is another technique using X-ray, neutron, or electron diffraction on powder or microcrystalline samples for structural characterization of materials. In this dissertation, this method was applied to identify and ensure that pure phase compounds were obtained. Powder X-ray diffraction patterns were collected on a Bruker D4 Endeavor diffractometer, equipped with a CuKα (λ = 1.54187 Å) tube and a one-dimensional silicon strip LynxEye detector (Bruker). (Fig. 2.7) Using a voltage equal 40 kV and an electric current equal 40 mA (1.6 kW). Data were recorded in the range of $2\theta = 0° - 80°$ (total counting time = 10 sec/step with the step width of = 0.02°). The aperture of the fixed divergence and receiving slit was set to 0.2 mm and 8.0 mm, respectively.

***Figure 2.7**: (a) Bruker D4 Endeavor diffractometer; (b) the sample holder; (c) the inside chamber of the diffractometer.*

2.3.3 Raman and IR Spectroscopy

In this dissertation, unpolarized Raman spectra were recorded with a Horiba LabRAM HR spectrometer (Fig. 2.8a) using a peltier cooled multi-channel CCD detector. An objective with a 50x magnification was linked to the spectrometer allowing the analysis of samples as small as 2 μu in diameter. The sample was in the form of a polycrystalline powder. The incident radiation was produced by a HeNe laser at a power of 17 mW (λ = 632.81 nm). The focal length of the spectrometer was 800 mm and a 1800 gr/mm grating was used. The spectral resolution was around 1 cm^{-1} with a slit of 100 μu. Spectra was recorded in the range 50 – 1250 cm^{-1}. No significant photoluminescence was observed.

A Bruker Equinox spectrometer (Fig. 2.8b) was used for the IR experiments, and the KBr pellet technique was applied for sample preparation. For this purpose, approximately 200 mg of KBr and 2 mg of each sample were mixed carefully, and a pressure of 10 tons was applied and held constant for 3 min to prepare each pellet. The IR spectra were recorded in the range from 400 to 4000 cm^{-1}. A pure KBr pellet, which was prepared under the same experimental conditions, was used as a blank sample.

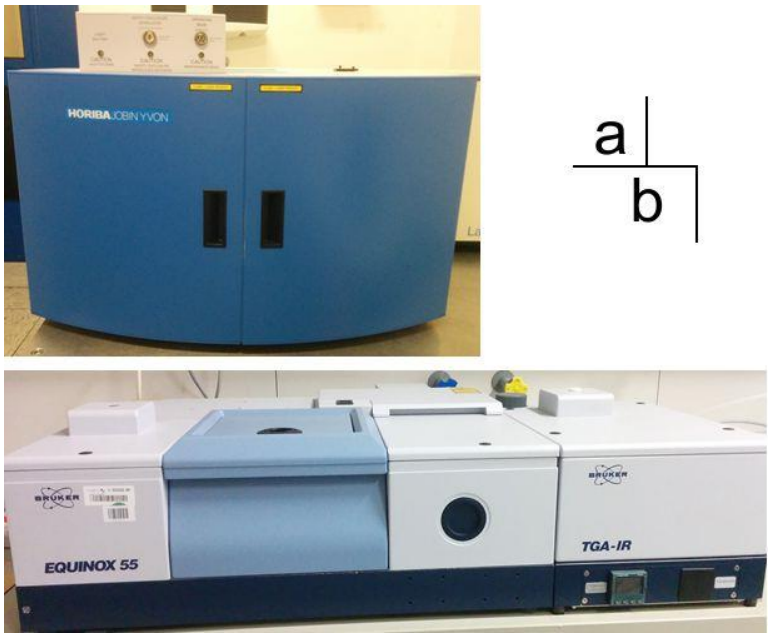

***Figure 2.8**: (a) Horiba LabRAM HR spectrometer for Raman experiments; (b) Bruker Equinox spectrometer for IR experiments*

2.3.4 Element analysis

In this dissertation, chemical compositions analysis was performed using a scanning electron microscopy combined with energy-dispersive spectroscopy (SEM/EDS) (FEG, Quanta 200 F, 60 Pa, 30kV).(Fig. 2.9) The EDS detector is the Apollo ssd. All the data were calibrated with standards and confirm the chemical composition found in the structure refinements.

Figure 2.9*: Scanning electron microscopy for element analysis*

2.3.5 TG-DCS Experiment

In this dissertation, the thermal behavior of the dried powders was studied from room-temperature to 1273 K by differential scanning calorimetry analysis (DSC) coupled with thermo gravimetric (TG) in air at a heat rate of 10 K/min using a Netzsch STA 449C Jupiter apparatus. (Fig. 2.10) Each sample (20 mg) was loaded in a platinum crucible, which was closed with a platinum cover. During the measurements a constant air flow of 20 – 30 mL/min was applied.

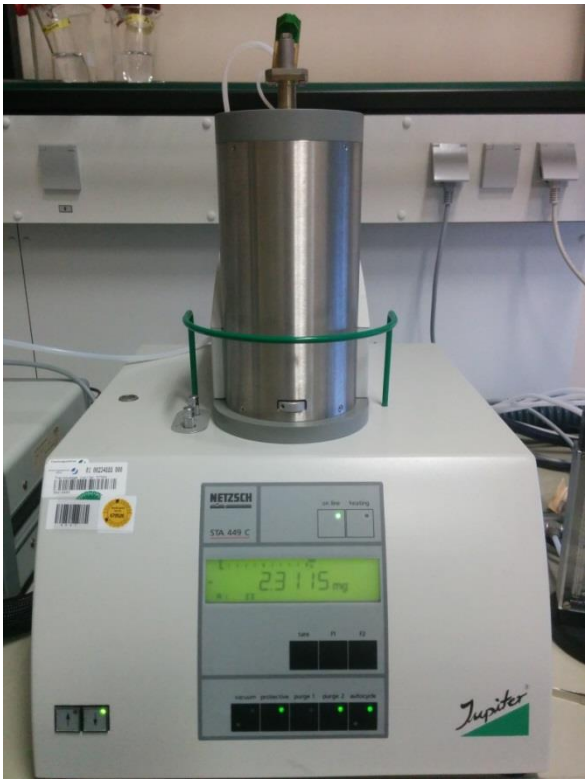

Figure 2.10*: Netzsch STA 449C Jupiter apparatus for TG- DCS experiment*

2.4 Structure Determination from Single Crystals

In this dissertation, all single crystals were picked in the air and mounted on a glass fiber with epoxy glue. A routine X-ray diffraction experiment is highly automated and requires no intervention in the data collection and reduction steps. All the diffraction data were collected by the CCD detector, using a narrow-frame method with the ω-scan mode under λ= 0.71073 Å and T= 293(2) K. The data were integrated using the CrysAlisPro program, and the intensities were corrected for Lorentz polarization and absorption attributable to the variation in the path length through the detector faceplate. After the data reduction, absorption correction was made by the Multiscan technique. With those data, the structures were solved by SHELXS-97[10]. The process of the crystal structure solution and refinement is shown in the Fig. 2.11. The space group is defined by the extinction law and heavy atoms will be located. The data will be refined by Fourier Transform to obtain the locations of the other atoms. After that, all the atom's locations and Anisotropy Coefficients are be refined to complete convergence by a full-matrix least-squares refinement on F2 with SHELXL-97 found in the software suite WinGX v1.80.05.[11] The structure pictures were drawn by Crystalmaker.

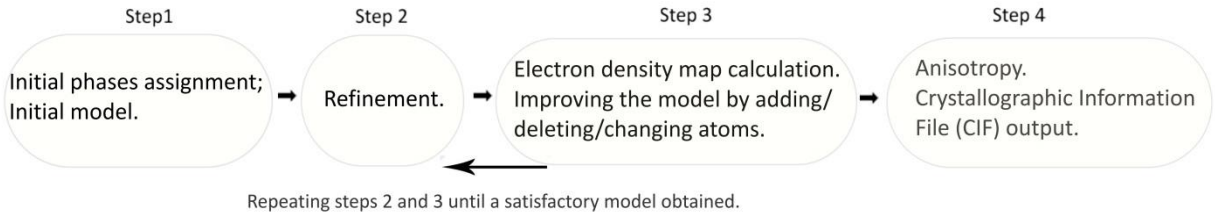

Figure 2.11*: The process of the crystal structure solution and refinement. CIF file contains all necessary data on crystal structure model, e.g. unit cell parameters, symmetry, atomic coordination, experiment details. The R1 value is usual reference to experiment quality and reflects difference between calculated and experimental intensities.*

2.5 Bond Valence Analysis

The approach of bond valence has been widely used in solid-state chemistry to predict and express the bond lengths in crystals. That is owing to the fact that, by approximation, the bond length represents a special bond valence function. Given the definition of vii, the valence of a bond between atoms i and j, the total amount of the valences from atom i with valence vi follows the rule of:

$$\sum_j \mathrm{vij} = \mathrm{Vi} \qquad \text{(2.II)}$$

The most frequently applied function with bond valence to interpret the bond length variation is

$$v_{ij} = \exp\left[(R_{ij} - d_{ij})/b\right] \qquad \text{(2.III)}$$

Hereby *Rij* is referred to being the bond valence parameter which can be looked up from the Ref. [12, 13]. Usually, the value of b, which is adopted throughout the calculation, is a 'universal' constant that equals to 0.37 Å.[12] But for Uranium(VI), with the different coordination numbers, the *Rij* and b is variable. Peter C. Burns gives the below parameters: for UO_6 polyhedral, *Rij* = 2.074 Å, *b* = 0.554 Å, for UO_7 polyhedral, *Rij* = 2.045 Å, *b* = 0.510 Å and for UO_8 polyhedral, *Rij* = 2.042 Å, *b* = 0.506 Å.[14]

2.6 References

1. K. Byrappa; M. Yoshimura, *Handbook of Hydrothermal Technology*. Noyes Publications: Norwich, New York, 2001.
2. N. Yu; V.V. Klepov; E.M. Villa; D. Bosbach; E.V. Suleimanov; W. Depmeier; T.E. Albrecht-Schmitt ; Alekseev, E. V., *J.Solid State Chem.* **2014,** *215*, 152-159.
3. Anthony R. West, *Solid State Chemistry and its Applications*. John Wiley & Sons: 2005.
4. B. Gerand; G. Nowogrocki; J. Guenot; M. Figlarz, *Preparative methods in Solid State Chemistry*. Academic press: New York, 1972.
5. Yu, N.; Klepov, V. V.; Kegler, P.; Bosbach, D.; Albrecht-Schmitt, T. E.; Alekseev, E. V., *Inorganic chemistry* **2014,** *53*, 8194-8196.
6. H.J. Michael; D. Howard, Introduction to Crystallography and Mineral Crystal Systems. In Bob's Rock Shop: 1998.
7. A. Guinier, X-ray Crystallographic Technology. In Hilger and Watts LTD: London, 1952.
8. W.H. Bragg, *Nature* **1913,** *90*, 572.
9. N. Yu; V.V. Klepov; G. Modolo; D. Bosbach; E.V. Suleimanov; T.M. Gesing; L. Robben; E.V. Alekseev, *Inorg. Chem.,* **2014,** *53*, 11231-11241.
10. G. M. Sheldrick, *Acta Crystallogr. A,* **2007,** *64*, 112-122.
11. Farrugia; J. Louis, *J. Appl. Crystallogr.,* **2012,** *45*, 849-854.
12. I. D. Brown; D. Altermatt, *Acta Cryst.,* **1985,** *B41*, 244-247.
13. N. E. Brese; M. O'Keeffe, *Acta Cryst.,* **1991,** *B47*, 192-197.
14. P.C. Burns, *Can. Miner.,* **1997,** *35*, 1551-1570.

Chapter 3 TOPOLOGICALLY IDENTICAL, BUT GEOMETRICALLY ISOMERIC LAYERS IN ANHYDROUS $Rb[UO_2(AsO_3OH)(AsO_2(OH)_2)]$ AND HYDROUS α- and β-$Rb[UO_2(AsO_3OH)(AsO_2(OH)_2)]\cdot H_2O$

3.1 Abstract

The hydrothermal reaction of uranyl nitrate with rubidium nitrate and arsenic (III) oxide results in the formation of polymorphic α- and β-$Rb[UO_2(AsO_3OH)(AsO_2(OH)_2)]\cdot H_2O$ (**RbUAs-2**, **3**) and the anhydrous phase $Rb[UO_2(AsO_3OH)(AsO_2(OH)_2)]$ (**RbUAs-1**). These phases were structurally, chemically and spectroscopically characterized. The structures of all three compounds are based upon topologically identical, but geometrically isomeric layers. The layers are linked with each other by means of the Rb cations and hydrogen bonding. Dehydration experiments demonstrate that water deintercalation from hydrous **RbUAs-2**, **3** yields anhydrous **RbUAs-1** via topotactic reactions.

3.2 Introduction

Uranyl (U^{6+}) arsenates and phosphates are commonly found in nature, mostly as minerals belonging to the autunite or phosphouranylite groups.[1-3] A deeper knowledge of uranium bearing arsenates and phosphates is desirable as this may contribute to a better understanding of how uranium and other actinides can behave in nature, for example, of how they migrate within the environment.[4-7] Understanding the structures, stabilities and redox properties of uranium bearing phases with Group V elements is also important for the safe management of nuclear waste.

The early actinides, including uranium, show complex redox and coordination behavior. Usually, U(VI) forms the linear uranyl group (UO_2^{2+}) with variable numbers of bonding partners in the equatorial plane, most commonly four, five or six, which give rise to the formation of square, pentagonal or hexagonal bipyramids.[8] The presence of phosphates or arsenates adds to the diversity of the structures as these elements can form various different building units, such as $\boldsymbol{T}O_4$ single tetrahedra, $\boldsymbol{T}_2O_7$ dimers, $\boldsymbol{T}_3O_{10}$ trimers, $\boldsymbol{T}_4O_{10}$ tetramers or infinite polymeric $\boldsymbol{T}O_3$ chains (***T*** = P, As).[9-15] Moreover, the linkage between the U bipyramids and the ***T*** polyhedra can be quite diverse. This has resulted in a large number of known uranyl based oxo-compounds with Group V cations (P or As).[1-3, 16-21] To extend the knowledge on the actinide - phosphorus systems, recently hydrothermal reactions in the ***An*** (= Th, U, Np) - phosphite (P(III)) system have been explored.[21-24] By varying the experimental conditions and reaction times phosphites, mixed phosphate-phosphites and phosphates were obtained. Phases with mixed-valent U(IV)- U(VI) compounds were also detected. It was

concluded that the phosphite anion (HPO_3^{2-}) can create reducing conditions that are able to stabilize the lower oxidation states of actinides in solutions. This observation is potentially beneficial for limiting the mobility of actinide compounds, as it is known that the solubility of, e.g. U(IV) is, in general, lower than that of U(VI) compounds.

Given that the crystal chemistry of arsenic is, in general, quite similar to that of phosphorus, we decided to explore the As(III) – U(VI) – Rb system, with As_2O_3 as starting material. In the course of this study we have isolated three new uranyl arsenates having similar compositions but different crystal structures: one anhydrous phase **RbUAs-1** and two polymorphic monohydrates, viz. **RbUAs-2**, **3**. Here we report on structural, topological and spectroscopic properties of the three compounds, and shortly report on experiments which check the stability of the hydrous compounds against thermal degradation.

3.3 Synthesis

Caution! *The $UO_2(NO_3)_2{\cdot}6H_2O$ used in this study contained depleted uranium; nevertheless the standard precautions for handling radioactive materials were obeyed.*

In our previous work we have obtained several phosphites and mixed valence phosphite-phosphates from the U(VI) – P(III) system by varying the concentration of the phosphorus component, the pH of the solution and the reaction time. Since the solubility of As_2O_3 is much lower than that of H_3PO_3, it is not possible to significantly change the concentration of the arsenic component which prevented us from using a procedure similar to that which was used for the phosphorus system. In addition, it is known that the range of As(III) stability in acidic aqueous solutions is different from that of P(III). Finally, the use of nitrates as starting materials provided fairly oxidizing conditions for the reactions. As a consequence the compounds obtained in this study differ from those of the phosphite studies in that they contained only fully oxidized U(VI) and As(V).

Table 3.1: The Experimental Reactants used in this chapter

Compound Name	**Purity**	**Company**
Uranyl nitrate ($UO_2(NO_3)_2 \cdot 6H_2O$)	- -	International Bioanalytical Industries
Rubidium nitrate ($RbNO_3$)	99.9%	Alfa-Aesar
Arsenic(3+) oxide (As_2O_3)	97%	Alfa-Aesar

The synthesis following the Fig. 2.1 processes, and the information about the reactants was given in the Table 3.1. The reactants were mixed in their appropriate ratios and loaded into a 23 mL PTFE-lined autoclave together with 0.2 mL distilled water. (Table 3.2)

Table 3.2: Synthesis data and crystal profile of **RbUAs-1**, **2**, and **3**

	uranyl nitrate	**$RbNO_3$**	**As_2O_3**	**distilled water**	**$Rb^{I}:U^{VI}:As^{III}$**	**Colour/shape**
RbUAs-1	100.4 mg	265.4 mg	395.5 mg	0.2 mL	9: 1: 10	yellow-green block
RbUAs-3						green block
RbUAs-2	100.4 mg	29.5 mg	395.5 mg	0.2 mL	1: 1: 10	green block

After sealing, the autoclave was placed into a programmable box furnace. The furnace was ramped up to 150 °C, left there for 48 hours and then slowly cooled down to room temperature at a rate of 5 °C/h. (Fig. 3.1) After washing, single crystal could be obtained which were suitable for crystallographic studies.

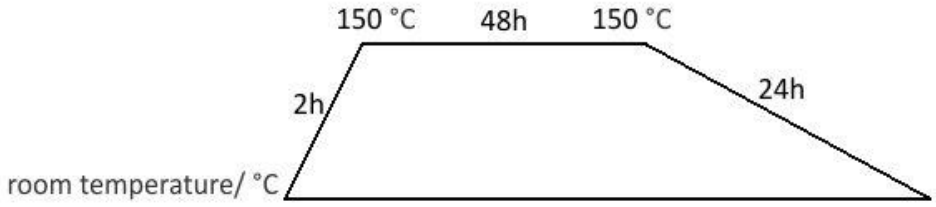

Figure 3.1*: The tempering profile of the furnace.*

All obtained phases formed within green-yellowish amorphous matrices. We were not able to separate the crystalline phases from the amorphous matrices. Therefore, it was not possible to study the dehydration behaviour on powder samples, e.g. by DSC experiments, in order to obtain statistically meaningful results. We rather had to perform *in situ* dehydration studies on each hydrous phase using single crystals.

The dehydration experiments on **RbUAs-2** and **RbUAs-3** have been performed using a hot stream of dry nitrogen generated by a Cryojet (Oxford Instruments) device. The standard protocol for the experiments was as follows: A single crystal of the respective phase was mounted on the diffractometer, and then the temperature was raised stepwise (steps of 20 K during 5 min) from the starting point at 50°C. After each step the unit cell parameters were determined. The dehydration of both phases (**RbUAs-2** and **RbUAs-3**) was considered complete when we detected the unit cell parameters of single-crystalline anhydrous **RbUAs-1**. This fact, together with the structural details (see below), was taken as evidence that both dehydration processes are in fact topotactic reactions.

In these experiments we have observed the occurrence of the lattice parameters of anhydrous **RbUAs- 1** at 170°C and 220°C for **RbUAs- 2** and **RbUAs- 3**, respectively. Without further information it is not possible to decide whether the difference in temperature indicates a slightly higher thermodynamic stability of **RbUAs- 3** or whether this is rather due to kinetic effects, although we think the latter is true.

3.4 Single Crystal X-ray Diffraction

The data were collected and refined follow the details as section **2.4** mentioned. All the structures were checked for possible higher symmetry using the ADDSYM algorithm from the program PLATON[25], but none were found. Relevant crystallographic data and details of the experimental conditions for all the three crystals are summarized in Table 3.3 and selected interatomic distances in Table 3.4.

Table 3.3: Crystallographic Data for **RbUAs- 1**, **2**, and **3**

Compound	**RbUAs- 1**	**RbUAs- 2**	**RbUAs- 3**
space group	*P* $2_1/n$	*P* $2_1/n$	*P* $2_1/n$
a/Å	6.7154(3)	8.3912(4)	12.9225(2)
b/Å	12.0642(4)	11.9725(4)	12.0485(2)
c/Å	11.5500(5)	10.0136(8)	26.6027(4)
α/°	90	90	90
β/°	94.726(3)	90.132(6)	98.650(2)
γ/°	90	90	90
V/ $Å^3$	932.55(6)	1006.00(1)	4094.8 (1)
Dcalc(g/cm^{-3})	4.5	4.3	4.213
Z	4	4	16
Temperature (K)	293(2)	293(2)	293(2)
λ (Å)	0.71073	0.71073	0.71073
F (000)	1100	1132	4528
R1	0.0273	0.0227	0.0556
wR2	0.0599	0.0582	0.1343

$R(F) = \Sigma||Fo| - |Fc||/\Sigma|Fo|$. $wR(Fo^2) = [\Sigma w(Fo^2 - Fc^2)^2/\Sigma w(Fo^2)^2]^{1/2}$.

Table 3.4: Selected interatomic distances /Å in the structure **RbUAs-1**, **2**, and **3**

RbUAs- 1							
U1–O_{Ur}8	1.778(4)	U1–O_{eq}4	2.377(4)	As1–O_{eq}1	1.661(4)	As2–O_{eq}4	1.652(3)
U1–O_{Ur}5	1.775(3)	U1–O_{eq}9	2.381(4)	As1–O_{eq}9	1.661(4)	As2–O_{eq}3	1.660(3)
U1–O_{eq}1	2.304(4)	U1–O_{eq}3	2.454(3)	As1–O_{eq}2	1.664(3)	As2–O_{Hf}7	1.722(4)
U1–O_{eq}2	2.337(3)			As1–O_{H}10	1.741(4)	As2–O_{Hf}6	1.730(4)
RbUAs- 2							
U1–O_{Ur}5	1.784(2)	U1–O_{eq}3	2.389(2)	As1–O_{eq}3	1.653(2)	As2–O_{eq}4	1.655(2)
U1–O_{Ur}8	1.796(2)	U1–O_{eq}2	2.398(2)	As1–O_{eq}6	1.656(2)	As2–O_{eq}1	1.671(2)
U1–O_{eq}4	2.317(2)	U1–O_{eq}6	2.407(2)	As1–O_{Hf}9	1.719(3)	As2–O_{eq}2	1.680(2)
U1–O_{eq}1	2.323(2)			As1–O_{Hf}10	1.720(3)	As2–O_{H}7	1.720(3)
RbUAs- 3							
U1-O_{Ur}27	1.779(9)	U2-O_{Ur}4	1.76 (10)	U3-O_{Ur}9	1.78(10)	U4-O_{Ur}24	1.79(11)
U1-O_{Ur}21	1.79 (10)	U2-O_{Ur}14	1.792(9)	U3-O_{Ur}6	1.79(10)	U4-O_{Ur}25	1.79(11)
U1-O_{eq}32	2.29 (11)	U2-O_{eq}1	2.319(9)	U3-O_{eq}8	2.301(9)	U4-O_{eq}19	2.31(10)
U1-O_{eq}18	2.36 (10)	U2-O_{eq}2	2.320(9)	U3-O_{eq}3	2.311(9)	U4-O_{eq}13	2.36(10)
U1-O_{eq}29	2.38(12)	U2-O_{eq}12	2.378(9)	U3-O_{eq}17	2.40(10)	U4-O_{eq}36	2.40(12)
U1-O_{eq}31	2.39 (11)	U2-O_{eq}5	2.41 (10)	U3-O_{eq}15	2.412(9)	U4-O_{eq}16	2.411(9)
U1-O_{eq}10	2.403(9)	U2-O_{eq}11	2.420(9)	U3-O_{eq}7	2.414(9)	U4-O_{eq}23	2.41(10)
As1-O_{eq}17	1.65(10)	As2-O_{eq}3	1.66(10)	As3-O_{eq}13	1.66(10)	As4-O_{eq}19	1.66(10)
As1-O_{eq}1	1.661(9)	As2-O_{eq}12	1.667(9)	As3-O_{eq}29	1.67 (11)	As4-O_{eq}32	1.67(11)
As1-O_{eq}2	1.665(9)	As2-O_{eq}8	1.671(9)	As3-O_{eq}18	1.68(10)	As4-O_{eq}16	1.682(9)
As1-O_{H}28	1.73(10)	As2-O_{H}30	1.74(11)	As3-O_{H}26	1.71(11)	As4-O_{H}37	1.71(12)
As5-O_{eq}15	1.650(9)	As6-O_{eq}10	1.642(9)	As7-O_{eq}7	1.637(9)	As8-O_{eq}36	1.62(12)
As5-O_{eq}5	1.65(10)	As6-O_{eq}31	1.66 (11)	As7-O_{eq}11	1.650(9)	As8-O_{eq}23	1.66(10)
As5-O_{Hf}22	1.72(10)	As6-O_{Hf}38	1.72(11)	As7-O_{Hf}20	1.72(10)	As8-O_{Hf}33	1.70(11)
As5-O_{Hf}35	1.73(11)	As6-O_{Hf}39	1.74(11)	As7-O_{Hf}34	1.73(11)	As8-O_{Hf}40	1.78(14)

3.5 Chemical Composition

The electronic-microscopic image was shown in the Fig.3.2, and the experimental data as well as the calculated stoichiometry was shown in the Table 3.5.

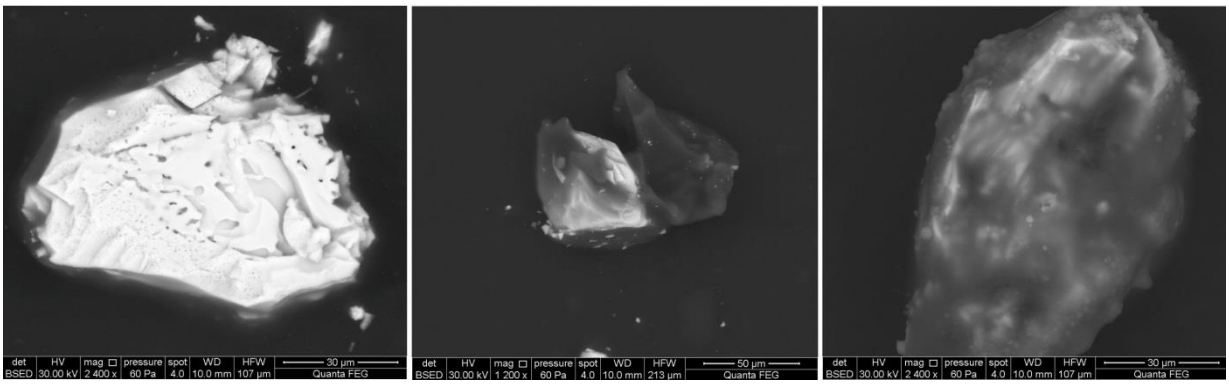

Figure 3.2*: Electronic-microscopic image of a crystal of* ***RbUAs- 1****,* ***2****, and* ***3***

Table 3.5: EDX elemental analysis and stoichiometry for **RbUAs- 1**, **2**, and **3**

Element / Compound	Molar ratio, %			Total, %
	As	Rb	U	
RbUAs- 1	50.3	24.3	25.4	100
RbUAs- 2	51.3	24.0	24.7	100
RbUAs- 3	52.4	24.2	23.4	100
Calculated data	50	25	25	100

The results of EDX elemental analysis are in good agreement with those of the single crystal X-ray diffraction studies. Proton positions could not be determined in the X-ray studies.

3.6 Bond Valence Analysis

Here, the presence of OH^- groups in the structures was deduced from and their location determined by calculation of bond valence sums (BVS). [26-28] As section 2.5 mentioned, for uranium, the bond valence parameters variable from their coordination numbers. In this chapter, uranium was coordinated to seven oxygen atoms in all three compounds. So, The bond-valence parameters provided by Burns is $Rij_{(U)}$ =2.045, b_U= 0.51. While, according to Brown, $Rij_{(As)}$ =1.767, $Rij_{(Rb)}$ =2.26, $b_{(As\ and\ Rb)}$= 0.37. The results of the BVS calculation of all cations and O atoms in three phases were given in the Table 3.6-3.8.

Table 3.6: Bond-valence analysis for **RbUAs- 1**

	U1	As1	As2	Rb1	Σ
O1	0.602	1.332		0.042	1.98
O2	0.564	1.321		0.190	2.08
O3	0.448		1.335		1.78
O4	0.522		1.365	0.157	2.04
O5	1.698			0.189	1.89
O6*			1.105	0.042	1.15
O7*			1.129	0.091	1.22
O8	1.688			0.086	1.82
				0.049	
O9	0.517	1.332			1.85
O10*		1.073		0.069	1.19
				0.053	
Σ	6.04	5.06	4.93	0.97	

O* stands for O atom in the OH-group.

Table 3.7: Bond-valence analysis for **RbUAs- 2**

	U1	As1	As2	Rb1	Σ
O1	0.580		1.296	0.180	2.06
O2	0.500		1.265		1.76
O3	0.509	1.361			1.87
O4	0.587		1.354		1.94
O5	1.668			0.184	1.95
				0.086	
O6	0.492	1.350			1.84
O7*			1.135	0.164	1.30
O8	1.629			0.126	1.74
O9*		1.139		0.131	1.27
O10*		1.135		0.110	1.25
Σ	5.96	4.98	5.05	1.04	

O* stands for O atom in the OH-group.

Table 3.8: Bond-valence analysis for **RbUAs- 3**

	U1	U2	U3	U4	As1	As2	As3	As4
O1		0.584			1.332			
O2		0.583			1.317			
O3			0.583			1.332		
O4		1.745						
O5		0.488						
O6			1.642					
O7			0.479					
O8			0.584			1.296		
O9			1.745					
O10	0.495							
O11		0.479						
O12		0.521				1.310		
O13				0.583			1.343	
O14		1.642						
O15			0.488					
O16				0.488				1.258
O17			0.521		1.357			
O18	0.535						1.279	
O19				0.584				1.346
O20*								
O21	1.642							
O22*								
O23				0.479				
O24				1.745				
O25				1.642				
O26*							1.173	
O27	1.682							
O28					1.105			
O29	0.523						1.289	
O30*						1.082		
O31	0.508							
O32	0.616							1.303
O33*								
O34*								
O35*								
O36				0.521				
O37*								1.167
O38*								
O39								
O40*								
	U1	**U2**	**U3**	**U4**	**As1**	**As2**	**As3**	**As4**
Σ	**6.00**	**6.04**	**6.04**	**6.04**	**5.11**	**5.02**	**5.08**	**5.07**

Table 3.8: (Continued)

	As5	As6	As7	As8	Rb1	Rb2	Rb3	Rb4
O1								0.090
O2								
O3							0.124	
O4					0.148			
O5	1.361				0.135			
O6						0.159		
O7			1.421			0.127		
O8								
O9					0.122		0.166	
O10		1.402						0.121
O11			1.372					
O12								
O13					0.100			
O14						0.113		0.148
O15	1.372							
O16							0.084	
O17								
O18								
O19							0.061	
O20*			1.123			0.071		
O21						0.072		0.139
O22*	1.139				0.077			
O23				1.354				
O24							0.061	
O25					0.149			
O26*						0.137		0.027
O27								0.111
O28						0.031		0.067
O29								
O30*					0.055		0.128	
O31		1.346				0.058		
O32								
O33*				1.192				0.094
O34*			1.108				0.069	
O35*	1.105							0.093
O36				1.492	0.025		0.113	
O37*					0.087			
O38*		1.145					0.074	
O39		1.076						
O40*				0.968		0.023		
	As5	**As6**	**As7**	**As8**	**Rb1**	**Rb2**	**Rb3**	**Rb4**
Σ	**4.98**	**4.97**	**5.02**	**5.01**	**1.07**	**0.91**	**1.04**	**1.07**

O* stands for O atom in the OH-group.

3.7 Structure Description

All three phases crystallize in the monoclinic, centrosymmetric space group $P2_1/n$. **RbUAs-3** has a quadrupled unit cell volume compared with **RbUAs-2** and **RbUAs-1**. It should be noted that, despite that the same space group type $P2_1/n$ is assigned to all three phases, the space group of **RbUAs-3** is not in a simple isomorphic group-subgroup relationship with those of **RbUAs-2** and **RbUAs-1**. The crystal structures of all three phases are based upon layered motifs, which consist of the same building units arranged in the same manner (Fig. 3.3).

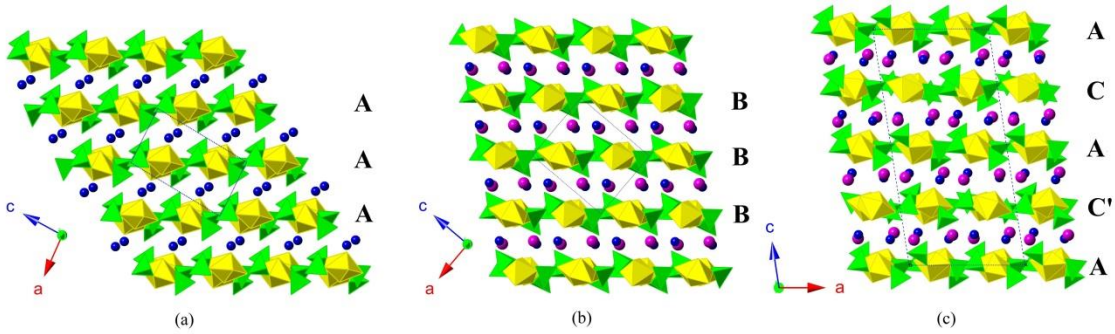

Figure 3.3*: Structural fragments of (a)* ***RbUAs-1****, (b)* ***RbUAs-2*** *and (c)* ***RbUAs-3*** *with unit cells outlined and different layer isomers indicated by capital letters, see text for more details. U and As polyhedra are shown in yellow or green, respectively; Rb atoms are in blue and H_2O molecules are shown in magenta. O atoms are omitted for clarity.*

Uranium makes short bonds with two O atoms to form linear uranyl groups (UO_2^{2+}); for the sake of discussion these oxygens will be designated O_{Ur}. Five longer bonds with O atoms in the equatorial plane, O_{eq}, complete the pentagonal bipyramidal coordination geometry around uranium. There are two different oxo-arsenate groups in each layer, namely a mono-hydroxy $(AsO_3OH)^{2-}$ tetrahedron and a di-hydroxy $(AsO_2(OH)_2)^-$ tetrahedron. All unprotonated oxygens in these groups are O_{eq}, in other words the As tetrahedra share these oxygens with U bipyramids. The oxygens of the terminal hydroxyl group in $(AsO_3OH)^{2-}$ will be called O_H, and the corresponding ones of the $(AsO_2(OH)_2)^-$ group O_{Hf}. Each UO_7 bipyramid is linked to five arsenic based tetrahedra via common O_{eq}, each arsenic based tetrahedron is connected via common O_{eq} with either two UO_7 bipyramids in the case of $(AsO_2(OH)_2)^-$, or three for $(AsO_3OH)^{2-}$, to form the 2D uranyl hydroxy-arsenate layers of composition $[UO_2(AsO_3OH)(AsO_2(OH)_2)]^-$. The Rb^+ cations and water molecules (for the hydrated phases) are located within the interlayer space and link the layers into a 3D framework (Fig. 3.3). The fact that the $(AsO_2(OH)_2)^-$ and $(AsO_3OH)^{2-}$ tetrahedra are linked with two or three UO_7 bipyramids, respectively, is important. The $(AsO_3OH)^{2-}$ tetrahedra with three O_{eq} and one O_H are firmly bonded by three U bipyramids, thereby fixing the terminal OH^- group in either "up"

or “down” orientation with respect to the layer. The oxygens of the $(AsO_2(OH)_2)^-$ group are two O_{eq} and two O_{Hf}. The edge formed by the two O_{eq} is connected with two U bipyramids, whereas the edge formed by the two terminal O_{Hf} is free. Thus, this tetrahedron has a rotational degree of freedom about the edge which is formed by the two O_{eq}. The energy cost for a tilting about this edge can be supposed to be quite low, because no strong bonds are broken and no intra-polyhedron bond angles are involved. Thus, the $(AsO_2(OH)_2)^-$ tetrahedron is re-orientable. In a hypothetical free-standing layer the $(AsO_2(OH)_2)^-$ tetrahedron could be supposed to be in a “neutral” position where the projection of the O_{eq} - O_{eq} edge bisects the opposite O_{Hf} - O_{Hf} edge. For the same layer built into a 3D structure the two O_{Hf} groups might be subject to different non-covalent forces, and this difference might be strong enough to overcome the energy barrier and to tilt the tetrahedron in one or the other orientation. Similar to the $(AsO_3OH)^{2-}$ groups we will distinguish “up” and “down” orientations for the $(AsO_2(OH)_2)^-$ groups, but in contrast to the former these orientations are interchangeable in the latter.

As mentioned before, protons could only be located by BVS calculations. Nevertheless, this procedure allowed hydrogen bonding (h. b.) systems to be identified. Donors of the h. b. are O_{Hf}, O_H or water, possible acceptors of h.b. are $O_{Ur,}$ O_{eq}, water or O_{Hf}. Because of the rotational degree of freedom of the re-orientable $(AsO_2(OH)_2)^-$ groups, it is the h.b. involving the O_{Hf} which are likely to give rise to conformational changes of the uranyl hydroxy-arsenate layers, i.e. to $(AsO_2(OH)_2)^-$ groups, pointing either “up” or “down”..

RbUAs-1 is an anhydrous phase. The average $U{=}O_{Ur}$ bond length in UO_2^{2+} is 1.77 Å and the $U–O_{eq}$ range from 2.304(4) Å to 2.454(3) Å. (Table 3.4). In the tetrahedral oxo-arsenate groups $[AsO_3OH]^{2–}$ and $[AsO_2(OH)_2]^–$, $As–O_{eq}$ bond lengths are between 1.652(3) and 1.664(3) Å, whereas $As–O_H$ and $As–O_{Hf}$ bond lengths are between 1.722(4) and 1.741(4) Å. Rb is 10-fold coordinated by O atoms, with interatomic distances ranging from 2.874(4) to 3.437(4) Å (Fig. 4a, Table 3.9). The coordination around Rb is rather irregular, but the charge distribution remains fairly isotropic. Five out of the ten O neighbours of Rb belong to a uranyl hydroxy-arsenate layer "above" (2 $O_{Ur,}$ $1O_{eq}$, $1O_H$ and 1 O_{Hf}), a second group resides in the layer "below" (1 $O_{Ur,}$ $2O_{eq}$, $1O_H$ and 1 O_{Hf}). Two systems of fairly strong hydrogen bonds (h.b.) span the interlayer space and thus stitch the layers together, viz. dimers of $O_{Hf}{\cdots}O_{eq}$ (about 2.68 Å) and dimers of $O_H{\cdots}O_{Ur}$ (2.89 Å). A second system of $O_{Hf}{\cdots}O_{eq}$ h.b. (about 2.79 Å) occurs within the layers and adds to the stability of the latter. A short distance between this O_{Hf} and an O_{Ur} (3.08 Å) might indicate a bifurcation of the h.b. donated by this O_{Hf}. The h.b. involving O_{Hf} emerge from the same $(AsO_2(OH)_2)^-$ group and tilt this group into the either “up” or “down” orientation (Fig. 3.5).

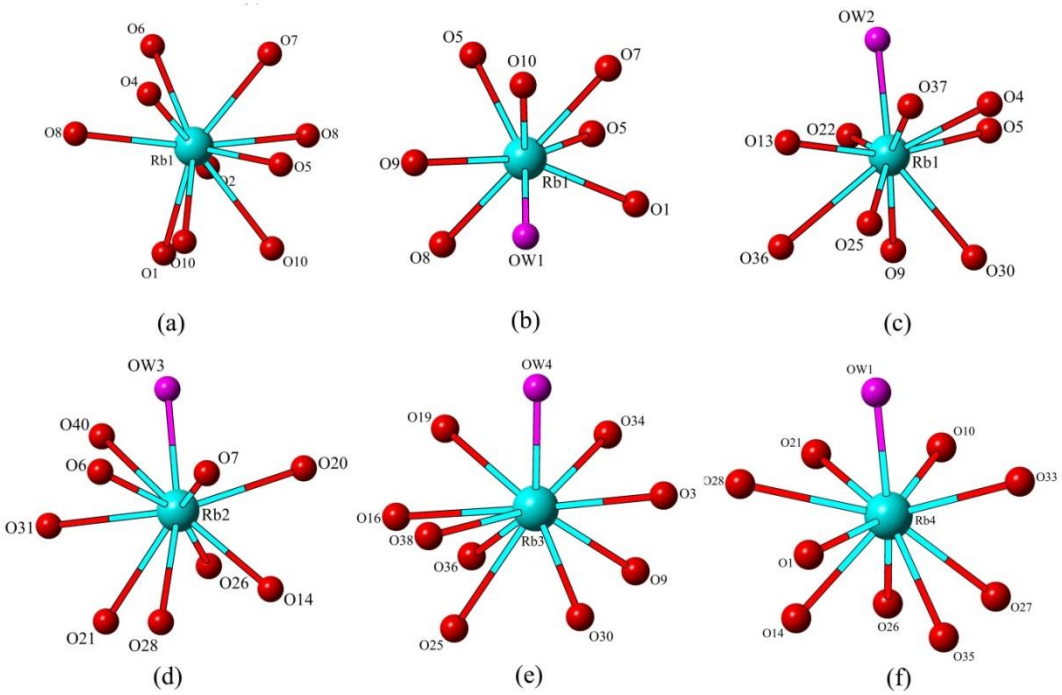

Figure 3.4*: The coordination environments of Rb atoms in (a)* ***RbUAs-1****, (b)* ***RbUAs-2*** *and (c,d,e,f)* ***RbUAs-3****.*

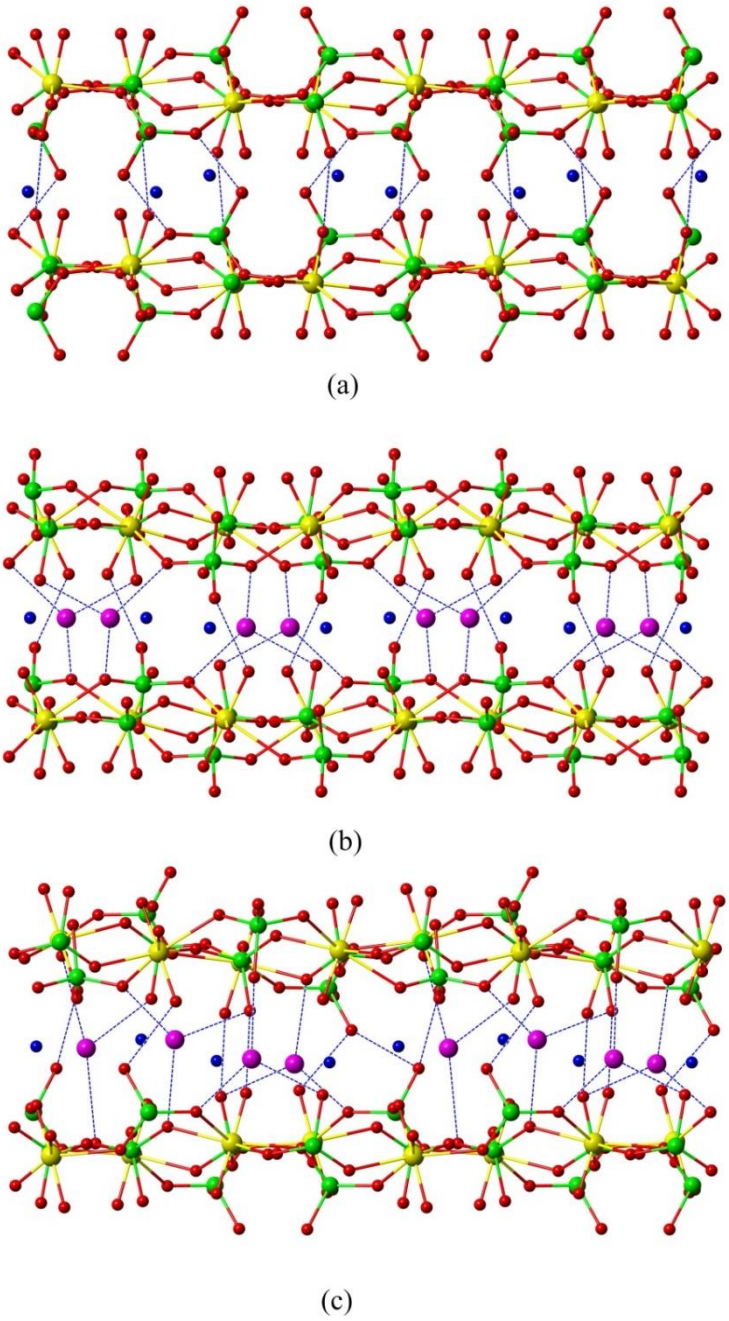

Figure 3.5: *Ball-and stick models of two layers and the interlayer space in (a)* ***RbUAs-1****, (b)* ***RbUAs-2*** *and (c)* ***RbUAs-3****. U, As, O and Rb atoms are shown as yellow, green, red and blue spheres, respectively, whereas water molecules are shown in magenta. Possible hydrogen bonds are shown as blue dashed lines. Only interlayer hydrogen bonds are marked, interlayer hydrogen bonds are omitted for clarity.*

Table 3.9: Coordination environment of rubidium atoms in the structures of **RbUAs-1**, **2** and **3,** i) Compound coordination center layer, ii) A in **RbUAs-1**, iii) Layer B in **RbUAs-2**, iv) Layer A, C in **RbUAs-3**, v) Layer above, vi) Interlayer Space, vii) Layer below, r is distance of Rb-O, Å

i	ii		iii		iv							
	Rb1	*r*	Rb1	*r*	Rb1	*r*	Rb2	*r*	Rb3	*r*	Rb4	*r*
	$O_{Ur}5$	2.88	$O_{Ur}8$	3.03	$O_{Ur}4$	2.97	$O_{Ur}6$	2.94	$O_{Ur}9$	2.93	$O_{Ur}14$	2.90
	$O_{Ur}8$	3.17	$O_{Ur}5$	2.89	$O_{Ur}9$	3.04	$O_{Ur}14$	3.07	$O_{eq}3$	3.03	$O_{eq}1$	3.15
v	$O_{eq}4$	2.95	$O_{Hf}9$	3.01	$O_{eq}5$	3.00	$O_{eq}7$	3.02	$O_{H}30$	3.02	$O_{H}35$	3.14
	$O_{Hf}7$	3.15	$O_{Hf}10$	3.08	$O_{Hf}22$	3.21	$O_{H}28$	3.54	$O_{H}34$	3.25	$O_{H}28$	3.26
	$O_{H}10$	3.25					$O_{H}2$	3.24				
vi			OW1	2.97	OW2	2.91	OW3	3.03	OW4	2.93	OW1	2.90
	$O_{Ur}8$	3.38	$O_{Ur}5$	3.17	$O_{Ur}25$	2.96	$O_{Ur}21$	3.24	$O_{Ur}25$	3.30	$O_{Ur}21$	2.99
	O_{eq} 2	2.87	$O_{eq}1$	2.89	$O_{eq}13$	3.11	$O_{eq}31$	3.31	$O_{eq}16$	3.18	$O_{Ur}27$	3.08
vii	O_{eq} 1	3.44	$O_{H}7$	2.93	$O_{eq}36$	3.63	$O_{H}26$	3.00	$O_{eq}36$	3.07	$O_{eq}10$	3.04
	$O_{H}10$	3.35			$O_{H}30$	3.34	$O_{Hf}40$	3.66	$O_{H}38$	3.22	$O_{H}26$	3.60
	$O_{Hf}6$	3.44			$O_{H}37$	3.16			$O_{H}19$	3.30	$O_{Hf}33$	3.14

The groups including O atoms are given in brackets: O_{eq} - oxygen atoms from equatorial plane of UO_7 polyhedra; O_{Ur} - oxygen atoms from uranyl groups, O_H and O_{Hf} - oxygen atoms from $AsO_2(OH)_2$ groups and $AsO_3(OH)$ arsenate groups, respectively; OW -oxygen from water molecules.

RbUAs- 2 is a hydrated form of **RbUAs- 1** and its structure is shown in Fig. 3.4b. The layer composition is identical to that described above. U-O and As-O interatomic distances are within the expected range (Table 3.4). The Rb atoms and the water molecule are located in the interlayer space. Rb sites are 8-fold coordinated by one water molecule and additional seven O atoms with interatomic distances ranging from 2.886(2) to 3.166(3) Å (Fig. 3.5b). Two O_{Ur} and two O_{Hf} reside in the layer "above" the interlayer space, one O_{Ur}, one O_{eq} and one O_H are located in the adjacent layer "below". (Table 3.9) Compared to **RbUAs-1** the presence of water molecules in the interlayer space does not only change the Rb coordination, but also the h.b. system and thereby the configuration of the layers. Water donates two h.b. to two O_{eq} in neighbouring layers (about 2.83 and 2.87 Å) and accepts one h.b. from an O_H in an adjacent layer (about 2.65 Å) (Table 3.10); Rb at a distance slightly shorter than 3 Å completes the fairly tetrahedral coordination around water. In addition to h.b. involving water there is one interlayer O_{Hf} ··· O_{Ur} h.b. (about 2.89 Å). This means that, at variance with the case of anhydrous **RbUAs- 1,** the O_{Hf} now bonds with O_{Ur}, and causes an orientation of the $(AsO_2(OH)_2)^-$ polyhedron which is different from what was observed in **RbUAs- 1**. The tilting is assisted by an interlayer O_{Hf} ··· O_{eq} h.b. (about 2.68 Å) donated by the same $(AsO_2(OH)_2)^-$ group.

Table 3.10: Possible hydrogen bonds in **RbUAs-1**, **2** and **3**, and distances [Å] between supposed donor and acceptor oxygens. # denotes intralayer hydrogen bonds.

RbUAs-1		**RbUAs- 2**		**RbUAs- 3**	
$O_{Hf}6\cdots O_{eq}3$	2.68(10)	$OW1\cdots O_{eq}3$	2.87(2)	$OW1\cdots O_{eq}2$	2.92(2)
$O_{Hf}7\cdots O_{eq}9$ #	2.79(11)	$OW1\cdots O_{eq}6$	2.83(2)	$OW1\cdots O_{eq}23$	2.82(2)
$O_{Hf}7\cdots O_{Ur}8$	3.08(10)	$O_H7\cdots OW1$	2.65(2)	$O_H37\cdots OW1$	2.74(2)
$O_H10\cdots O_{Ur}5$	2.89(10)	$O_{Hf}9\cdots O_{eq}2$ #	2.68(12)	$OW2\cdots O_{eq}15$	2.77(2)
		$O_{Hf}10\cdots O_{Ur}8$	2.89(12)	$OW2\cdots O_{eq}18$	2.87(2)
				$O_H28\cdots OW2$	2.74(2)
				$OW3\cdots O_{eq}11$	2.81(2)
				$O_H30\cdots OW3$	2.68(2)
				$O_{Hf}40\cdots OW3$	2.81(2)
				$O_H26\cdots OW4$	2.77(2)
				$O_H28\cdots O_{Ur}21$	2.82(2)
				$O_H37\cdots O_{Ur}4$	2.74(2)
				$O_{Hf}22\cdots O_{eq}17$ #	2.66(14)
				$O_{Hf}35\cdots O_{Ur}27$	2.73(2)
				$O_{Hf}38\cdots O_{eq}16$ #	2.56(13)
				$O_{Hf}39\cdots O_{Ur}6$	2.81(2)
				$O_{Hf}20\cdots O_{eq}12$ #	2.67(13)
				$O_{Hf}34\cdots O_{Ur}24$	2.90(2)
				$O_{Hf}33\cdots O_{eq}29$ #	2.70(2)
				$O_{Hf}40\cdots O_{Ur}24$ #	3.01(2)
				$O_{Hf}35\cdots O_{Hf}39$	2.83(2)
				$O_{Hf}38\cdots O_{Hf}40$ #	2.87(2)

Water contributes about 15% to the BVS of Rb, meaning that the total contribution of the O_{Ur}, O_{eq}, O_H and O_{Hf} decreases. Furthermore, the reorganization of the configuration of the building units within the layers as a consequence of the changed h.b. system results also in a rearrangement of the bond valences around the rubidium, however, the overall charge distribution around Rb remains more or less isotropic.

The structure of **RbUAs- 3** is a polymorphic modification of **RbUAs- 2** (Fig. 3.3c). With a quadrupled unit cell, there are four crystallographically distinct uranium, rubidium and water sites, eight arsenic sites and the corresponding numbers of O_{Ur}, O_{eq}, O_H and O_{Hf}. Given this higher complexity of the structure, combined with lower quality of diffraction data and refinement results, the situation for this phase is less intelligible than for **RbUAs-2** and **RbUAs-1,** in particular with respect to water positions and h.b. systems. For the heavier atoms the

interatomic distances are within the expected range (see Table 3.4).The uranyl hydroxy-arsenate layers are topologically identical with, but geometrically different from the corresponding layers in **RbUAs-2** and **RbUAs-1**. There are two different layer types in the structure of **RbUAs-3** (see below). Clearly, the different geometry of the layers is the result of different h.b. systems. Several possible h.b. involving water and interlayer as well as intralayer h.b. could be identified (Table 3.9). Two out of the four water molecules, viz. OW1 and OW2, have coordination similar to that observed for water in **RbUAs-2**: Both donate two h. b. to O_{eq} in neighbouring layers, and accept one h. b. from an O_H. Rb is at a distance of about 2.9 Å in both cases. OW3 is different in that it accepts h. b. from one O_H and one O_{Hf} from adjacent layers, but seems to donate only one h.b. to an O_{eq}. The distance to Rb is about 3 Å. According to the data at hand, OW4 is clearly different. It receives one fairly strong h.b. from an O_H (2.77 Å). Two interatomic distances of about 3.10 Å to an O_{Hf} and 3.18 Å to an O_{eq} can only be considered as weak h.b., if ever. Thus, the space around OW4 seems to be depleted in h.b. density, which might well be in accordance with the observed larger molar volume (+1.75 %) of **RbUAs-3** compared with **RbUAs-2** and, hence, the lower density of the former. A particularity of **RbUAs-3** is the observation of possible interlayer and intralayer h. b. (2.83 – 2.87 Å) between O_{Hf} of different $(AsO_2(OH)_2)^-$ groups. The coordination sphere of all Rb atoms contains one water molecule and additionally nine oxygens from neighbouring layers; the charge distribution around Rb being virtually isotropic.

3.8 Graph Representation of Structure Topology, Geometric Isomerism and Topotactic Dehydration Reactions

In the preceding paragraphs we have deduced that the geometrical isomerism of the topologically equivalent layers in the three title compounds is a consequence of the different h.b. systems and their influence on the re-orientable $(AsO_2(OH)_2)^-$ tetrahedra. Now we will present a schematic picture of the relationships by using graph representations.

The three topologically identical, but geometrically different uranyl hydroxy-arsenate layers are marked A, B and C in Fig. 3.7. Within the layers, each UO_7 bipyramid is linked to five arsenic based tetrahedra. Two of these five tetrahedra are re-orientable $(AsO_2(OH)_2)^-$ groups and three are fixed $(AsO_3OH)^{2-}$ groups. The difference between the A, B and C layer types is in the “up” and “down” orientation of the re-orientable tetrahedra. This difference can be clearly seen from Fig. 3.6 where we have marked the “up” and "down" oriented tetrahedra in green or red colour, respectively. Note, that the three $(AsO_3OH)^{2-}$ groups around a U bipyramid also occur in the “up” or “down” orientation, but, in contrast to the $(AsO_2(OH)_2)^-$ groups, they are not re-orientable and the corresponding colour code for these groups is the same for all three layer types A, B and C. The unit cells of **RbUAs-1** and **RbUAs-2** contain only one single layer type, viz. A or B, respectively. (Fig. 3.7a and b) The structure of **RbUAs-3** is

more complex with two layer types, A and C, in the unit cell with a sequence (A/C/A/C'/A) (Fig. 3.7c). Here, layer C' is related to C by the application of the inversion. To show the difference between the layers in more detail, we have chosen the key structural fragments within the layers. These are complexes of a uranium bipyramid and five surrounding As based tetrahedra. There are two different complexes, designated Type I and II. These fragments are schematically shown in Figs. 3.6a and b. The pentagon represents a UO_7 bipyramid, the circles with a dot indicate the "up" As tetrahedra and those with a cross the "down" As tetrahedra. In type I "up" and "down" configurations alternate and no more than two arsenate tetrahedra with the same orientation are neighbors, e.g. UDUDD. In contrast, in type II all arsenate tetrahedra with the same orientation are grouped together, e.g. UUUDD. Layer A contains only type I, layer B only type II, while the C-layer contains both, I and II types. Complexes of types I and II share common As based tetrahedra to yield the periodic 2D structures of the layers. Within the A-layer we can separate a regularly repeatable 1D fragment (Fig. 3.6a, shown in light blue) along the ***b*** axis. There are two different bridging tetrahedra having opposite orientation. Thus, within this layer we can see two chains of red ("down") and green ("up") tetrahedra directed along the ***b*** axis (Fig. 3.6a). When we separate the corresponding fragment within layer B, we can see that there are no red and green chains, but we have regular alternation of "up" (green) and "down" (red) tetrahedra along the ***b*** axis (Fig. 3.6b, shown in magenta). In layer C the two arrangements alternate along the ***a*** axis (Fig. 3.6c).

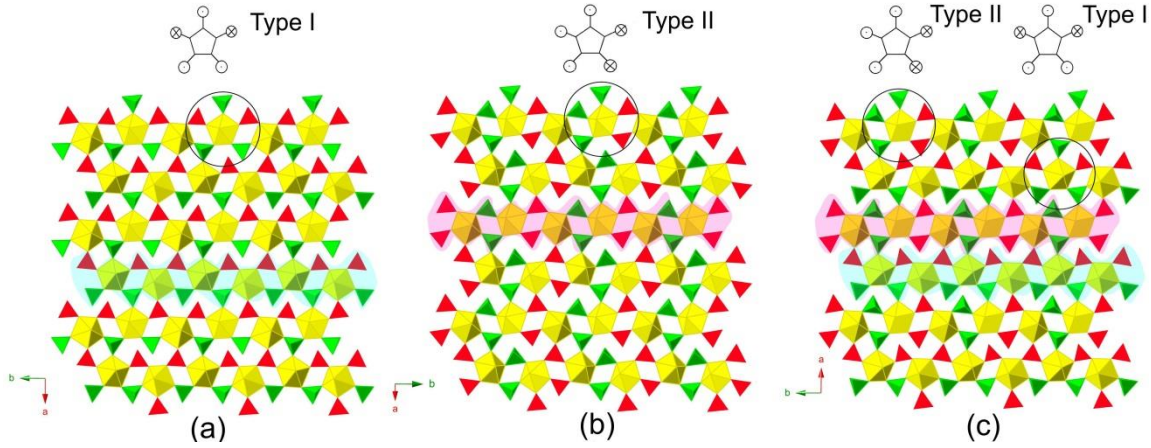

Figure 3.6: *(a) Schematic representation of layers A in* ***RbUAs-1*** *and* ***RbUAs-3****; (b) layer B in* ***RbUAs-2*** *and (c) layer C in* ***RbUAs-3****. Two different coordination environments of U polyhedra are observed within the layers, viz. types I and II, which are shown schematically on the top. See text for discussion of type I and II. U polyhedra are shown in yellow, "up" and "down" pointing As tetrahedra are shown in green or red, respectively.*

During the dehydration process both, **RbUAs-2**, **3** lose their water molecules to form the anhydrous **RbUAs-1**. It has been stated earlier that the transformations proceed via topotactic reactions. During these reactions one observes significant changes of the interlayer distances (~0.5Å) and changes of the layers' configuration. In order to describe the topotactic transitions we can use a graph representation of the A, B, and C layers. All these layers have the same black (U centers) and white (As centers) topological graph shown in Fig. 3.8a, which can be classified as cc2–1:2–5[27]. We use colour codes to show the difference in the As-based tetrahedra orientation which we described above. The coloured graphs of **RbUAs-1**, **2**, and **3** are shown in Figs. 3.8b, c and d, respectively. Green and red colour represent "up" and "down" tetrahedra, resepctively. On the graphs one can clearly distinguish the three- and double-connected As groups. Obviously, the fixed (three connected) tetrahedra cannot change their orientation during the dehydration process and changes of the layer configurations occur via re-orientation of the double connected tetrahedra. The groups of tetrahedra that have to change their orientation in order to transform layers B and C into layers A are marked with blue translucent colour on Figs. 3.7c and d, respectively. Within the B-layers all double-connected tetrahedra have to change their orientation whereas in the C layers only half of them need re-orientation.

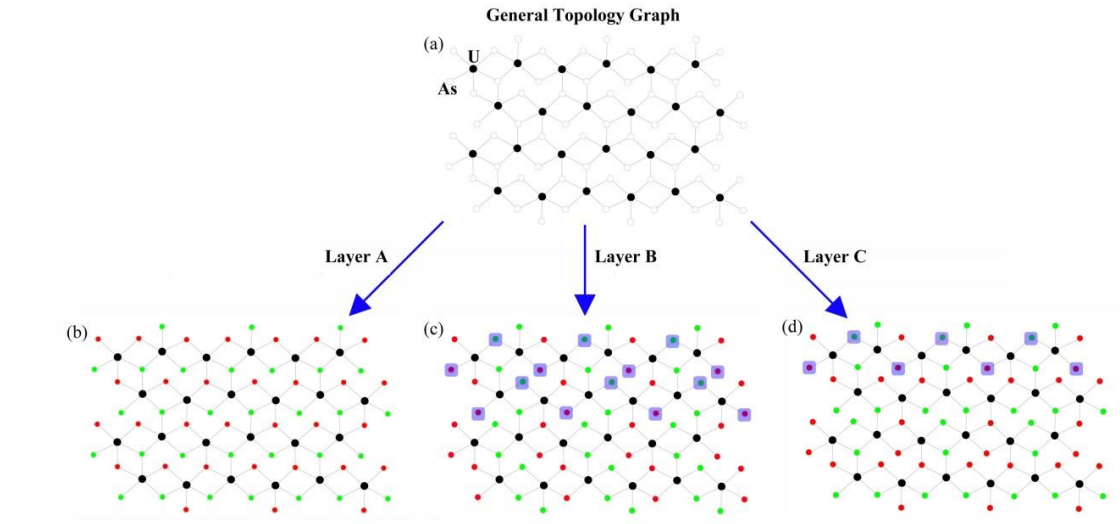

Figure 3.7: *(a) Black-and-white graph of the $[UO_2(AsO_3OH)(AsO_2(OH)_2)]^-$ layer. Colored graph of (b) A-layers, (c) B-layer and (c) C-layer. U sites are black circles, As sites are white circles on (a). Green circles are "up" and red are "down" As tetrahedra sites (see text for details). During the topotactic dehydration of* ***RbUAs-1*** *and* ***RbUAs-2,*** *the marked As tetrahedra in layers B and C have to change their orientation.*

Figure 3.8 also gives the changes of the Rb coordination environment during the dehydration process. In the layer B, only the O9 and O10 which connected to As1 atom are the free O atoms (shown in orange); In the layer C, only the O33 and O40 which connected to Rb4 and Rb2 respectively are flexible O atoms (shown in orange). Via dehydration process, layer B in α- RbUAs phase will change to layer A in RbUAs and layer C in β- RbUAs phase will change to layer A in RbUAs.

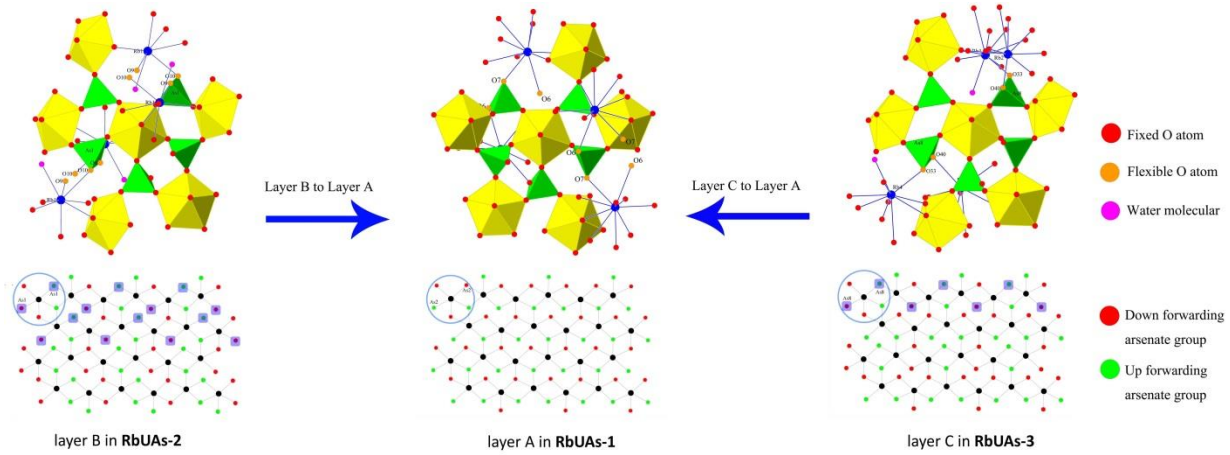

Figure 3.8*: The changes of Rb coordinations via dehydration process,*

3.9 Raman Spectroscopy

The Raman spectra obtained from single crystals of **RbUAs- 1, 2** and **3** are presented in Fig. 3.2 and band assignments are given in Table 3.11. The spectrum of **RbUAs- 1** possesses a strong polarized band at 818 cm^{-1} which according the literature data can be attributed to symmetric stretching vibrations of uranyl groups $(UO_2)^{2+}$ (Fig. 3.9a).[3] It was reported that, bands at 915 cm^{-1}, 843 cm^{-1}, 765 cm^{-1} and 745 cm^{-1} can be attributed to the bending vibrations of asymmetric stretch As – O, polymeric vibration, asymmetric stretch As–OH and symmetric stretch As–OH, respectively.[29-31] Thus four bands at 918 cm^{-1}, 846 cm^{-1}, 768 cm^{-1} and 742 cm^{-1} (Fig. 3.9a) can be attributed to the corresponding vibrations with small shift. The depolarized band which has been observed around 863 cm^{-1} is due to the asymmetric stretch of As – O bonds.

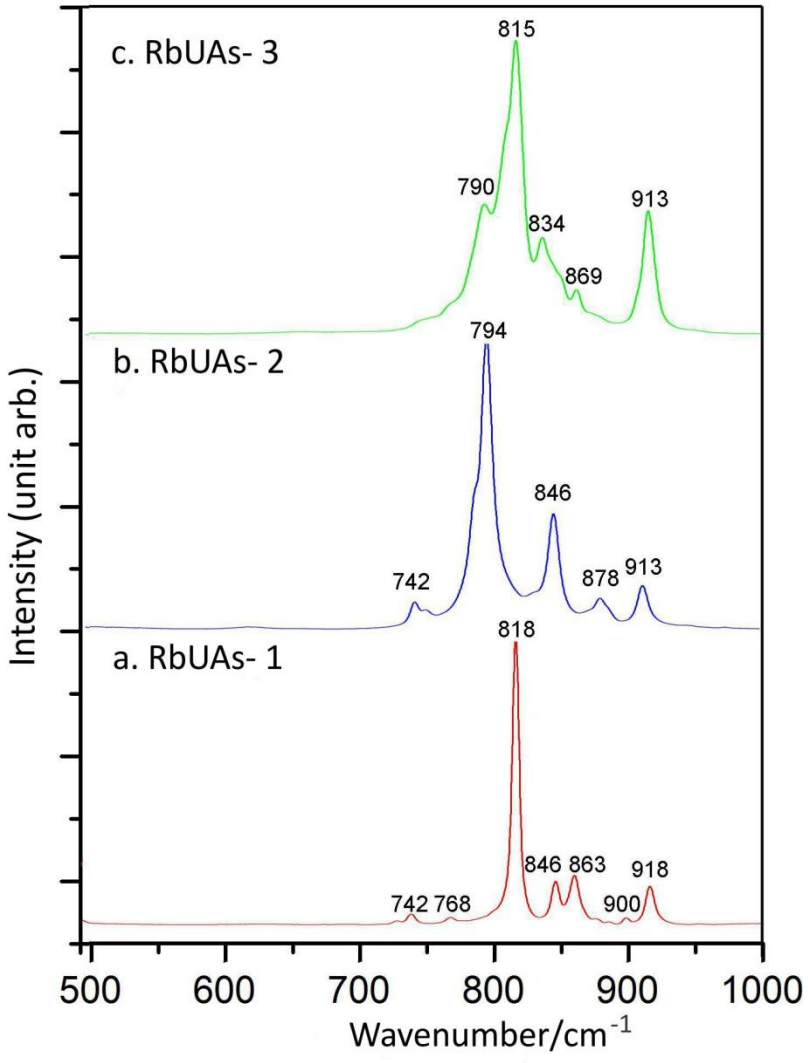

Figure 3.9: *The Raman spectra of (a)**RbUAs- 1**, (b)**RbUAs- 2** and (c)**RbUAs- 3***

In the Raman spectra of **RbUAs- 2** we observed a red shift of symmetric stretch in uranyl group. According to the literature [3, 19, 20, 29, 30], the bands at 913 cm^{-1}, 878 cm^{-1}, 846 cm^{-1}, 794 cm^{-1} and 742 cm^{-1} in Raman spectrum of **RbUAs- 2** (Fig. 3.9b) can be attributed to the bending vibrations of asymmetric stretch As–O, symmetric stretch As–O, polymeric vibration, $(UO_2)^{2+}$ units and symmetric stretch As–OH, respectively. The bands at about 750cm^{-1} in the spectrum of **RbUAs- 3** are not well defined which can be an effect of single crystal orientation. The other bands at 913 cm^{-1}, 869 cm^{-1}, 834 cm^{-1} 815 cm^{-1} and 790 cm^{-1} (Fig. 3.9c) can be attributed to the bending vibrations of asymmetric stretch As–O, symmetric stretch As–O, polymeric vibration, $(UO_2)^{2+}$ units and symmetric stretch As–OH, respectively.

Table 3.11: Raman band positions in **RbUAs- 1**, **2**, and **3**

		This study	Ref Data	Assignment	Ref
RbUAs- 1	$(UO_2)^{2+}$	818	818	Symmetric stretch	(3)
	$AsO_2(OH)_2^-$	742	745	Symm stretch As-OH	(28,32)
	$AsO_3(OH)^{2-}$	768	765	Asymm stretch As-OH	(28,32)
		846	843	Polymeric vibration	(28,32)
		918	915	Asymm stretch As-O	(28,32)
RbUAs- 2	$(UO_2)^{2+}$	794	790	Symmetric stretch	(20)
	$AsO_2(OH)_2^-$	742	745	Symm stretch As-OH	(28,32)
	$AsO_3(OH)^{2-}$	846	843	Polymeric vibration	(28,32)
		878	875	Symm stretch As-O	(28,32)
		913	915	Asymm stretch As-O	(28,32)
RbUAs- 3	$(UO_2)^{2+}$	790	790	Symmetric stretch	(20)
		815	818	Symmetric stretch	(3)
	$AsO_2(OH)_2^-$	834	838	Symm stretch As-O	(28,32)
	$AsO_3(OH)^{2-}$	869	866	Asymm stretch As-O	(28,32)
		913	915	Asymm stretch As-O	(28,32)

3. 10 Conclusions

The formation of geometric isomers of the topologically identical uranyl-arsenate layers in the three title compounds is not primarily due to any specific reason relative to the presence of uranium. The difference is rather the consequence of the presence of re-orientable $(AsO_2(OH)_2)^-$ groups in the layers and of water, in the case of the hydrated phases. The $(AsO_2(OH)_2)^-$ groups are able to change their tilting state by forming or losing hydrogen bonds in the course of hydration/dehydration reactions. These reactions are topotactic. The Rb coordination in all three structures are virtually isotropic and is therefore supposed to play no structure-directing role. It rather follows the situation created by the interplay between uranyl-arsenate layers and hydrogen bonds.

3.11 References

1. A.J. Locock; P.C. Burns; M.J.M. Duke; T.M. Flynn, *Can. Miner.,* **2004,** *42*, 973-996.
2. A.J. Locock; P.C. Burns; T.M. Flynn, *Can. Miner.,* **2004,** *42*, 1699-1718.
3. L.F. Ray, *Spectrochim. Acta Part A.* **2004,** *60*, 1469–1480.
4. C. Rodney; Wang, L. M., *Rev. Miner. Geochem.,* **2002,** *48* 673-699.
5. V. Brandel; N. Dacheux; M. Genet, *Radiochem.,* **2001,** *43*, 16-23.
6. G.J. Lumetta; B.K. McNamara; E.C. Buck; S.K. Fiskum; L.A. Snow, *Environ. Sci. Technol.,* **2009,** *43*, 7843-7848.
7. G.J. Lumetta; J.C. Braley; J.M. Peterson; S.A. Bryan; T.G. Levitskaia, *Environ. Sci. Technol.,* **2012,** *46*, 6190-6197.
8. P.C. Burns; M.L. Miller; R.C. Ewing, *Can. Mineral.,* **1996,** *34*, 845-880.
9. E.V. Alekseev; S.V. Krivovichev; W. Depmeier, *Z. Anorg. Allg. Chem.,* **2007,** *633*, 1125-1126.
10. E.V. Alekseev; S.V. Krivovichev; W. Depmeier; K. Knorr, *Z. Anorg. Allg. Chem.,* **2008,** *634*, 1527-1532.
11. E.V. Alekseev ; S.V. Krivovichev ; W. Depmeier, *J. Solid State Chem.,* **2009,** *182*, 2074-2080.
12. E.V. Alekseev ; S.V. Krivovichev ; W. Depmeier, *J. Mater. Chem.,* **2009,** *19*, 2583-2587.
13. E.V. Alekseev; S.V. Krivovichev; W. Depmeier, *Cryst. Growth Des.,* **2011,** *11*, 3295-3300.
14. E.V. Alekseev ; S.V. Krivovichev ; W. Depmeier, *J. Solid State Chem.,* **2009,** *182*, 2977-2984.
15. E.V. Alekseev; S.V. Krivovichev; T. Malcherek; W. Depmeier, *J. Solid State Chem.,* **2008,** *181*, 3010-3015.
16. S.V. Krivovichev; P.C. Burns; I.G. Tananaev, *Structural Chemistry of Inorganic Actinide Compounds*. Elsevier: Amsterdam, 2007.
17. E.M. Villa; E.V. Alekseev; W. Depmeier; T.E. Albrecht-Schmitt, *Cryst. Growth Des.,* **2013,** *13*, 1721-1729.
18. A.J. Locock; Burns, P. C., *Can. Miner.,* **2003,** *41*, 489-502.
19. L.F. Ray; M.L. Weier; W.N. Martens; J.T. Kloprogge, *J. Raman Spectrosc.,* **2005,** *36*, 797-805.
20. L.F. Ray; M.L. Weier, *J. Raman Spectrosc.,* **2006,** *37*, 585-590.
21. E.M. Villa; C.J. Marr; L.J. Jouffret; E.V. Alekseev; W. Depmeier; T.E. Albrecht-Schmitt, *Inorg. Chem.,* **2012,** *51*, 6548-6558.
22. E.M. Villa; S. Wang; E.V. Alekseev; W. Depmeier; T.E. Albrecht-Schmitt, *Eur. J. Inorg. Chem.,* **2011,** *25*, 3749-3754.
23. E.M. Villa; C.J. Marr; D. Juan; E.V. Alekseev; W. Depmeier; T.E. Albrecht-Schmitt, *Inorg. Chem.,* **2013,** *52*, 965-973.

24. N.C. Justin; E.M. Villa; S. Wang; J. Diwu; M.J. Polinski; T.E. Albrecht-Schmitt, *Inorg. Chem.,* **2012,** *51*, 8419-8424.
25. A.L. Spek, *J. Appl. Crystallogr.,* **2003,** *36*, 7-13.
26. P.C. Burns, *Can. Miner.,* **1997,** *35*, 1551-1570.
27. I. D. Brown; D. Altermatt, *Acta Cryst.,* **1985,** *B41*, 244-247.
28. N. E. Brese; M. O'Keeffe, *Acta Cryst.,* **1991,** *B47*, 192-197.
29. S. Goldberg; C.T. Johnston, *J. Colloid Interface Sci.,* **2001,** *234*, 204-216.
30. J. Čejka Jr; A. Muck; J. Čejka, *Phys. Chem. Miner.,* **1984,** *11*, 172.
31. L. Maya; G.M. Begun, *J. Inorg, Nucl. Chem.,* **1981,** *43*, 2827-2832.
32. V. Sidey, *Acta Cryst.,* **2011,** *B67*, 263-265.

Chapter 4 MORPHOTROPY AND TEMPERATURE DRIVEN POLYMORPHISM IN **A**$_2$Th(AsO$_4$)$_2$ (**A**= Li, Na, K, Rb, Cs) SERIES

4.1 Abstract

A new alkaline thorium arsenate family was obtained and systematically investigated. The structures of $A_2Th(AsO_4)_2$ (A = Li, Na, K, Rb, Cs) were determined from single crystal X-ray diffraction data. $Li_2Th(AsO_4)_2$ and either isostructural $K_2Th(AsO_4)_2$ and $Rb_2Th(AsO_4)_2$ crystallize in monoclinic crystal system. $Na_2Th(AsO_4)_2$ and $Cs_2Th(AsO_4)_2$ crystallize in orthorhombic and tetragonal crystal systems, respectively. $Li_2Th(AsO_4)_2$ consists of $[Th(AsO_4)_2]^{2-}$ layers with Li atoms in the interlayer space. The rest of compounds are based on 3D frameworks. Differences in local environment of ThO_8 coordination polyhedra are described in relation to the symmetry. Despite different local environments of ThO_8 coordination polyhedra and different structural symmetry, underlying nets of $A_2Th(AsO_4)_2$ (A= Na, K, Rb, Cs) were shown to be the same. Single crystal and powder Raman spectra were measured and bands are assigned. DSC measurements showed phase transition in $K_2Th(AsO_4)_2$ and $Rb_2Th(AsO_4)_2$ which were studied with high-temperature powder X-ray diffraction (HT-PXRD). The data of HT-PXRD demonstrates two high-temperature polymorphic modification of $K_2Th(AsO_4)_2$ and only one for isostypic $Rb_2Th(AsO_4)_2$. The phases transition in both K and Rb phases are reversible.

4.2 Introduction

Actinide inorganic chemistry is of great importance both from fundamental and applied point of view. The main feature of the actinides in comparison to the other elements is the presence of 5f electrons that leads to a variety of oxidation states (from +2 to +8[1-3]) of light actinides and, therefore, diversity of their chemical properties. Synthetic conditions have a strong influence on phase formation in actinide chemistry. [4-6] For example, there are two most stable oxidation states for uranium, namely +4 and +6. U(IV) compounds are usually obtained in reductive media and U(IV) in the structures of such compounds plays role of tetravalent cation. In contrast, U(VI) shows a strong tendency of linear divalent uranyl cation UO_2^{2+} formation, which, to wide extend, determines the crystal chemical properties of U(VI). Comparing to U(IV), only few research have been carried out on investigation of Np(IV)- and Pu(IV)-containing phases due to higher radioactivity of the latter. Much less radioactive Th(IV) has quite similar coordination chemistry with Np(IV) and Pu(IV)[7-10] as well as with U(IV) that makes Th(IV) highly suitable to model the behavior of those elements.

Actinide phosphates and polyphosphates attract significant interest as they show both structural and chemical diversity as well as promising properties. One of examples of the latter is thorium phosphate diphosphate $Th_4(PO_4)_4(P_2O_7)$ which is proposed as a host matrix for large amounts of uranium and plutonium.[11-15] The structural diversity of Th and U phosphates can be illustrated by a number of works published during last decade.[16-22] Recently, a number of research focused on alkaline thorium phosphates have been performed.[16, 23-26] Nevertheless, data on thorium arsenates are not so plentiful, although arsenates can serve as a comparative element due to similarities between arsenate and phosphate ions. For example, the crystal structure of α-$Li[(UO_2)(AsO_4)]$ is isomorphic structure of α-$Li[(UO_2)(PO_4)]$[22], and $Li(UO_2)_4(AsO_4)_3$[27] is topologically identical to the structure of $Li(UO_2)_4(PO_4)_3$.[20] In this respect we carried out a systematical investigation of $A^I - As_2O_5 - ThO_2$ (A^I = Li, Na, K, Rb, Cs) system. In this work we report the details of synthesis, crystal structures, thermal behavior, polymorphism and spectroscopic properties of novel thorium arsenate series with $A_2Th(AsO_4)_2$ (A= Li, Na, K, Rb, Cs) general formula.

4.3 Synthesis

Caution! *Although ^{232}Th (T1/2 = 1.4 10^10 yrs.) present a low specific activity, standard precautions for handing radioactive materials should be followed when working with the quantities used in the syntheses that follow.*

The synthesis following the Figure 2.2 processes, and the information about the reactants was given in the Table 4.1. The chemicals used were of analytical reagent grade and without any other further purification. The reactants were thoroughly ground together with their appropriate ratios and loaded into a platinum crucible. (Table 4.2)

Table 4.1: The Experimental Reactants used in this chapter

Compound Name	**Purity**	**Company**
Thorium nitrate ($Th(NO_3)_4{\cdot}5H_2O$)	- -	Merck
Ammonium dyhydrogen arsenate ($NH_4H_2AsO_4$)	98%	Alfa-Aesar
Lithium nitrate ($LiNO_3$)	99.9%	Alfa-Aesar
Sodium nitrate ($NaNO_3$)	99.9%	Alfa-Aesar
Potassium nitrate (KNO_3)	99.9%	Alfa-Aesar
Rubidium nitrate ($RbNO_3$)	99.9%	Alfa-Aesar
Cesium nitrate ($CsNO_3$)	99.9%	Alfa-Aesar

Table 4.2: Synthesis data and crystal profile of $A_2Th(AsO_4)_2$ (A = Li, Na, K, Rb, Cs)

Compound	**Formula**	**Th: As^V: A^I**	**Aimed temperature (K)**	**Colour/shape**
LiThAsO-1	$Li_2Th(AsO_4)_2$	1:10:2	1273	colorless block-like crystals
NaThAsO-1	$Na_2Th(AsO_4)_2$	1:10:3	1273	
KThAsO-1	$K_2Th(AsO_4)_2$	1:8:1	1123	
RbThAsO-1	$Rb_2Th(AsO_4)_2$	1:10:3	1223	
CsThAsO-1	$Cs_2Th(AsO_4)_2$	1:10:3	1273	

After the reactants were thoroughly ground together with their appropriate ratios and loaded into a platinum crucible. The furnace was ramped up to the aimed temperature by the heating rate of 873 K/h, left there for 2 hours and then slowly cooled down to room temperature at a rate of 5 K/h. The titled crystals will be isolated from the reaction product.

4.4 Single Crystal X-ray Diffraction

The data were collected and refined follow the details as section 2.4 mentioned. All the structures were checked for possible higher symmetry using the ADDSYM algorithm from the program PLATON [28, 29], but none were found. Relevant crystallographic data and details of the experimental conditions for all the three crystals are summarized in Table 4.3. All crystal chemical calculations were performed with TOPOS software package (http://topos.samsu.ru).[30, 31]

Table 4.3: Crystallographic data for $A_2Th(AsO_4)_2$ (A=Li, Na, K, Rb, Cs)

Compound	**$Li_2Th(AsO_4)_2$**	**$Na_2Th(AsO_4)_2$**	**$K_2Th(AsO_4)_2$**	**$Rb_2Th(AsO_4)_2$**	**$Cs_2Th(AsO_4)_2$**
space group	*P* $2_1/a$	*F ddd*	*P* $2_1/n$	*P* $2_1/n$	*I* $4_1/amd$
a /Å	5.6416(3)	7.0425(3)	7.7576(3)	8.0380(8)	7.3205(5)
b /Å	13.7733(7)	12.3268(4)	11.3648(3)	11.4510(9)	a
c /Å	9.1894(5)	18.2185(5)	9.4826(4)	9.6692(10)	18.623(2)
β /°	106.443(6)	90.00	110.756(5)	111.137(12)	90.00
V /$Å^3$	684.84(7)	1581.58(10)	781.75(5)	830.11(14)	998.0(1)
D_{calc} /g/cm^3	5.08	4.669	4.997	5.448	5.163
Z	4	8	4	4	4
λ /Å	0.71073	0.71073	0.71073	0.71073	0.71073
F(000)	904	1936	1032	1176	1320
R1	0.0396	0.0144	0.0317	0.0346	0.0384
wR2	0.0910	0.0273	0.0935	0.0709	0.1117

$R(F) = \Sigma||F_o| - |F_c||/\Sigma|F_o|$. $wR(F_o^2) = [\Sigma w(F_o^2 - F_c^2)^2/\Sigma w(F_o^2)^2]^{1/2}$.

4.5 Chemical Compositions

The electronic-microscopic image was shown in the Fig. 4.1, and the experimental data as well as the calculated stoichiometry was shown in the Table 4.4.

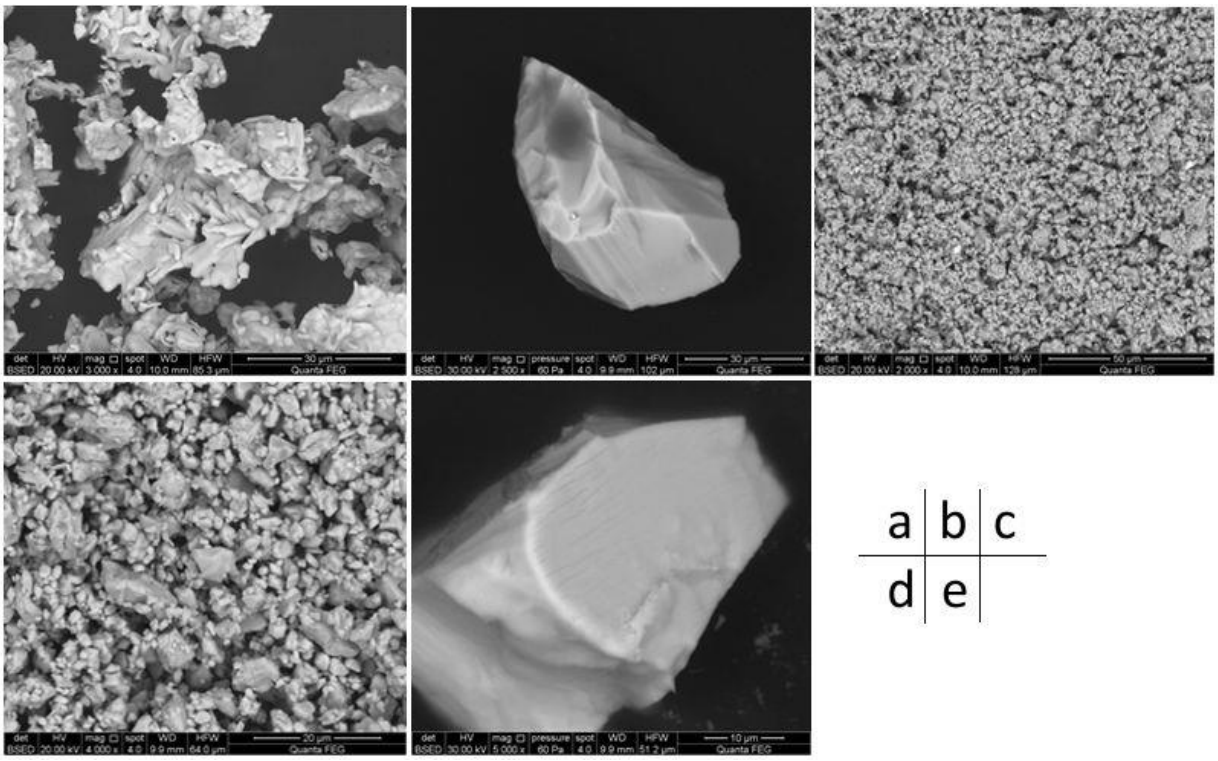

***Figure 4.1**: Electronic-microscopic image of $Li_2Th(AsO_4)_2$ (a), $Na_2Th(AsO_4)_2$ (b), $K_2Th(AsO_4)_2$ (c), $Rb_2Th(AsO_4)_2$ (d), and $Cs_2Th(AsO_4)_2$ (e).*

Table 4.4: EDX elemental analysis and stoichiometry for $A_2Th(AsO_4)_2$ A = (Li, Na, K, Rb, and Cs).

Element / Compound	Molar ratio, %			Total, %
	Th	As	A	
$Li_2Th(AsO_4)_2$*	35.1	64.9		100
$Na_2Th(AsO_4)_2$	19.9	40.0	40.1	100
$K_2Th(AsO_4)_2$	20.8	39.4	39.8	100
$Rb_2Th(AsO_4)_2$	18.7	40.5	40.8	100
$Cs_2Th(AsO_4)_2$	20.1	38.0	41.9	100
$A_2Th(AsO_4)_2$	20	40	40	100

*as Li cannot be detected by EDX, only As and Th is listed; theoretical Th : As ratio = 0.33 : 0.67

The results of EDX elemental analysis are in good agreement with those of the single crystal X-ray diffraction studies. Proton positions could not be determined in the X-ray studies

4.6 Pure Powder Samples Preparation and Powder X-ray Diffraction

The pure phase powders of all 5 alkaline thorium arsenate compounds were prepared according to 1 : 2 : 2 stoichiometric ratio of $Th(NO_3)_4 \cdot 5H_2O$, $NH_4H_2AsO_4$, and ANO_3, where A = Li, Na, K, Rb, and Cs. Initial mixtures of reagents were finely ground, heated up to 723 K in air and exposed at this temperature for 30 hours. After cooling, the samples were ground and room-temperature powder X-ray diffraction was employed to check the purity of the polycrystalline samples. In case of inconsistency between experimental powder diffraction patterns and those calculated from single crystal X-ray diffraction, the samples were heated up to higher temperature until the pure phase powder samples were obtained. This procedure was performed with 50K/step and 20 K/step temperature increase for the temperature ranges of 723 – 873 K and 873 – 1073 K, respectively. The final temperatures of pure phase formation are 1073, 993, 993, 1033, and 913 K for A = Li, Na, K, Rb, and Cs, respectively.

The Experimental and theoretical powder diffraction patterns of $A_2Th(AsO_4)_2$ (A=Li, Na, K, Rb, Cs) were shown in Fig. 4.2- 4.6. It can be seen that, the powder X-ray diffraction patterns of the pure phase powder of $A_2Th(AsO_4)_2$ (A=Li, Na, K, Rb, Cs) match well with the theoretical simulations from single crystal structures.

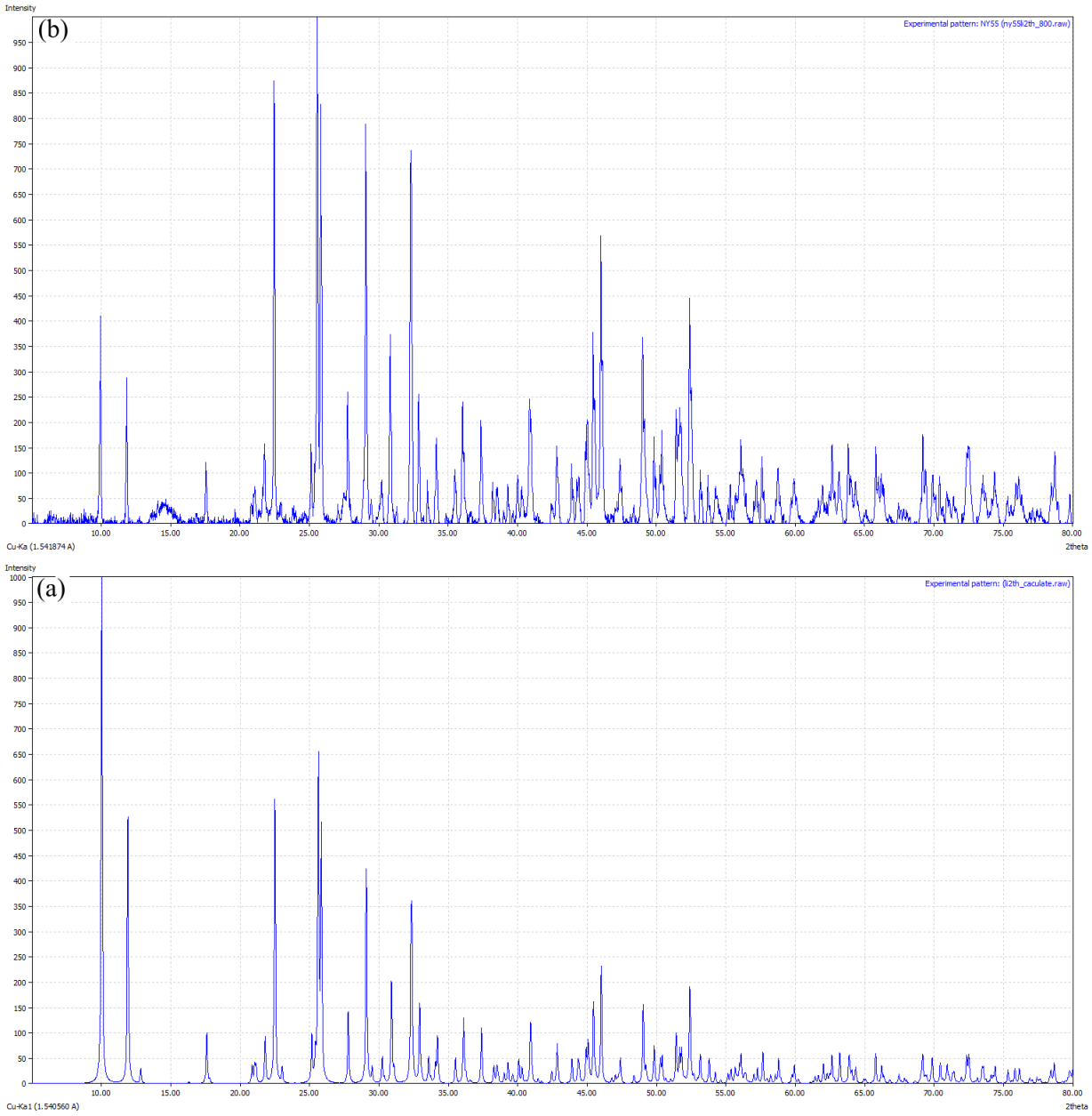

***Figure 4.2**: The powder X-ray diffraction patterns of the pure phase powder of $Li_2Th(AsO_4)_2$ and the theoretical simulations from single crystal structures. (up is theoretical data, down is experimental data)*

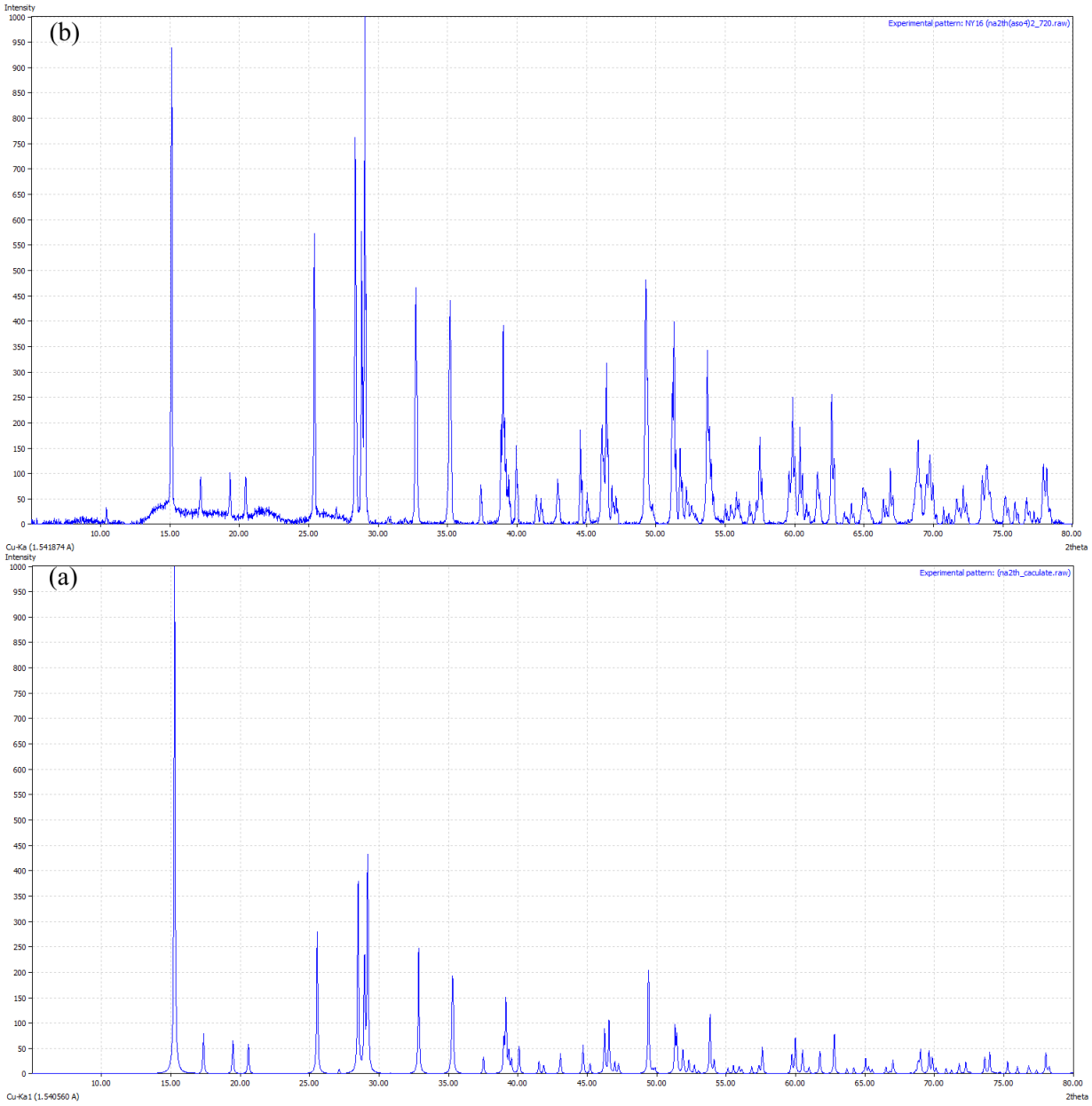

***Figure 4.3**: The powder X-ray diffraction patterns of the pure phase powder of $Na_2Th(AsO_4)_2$ and the theoretical simulations from single crystal structures. (up is theoretical data, down is experimental data)*

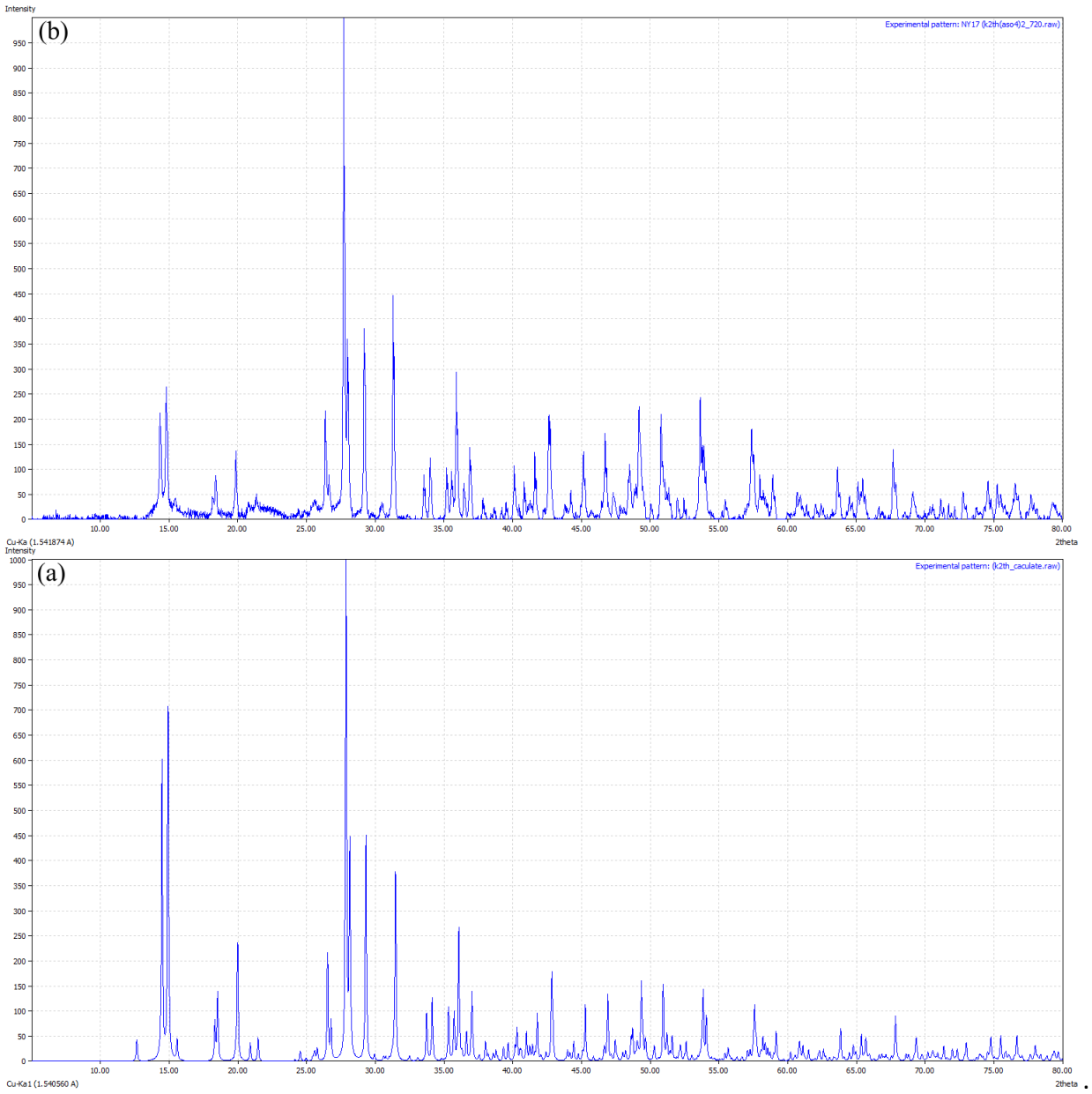

***Figure 4.4**: The powder X-ray diffraction patterns of the pure phase powder of $K_2Th(AsO_4)_2$ and the theoretical simulations from single crystal structures. (up is theoretical data, down is experimental data)*

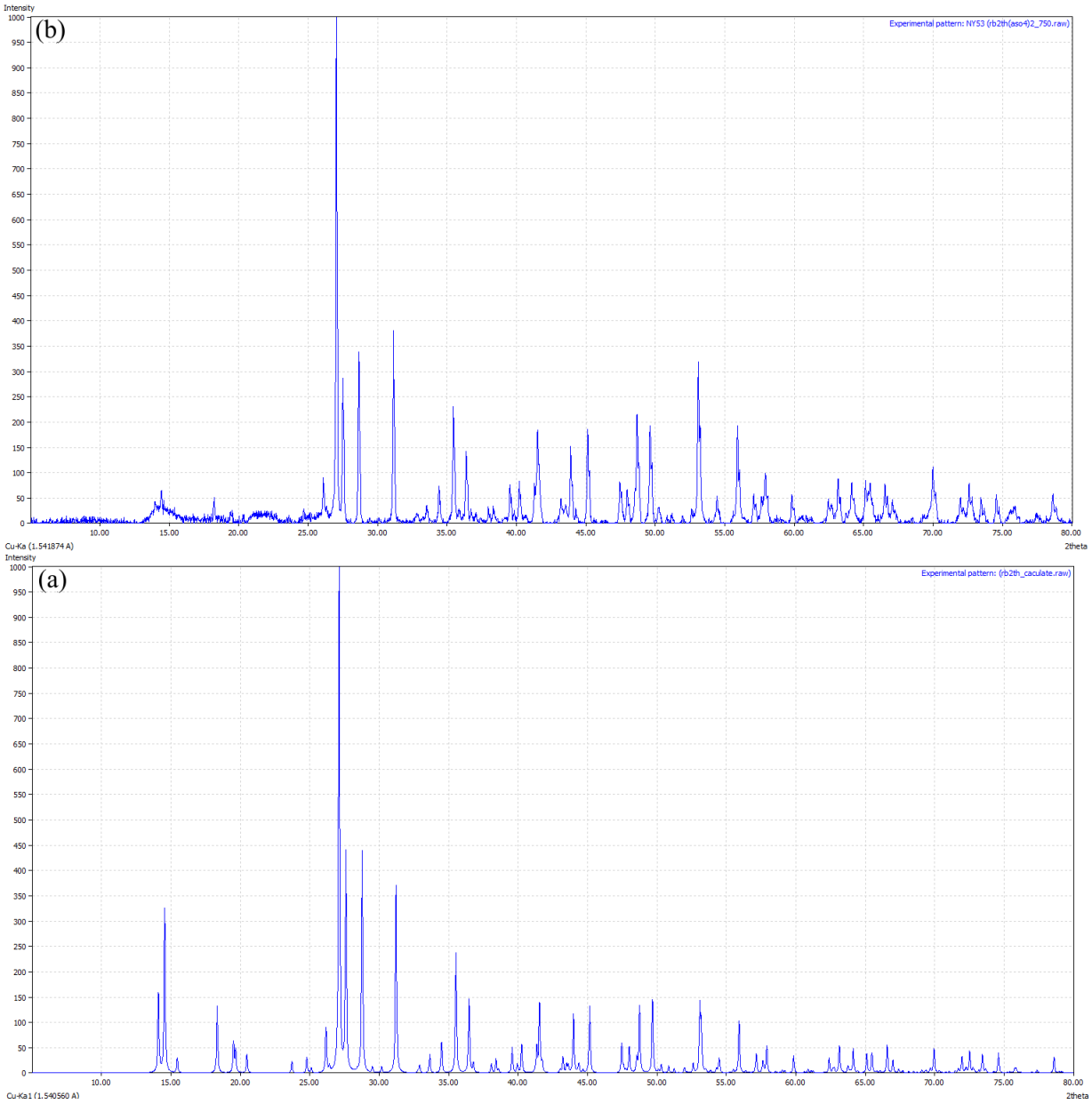

***Figure 4.5**: The powder X-ray diffraction patterns of the pure phase powder of $Rb_2Th(AsO_4)_2$ and the theoretical simulations from single crystal structures. (up is theoretical data, down is experimental data)*

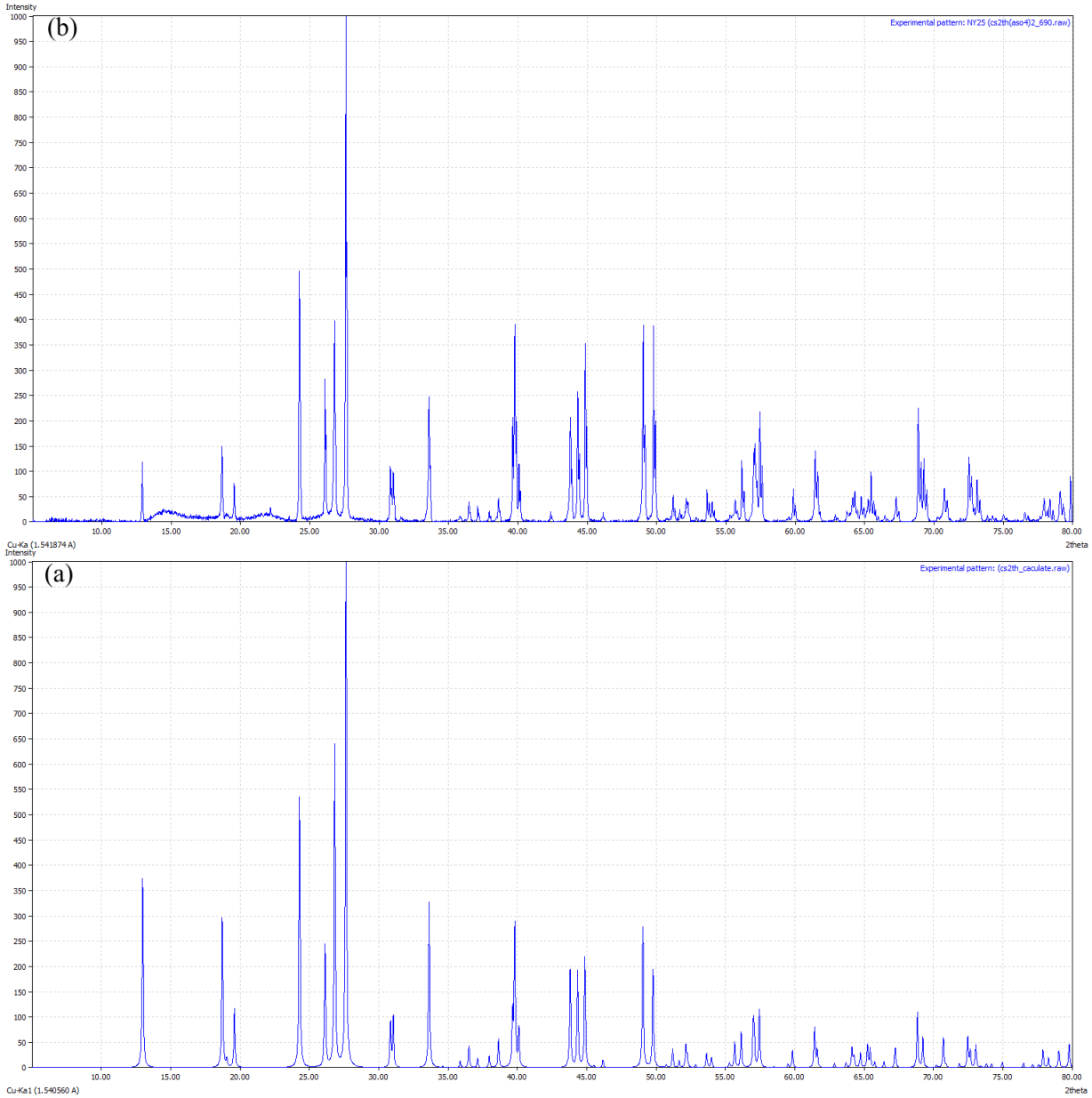

***Figure 4.6**: The powder X-ray diffraction patterns of the pure phase powder of $Cs_2Th(AsO_4)_2$ and the theoretical simulations from single crystal structures. (up is theoretical data, down is experimental data)*

4.7 Bond Valence Analysis

Bond-valence sums (BVS) for all atom positions in $A_2Th(AsO_4)_2$ (A = Li, Na, K, Rb, Cs) phases were calculated, and the results are given in Table 4.5-4.9. The bond-valence parameters for Th(IV)-O, A(I)-O, and As(VI)-O are used according to Brese and O'Keeffe.[32]

Table 4.5: Bond-valence analysis for $Li_2Th(AsO_4)_2$

	Th1	As1	As2	Li1	Li2	∑
O1	0.437		1.160			1.991
	0.394					
O2	0.582	1.282			0.236	2.101
O3	0.474	1.142				1.937
	0.321					
O4			1.368	0.293		1.947
				0.285		
O5	0.413	1.272				1.685
O6	0.377		1.199		0.102	2.005
	0.328					
O7	0.605		1.251		0.092	1.948
O8		1.325		0.285	0.212	2.034
				0.212		
∑	3.93	5.02	4.98	1.07	0.64	

Table 4.6: Bond-valence analysis for $Na_2Th(AsO_4)_2$

	Th1	As1	Na1	∑
O1	$0.360^{\times 4\downarrow}$	$1.241^{\times 2\downarrow}$	$0.217^{\times 2\downarrow}$	1.901
			$0.083^{\times 2\downarrow}$	
O2	$0.660^{\times 4\downarrow}$	$1.289^{\times 2\downarrow}$	$0.122^{\times 2\downarrow}$	2.071
∑	4.08	5.06	0.84	

Table 4.7: Bond-valence analysis for $K_2Th(AsO_4)_2$

	Th1	As1	As2	K1	K2	∑
O1	0.502		1.262	0.106	0.096	2.02
					0.051	
O2	0.578	1.262		0.099	0.064	2.00
O3	0.394	1.238			0.245	1.93
					0.056	
O4	0.422	1.221		0.156	0.239	2.12
				0.079		
O5	0.385		1.225	0.207		2.01
				0.189		
O6	0.462		1.235	0.265	0.141	2.10
O7	0.562	1.296		0.102	0.089	2.05
O8	0.550		1.248		0.159	1.96
∑	3.86	5.02	4.97	1.20	1.14	

Table 4.8: Bond-valence analysis for $Rb_2Th(AsO_4)_2$

	Th1	As1	As2	Rb1	Rb2	∑
O1	0.482		1.221	0.118	0.088	1.97
					0.065	
O2	0.400	1.192		0.183	0.249	2.12
				0.093		
O3	0.526	1.289		0.101	0.103	2.06
				0.037		
O4	0.455		1.231	0.260	0.185	2.13
O5	0.373	1.275			0.226	1.96
					0.090	
O6	0.595	1.235		0.110	0.052	1.99
O7	0.523		1.238	0.039	0.173	2.00
					0.022	
O8	0.398		1.238	0.232		2.06
				0.232		
∑	3.75	4.99	4.93	1.33	1.23	

Table 4.9: Bond-valence analysis for $Cs_2Th(AsO_4)_2$

	Th1	As1	Cs1	∑
O1	$0.602^{\times 4\downarrow}$	$1.279^{\times 2\downarrow}$	$0.049^{\times 4\downarrow}$	1.93
O2	$0.370^{\times 4\downarrow}$	$1.245^{\times 2\downarrow}$	$0.212^{\times 4\downarrow}$	2.04
∑	3.89	5.05	1.04	

4.8 Crystal Structure Description

$Li_2Th(AsO_4)_2$ crystallizes in the centrosymmetric monoclinic space group $P2_1/a$ (Table 4.3) and based upon $[Th(AsO_4)_2]^{2-}$ 2D layers. The Li cations are located within the interlayer space (Fig. 4.7a). Thorium atoms occupy a single crystallographic position and possess nine-fold oxygen coordination. The Th – O bond distances are in the range of 2.353(10) – 2.587(8) Å. Two symmetrically independent arsenic atoms form AsO_4 tetrahedra with As – O bond lengths ranging from 1.651(9) to 1.718(9) Å. Arsenate anions can be assigned to T^{21} and T^{31} coordination types (Fig. 4.8 a and b) according to the classification given in the literature.[33, 34] The uppercase of given designation describes a number of donor oxygen atoms coordinating on Th atoms (M, B, T, K, etc. for mono-, bi-, tri-, tetradentate ligands[33]). The superscript numbers equals to the amount of Th atoms connected through one, two, three, etc. donor O atoms, respectively. AsO_4 groups are coordinated to Th atoms only by three O atoms and have one terminal oxygen atom in the crystal structure of $Li_2Th(AsO_4)_2$ (Fig. 4.8 a and b). One can find that first two superscript positions are equal to the number of Th coordination polyhedra that share corner or edge with one arsenic polyhedron. Both ThO_9 and AsO_4 polyhedra form corrugated sheets parallel to (001) (Fig. 4.7a).

There are two independent Li sites within the interlayer space that serve for a charge balancing and a connection of the layers into 3D assembly. Both Li atoms have four-fold oxygen coordination with Li–O bond distances ranging from 1.92(3) to 2.35(4) Å.

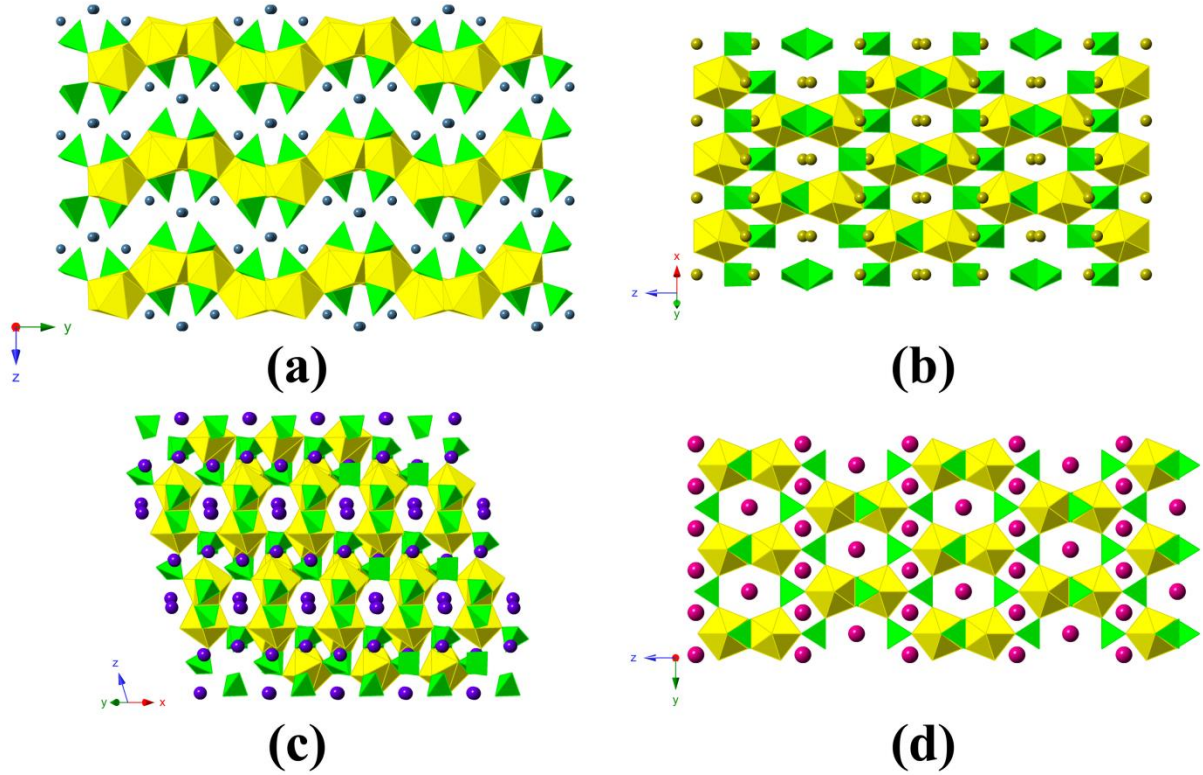

Figure 4.7*: Polyhedra representation of the crystal structures of $Li_2Th(AsO_4)_2$ (a), $Na_2Th(AsO_4)_2$ (b), $K_2Th(AsO_4)_2$ (c), and $Cs_2Th(AsO_4)_2$ (d). $Rb_2Th(AsO_4)_2$ is isostructural with $K_2Th(AsO_4)_2$. Th and As polyhedra are shown in yellow and green, respectively, alkaline atoms as colored spheres.*

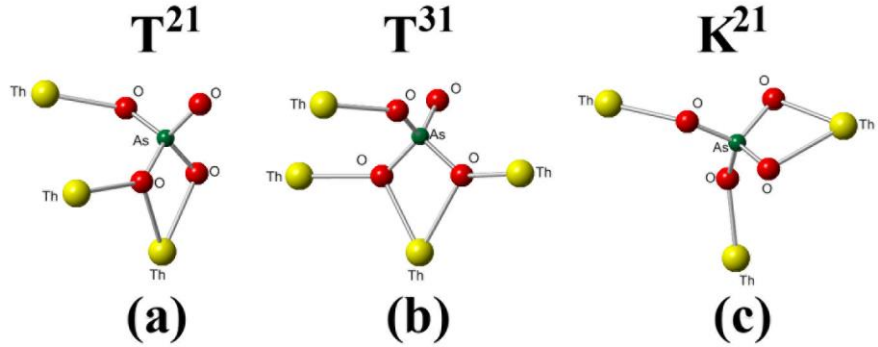

Figure 4.8: *Coordination types of arsenate-anions in the crystal structures of $A_2Th(AsO_4)_2$ (A = Li, K, Rb, and Cs).*

$Na_2Th(AsO_4)_2$ crystallizes in a orthorhombic space group *F*ddd (Table 4.3) and based upon 3D framework. The structure of $Na_2Th(AsO_4)_2$ (Fig. 4.7b) shows significant differences compared to the chemically similar $Li_2Th(AsO_4)_2$. It contents only one symmetrically independent Th atom which occupy a single site with D_2 local symmetry and is connected to eight O atoms with Th–O distances ranging from 2.3211(15) to 2.5453(14) Å. The arsenic atoms also occupy a single crystallographic position with C_2 site-symmetry. The As – O bond lengths in AsO_4 tetrahedra are equal to 1.6729(15) and 1.6872(15) Å. The arsenate anion is connected to three Th atoms with the mode shown in Fig. 4.8c. The denticity of the arsenate-anions is four and can be designated with K letter. Thus, the coordination type of arsenate-anions in the crystal structure of $Na_2Th(AsO_4)_2$ is K^{21}, which means that AsO_4 polyhedron shares two corners and one edge with three different ThO_8 polyhedra. It is noteworthy that the edge-sharing arsenate-anions are in *trans*-positions within the coordination environment of Th atoms (Fig. 4.7a). The $[Th(AsO_4)_2]^{2-}$ framework contains chains of cages along [110] directions. The cages are occupied by Na atoms (Fig. 4.7b) with the shortest Na – Na distances are 3.6061(4) Å.

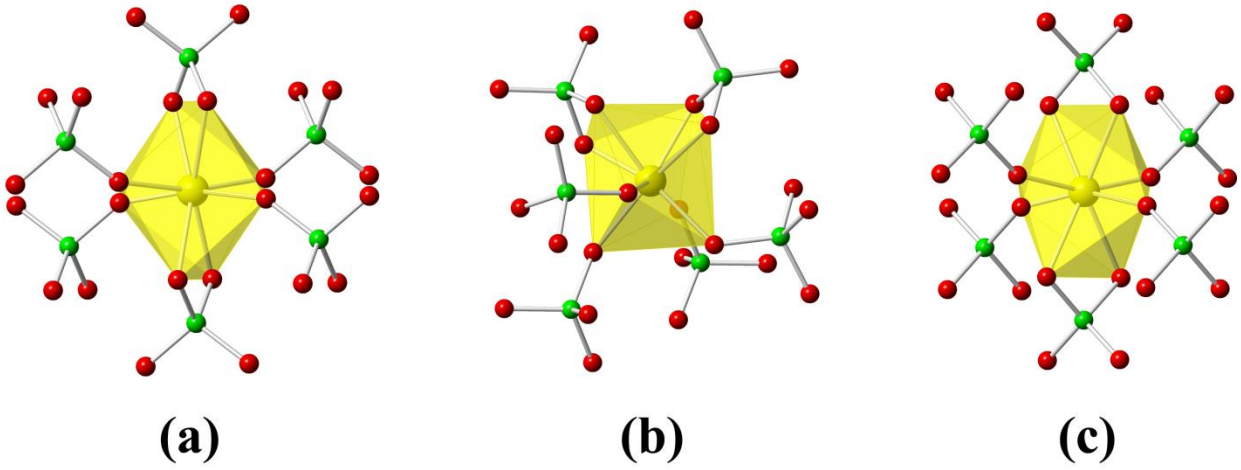

Figure 4.9: *Second neighbor coordination of Th atoms in the crystal structures of $Na_2Th(AsO_4)_2$ (a), $A_2Th(AsO_4)_2$ (A = K, Rb) (b), and $Cs_2Th(AsO_4)_2$ (c). Th polyhedra are shown in yellow, As and O atoms are green and red, respectively.*

$K_2Th(AsO_4)_2$ and **$Rb_2Th(AsO_4)_2$** are isostructural and crystallize in $P2_1/n$ space group. Both crystal structures are based on 3D framework that consists of corner- and edge-sharing ThO_8 and AsO_4 polyhedra (Fig. 4.7c). Th atoms occupy a single crystallographic position and are bound to eight O atoms with bond distances in the ranges of 2.370(4) – 2.520(4) Å and

2.363(6) – 2.532(6) Å for A = K and Rb, respectively. Arsenate anions possess same K^{21} coordination type as observed in $Na_2Th(AsO_4)_2$. As – O distances vary from 1.671(4) Å to 1.693(3) Å and 1.670(6) Å to 1.708(6) Å for A = K and Rb, respectively. The symmetry change, comparing to $Na_2Th(AsO_4)_2$, is raised from a stereometric change of Th atom environment that expressed in *cis*-positioning of the edge-sharing arsenate groups (Fig. 4.9b). The chains of cages similar to that in $Na_2Th(AsO_4)_2$ are also existing in the structures of $K_2Th(AsO_4)_2$ and $Rb_2Th(AsO_4)_2$. The potassium and rubidium atoms reside in these cages with shortest interatomic d(A–A) distances in ranges of 3.51 – 3.62 Å and 3.54 – 3.68 Å for A = K and Rb, respectively.

$Cs_2Th(AsO_4)_2$ crystallize in a tetragonal space group $I4_1/amd$, which represents the highest symmetry of the series discussed here. It is a 3D framework based upon eightfold coordinated Th atoms surrounded by arsenate anions (Fig. 4.7d). The Th–O and As–O bond distances are in ranges of 2.355(10) – 2.535(10) Å and 1.676(10) – 1.686(10) Å, respectively. The crystal structure of $Cs_2Th(AsO_4)_2$ contains arsenate-anions with K^{21} coordination type, and Th atoms coordinated by bidentate arsenate groups in *trans*-positions. Generally, the structure of $Cs_2Th(AsO_4)_2$ shows more similarities to the crystal structure of $Na_2Th(AsO_4)_2$ than with those of $A_2Th(AsO_4)_2$ (A = K, Rb). Therefore, the lower symmetry in $Na_2Th(AsO_4)_2$ crystal structure compared to those of $Cs_2Th(AsO_4)_2$ is due to the rather slight deformation of the Th and As polyhedra and the resulting rearrangement of the Na atom. This is reflected in geometry of ThO_8 polyhedra as could be seen in Fig. 4.9. For example, a degree of inclination is equals to 90° for the bidentate arsenate anions which are in *trans*-positions in ThO_8 polyhedron within $Cs_2Th(AsO_4)_2$. The same parameter in $Na_2Th(AsO_4)_2$ equals to 38°. The crystal structure of $Cs_2Th(AsO_4)_2$ possesses a group of channels along [110] directions occupied by Cs atoms with d(Cs–Cs) = 3.6602(3) Å. It is worth to note that despite the significant difference in the cationic radii the A – A interatomic distances are still comparable in both crystal structures of $Na_2Th(AsO_4)_2$ and $Cs_2Th(AsO_4)_2$ (3.6061(4) and 3.6602(3) Å for A = Na and Cs, respectively). It can be achieved by arranging of Cs atoms in rows within $Cs_2Th(AsO_4)_2$, while Na atoms in $Na_2Th(AsO_4)_2$ are distributed along zigzag chains.

Taking similar synthetic conditions, composition and nature of outer-sphere cations in $A_2Th(AsO_4)_2$(A = Li, Na, K, Rb, Cs) series into account we can assume that the structure formation is driven by size of alkaline cations. The smallest one (Li) leads to formation of layered structure of $Li_2Th(AsO_4)_2$ which differs significantly from other representatives of this series. The rest of the alkali metal cations show rather similar properties. Nevertheless, formation of the crystal structures with appropriate for outer-sphere cations “pores” size is facilitated. The interesting point is the lowering of symmetry from orthorhombic, in case of $Na_2Th(AsO_4)_2$, to monoclinic, in case of $A_2Th(AsO_4)_2$ (A = K, Rb), followed by a change of the structure type and subsequent increase of the crystal symmetry in $Cs_2Th(AsO_4)_2$. Despite similarities in a coordination polyhedra topology in the crystal structures of $Na_2Th(AsO_4)_2$ and

$Cs_2Th(AsO_4)_2$, higher symmetry of the least one is caused by exact match of Cs cation size to the "pore" size for a selected structure type.

Previously a number of compounds with the $A_2T(PO_4)_2$ general formula were reported (for example, $A_3Ce_{1.5}(PO_4)_3 = A_2Ce(PO_4)_2$, where A = Li, Na, K) but only one of them, $Na_2Th(PO_4)_2$, contains thorium.[35, 36] The latter compound crystallizes in space group $P2_1/c$ with unit cell parameters a = 7.055(4) Å, b = 21.66(1) Å, c = 9.095(5) Å, and β = 111.56(2)°. In both $Na_2Th(AsO_4)_2$ and $Na_2Th(PO_4)_2$, arsenate and phosphate

anions possess the same K^{21} coordination type. There are two crystallographically different Th atoms that adopt edge-sharing arsenate-anions in *cis*- and *trans*-configuration in the $Na_2Th(PO_4)_2$ structure. As we mentioned above, for ThO_8 polyhedra in $A_2Th(AsO_4)_2$ (A = Na, K, Rb, and Cs), the edge-sharing arsenate-anions occupy only *trans*- or *cis*-positions. Due to this, the crystal structure of $Na_2Th(PO_4)_2$ could be subdivided into two parts and presented as a combination of the structural units taken from crystal structures of $Na_2Th(AsO_4)_2$ and $K_2Th(AsO_4)_2$. One of these parts contains only Th1 with edge-sharing $\boldsymbol{T}O_4$ groups located in *trans*-position of ThO_8 polyhedra, part **I.** The second one contains Th2 with edge-sharing $\boldsymbol{T}O_4$ groups occupying *cis*-positions, part **II**. (Fig. 4.10) illustrates the crystal structure of $Na_2Th(PO_4)_2$ built upon continually repeated units **I** and **II**.

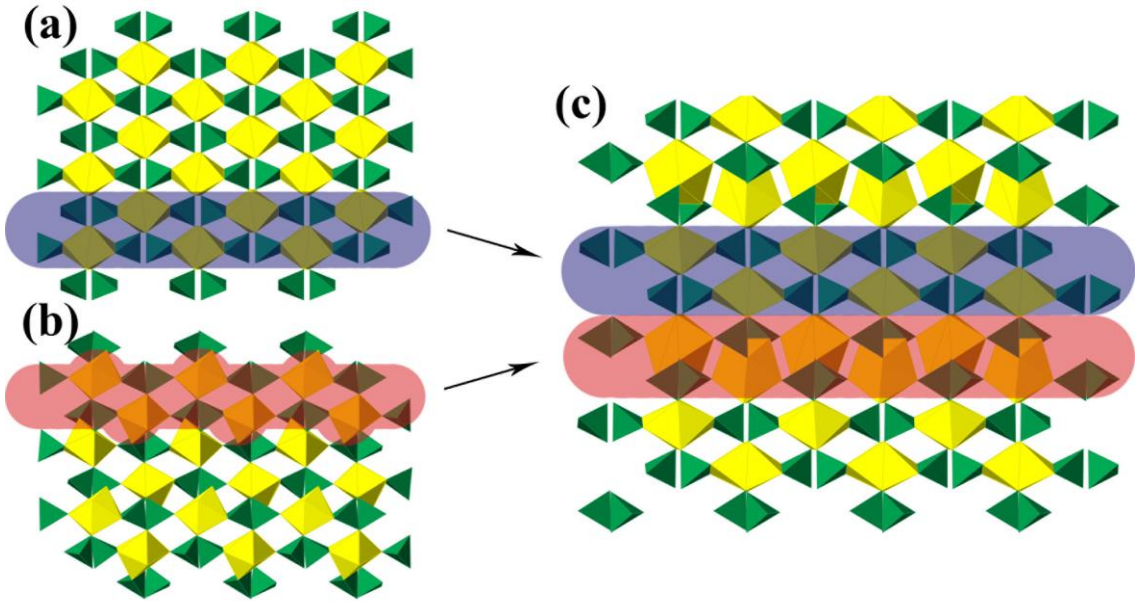

Figure 4.10: *Comparison of the crystal structures of $Na_2Th(PO_4)_2$ (c) and $A_2Th(AsO_4)_2$ (A = Na, K) (a, b, respectively) along [100]. Th and As polyhedra are shown in yellow and green, respectively.*

4.9 Properties and Topology

4.9.1 TG-DCS Experiment

The thermal behavior of the dried powders was studied from room-temperature to 1273 K by differential scanning calorimetry analysis (DSC) coupled with thermogravimetry (TG) in air at a heat rate of 10 K/min using a Netzsch STA 449C Jupiter apparatus. Each sample (20 mg) was loaded in a platinum crucible, which was closed with a platinum cover. During the measurements a constant air flow of 20 – 30 mL/min was applied.

The DSC and TGA curves $K_2Th(AsO_4)_2$ and $Rb_2Th(AsO_4)_2$ are shown at Fig. 4.11. The DSC curves of $Li_2Th(AsO_4)_2$ as well as $Na_2Th(AsO_4)_2$ show only one strong endothermic peak that corresponds to the melting point. Melting of $Li_2Th(AsO_4)_2$ and $Na_2Th(AsO_4)_2$ starts at 1324(3) and 1383(3) K, respectively, and is followed by decomposition of the compounds which is clearly seen from TG curves due to mass loss. Both direct and reverse thermal measurements for $K_2Th(AsO_4)_2$ and $Rb_2Th(AsO_4)_2$ were carried out up to 1273 K. Despite the fact that these compounds are isostructural, they show different thermal behavior. The heating DSC curve of $K_2Th(AsO_4)_2$ has four prominent endothermal effects with onset temperatures at 1019(3), 1069(3), 1149(3) and 1189(3) K without any change of sample weight, where the first one is very broadened. Cooling DCS curve of $K_2Th(AsO_4)_2$ contains three strong peaks with the onset temperatures of 1144(3), 1039(3) and 1019(3) K. There is also a minor peak starting at 1184 K. Therefore, all the effects observed in the heating DCS are reversible and show hystereses of 5 – 30 K. Both the heating and cooling runs of $Rb_2Th(AsO_4)_2$ DSC curves contain two peaks. The heating data show a strong endothermal peak with an onset temperature of 779(3) K and a moderate peak at 1179(3) K. The respective cooling curve shows a split moderate endothermal peak starting at 1139(3) K and a strong exothermal signal at 669(3) K. As both peaks at 779 and 669 K are similar (excepting sign of thermal effect) on the heating and cooling curves, we will show that they correspond to a reversible phase transition showing a hysteresis of 110 K. The higher hysteresis value in $Rb_2Th(AsO_4)_2$ compared to $K_2Th(AsO_4)_2$ is due to the lower temperature of the phase transition and, therefore, lower phase transition rate. To study phase transitions of both $K_2Th(AsO_4)_2$ and $Rb_2Th(AsO_4)_2$ high-temperature powder X-ray diffraction method was employed.

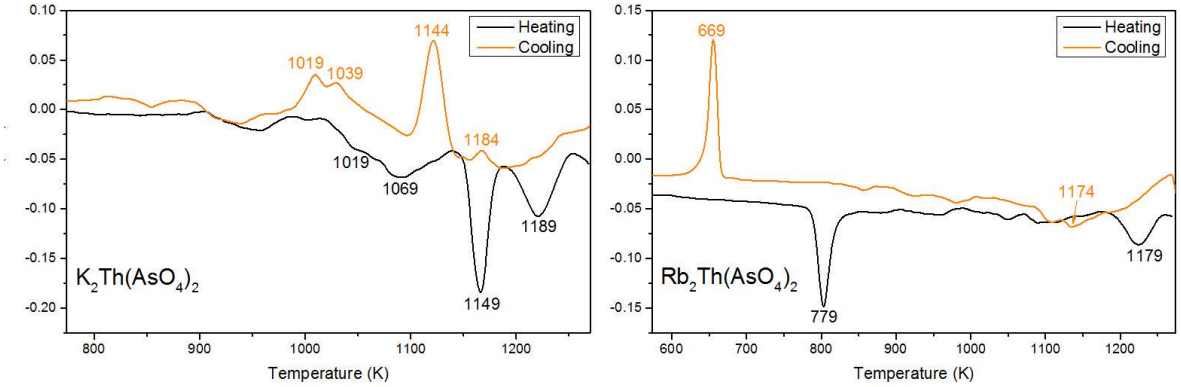

Figure 4.11: *The DSC and TA curves of $K_2Th(AsO_4)_2$ and $Rb_2Th(AsO_4)_2$. The peaks are marked with the corresponding onset temperatures.*

4.9.2 High-temperature (**HT**) Powder XRD and Phase Transition

The **HT**-PXRD and the autocorrelation analysis of the temperature-dependent X-ray diffraction data was carried out by Prof. Dr. Thorsten M. Gesing in Bremen University. The temperature-dependent X-ray powder diffraction data were collected on a Panalytical MPD powder diffractometer using Bragg-Brentano geometry. The setup was equipped with a secondary Ni filter, CuKα radiation, a X'Celerator multi strip detector and an Anton Paar HTK1200N heating chamber. The samples were placed as slurry of a sample-acetone mixture on a flat corundum holder resulting in small evaporation channels after drying which served for optimum space during thermal expansion of $K_2Th(AsO_4)_2$ and $Rb_2Th(AsO_4)_2$. Diffraction was carried out between 300 K and 1220 K with a ramping slice of 20 K. Each diffraction pattern was recorded from 4° to 85° 2θ with a step size of 0.0167° and a 69.85 s/step total data collection time. The fundamental parameter approach, where the fundamental parameters were fitted against a LaB_6 standard material, was applied for the Rietveld refinement using "Diffrac^{Plus} Topas 4.2" software (Bruker AXS GmbH, Karlsruhe). For this purpose the starting atomic coordinates were taken from the single crystal diffraction quality data. The metric parameters further used for the description of the compounds were evaluated in that way in a very accurate manner. The high-temperature X-ray powder diffraction pattern of $K_2Th(AsO_4)_2$ and $Rb_2Th(AsO_4)_2$ were shown in Fig. 4.12. The metric parameters of both samples were refined for the room-temperature modification of the respective phases as described above till the first phase transition occurred. Although the lattice parameters of the high-temperature phases are similar to the metric of the sodium and caesium compounds the structures could not be refined with isotypic structural models. For $K_2Th(AsO_4)_2$ two phase-transitions, first to an orthorhombic and thereafter to a tetragonal

metric are observed, whereas for $Rb_2Th(AsO_4)_2$ a direct phase-transition from the monoclinic metric of the low-temperature phase to a tetragonal one for the high-temperature structure was found.

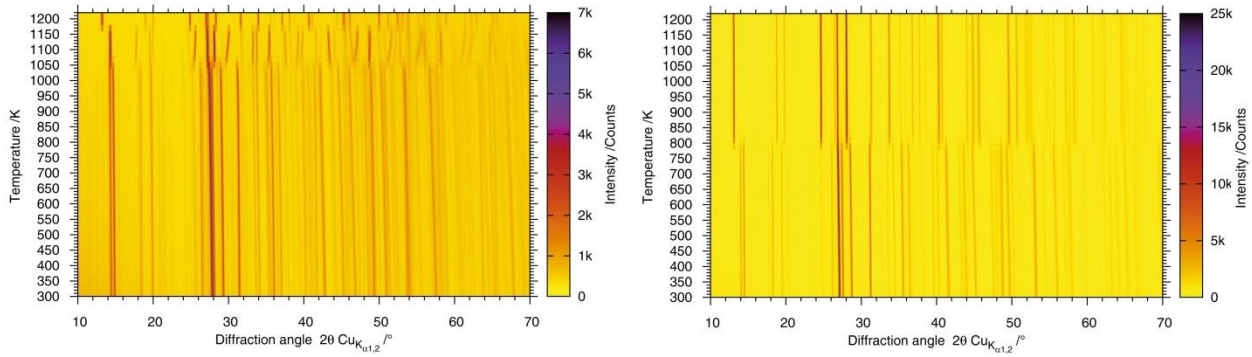

Figure 4.12: *2D plot of the temperature-dependent powder pattern of $K_2Th(AsO_4)_2$ (left) and $Rb_2Th(AsO_4)_2$ (right).*

The autocorrelation analysis was carried out by Dr. Lars Robben. For the autocorrelation analysis of the temperature-dependent X-ray diffraction data of $K_2Th(AsO_4)$ and $Rb_2Th(AsO_4)$ a suitable data range was selected (10° to 16° 2ϑ) and cut from the data sets. The selected data range was slightly denoised and the autocorrelations of the data segments were calculated according to the formula: $\mathrm{Corr}(f, f, \omega') = \int_{-\infty}^{\infty} f^*(\omega) f(\omega + \omega') d\omega$ (where f is the measured intensity at the 2θ value ω and ω' is the lag). From this autocorrelation data the normalized autocorrelation for a lag of ω' = 1 (*$Corr_{Norm}(1)$*) was chosen to characterize each single temperature data segment. The temperature-dependent development of the *$Corr_{Norm}(1)$* parameter for $K_2Th(AsO_4)$ and $Rb_2Th(AsO_4)$ are shown in Figure 4.13. For $K_2Th(AsO_4)$ *$Corr_{Norm}(1)$* remains constant up to the measurement at 1060 K and decreases linearly with increasing temperature. To establish an onset temperature for the phase transition, regression lines were fitted to both parts and their intersection calculated. By this procedure 1088 K could be deduced as onset temperature for the first phase transformation. The *$Corr_{Norm}(1)$* parameter for the $Rb_2Th(AsO_4)$ shows an initial constant behavior up to 780 K, although the scattering of the values is generally higher for the Rb-compound than for the potassium compound. In the temperature range from 800 K to 1100 K *$Corr_{Norm}(1)$* decreases with a much smaller slope than in the $K_2Th(AsO_4)$ case. The *$Corr_{Norm}(1)$* values for temperatures higher than 1100 K could be interpreted as a level-out at a constant value, because the X-ray diffraction patterns do not show any hint for a second change of the compound's structure. Accordingly three linear regressions were chosen to determine the boundary temperatures of the respective ranges by the intersections of the linear regressions.

The first phase transition temperature could be determined at 749 K and the temperature at which the high temperature phase is stabilized is 1170 K.

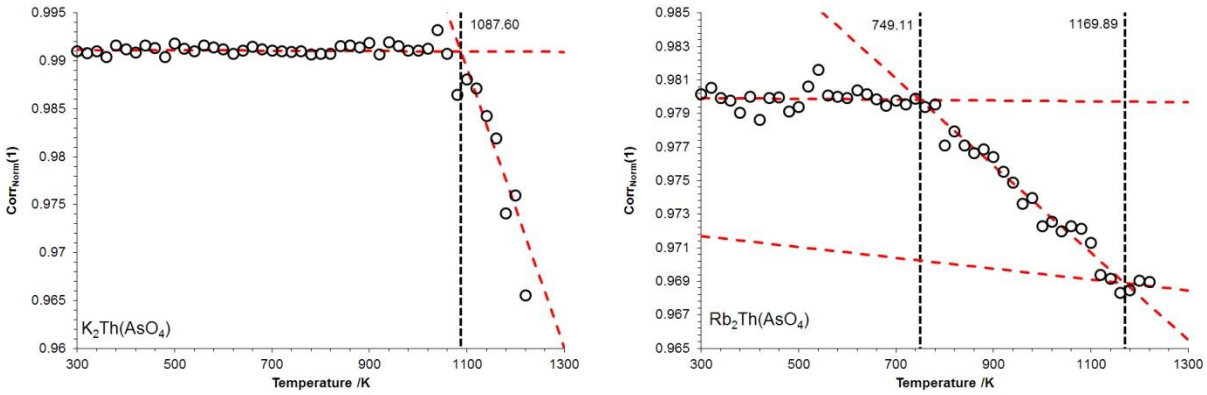

Figure 4.13: *Temperature-dependent development of the autocorrelation parameter of $K_2Th(AsO_4)_2$ (left) and $Rb_2Th(AsO_4)_2$ (right) together with the respective evaluation of transition temperatures.*

Comparing these temperatures with those obtained from DSC data (Fig. 4.14) of the two compounds, one very prominent signal for the $K_2Th(AsO_4)$ could be found in the DSC signal with an onset temperature of 1149 K. In the case of the $Rb_2Th(AsO_4)$ the DSC signal shows one signal with an onset of 779 K and a weaker one with an onset temperature of 1179 K. The transition temperatures obtained by the autocorrelation analysis are lower than these due to the different heating rates used in both measurements and the additional holding times in the X-ray measurements. In the case of $K_2Th(AsO_4)$, the second phase transition could not be observed in the autocorrelation of the selected range because there is only one observed reflection, which does not change in the course of the transition. Considering other ranges with visible changes due to the second phase transition the calculated $Corr_{Norm}(1)$ values do not give a clear signal due to the bad definition of the X-ray diffraction data close to the transition temperature.

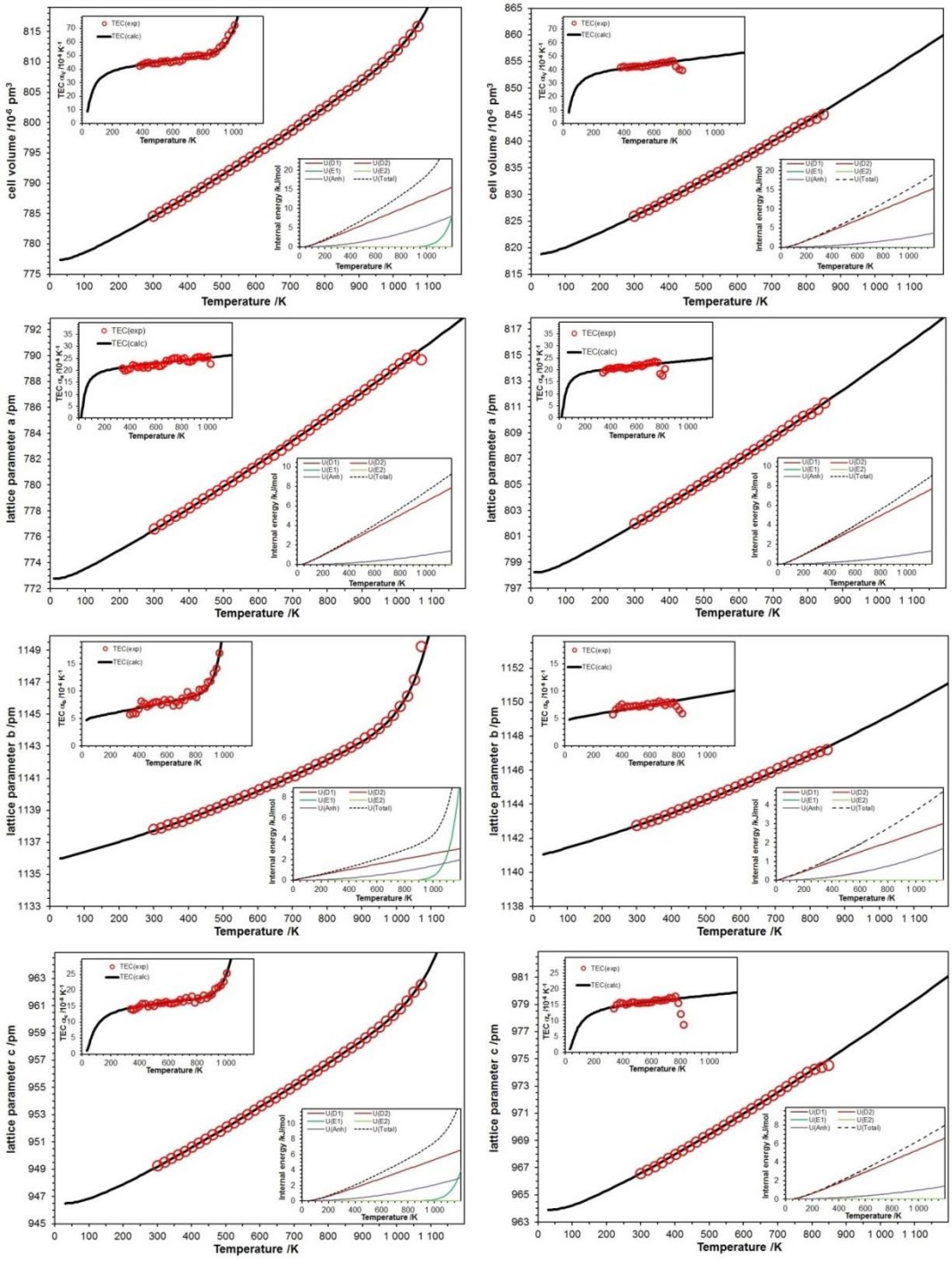

Figure 4.14: *Temperature-dependent metric parameters and thermal expansion coefficients (TEC, inset top) together with the respective DEA fit results and single energy term contribution (insert bottom) for the X-ray powder data of room-temperature phases of* $K_2Th(AsO_4)_2$ *(left) and* $Rb_2Th(AsO_4)_2$ *(right).*

To get intrinsic energy information of the phases the thermal expansion of solids can be adequately modeled using both Debye quasi-harmonic and Einstein harmonic models. In the Einstein harmonic model the atoms in a solid are independent oscillators and free from other sources of dynamical entropy. The Debye quasi-harmonic model also assumes independent oscillators, however, with altered frequencies. None of the thermal expansion coefficient (TEC) of the metric parameters saturate at a temperature-independent region for the observed range (Fig. 4.14, inset), which is assumed to be associated with intrinsic anharmonicity leading to anisotropic and anomalous thermal expansion. Because of this observation we carried the first refinements of both phases out using one Debye and the Anharmonicity term (d = 1, e = 0, k_A) in the general equation:

$$M(T) = M_0 + \sum_{i=1}^{d} k_{Di} U_{Di}(T) + \sum_{i=1}^{e} k_{Ei} U_{Ei}(T) + k_A U_A(T)$$

equation 4.1

as given together with further details elsewere[37]. In this equation, *M(T)* refers to any of the temperature-dependent metric parameters (*V(T)*, *a*(*T*)*, b*(*T*) and *c*(*T*)), k_{Di}, k_{Ei} and k_A are adjustable fitting parameters representing thermoelastic information, contributing to Debye (U_{Di}), Einstein (U_{Ei}) and anharmonic (U_A) internal energies, respectively. From these refinements it could be deduced that the high-temperature behavior of the phases is influenced by the anharmonic phonon behavior whereas the harmonic part could nicely be described using quasi-harmonic Debye oscillators. Without data from room-temperature down close to 0 K only one Debye term is necessary to describe this phonon/energy contribution.

For the refinement of the thermal behaviour of $Rb_2Th(AsO_4)_2$ the Debye-Anharmonicity (DA) model (d = 1, e = 0, k_A) describes the temperature dependency of the all metric parameters as well as the respective thermal expansion coefficient (TEC) as could be seen in Figure 4.14. Fitted values are given in Table 4.10. The slight deviations from the calculated curves at high temperatures represent the beginning phase-transition. In this respect the thermal behavior of $Rb_2Th(AsO_4)_2$ could be compared with the chemically similar $Rb_2Th(MoO_4)_3$ phase[38]. But, whereas for $Rb_2Th(MoO_4)_3$ a displacive phase-transition was assumed, a clear observation of a phase-transition for $Rb_2Th(AsO_4)_2$ could be reported here. Because the X-ray powder pattern are similar before and after the heating measurements a displacive phase-transition is very likely.

Table 4.10: Values resulting from the fitting of the temperature-dependent metric parameters

Metric parameter	*V*	*a*	*b*	*c*	*V*	*a*	*b*	*c*
	$K_2Th(AsO_4)_2$				$Rb_2Th(AsO_4)_2$			
Model [b]	DEA	DA	DEA	DEA	DA	DA	DA	DA
0 K [a]	777.32	772.78	1135.89	946.52	818.84	798.22	1140.92	963.90
$k_{D1}/10^{-14}$	1400.61	698.10	253.56	613.88	1387.83	684.81	252.95	613.88
θ_{D1}/K	223.53	177.35	24.83	336.51	225.73	177.69	24.12	336.51
$k_{E1}/10^{-14}$	2.4 10^8	-	8.0 10^8	1.7 10^8	-	-	-	-
θ_{E1}/K	18653	-	19826	19091	-	-	-	-
$k_A/10^{-12}$	-518.72	-200.38	-280.49	-193.48	-511.49	-191.71	-237.63	195.58

[a] Cell parameters *a*, *b*, *c* and cell volume *V* at 0 K given in pm and $10^6 pm^3$, respectively, with errors estimated from the calculations to 5 %. [b] DA = single Debye Anharmonic model, DEA = single Debye single Einstein Anharmonic model, $\theta_A = \theta_{D1}$.

In $K_2Th(AsO_4)_2$ only the *a* lattice parameter behaves like the isotypic $Rb_2Th(AsO_4)_2$ compound while heating and could also be described using a DA model. The Debye contribution is nearly the same (Table 4.10) showing only a 15 K higher Debye-temperature of the potassium compound than the rubidium one. This correlates with a ~ 5 % higher thermoelastic constant for the anharmonicity contribution. The deviations of the proposed lattice parameters at 0 K are due to different cation sizes. For the *b* and *c* lattice parameter and consequently, because no negative thermal expansion was observed, also for the unit cell volume only a DEA fitting using one Debye, one Einstein and the anharmonicity term (d = 1, e = 1, $k_A \neq 0$) lead to reasonable fits of the metric parameter developments as well as the thermal expansion coefficients. But also in this case k_{D1}, θ_{D1} and k_A were found to show comparable values for $K_2Th(AsO_4)_2$ and $Rb_2Th(AsO_4)_2$ (Table 4.10). It is only that a strong increase of the metric parameters and as a consequence a strong TEC increase has to be modeled by the respective Einstein contributions. This strong increase of the *b* lattice parameter in $K_2Th(AsO_4)_2$ is comparable to the strong temperature-dependent increase of the cubic *a* lattice parameter found for the tri-critical displacive phase transition of nitrate-sodalites[39], hence is also explained in this case as indicator for a phase transition with a second-order/tri-critical phase transition. Further investigations searching for the order parameter of the respective phase transition must confirm a bigger change of the order parameter during the monoclinic – orthorhombic phase transition in $K_2Th(AsO_4)_2$ and a less pronounced behavior or different mechanism for the monoclinic – tetragonal phase-transition in $Rb_2Th(AsO_4)_2$ to understand the different expansion behavior close to and around the phase-transition temperature.

4.9.3 Topological Studies

Topological analysis[40] shows crystal structures of $A_2Th(AsO_4)_2$ (A = Na, K, Rb, and Cs) based on 3,6-coordinated net (Fig. 4.15). Classification of these underlying nets with ADS program of TOPOS software package reveals **ant** (anatase) topological type found in Reticular Chemistry Structure Resource (RCSR)[41]. Variation in outer-sphere cation radii and Th atom coordination in the $A_2Th(AsO_4)_2$ (A = Na, K, Rb, Cs) series shows no changes in the topology of these compounds, although the symmetry of the crystal structures varies from monoclinic (A = K and Rb) to tetragonal (A = Cs). The last is identical to **ant** topological type highest symmetry ($I4_1/amd$[41]). Due to similarities of coordination environments in the crystal structure of $Na_2Th(PO_4)_2$ and the titled compounds, the former one is also based on 3,6-coordinated underlying net. Nevertheless, its topology does not coincide with the topology of $A_2Th(AsO_4)_2$ (A = Na, K, Rb, and Cs) and cannot be assigned by TOPOS due to absence of this topological type in its database. As well, analysis reveals that the underlying net of $Na_2Th(PO_4)_2$ contains four independent nodes with different point symbols (**PS**)[42]: $4^2.6$, 4^3, $4^5.6^4.8^6$, and $4^5.6^4.8^5.10$, while PS of nodes in nets of $A_2Th(AsO_4)_2$ (A = Na, K, Rb, Cs) are $4^2.6$ and $4^4.6^2.8^8.10$. This difference reflects the above discussed fact of presence of both ThO_8 coordination polyhedra with edge-sharing anions in *cis*- and *trans*-positions. It is not surprising that repeating of the structural units in the crystal structures of $A_2Th(AsO_4)_2$ (A = Na, K) (see above) results in a simpler topology than the topology of their combination in the crystal structure of $Na_2Th(PO_4)_2$. Thus, the nature of oxo-anion centers has an influence on the geometry of Th coordination polyhedra, as well as on the topology of their crystal structures. The underlying net in $Na_2Th(PO_4)_2$ is more complex since it contains four independent nodes opposite to two in the case of $A_2Th(AsO_4)_2$ (A = Na, K, Rb, Cs).

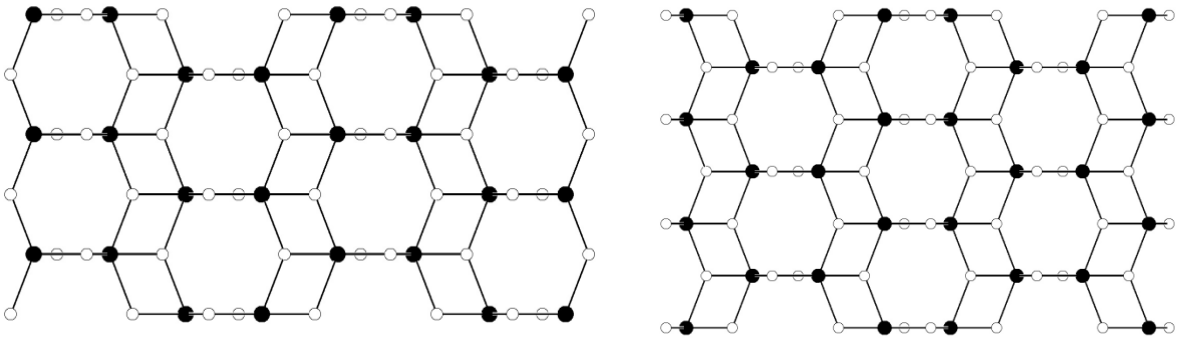

Figure 4.15: *View on underlying net of $Cs_2Th(AsO_4)_2$ (**ant** topological type[41]) along [100] (up) and [010] (right). Black and white sphere corresponds to Th and As atoms, respectively.*

The topology of $Li_2Th(AsO_4)_2$ is quite different from the above described because the structure is two dimensional. The arsenate anions possess two different coordination types (T^{21} and T^{31}) and each Th atom is surrounded by 7 arsenate-anions. Due to this, the crystal structure of $Li_2Th(AsO_4)_2$ is based on a 3,4,7-coordinated net which is classified by TOPOS as 3,4,7L1 topological type and relates to square plane net by removing 3-coordinated node.

4. 10 Raman and IR Spectroscopy

The Raman spectra of the $A_2Th(AsO_4)_2$ (A = Li, Na, K, Rb, Cs) are presented in Figure 4.16. The spectra could be divided into low- and high-frequency parts with the ranges of 200 – 550 cm^{-1} and 798 – 958 cm^{-1}. According to literature data[43-47], the low-frequency part corresponds to symmetric bending (υ_2) and out-of-plane bending (υ_4) modes, while high-frequency region corresponds to symmetric (υ_1) and anti-symmetric (υ_3) stretching vibrations. The band wavenumbers and their assignments are given in Table 4.11.(υ_1 – symmetric stretching vibrations; υ_2 – symmetric bending vibrations; υ_3 – antisymmetric stretching vibrations; υ_4 – out-of-plane bending vibrations.) General tendency of the spectra is that frequency of the most intensive bands (874, 888, 853, 851, and 870 cm^{-1} for A = Li, Na, K, Rb, and Cs, respectively) is in an inverted correlation with the average As–O bond distances (1.685, 1.680, 1.685, 1.689, and 1.681 Å, respectively).

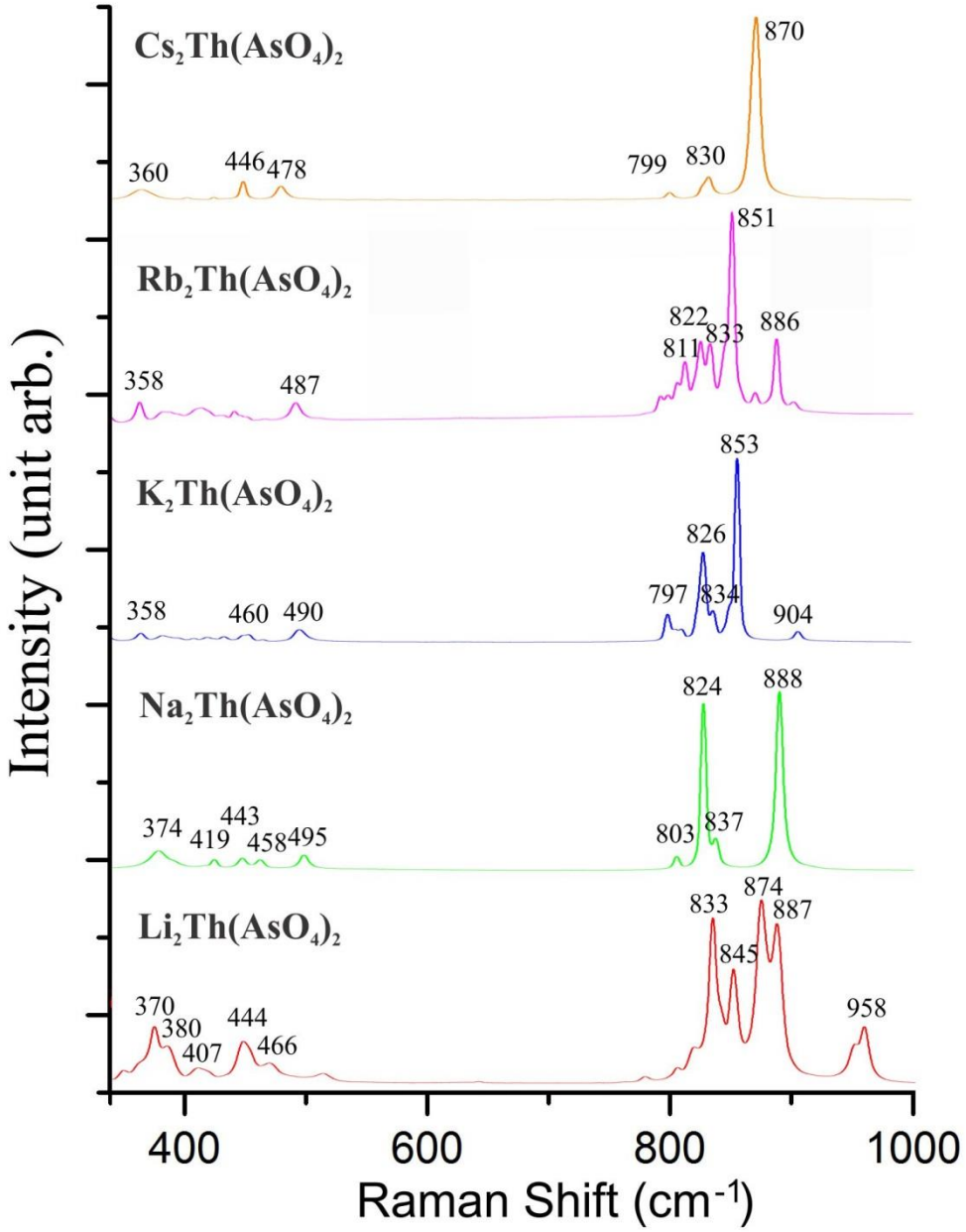

Figure 4.16: *Raman spectra of $A_2Th(AsO_4)_2$ (A = Li, Na, K, Rb, Cs).*

Table 4.11: Assignment of selected Raman bands corresponding to AsO_4 vibrational modes, a) the data of this study; b) the data of known Ref; c) assignment; d) Ref. Nr.

compound	a	b	c	d	compound	a	b	c	d
Li	958		Not assigned.		**K**	904	905	υ_1 and υ_3	37
	887	884	υ_1 and υ_3	35		853	853		38
	874	877		36		834	832		35
	845	849		36		826	823		35
	833	832		36		797	798		39
	466	467	υ_4	37		490	496	υ_2 and υ_4	36
	444	446		36		460	460		36
	407	398		36		358	360		36
	380	382		36	**Rb**	886	884	υ_1 and υ_3	36
	370	368		36		851	853		37
Na	888	884	υ_1 and υ_3	36		833	832		36
	837	832		38		822	822		36
	824	823		36		813	815		36
	803	808		36		487	482	υ_2 and υ_4	36
	495	496	υ_4	36		358	360		36
	458	460		36	**Cs**	870	873	υ_1 and υ_3	38
	443	446		36		830	832		36
	419	416		36		799	797		37
	374	377		37		478	478	υ_2 and υ_4	36
						446	446		36
						360	360		36

*υ_1 – symmetric stretching vibrations; υ_2 – symmetric bending vibrations; υ_3 – antisymmetric stretching vibrations; υ_4 – out-of-plane bending vibrations.

Same as Raman, IR spectra of the compounds consist of two parts: high-wavelength one with a range of 700 – 1000 cm^{-1} and low-wavelength one with a range of 400 – 600 cm^{-1} (Fig. 4.17) High-wavelength region corresponds to the stretching vibrations, while low-wavelength – to the bending ones.

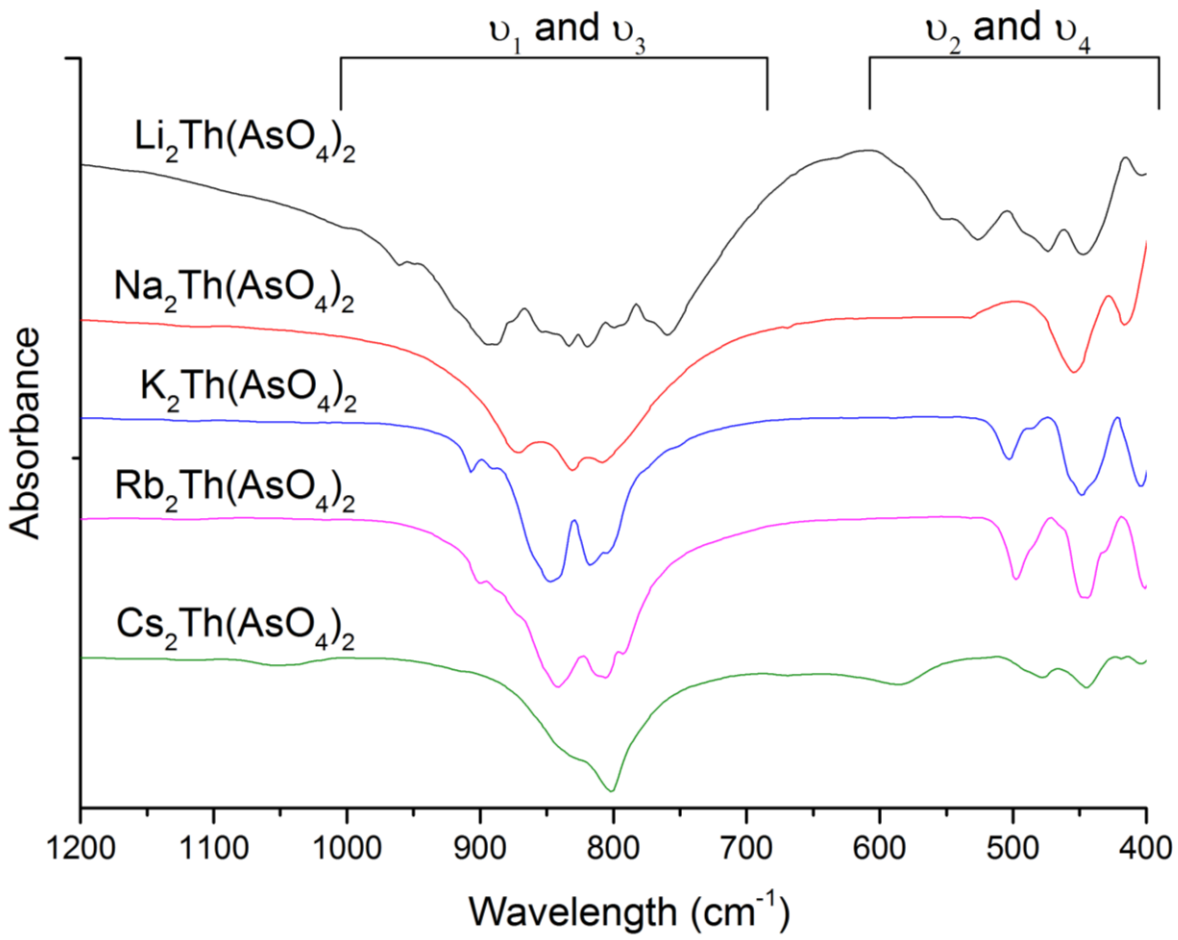

***Figure 4.17**: IR spectra of $Li_2Th(AsO_4)_2$, $Na_2Th(AsO_4)_2$, $K_2Th(AsO_4)_2$, $Rb_2Th(AsO_4)_2$, and $Cs_2Th(AsO_4)_2$.*

4.11 Conclusions

A high temperature solid state reaction method was employed to obtain single crystals and pure powder samples of five novel thorium arsenate compounds with the general formula $A_2Th(AsO_4)_2$ (A= Li, Na, K, Rb, Cs). Despite the same stoichiometry, the crystal structures and thermal/spectroscopic properties of these compounds are significantly influenced by the size of the outer-sphere alkali cations. The crystal structure of the Li-containing compound is 2D, while those of other compounds are 3D. In the structures of $A_2Th(AsO_4)_2$ (A= Na, K, Rb, Cs), arsenate anions are tetradentate and adopt K^{21} coordination type and Th atoms are eightfold coordinated. Same coordination modes of the AsO_4 groups and coordination numbers of the Th atoms lead to a common for these compounds

underlying net with **ant** topological type. Symmetry of the structures varies from monoclinic to tetragonal and relates to environment of the Th atoms. In orthorhombic $Na_2Th(AsO_4)_2$ and tetragonal $Cs_2Th(AsO_4)_2$, a Th atom coordinates edge-sharing arsenate anions in *trans*-positions, while in isotypic monoclinic $K_2Th(AsO_4)_2$ and $Rb_2Th(AsO_4)_2$ – in *cis*-positions. The difference in symmetry between $Na_2Th(AsO_4)_2$ and $Cs_2Th(AsO_4)_2$ is due to a variation of outer-sphere cation size, though motifs of these structures are similar.

Difference in size of K and Rb cations has no significant influence on room-temperature crystal structures of $K_2Th(AsO_4)_2$ and $Rb_2Th(AsO_4)_2$ since both compounds are isotypic. Nevertheless, thermal behavior of these compounds is defined by the nature of the outer-sphere cations. Two temperature-induced phase transitions were found in both $K_2Th(AsO_4)_2$ and $Rb_2Th(AsO_4)_2$ by means of high-temperature powder XRD accompanied by DSC in a range of 300 – 1220 K. The structure of $K_2Th(AsO_4)_2$ changes twice upon heating, first from monoclinic to an orthorhombic metric at 1088 K and therefore to a tetragonal one in a range of 1150 – 1200 K. One phase transition in $Rb_2Th(AsO_4)_2$ at 749 K is followed by a direct monoclinic-tetragonal metric transformation, while another one at 1170 K is not related to any structural change, but to stabilization of high-temperature phase. Despite the fact that metrics of high temperature modifications of $K_2Th(AsO_4)_2$ and $Rb_2Th(AsO_4)_2$ are similar to the corresponding metrics of the room temperature modifications of orthorhombic $Na_2Th(AsO_4)_2$ and tetragonal $Cs_2Th(AsO_4)_2$, the single crystal structures of the least two does not fit high temperature diffraction patterns of $K_2Th(AsO_4)_2$ and $Rb_2Th(AsO_4)_2$.

4.12 References

1. J. J. Katz; L. R. Morss; G. T. Seaborg, *The Chemistry of the Actinide and Transactinide Elements*. Springer Science+Business Media B.V: Dordrecht, 2011; Vol. 1-6.
2. I. G. Tananaev; M. V. Nikonov; B. F. Myasoedov; D. L. Clark, *J. Alloy. Comp.,* **2007**, 444-445, 668- 672.
3. M.R. MacDonald; M.E. Fieser; J.E. Bates; J.W. Ziller; F. Furche; W.J. Evans, *J. Am. Chem. Soc.,* **2013,** *135*, 13310-13313.
4. J. Yeon; M. D. Smith; J. Tapp; A. Möller; H.-C. zur Loye, *J. Am. Chem. Soc.,* **2014,** *136*, 3955-3963.
5. E. M. Villa; C. J. Marr; J. Diwu; E. V. Alekseev; W. Depmeier; T. E. Albrecht-Schmitt, *Inorg. Chem.,* **2013,** *52*, 965-973.
6. E. M. Villa; C. J. Marr; L. J. Jouffret; E.V. Alekseev; W. Depmeier; T. E. Albrecht-Schmitt, *Inorg. Chem.,* **2012,** *51*, 6548-6558.
7. V. Brandel; N. J. Dacheux, *Solid State Chem.,* **2004,** *177*, 4755-4767.
8. E. M. Villa; S. Wang; E. V. Alekseev; W. Depmeier; T. E. Albrecht-Schmitt, *Eur. J. Inorg. Chem.,* **2011,** *2011*, 3749-3754.
9. G. Wallez; D. Bregiroux; K. Popa; P. E. Raison; C. Apostolidis; P. Lindqvist-Reis; R. J. M. Konings; A. F. Popa, *Eur. J. Inorg. Chem.,* **2011,** *2011*, 110-115.
10. P. Raison; R. Jardin; D. Bouëxière; R. M. Konings; T. Geisler; C. Pavel; J. Rebizant; K. Popa, *Phys. Chem. Miner.,* **2008,** *35*, 603-609.
11. N. Dacheux; A. C. Thomas; V. Brandel; M. Genet, *J. Nucl. Mater.,* **1998,** *257*, 108-117.
12. N. Dacheux; N. Clavier; G. Wallez; V. Brandel; J. Emery; M. Quarton; M. Genet, *Mater. Res. Bull.,* **2005,** *40*, 2225-2242.
13. N. Dacheux; R. Podor; B. Chassigneux; V. Brandel; M. Genet, *J. Alloys Compd.,* **1998**, 271-273, 236-239.
14. N. Dacheux; R. Podor; V. Brandel; M. Genet, *J. Nucl. Mater.,* **1998,** *252*, 179.
15. P. Bénard; V. Brandel; N. Dacheux; S. Jaulmes; S. Launay; C. Lindecker; M. Genet; D. Louër; M. Quarton, *Chem. Mater.,* **1996,** *8*, 181-188.
16. N. Dacheux; N. Clavier; G. Wallez; Quarton, M., *Solid State Sci.,* **2007,** *9*, 619-627.
17. G. Wallez; P.E. Raison; N. Dacheux; N. Clavier; D. Bykov; L. Delevoye; K. Popa; D. Bregiroux; A.N. Fitch; R.J.M. Konings, *Inorg. Chem.,* **2012,** *51*, 4314-4322.
18. M.A. Salvadó; P. Pertierra; A.I. Bortun; C. Trobajo; J.R. García, *Inorg. Chem.,* **2008,** *47*, 7207-7210.
19. E. M. Wylie; C. M. Dawes; Burns, P. C., *J. Solid State Chem.,* **2012,** *196*, 482-488.
20. C. Renard; S. Obbade; F. J. Abraham, *Solid State Chem.,* **2009,** *182*, 1377-1386.
21. N. P. Deifel; K. T. Holman; C. L. Cahill, *Chem. Commun.,* **2008**, 6037-6038.
22. E.V. Alekseev; S.V. Krivovichev; T. Malcherek; W. Depmeier, *J. Solid State Chem.,* **2008,** *181*, 3010-3015.

23. K. Krishnan; S.K. Sali; K.D. Singh Mudher, *J. Alloys Compd.,* **2006,** *414*, 310-316.
24. V.B. Kalinin; A.M. Golubev; V.A. Tafeenko; S.Y. Stefanovich, *Sov. Phys. Crystallogr.,* **1992,** *37*, 1220-1226.
25. B. Matkovic; B. Prodic; Sljukic, M., *Croat. Chem. Acta,* **1968,** *40*, 147.
26. B. Matkovic; B. Kojic-Prodic; M. Sljukic; M. Topic; R.D. Willett; F. Pullen, *Inorg. Chim. Acta,* **1970,** *4*, 571.
27. E.V. Alekseev ; S.V. Krivovichev ; W. Depmeier, *J. Solid State Chem.,* **2009,** *182*, 2977-2984.
28. G. M. Sheldrick, *Acta Crystallogr. A,* **2007,** *64*, 112-122.
29. L. J. Farrugia, *J. Appl. Crystallogr.,* **2012,** *45*, 849-854.
30. V.A. Blatov; V.N. Serezhkin, *Russ. J. Inorg. Chem.,* **2000,** *45*, S105-S222.
31. V.A. Blatov; A. P. Shevchenko; V.N. Serezhkin, *J. Appl. Crystallogr.,* **2000,** *33*, 1193-1193.
32. N. E. Brese; M. O'Keeffe, *Acta Cryst.,* **1991,** *B47*, 192-197.
33. V.N. Serezhkin; A.V. Vologzhanina; L.B. Serezhkina; E.S. Smirnova; E.V. Grachova; P.V. Ostrova; M.Y. Antipin, *Acta Crystallogr. B,* **2009,** *65*, 45-53.
34. A.V. Vologzhanina; L.B. Serezhkina; N.A. Neklyudova; V.N. Serezhkin, *Inorg. Chim. Acta,* **2009,** *362*, 4921-4925.
35. A.I. Orlova; D.B. Kitaev; N.G. Kazantsev; S.G. Samoilov; V.S. Kurazhkovskaya; E.N. Vopilina, *Radiochem.,* **2002,** *44*, 326-331.
36. N. Galesic; B. Matković; M. Topić; E. Coffou; M. Šlijukić, *Croat. Chim. Acta,* **1984,** *57*, 597.
37. M.M. Murshed; T.M. Gesing, *Mater. Res. Bull.,* **2013,** *48*, 3284-3291.
38. B. Xiao; T.M. Gesing; P. Kegler; G. Modolo; D. Bosbach; H. Schlenz; E.V. Suleimanov; E.V. Alekseev, *Inorg. Chem.,* **2014,** *53*, 3088-3098.
39. C.H. Rüscher; T.M. Gesing; J.-C. Buhl, *Z. Für Krist.,* **2003,** *218*, 332-344.
40. E.V. Alexandrov; V.A. Blatov; A.V. Kochetkov; D.M. Proserpio, *CrystEngComm,* **2011,** *13*, 3947.
41. M. O'Keeffe; M.A. Peskov; A.J. Ramsden; O.M. Yaghi, *Acc. Chem. Res.,* **2008,** *41*, 1782-1789.
42. V.A. Blatov; M. O'Keeffe; D.M. Proserpio, *CrystEngComm,* **2010,** *12*, 44.
43. M.T. Paques- Ledent; P.Tarte, *Spectrochim. Acta Part A,* **1974,** *30*, 673-689.
44. R.L. Frost; J.T. Kloprogge, *Spectrochimi. Acta Part A,* **2003,** *59* 2797-2804.
45. W. Martens; R.L. Frost; J.T. Kloprogge, *J. Raman Spectrosc.,* **2003,** *34*, 90-95.
46. R.L. Frost; W. Martens; P.A. Williams; J.T. Kloprogge, *J. Raman Spectrosc.,* **2003,** *34*, 751-759.
47. R.L. Frost; W.N. Martens; P.A. Williams, *J. Raman Spectrosc.,* **2002,** *33*, 475-484.

Chapter 5 STRUCTURAL EVOLUTION OF THORIUM PHOSPHATE FAMILY $A_2Th(PO_4)_2$ (A= Li, Na, K, Rb, Cs)

5.1 Abstract

A new alkaline thorium phosphate family was obtained and systematically investigated. The structures of $A_2Th(PO_4)_2$ (A = Li, Na, K, Rb, Cs) were determined from single crystal X-ray diffraction data. The structural evolution of this family is of great interest, because of its comparative similarity to that of $A_2Th(AsO_4)_2$ (chapter 4). The fundamental coordination environment of phosphorus and thorium as well as the cations has been taken into account for analysis of crystal chemistry of obtained materials.

5.2 Introduction

Actinide phosphates are of great interest due to their structural diversity and possible applications in nuclear waste processing.[1-6] As it has been mentioned in section 1.4, several series torium phosphates have been synthesized and studied previously. However, according to the ICSD only very limited structural data on these phases were reported. Four alkaline thorium phosphates compounds with general compositions $ATh_2(PO_4)_3$ (A=Na[7], K[8], Rb[9], Cs[9]), which all adopt same $KTh_2(VO_4)_3$[10] structure type, have been reported. $KTh(P_3O_{10})$[11] was the only known structure with the P_3O_{10} chain among the inorganic alkaline thorium compounds. $Na_6[Th(PO_4)(P_2O_7)]_2$[12] is based upon the 3D framework, which is constructed by the $Th(P_2O_7)$ layer and bridging PO_4 groups. Apart to these compounds, no further data of inorganic alkaline thorium phosphates were reported. In this dissertation, as chapter 4 described, we synthesized and characterized a new alkaline thorium arsenate family $A_2Th(AsO_4)_2$ (A= Li, Na, K, Rb, Cs)[13]. Considering that arsenates can serve as a comparative element due to similarities between oxo-arsenate and oxo-phosphate ions, so in this work, we carried out a systematical investigation of ThO_2-P_2O_5 - A^I(A^I = Li, Na, K, Rb, Cs) system. Novel thorium phosphate series with $A_2Th(PO_4)_2$ (A= Li, Na, K, Rb, Cs) general formula was obtained. $Na_2Th(PO_4)_2$[14] was only one known compound belonging to this family.

5.3 Synthesis

Caution! *Although ^{232}Th (T1/2 = 1.4 10^10 yrs.) present a low specific activity, standard precautions for handing radioactive materials should be followed when working with the quantities used in the syntheses that follow.*

The synthesis was performed following the Figure 2.2 processes, and the information on the reactants is given in the Table 5.1. The used chemicals were of analytical reagent grade and without any other further purification. The reactants were thoroughly ground together with their appropriate ratios and loaded into a platinum crucible. (Table 5.2)

Table 5.1: The Experimental Reactants used in this chapter

Compound Name	**Purity**	**Company**
Thorium nitrate ($Th(NO_3)_4{\cdot}5H_2O$)	- -	Merck
Ammonium dyhydrogen phosphate ($NH_4H_2PO_4$)	98%	Alfa-Aesar
Lithium carbonate (Li_2CO_3)	99.9%	Alfa-Aesar
Sodium nitrate ($NaNO_3$)	99.9%	Alfa-Aesar
Potassium chlorate (KCl)	98%	Alfa-Aesar
Rubidium nitrate ($RbNO_3$)	99.9%	Alfa-Aesar
Cesium nitrate ($CsNO_3$)	99.9%	Alfa-Aesar

Table 5.2: Synthesis data and crystal profile of $A_2Th(PO_4)_2$ (A = Li, Na, K, Rb, Cs)

Compound	**Formula**	**Th: P^V: A^I**	**Aimed temperature (K)**	**Colour/shape**
LiThPO-1	$Li_2Th(PO_4)_2$	1:7:10	1273	colorless block-like crystals
NaThPO-1	$Na_2Th(PO_4)_2$	1:2:2	1473	
KThPO-1	$K_2Th(PO_4)_2$	1:16:77*	1123	
RbThPO-1	$Rb_2Th(PO_4)_2$	1:10:10	1223	
CsThPO-1	$Cs_2Th(PO_4)_2$	1:2:2	1323	
* Here, the synthesis adopted KCl as the flux, so experimental molar ratio is Th: Cs: P^{III}: A^I= 1: 4: 16: 77, while $K_2Th(PO_4)_2$ is isolated from the products.				

The platinum crucible then transferred into a furnace. The furnace was ramped up to the aimed temperature by the heating rate of 873 K/h, left there for 2 hours and then slowly cooled down to room temperature at a rate of 5 K/h. The titled crystals were isolated from the reaction product.

5.4 Single Crystal X-ray Diffraction

The data were collected and refined follow the details as section 2.4 mentioned. All the structures were checked for possible higher symmetry using the ADDSYM algorithm from the program PLATON[28], but none were found. Relevant crystallographic data and details of the experimental conditions for all the three crystals are summarized in Table 5.3 and the selected bond length in Table 5.4.

Table 5.3: Crystallographic data for $\mathbf{A}_2Th(PO_4)_2$ (**A** = Li, Na, K, Rb, Cs)

Compound	**$Li_2Th(PO_4)_2$**	**$Na_2Th(PO_4)_2$**	**$K_2Th(PO_4)_2$**	**$Rb_2Th(PO_4)_2$**	**$Cs_2Th(PO_4)_2$**
space group	*P* $2_1/a$	*P* $2_1/c$	*P* $2_1/n$	*I* $4_1/amd$	*I* $4_1/amd$
a /Å	5.4355(2)	7.0684(3)	7.7114(3)	7.0416(2)	7.1769(2)
b /Å	13.5476(3)	21.7041(6)	10.9562 (3)	7.0416(2)	7.1769(2)
c /Å	8.8730(2)	9.1198(3)	9.1956(4)	17.6784(4)	17.6297(8)
β /°	105.971(3)	111.610(4)	111.437(4)	90.00	90.00
V /$Å^3$	628.16(3)	1300.76(8)	723.17(5)	876.58(3)	908.06(5)
D_{calc} /g/cm^3	4.609	4.779	4.594	4.493	5.031
Z	4	8	4	4	4
λ /Å	0.71073	0.71073	0.71073	0.71073	0.71073
F(000)	760	1648	888	1032	1176
R1	0.0241	0.0242	0.0324	0.0146	0.0252
wR2	0.0589	0.1097	0.0608	0.0332	0.0795

$R(F) = \Sigma||F_o| - |F_c||/\Sigma|F_o|$. $wR(F_o^2) = [\Sigma w(F_o^2 - F_c^2)^2/\Sigma w(F_o^2)^2]^{1/2}$.

Table 5.4: Selected interatomic distances /Å in the structure $\mathbf{A}_2Th(PO_4)_2$ (**A** = Li, Na, K, Rb, Cs)

$Li_2Th(PO_4)_2$							
Th1– O5	2.362(5)	Li1– O8	2.13(3)	Li3– O6	2.03(3)	P1– O4	1.506(5)
Th1– O1	2.369(5)	Li1– O5	2.20(3)	Li3– O4	2.11(3)	P1– O5	1.523(5)
Th1– O2	2.447(5)	Li1– O7	2.35(3)	Li3– O8	2.56(3)	P1– O3	1.555(5)
Th1– O6	2.466(5)	Li1– O1	1.96(3)	Li3– O6	1.87(3)	P1– O7	1.561(5)
Th1– O3	2.473(5)						
Th1– O3	2.494(5)	Li2– O8	1.933(15)			P2– O8	1.511(5)
Th1– O7	2.504(5)	Li2– O4	1.950(15)			P2– O1	1.533(5)
Th1– O2	2.540(5)	Li2– O8	1.978(15)			P2– O6	1.543(5)
Th1– O7	2.565(5)	Li2– O4	1.898(15)			P2– O2	1.574(5)
$Na_2Th(PO_4)_2$							
Th1– O1	2.340(5)	Th2– O16	2.297(5)	P1– O7	1.514(5)	P3– O3	1.521(5)
Th1– O3	2.346(5)	Th2– O14	2.333(5)	P1– O9	1.532(6)	P3– O10	1.539(5)
Th1– O7	2.420(5)	Th2– O6	2.388(5)	P1– O13	1.550(6)	P3– O5	1.539(6)
Th1– O8	2.435(5)	Th2– O4	2.405(5)	P1– O4	1.550(5)	P3– O14	1.548(5)
Th1– O5	2.524(5)	Th2– O9	2.414(6)				
Th1– O2	2.529(5)	Th2– O1	2.422(6)	P2– O8	1.516(5)	P4– O12	1.528(5)
Th1– O11	2.537(5)	Th2– O13	2.630(5)	P2– O1	1.530(6)	P4– O11	1.538(5)

Th1– O12	2.551(5)	Th2– O15	2.707(5)	P2– O6	1.546(5)	P4– O2	1.538(6)
Th1– O15	2.993(5)			P2– O25	1.553(6)	P4– O16	1.547(5)
Th1– O13	3.004(5)						
Na1– O2	2.457(6)	Na2– O5	2.421(6)	Na3– O2	2.395(6)	Na4– O5	2.363(6)
Na1– O13	2.486(7)	Na2– O1	2.446(7)	Na3– O11	2.403(6)	Na4– O10	2.413(6)
Na1– O9	2.539(7)	Na2– O15	2.509(7)	Na3– O10	2.597(6)	Na4– O11	2.552(6)
Na1– O4	2.631(6)	Na2– O4	2.515(6)	Na3– O3	2.691(6)	Na4– O12	2.665(6)
Na1– O6	2.654(6)	Na2– O6	2.710(6)	Na3– O8	2.760(6)	Na4– O16	2.709(6)
Na1– O9	2.743(6)	Na2– O1	2.797(6)	Na3– O14	2.801(6)	Na4– O1	2.777(5)
Na1– O6	2.796(6)	Na2– O7	2.800(6)	Na3– O9	2.917(6)	Na4– O8	2.861(6)
Na1– O8	2.914(6)	Na2– O4	2.873(7)	Na3– O7	2.918(7)	Na4– O7	2.981(6)
Na1– O14	2.954(7)	Na2– O14	2.924(7)				
K_2Th$(PO_4)_2$							
Th1– O5	2.374(4)	K1– O3	2.679(4)	K2– O1	2.685(4)	P1– O7	1.535(4)
Th1– O2	2.387(4)	K1– O6	2.704(4)	K2– O4	2.690(4)	P1– O8	1.537(4)
Th1– O8	2.394(4)	K1– O1	2.781(4)	K2– O8	2.786(4)	P1– O6	1.544(4)
Th1– O7	2.416(4)	K1– O6	2.803(4)	K2– O3	2.789(4)	P1– O3	1.547(4)
Th1– O3	2.449(4)	K1– O5	2.868(4)	K2– O4	2.961(4)		
Th1– O1	2.456(4)	K1– O2	2.888(4)	K2– O2	2.981(5)	P2– O2	1.529(4)
Th1– O6	2.496(4)	K1– O7	2.920(5)	K2– O7	3.026(4)	P2– O5	1.536(4)
Th1– O4	2.506(4)	K1– O1	2.924(4)	K2– O7	3.043(4)	P2– O4	1.537(4)
		K1– O8	3.296(5)	K2– O5	3.208(4)	P2– O1	1.548(4)
		K1– O2	3.406(4)	K2– O8	3.354(4)		
Rb_2Th$(PO_4)_2$							
Th1– O2	2.323(3)	Rb1– O1	2.898(2)	P1– O2	1.529(3)		
Th1– O2	2.323(3)	Rb1– O1	2.898(2)	P1– O2	1.529(3)		
Th1– O2	2.323(3)	Rb1– O1	2.898(2)	P1– O1	1.535(3)		
Th1– O2	2.323(3)	Rb1– O1	2.898(2)	P1– O1	1.535(3)		
Th1– O1	2.528(2)	Rb1– O2	3.344(2)				
Th1– O1	2.528(2)	Rb1– O2	3.344(2)				
Th1– O1	2.528(2)	Rb1– O2	3.344(2)				
Th1– O1	2.528(2)	Rb1– O2	3.344(2)				
Cs_2Th$(PO_4)_2$							
Th1– O2	2.361(5)	Cs1– O1	2.980(4)	P1– O1	1.536(5)		
Th1– O2	2.361(5)	Cs1– O1	2.980(4)	P1– O1	1.536(5)		
Th1– O2	2.362(5)	Cs1– O1	2.980(4)	P1– O2	1.552(6)		

Th1– O2	2.362(5)	Cs1– O1	2.980(4)	P1– O2	1.553(6)		
Th1– O1	2.501(5)	Cs1– O2	3.368(5)				
Th1– O1	2.501(5)	Cs1– O2	3.368(5)				
Th1– O1	2.501(5)	Cs1– O2	3.368(5)				
Th1– O1	2.501(5)	Cs1– O2	3.368(5)				

5.5 Bond Valence Analysis

Bond-valence sums (BVS) for all atom positions in $A_2Th(PO_4)_2$ (A = Li, Na, K, Rb, Cs) phases were calculated, and the results are given in Table 5.5-5.9. The bond-valence parameters for Th(IV)-O, A(I)-O, and P(V)-O are used according to Brese and O'Keeffe.[15]

Table 5.5: Bond-valence analysis for $Li_2Th(PO_4)_2$

	Th1	P1	P2	Li1	Li2	Li3	∑
O1	0.579		1.212	0.263			2.054
	0.469						
O2	0.365		1.084				1.919
	0.437						
O3	0.413	1.142					1.992
					0.270	0.175	
O4		1.303			0.311		2.060
O5	0.590	1.245		0.138			1.973
O6	0.446		1.179			0.218	2.178
	0.402					0.336	
O7	0.341	1.123		0.092			1.958
					0.283	0.052	
O8			1.286	0.166	0.251		1.620
∑	4.043	4.813	4.761	0.659	1.115	0.781	

Table 5.6: Bond-valence analysis for $Na_2Th(PO_4)_2$

	Th1	Th2	P1	P2	P3	P4	Na1	Na2	Na3	Na4	∑
		0.502		1.221				0.174		0.071	2.04
O1								0.068			
O2	0.376					1.195	0.173		0.200		1.94
O3	0.616				1.251				0.090		1.96
O4			1.157				0.106	0.145			1.99
	0.381	0.526			1.192			0.187		0.218	1.98
O5								0.055			
		0.550		1.170			0.101	0.085			1.98
O6							0.068				
O7	0.505		1.275					0.067	0.049	0.041	1.94
O8	0.485			1.269			0.049		0.075	0.057	1.93
O9		0.513	1.215				0.139		0.049		2.00
							0.078				
O10	0.354				1.221				0.118	0.192	1.89
O11	0.368					1.221			0.198	0.132	1.92
O12	0.627			1.157		1.255				0.097	1.98
O13	0.105	0.286	1.157				0.159				1.71
O14		0.644			1.189		0.045	0.048	0.065		1.99
O15	0.107	0.237						0.151			1.65
O16		0.717				1.189				0.069	1.98
∑	3.93	3.98	4.80	4.82	4.85	4.86	0.92	0.98	0.84	0.88	

Table 5.7: Bond-valence analysis for $K_2Th(PO_4)_2$

	Th1	P1	P2	K1	K2	∑
				0.172		
O1	0.458		1.163	0.117	0.223	2.13
				0.129		
O2	0.552		1.225	0.032	0.100	2.04
O3	0.467	1.167		0.227	0.168	2.03
					0.220	
O4	0.400		1.199		0.106	1.93
O5	0.572		1.202	0.136	0.054	1.96
				0.212		
O6	0.041	1.176		0.162		1.96
					0.089	
O7	0.510	1.205		0.118	0.085	2.01
					0.170	
O8	0.541	1.199		0.043	0.037	1.99
∑	3.91	4.75	4.79	1.32	1.22	

Table 5.8: Bond-valence analysis for $Rb_2Th(PO_4)_2$

	Th1	P1	Rb1	∑
O1	$0.377^{\times 4\downarrow}$	$1.205^{\times 2\downarrow}$	$0.178^{\times 4\downarrow}$	1.76
O2	$0.656^{\times 4\downarrow}$	$1.225^{\times 2\downarrow}$	$0.053^{\times 4\downarrow}$	1.93
∑	4.13	4.86	0.93	

Table 5.9: Bond-valence analysis for $Cs_2Th(PO_4)_2$

	Th1	P1	Cs1	∑
O1	$0.405^{\times 4\downarrow}$	$1.279^{\times 2\downarrow}$	$0.049^{\times 4\downarrow}$	1.93
O2	$0.592^{\times 4\downarrow}$	$1.245^{\times 2\downarrow}$	$0.212^{\times 4\downarrow}$	2.04
∑	3.99	5.05	1.04	

5.6 Crystal Structures Description

$Li_2Th(PO_4)_2$ crystallizes in the centrosymmetric monoclinic space group $P2_1/a$ (Table 5.3) and based upon $[Th(PO_4)_2]^{2-}$ 2D layers. The Li cations are located within the interlayer space (Fig. 5.1a). Thorium atoms occupy a single crystallographic position and possess nine-fold oxygen coordination. The Th – O bond distances are in the range of 2.362(5) – 2.565(5) Å.(Table 5.4) Two symmetrically independent phosphorus atoms form PO_4 tetrahedra with P – O bond lengths ranging from 1.506(5) to 1.574(5) Å. (Table 5.4) Phosphate anions can be assigned to T^{21} and T^{31} coordination types (Fig. 5.2a and b) according to the classification given in the literature.[16, 17] The uppercase of given designation describes a number of donor oxygen atoms coordinating on Th atoms (M, B, T, K, etc. for mono-, bi-, tri-, tetradentate ligands[17]). The superscript numbers equals to the amount of Th atoms connected through one, two, three, etc. donor O atoms, respectively. PO_4 groups are coordinated to Th atoms only by three O atoms and have one terminal oxygen atom in the crystal structure of $Li_2Th(PO_4)_2$. One can find that first two superscript positions are equal to the number of Th coordination polyhedra that share corner or edge with one arsenic polyhedron. Both ThO_9 and PO_4 polyhedra form corrugated sheets parallel to (001) (Fig. 5.1).

There are there independent Li sites within the interlayer space that serve for a charge balancing and a connection of the layers into 3D assembly. All Li atoms have four-fold oxygen coordination with Li–O bond distances ranging from 1.933(15) to 2.56(3) Å. Li1 and Li3 atoms are disordered in this structure, and both of them were partial occupied.

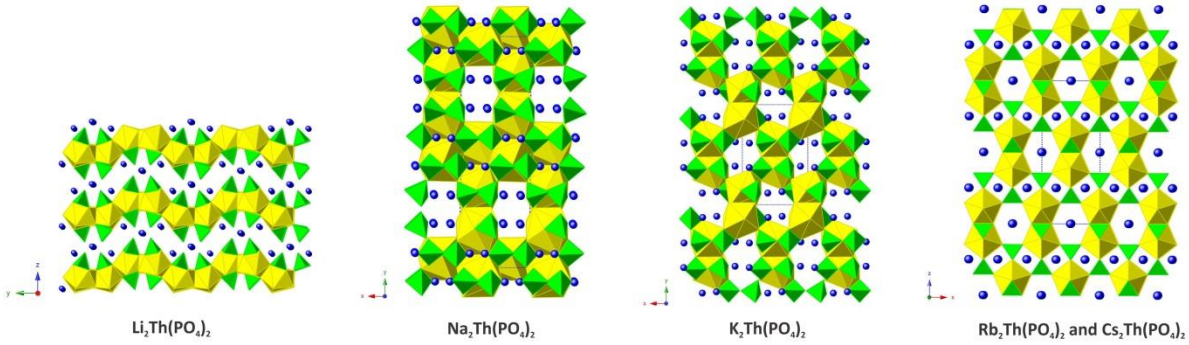

Figure 5.1: *Polyhedra representation of the crystal structures of $A_2Th(PO_4)_2$ (A= Li, Na, K, Rb, Cs). $Rb_2Th(PO_4)_2$ is isostructural with $Cs_2Th(PO_4)_2$. Th and P polyhedra are shown in yellow and green, respectively, alkaline atoms as blue spheres.*

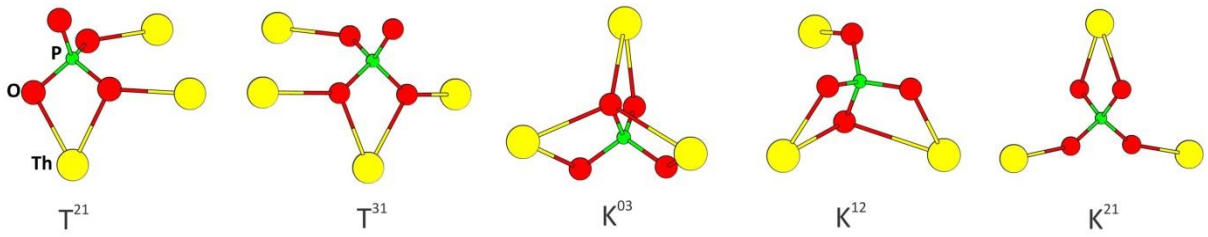

Figure 5.2: *Coordination types of phosphate-anions in the crystal structures of $A_2Th(PO_4)_2$ (A = Li, Na, K, Rb, and Cs).*

$Na_2Th(PO_4)_2$[18] was reported in 1984 and it crystallizes in the centrosymmetric monoclinic space group $P2_1/c$ (Table 5.3) and based upon 3D framework (Fig. 5.1b). It contents two symmetrically independent Th atom which occupy a single site with C_1 local symmetry and is connected to eight O atoms with Th–O distances ranging from 2.340(5) to 3.004(5) Å.(Table 5.3) The phosphorus atoms also occupy a single crystallographic position with C_1 site-symmetry. The P – O bond lengths in PO_4 tetrahedra are equal to 1.514(7) and 1.553(6) Å. (Table 5.4) The phosphate anion is connected to three Th atoms with the mode shown in Fig. 5.2c. The density of the phosphate-anions is four and can be designated with K letter. Thus, the coordination type of phosphate -anions in the crystal structure of $Na_2Th(PO_4)_2$ are K^{03} and K^{12}, which means that PO_4 polyhedron shares three edges and one corner plus two edges with three different ThO_8 polyhedra, respectively. It is noteworthy that the edge-sharing phosphate-anions are in *cis*-position and also cis- and trans- position within the coordination environment of Th atoms (Fig. 5.3a). For the *cis*-position, two bidentate chelating PO_4(I) and PO_4(II) tetrahedra are close to each other; while for *cis*- and *trans*-position, bidentate chelating PO_4(I) and PO_4(III) are close to PO_4(II) and PO_4(IV), respectively. While, PO_4(I) and PO_4(II) also opposite to PO_4(III) and PO_4(IV), respectively. The $[Th(PO_4)_2]^{2-}$ framework contains chains of cages along c axis. The cages are occupied by Na atoms (Fig. 5.1) with the shortest Na – Na distance in range of 3.232(5) to 3.993(6) Å.

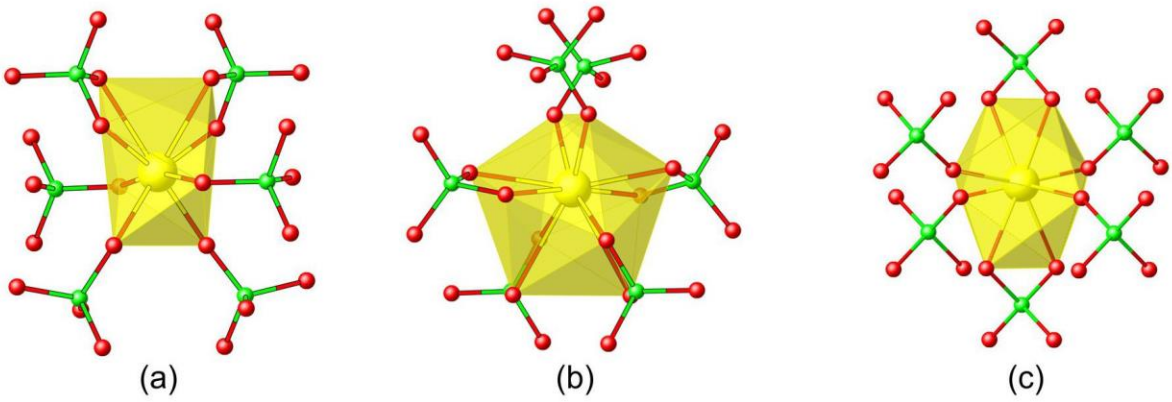

Figure 5.3: *The coordination of Th atoms in the crystal structures of $A_2Th(PO_4)_2$ (A = Na, K, Rb, and Cs). (a) cis-position, (b) cis- and trans- position, (c) trans- position. Th polyhedra are shown in yellow, P and O atoms are green and red, respectively.*

$K_2Th(PO_4)_2$ is isostructural to $K_2Th(AsO_4)_2$ (chapter 4) and crystallize in $P2_1/n$ space group.(Fig. 5.1) Th atoms occupy a single crystallographic position and are bound to eight O atoms with bond distances in the ranges of 2.374(4) – 2.506(4) Å. (Table 5.3) Phosphate anions possess same K^{21} coordination type. P – O distances vary from 1.535 (4) Å to 1.548(4) Å. (Table 5.4) The structural change, comparing to $Na_2Th(PO_4)_2$, is raised from a stereometric change of Th atom environment(Fig. 5.3b) together with coordination types of phosphate-anions(Fig. 5.2). In $K_2Th(PO_4)_2$, the Th adopted *cis*-position. The chains of cages are extending along the ^{19} direction. The potassium atoms reside in these cages with shortest interatomic d(A–A) distance in range of 3.465(2) to 3.480(2) Å.

The Fig. 5.5 concluded the combination of the coordination types of phosphate-anions and Th in the $A_2Th(PO_4)_2$ (A= Li, Na, K, Rb, Cs) family. As we mentioned above, there are two crystallographic different Th atoms in the $Na_2Th(PO_4)_2$ structure . Due to this, the crystal structure of $Na_2Th(PO_4)_2$ could be subdivided into two parts and presented as a combination of the structural units taken from crystal structures of $K_2Th(PO_4)_2$. One of these parts contains only *cis*-position located ThO_8 polyhedra**.** The second part contains *cis*-and *trans*- positions occupied ThO_8 polyhedra. Fig. 5.4 illustrates the differences between the crystal structure of $Na_2Th(PO_4)_2$ and $K_2Th(PO_4)_2$.

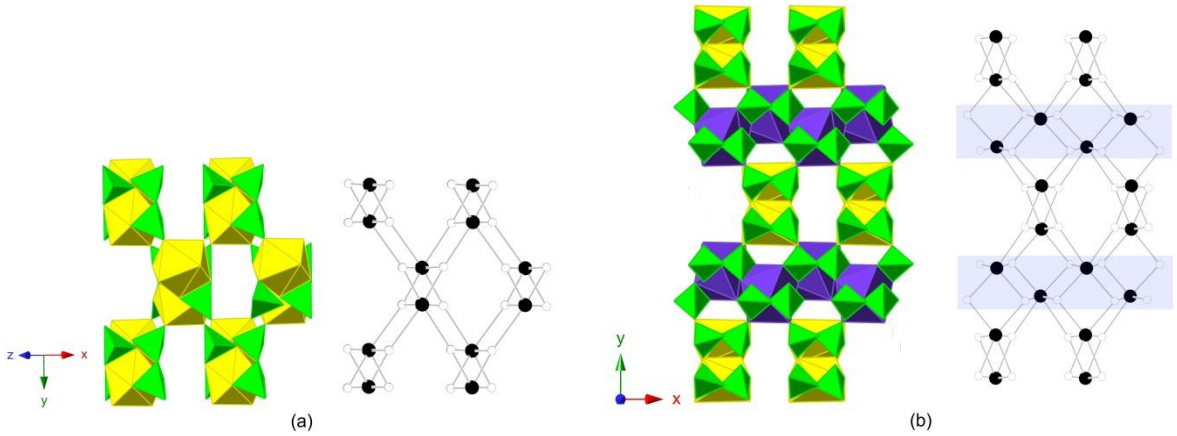

Figure 5.4: *(a) A fragment of the structure of $K_2Th(PO_4)_2$ along the direction shown in the picture. (b) A fragment of the structure of $Na_2Th(PO_4)_2$ along [001]. The yellow and purple polyhedra of thorium adopted the cis- position and cis- and trans- position, respectively; the black and white sphere corresponds to Th and P atoms, respectively.*

$Cs_2Th(PO_4)_2$ is isostructural to **$Cs_2Th(AsO_4)_2$** and crystallize in a tetragonal space group $I4_1/amd$. It is a 3D framework based upon eightfold coordinated Th atoms surrounded by phosphate anions (Fig. 5.1). The crystal structure of **$Cs_2Th(PO_4)_2$** contains phosphate-anions with K^{21} coordination type, and Th atoms coordinated by bidentate phosphate groups in *trans*-positions. The channels along directions were occupied by cations with the d(A–A) = of 3.521 and 3.591 Å for Rb and Cs, respectively.

The Fig. 5.5 gives the structural evolution of $\mathbf{A}_2Th(\boldsymbol{T}O_4)_2$ (**A**= **Li**, **Na**, **K**, **Rb**, **Cs**; ***T***= **P** and **As**) family. From the table, it can be seen that, the structure of $\mathbf{A}_2Th(\boldsymbol{T}O_4)_2$ (**A**= **Li**, **K, Cs**; ***T***= **P** and **As**) shows no changes when the anion changes from As to P. In the chapter 4, we assumed that the structure formation is driven by size of alkaline cations. The smallest one (Li) leads to the 2D layer motif, while the rest cations located within the 3D cages. So the Fig. 5.5 gives the d(A–A) in the $\mathbf{A}_2Th(\boldsymbol{T}O_4)_2$ (**A**= **Na**, **K**, **Rb**, **Cs**; ***T***= **P** and **As**), and from the Figure it can be concluded in $\mathbf{A}_2Th(AsO_4)_2$ family, the structure **Na** similar to **Cs** owing to the similar value of d(A–A), and **K** and **Rb** are isostructural to each other with the similar value range of d(A–A); while in $\mathbf{A}_2Th(PO_4)_2$ family, the structure **Na** shows more similarity to **K** owing to the similar value range of d(A–A), and **Rb** and **Cs** are isostructural to each other with the similar value of d(A–A). So in this $\mathbf{A}_2Th(PO_4)_2$ family, it proved that the structural evolution in $\mathbf{A}_2Th(\boldsymbol{T}O_4)_2$ (**A**= **Na**, **K**, **Rb**, **Cs**; ***T***= **P** and **As**) are raising from the location environment of cations.

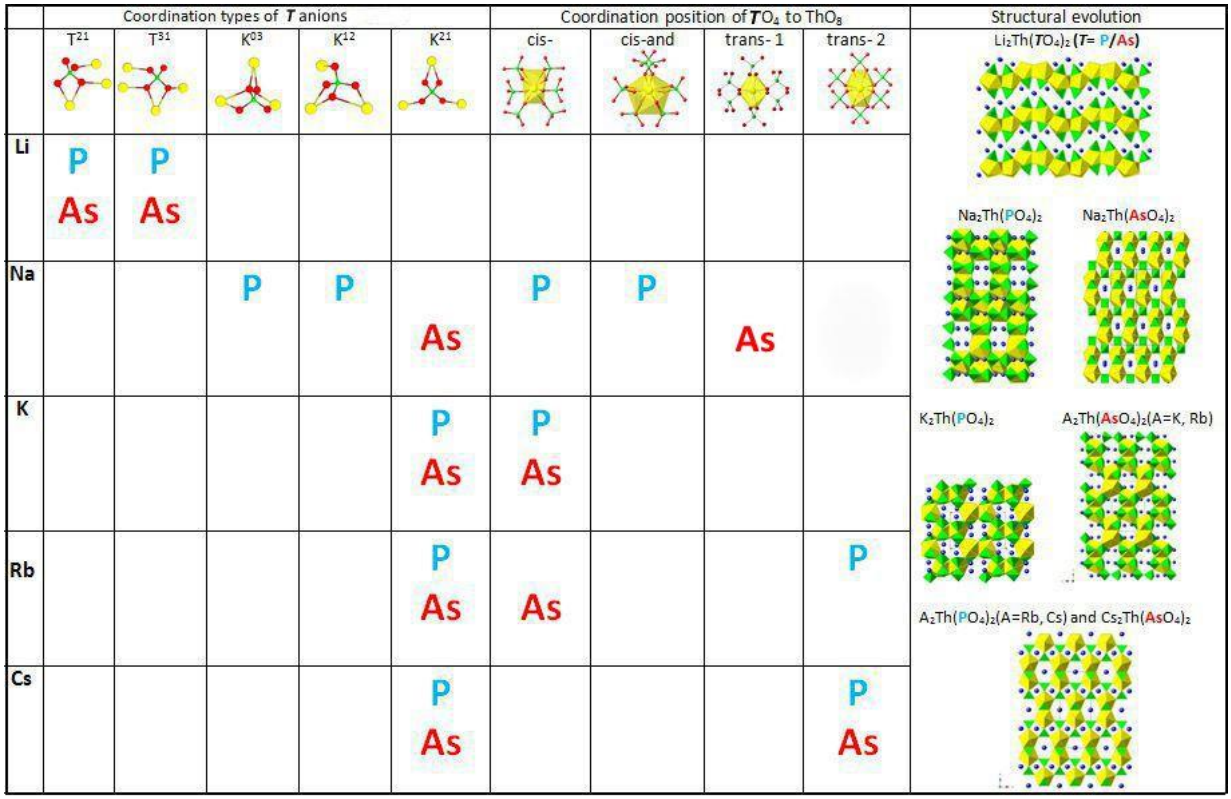

***Figure 5.5**: Structural evolution in **$A_2Th(TO_4)_2$** (**A= Li, Na, K, Rb, Cs; T= P** and **As**) family. The color assignment of all pictures is the same with above picture. **P** stands for **$A_2Th(PO_4)_2$**, and **As** stands for **$A_2Th(AsO_4)_2$**.*

Table 5.10: The distances between alkaline cation within the cages in **$A_2Th(TO_4)_2$** (**A**= **Na**, **K**, **Rb**, **Cs**; ***T***= **P** and **As**)

	$A_2Th(AsO_4)_2$	**$A_2Th(PO_4)_2$**
Na	3.61	3.23 – 3.99
K	3.54 – 3.62	3.46 – 3.48
Rb	3.54 – 3.68	3.52
Cs	3.66	3.59

5.7 Conclusions

The high temperature solid state reaction method was employed to obtain single crystals of phosphates compounds $A_2Th(PO_4)_2$ (A= Li, Na, K, Rb, Cs). $Na_2Th(PO_4)_2$ is a known structure, but in this chapter the structural evolution has been studied based on the similar research work of $A_2Th(AsO_4)_2$ (A= Li, Na, K, Rb, Cs) family. The results proved that the driving

force of the structural evolution is coordination environment of cations, As or P anions, and Th atoms in the structures.

5.8 References

1. E.V. Alekseev; S.V. Krivovichev; W. Depmeier; K. Knorr, *Z. Anorg. Allg. Chem.,* 2008, *634*, 1527-1532.
2. E. M. Villa; C. J. Marr; L. J. Jouffret; E.V. Alekseev; W. Depmeier; T. E. Albrecht-Schmitt, *Inorg. Chem.,* 2012, *51*, 6548-6558.
3. E. M. Villa; C. J. Marr; J. Diwu; E. V. Alekseev; W. Depmeier; T. E. Albrecht-Schmitt, *Inorg. Chem.,* 2013, *52*, 965-973.
4. E.M. Villa; E.V. Alekseev; W. Depmeier; T.E. Albrecht-Schmitt, *Cryst. Growth Des.,* 2013, *13*, 1721-1729.
5. E.H. Oelkers; J.M. Montel, *Mineral. Soc. America,* 2008, *4*, 113-116.
6. R.C. Ewing; L.M. Wang, *Mineral. Soc. America,* 2002, *48*, 673-699.
7. N. Galesic; B. Matkovic; M. Topic; E. Coffou; M. Sljukic, *Croat. Chem. Acta,* 1984, *57*, 597-608.
8. B. Matkovic; B. Prodic; M. Sljukic, *Croat. Chem. Acta,* 1968, *40*, 147-161.
9. K. Krishnan; S.K. Sali; K.D. Singh Mudher, *J. Alloy. Compd.,* 2006, *414*, 310-316.
10. M. Quarton; A. Kahn, *Acta Crystallog. B,* 1979, *35*, 2529-2532.
11. Z. Ruzic Toros; B. Kojic-Prodic; R. Liminga; S. Popovic, *Inorg. Chim. Acta,* 1974, *8*, 273-278.
12. B. Kojic-Prodic; M. Slukic; Z. Ruzic Toros, *Acta Crystallog. B* 1982, *38*, 67-71.
13. N. Yu; V.V. Klepov; G. Modolo; D. Bosbach; E.V. Suleimanov; T.M. Gesing; L. Robben; E.V. Alekseev, *Inorg. Chem.,* 2014, *53*, 11231-11241.
14. N. Galesic; B. Matkovic; M. Topic; E. Coffou; M. Sljukic, *Croat. Chem. Acta,* 1984, *57*, 597-608.
15. N. E. Brese; M. O'Keeffe, *Acta Cryst.,* 1991, *B47*, 192-197.
16. A.V. Vologzhanina; L.B. Serezhkina; N.A. Neklyudova; V.N. Serezhkin, *Inorg. Chim. Acta,* 2009, *362*, 4921-4925.
17. V.N. Serezhkin; A.V. Vologzhanina; L.B. Serezhkina; E.S. Smirnova; E.V. Grachova; P.V. Ostrova; M.Y. Antipin, *Acta Crystallogr. B,* 2009, *65*, 45-53.
18. V.B. Kalinin; A.M. Golubev; V.A. Tafeenko; S.Yu. Stefanovich, *Kristallografiya,* 1992, *37*, 1220-1226.
19. ALTERMATr, B. I. D. B. A. D., *Acta Cryst.* 1985, *B41*, 244-247.

Chapter 6 FURTHER INSIGHT INTO U AND Th METAPHOSPHATE CRYSTAL CHEMISTRY AND EFFECT OF Nd^{3+} INCORPORATION INTO U^{4+} METAPHOSPHATE

6.1 Abstract

Single crystals of a tetragonal modification of uranium polymetaphosphate $U(PO_3)_4$, of a mixed U^{4+}/Nd^{3+} polymetaphosphate "$(U_{0.62}Nd_{0.38})(PO_3)_4$", and of two new tetraphosphates, $Th(P_4O_{12})$ and $U(P_4O_{12})$, were synthesized. The structures of obtained materials were characterized by X-ray diffraction and Raman spectroscopy. The presence of Nd in "$(U_{0.62}Nd_{0.38})(PO_3)_4$" was proven by EDX and its measured degree of substitution for U agrees well with the results of X-ray crystallography, however the mechanism of the necessary charge compensation could not be identified yet. The cation arrangement in the crystal structures of Th/U polymetaphosphates has been studied in terms of Voronoi-Dirichlet polyhedra. Different conformations of the tetraphosphate poly-anions were observed in the crystal structures of $Th(P_4O_{12})$ and $U(P_4O_{12})$. The Raman spectrum of $Th(P_4O_{12})$ single crystal was recorded and bands assigned.

6.2 Introduction

The chemistry and crystal chemistry of the actinides attracts great interest not only because of their important role played in nuclear fuel reprocessing and waste management, but also because actinide compounds are most interesting objects for fundamental studies since they demonstrate great structural diversity and complexity[1-3], and even have potentially beneficial properties[4-9]. One of the most common uranium minerals, viz. autunite $Ca(UO_2)_2(PO_4)_2{\cdot}11H_2O$[10]. was shown to occur in the contaminated soils of Fernald Site in Ohio, USA, a former uranium reprocessing plant where tributyl phosphate was used as an extraction reagent[11]. Besides the autunite group compounds (with U^{6+}) which contained about 31% of the total U present, U^{4+} metaphosphates were found which represented around 20% of the U. The U^{4+} metaphosphate causes great challenges in the decontamination process due to its very low solubility in water and low solubility in mineral acids[11]. Owing to their stability with di- and trivalent cations, metaphosphates have potential as possible matrix for nuclear waste management [12].

Several studies have been devoted to the synthesis and structures of U and Th metaphosphates [13]. Baskin [14] reported on two polymorphic modifications of $U(PO_3)_4$ which were obtained by reactions of UP, UO_2, and U_3O_8 with concentrated phosphoric acid or P_2O_5. At temperatures below 500°C only β-$U(PO_3)_4$ was obtained with orthorhombic unit cell

parameters determined by single crystal X-ray diffraction as a = 13.80, b = 14.92, c = 9.00 Å (no e.s.d.'s available). At temperatures above 900°C only α-$U(PO_3)_4$ was formed with monoclinic unit cell parameters a = 23.42, b = 13.02, c = 23.00 Å, β = 90.0(2)° (no e.s.d.'s available for a, b and c), while reactions in the intermediate temperature range of 500–900°C resulted in a mixture of the α- and β-phases. Another polymorphic modification of $U(PO_3)_4$ (obtained along with orthorhombic phase by a reaction of orthophosphoric acid with uranyl nitrate at 400–600°C) with triclinic unit cell parameters a = 15.430(15), b = 8.147(6), c = 8.734(8) Å, α = 117.64(7), β = 112.59(5), γ = 89.08(5)°, as well as the isostructural $Th(PO_3)_4$ were reported by Masse and Grenier [15]. Linde et al. [16] describe the crystal structure of $U(PO_3)_4$ in space group *P*bcn with unit cell parameters a = 6.907(1), b = 14.947(2), and c = 8.986(1) Å [17], i.e. having a halved unit cell with respect to β-$U(PO_3)_4$ after [14], and stated that additional X-ray studies were required. Given the general similarity between the crystal chemistry of U^{4+} and Zr^{4+}, Locock pointed at the possibility that β-$U(PO_4)_3$ might well adopt the crystal structure of $Zr(PO_3)_4$, which has a quadrupled pseudo-orthorhombic unit cell with respect to the *P*bcn structure with parameters a = 13.495(1), b = 28.799(2), c = 8.658(1) Å, β = 90.04(2)° [10]. Indeed, Höppe and Daub [12] found a supercell and pseudo-merohedral twinning in $U(PO_3)_4$ and solved its structure in space group *C*2/c with unit cell parameters a = 13.786(3), b = 29.843(6), c = 8.972(2) Å, β = 90.01(3)°, thus corroborating Locock's suggestion.

Americium(III) and curium(III), due to their radiotoxicity, are two of the challenging elements present in spent nuclear fuel as products of nuclear reactions. The crystal chemical properties of these elements are very similar to those of trivalent lanthanides [18]. Therefore, Nd is often used as a surrogate for actinides in order to avoid the difficulties of handling radioactive materials. It should be noted that so far there is no direct experimental evidence for a possible Nd/Am/Cm substitution for U/Th in their metaphosphates. However, such effects are well known for uranium and thorium orthophosphates of the monazite and NZP (sodium zirconium phosphate) type [19-27].

In this chapter we have obtained new modifications of U and Th metaphosphates and a metaphosphate with isomorphic U/Nd substitution and describe their crystal structures.

6.3 Synthesis

Caution! *^{232}Th and ^{238}U are alpha-emitting radionuclides and standard precautions for handling radioactive materials should be followed.*

Analytical grade chemicals were used without further purification. Both tetragonal **tt-$U(PO_3)_4$** and "**$(U_{0.62}Nd_{0.38})(PO_3)_4$**" were obtained in the same batch. A powdered mixture of $UO_2(NO_3)_2{\cdot}6H_2O$ (0.1g, 0.20 mmol), $Nd(NO_3)_3{\cdot}6H_2O$ (0.175 g, 0.40 mmol) and Na_2CO_3 (0.0422 g, 0.20 mmol) was dissolved in 1 mL of 85% phosphoric acid and the resulting solution heated up to 500°C with a heating rate of 25°C/h. This procedure took place in a platinum crucible. After reaching the final temperature the furnace was switched off and let cool down to room

temperature. Emerald green crystals of **tt-$U(PO_3)_4$** and "**$(U_{0.62}Nd_{0.38})(PO_3)_4$**" were picked from the mother liquor and washed with distilled water.

Triclinic **tr-$Th(P_4O_{12})$** was obtained by heating of a reaction mixture consisting of ThO_2: $NH_4H_2PO_4$: $NaNO_3$ in a 1:10:1 molar ratio up to 1000°C in a Pt crucible . The melt was cooled slowly (5 °C/h) down to room temperature and then washed with distilled water resulting in colourless transparent crystals of $Th(P_4O_{12})$.

tr-$U(P_4O_{12})$ was obtained by the reaction of concentrated phosphoric acid (2 mL) with U_3O_8 (0.1 g, 0.12 mmol) in a porcelain crucible. The initial mixture of reagents was rapidly heated up to 850°C, kept at this temperature for 5 hours, and then cooled down to room temperature by switching off the furnace. The product consists of emerald green crystals.

As mentioned, the synthesis of tetragonal $U(PO_3)_4$ (**tt-$U(PO_3)_4$**) and "$(U_{0.62}Nd_{0.38})(PO_3)_4$" was performed in a platinum crucible, and both phases occurred in the same reaction batch, together with known phases such as $Nd(P_5O_{14})$, β-$U(PO_3)_4$ and, notably, small amounts of Pt(II) and Pt(IV) metaphosphates. An attempt to perform the reaction in corundum crucibles failed and resulted in a yellow viscous transparent solution without any precipitate. However, when the ceramic crucible contained a small ring of platinum the crystals of tt-$U(PO_3)_4$ and "$(U_{0.62}Nd_{0.38})(PO_3)_4$" grew at or close by the platinum ring. The same procedure performed with a copper ring failed again. These observations allow us to assume that the reduction of U^{6+} to U^{4+} is accompanied by oxidation of Pt^0. We have not further studied this remarkable effect.

6.4 Single Crystal X-ray Diffraction

The data were collected and refined follow the details as section 2.4 mentioned. All the structures were checked for possible higher symmetry using the ADDSYM algorithm from the program PLATON[28], but none were found. U and Nd atoms in the crystal structure of "$(U_{0.62}Nd_{0.38})(PO_3)_4$" were constrained to share the same site as well as thermal parameters. Relevant crystallographic data and details of the experimental conditions for all the three crystals are summarized in Table 6.1 and selected interatomic distances in Table 6.2.

Table 6.1: Crystallographic data for tetragonal $U(PO_3)_4$, "$(U_{0.62}Nd_{0.38})(PO_3)_4$", $Th(P_4O_{12})$, and $U(P_4O_{12})$

Compound	$U(PO_3)_4$	"$(U_{0.62}Nd_{0.38})(PO_3)_4$"	$Th(P_4O_{12})$	$U(P_4O_{12})$
space group	*I*422	*C*2/c	$P\bar{1}$	$P\bar{1}$
a, Å	11.30506(6)	16.3245(6)	8.2463(3)	8.1795(18)
b, Å	11.30506(6)	7.11053(14)	8.7976(4)	8.7073(12)
c, Å	14.92544(11)	9.5446(4)	14.6510(6)	14.474(3)
α, deg.	90.00	90.00	78.545(3)	78.724(14)
β, deg.	90.00	125.613(6)	74.701(3)	74.14(2)
γ, deg.	90.00	90.00	62.268(4)	62.094(19)
V, $Å^3$	1907.53(2)	900.69(5)	903.88(6)	873.5(3)
D_{calc}, g/cm^{-3}	3.858	3.819	4.026	4.212
Z	8	4	4	4
Temperature, K	299(2)	300(2)	293(2)	300(2)
λ, Å	0.71073	0.71073	0.71073	0.71073
F(000)	1984	943	984	992
R_1	0.0112	0.0192	0.0297	0.0427
wR_2	0.0317	0.0497	0.0808	0.1184
Flack	0.010(6)	–	–	–

Table 6.2: Bond distances in the crystal structures of tetragonal $U(PO_3)_4$, "$(U_{0.62}Nd_{0.38})(PO_3)_4$", and $Th(P_4O_{12})$.

Bond	d, Å	Bond	d, Å
Tetragonal $U(PO_3)_4$			
U1–O3 (×4)	2.348(2)	P1–O3	1.476(3)
U1–O6 (×4)	2.368(3)	P1–O4	1.477(3)
U2–O4 (×4)	2.362(3)	P2–O2	1.598(3)
U2–O5 (×4)	2.372(2)	P2–O5	1.482(2)
P1–O1	1.5682(13)	P2–O6	1.481(3)
P1–O2	1.587(3)	P2–O7	1.5850(16)
"$(U_{0.62}Nd_{0.38})(PO_3)_4$"			
U1–O3 (×2)	2.380(3)	P1–O2	1.590(3)
U1–O4 (×2)	2.342(3)	P1–O3	1.482(3)
U1–O5 (×2)	2.432(3)	P2–O1	1.593(3)
U1–O6 (×2)	2.391(3)	P2–O2	1.596(3)
P1–O1	1.581(3)	P2–O5	1.485(3)
P1–O4	1.489(3)	P2–O6	1.486(3)

$Th(P_4O_{12})$

Bond	d, Å		Bond	d, Å	
	$Th(P_4O_{12})$	$U(P_4O_{12})$		$Th(P_4O_{12})$	$U(P_4O_{12})$
An1–O3	2.379(4)	2.310(8)	P3–O5	1.587(4)	1.582(9)
An1–O9	2.356(4)	2.304(9)	P3–O8	1.580(4)	1.571(8)
An1–O11	2.390(4)	2.329(9)	P3–O9	1.488(4)	1.480(9)
An1–O12	2.397(4)	2.372(9)	P3–O10	1.470(4)	1.438(9)
An1–O15	2.403(4)	2.364(10)	P4–O1	1.591(4)	1.580(9)
An1–O17	2.404(4)	2.359(8)	P4–O8	1.584(4)	1.604(9)
An1–O18	2.431(4)	2.383(8)	P4–O11	1.480(4)	1.472(9)

$Th(P_4O_{12})$

Bond	d, Å		Bond	d, Å	
	$Th(P_4O_{12})$	$U(P_4O_{12})$		$Th(P_4O_{12})$	$U(P_4O_{12})$
An1–O22	2.453(4)	2.388(9)	P4–O12	1.486(4)	1.467(9)
An2–O4	2.418(4)	2.363(10)	P5–O13	1.587(4)	1.583(9)
An2–O6	2.411(4)	2.362(9)	P5–O14	1.591(4)	1.571(9)
An2–O7	2.418(4)	2.355(9)	P5–O15	1.477(4)	1.477(11)
An2–O10	2.429(4)	2.363(9)	P5–O16	1.485(4)	1.490(9)
An2–O16	2.343(4)	2.276(8)	P6–O13	1.584(4)	1.595(9)
An2–O21	2.371(4)	2.297(9)	P6–O14	1.590(4)	1.581(9)

An2–O23	2.384(4)	2.324(9)	P6–O17	1.479(4)	1.480(9)
An2–O24	2.388(4)	2.335(9)	P6–O18	1.479(4)	1.487(8)
P1–O1	1.601(4)	1.574(8)	P7–O19	1.587(4)	1.571(9)
P1–O2	1.580(4)	1.610(9)	P7–O20	1.592(4)	1.584(9)
P1–O3	1.485(4)	1.481(8)	P7–O21	1.485(4)	1.519(10)
P1–O4	1.468(4)	1.446(9)	P7–O22	1.474(4)	1.477(9)
P2–O2	1.590(4)	1.587(8)	P8–O19	1.591(4)	1.593(10)
P2–O5	1.590(4)	1.583(9)	P8–O20	1.575(4)	1.567(9)
P2–O6	1.478(4)	1.479(9)	P8–O23	1.479(4)	1.477(9)
P2–O7	1.492(4)	1.462(9)	P8–O24	1.482(4)	1.473(9)

6.5 Chemical Compositions

The electronic-microscopic image was shown in the Fig. 6.1, and the experimental data as well as the calculated stoichiometry was shown in the Table 6.3.

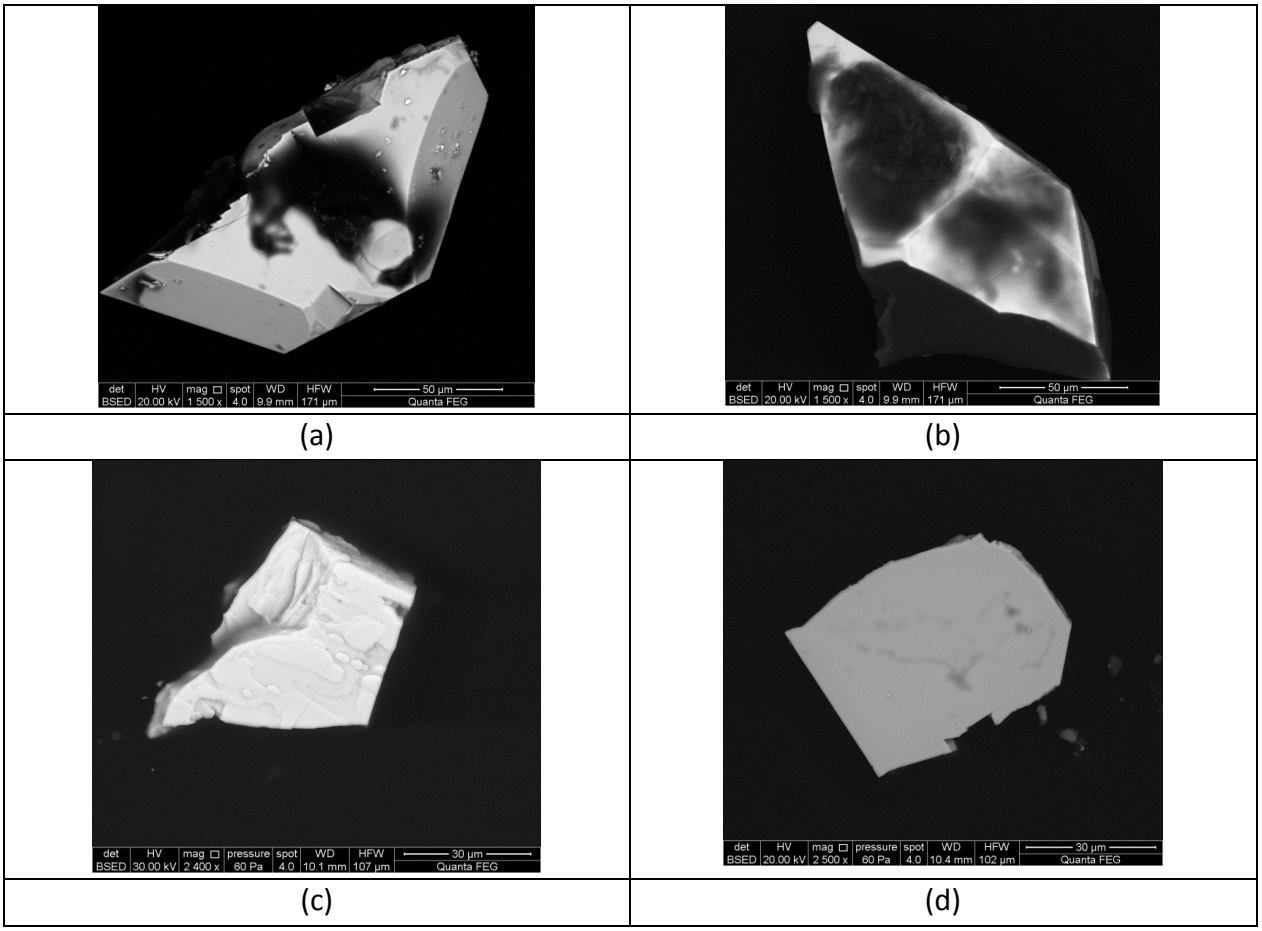

***Figure 6.1**: Electronic-microscopic image of tetragonal $U(PO_3)_4$ (a), $(U_{0.62}Nd_{0.38})(PO_3)_4$ (b), $Th(P_4O_{12})$ (c), and $U(P_4O_{12})$ (d).*

Table 6.3: Quantitate amounts of Th, U, Nd, and P (found by EDS and calculated according to formula) in the crystal of tetragonal $U(PO_3)_4$, $(U_{0.62}Nd_{0.38})(PO_3)_4$, $Th(P_4O_{12})$, and $U(P_4O_{12})$

Tetragonal $U(PO_3)_4$					$(U_{0.62}Nd_{0.38})H_{0.38}(PO_3)_4$				
Element	Found		Calculated		Element	Found		Calculated	
	Wt %	At %	Wt %	At %		Wt %	At %	Wt %	At %
P K	36.6	81.6	34.2	80.0	P K	40.0	81.6	37.3	80.0
U M	63.4	18.4	65.8	20.0	U M	45.3	12.0	48.8	13.6
					Nd L	14.7	6.4	13.9	6.4
Total	100	100	100	100	Total	100	100	100	100
$Th(P_4O_{12})$					$U(P_4O_{12})$				
Element	Found		Calculated		Element	Found		Calculated	
	Wt %	At %	Wt %	At %		Wt %	At %	Wt %	At %
P K	36.6	81.2	34.8	80	P K	34.8	80.4	34.2	80.0
Th M	63.4	18.8	65.2	20	Th M	65.2	19.6	65.8	20.0
Total	100	100	100	100	Total	100	100	100	100

The results of EDX elemental analysis are in good agreement with those of the single crystal X-ray diffraction studies. Proton positions could not be determined in the X-ray studies.

6.6 Structure Description

Tetragonal $U(PO_3)_4$ (tt-$U(PO_3)_4$) crystallizes in the non-centrosymmetric space group *I*422. Its choice was based on $|E^2-1|$ statistics which clearly indicated non-centrosymmetry. An attempt to solve the structure in I4/mmm failed. The crystal structure is based on a 3D framework consisting of uranium polyhedra and $(PO_3)_n^{n-}$ polymeric chains (Fig. 6.2a). There are two independent crystallographic positions for the U atoms with site-symmetry 4 and 222 for U1 and U2, respectively. Both crystallographically independent uranium atoms are coordinated by eight oxygen atoms of metaphosphate chains with U–O bond distances ranging from 2.348(2) to 2.372(2) Å. The UO_8 coordination polyhedra adopt square antiprismatic geometry that is slightly distorted in the case of U2 (Fig. 6.3a and b). The R_{SD} values (R_{SD} = radius of sphere the volume of which is equal to that of the corresponding Voronoi-Dirichlet polyhedron in a crystal structure (**VDP**) [28, 29]) of U atoms equal 1.386 Å and agree perfectly with the average value of 1.39(3) Å [29] found for $U(IV)O_n$ VDPs. Polymeric $(PO_3)_n^-$ chains are based upon eight corner-sharing PO_4 tetrahedra within a single periodic unit. This unit has a length of about 14.93 Å. The polymeric chains extend along the ***c*** axis and are helix-shaped as shown in Fig. 6.4a. The P–O bond distances are in the range of 1.476(3)–1.482(2) Å and 1.568(1)–1.598(3) Å for terminal and bridging O atoms, respectively, whereas

the O – P – O and P – O – P angles range from 99.4(2) to 118.8(2) and from 131.3(2) to 149.2(3)°, respectively.

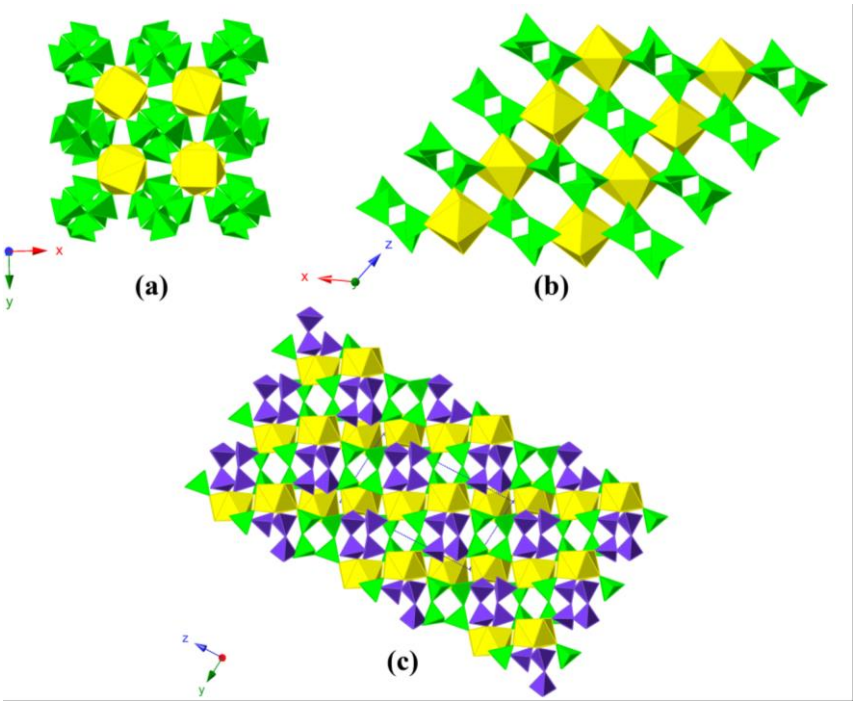

***Figure 6.2**: Crystal structure of tetragonal $U(PO_3)_4$ (a), "$(U_{0.62}Nd_{0.38})(PO_3)_4$" (b), and $Th(P_4O_{12})$ (c). $Th(P_4O_{12})$ and $U(P_4O_{12})$ are isostructural. U, U/Nd, and Th sites are yellow. PO_4 polyhedra are green (a and b) or purple. Green or purple (c) PO_4 tetrahedra are to show plain and distorted P_4O_{12} groups, respectively. O atoms omitted for clarity.*

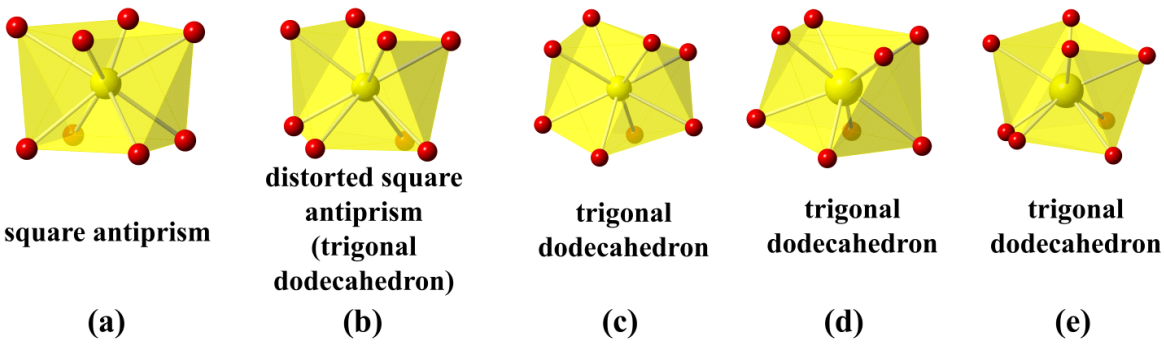

***Figure 6.3:** Metal atoms coordination polyhedra in $U(PO_3)_4$ (a and b for U1 and U2, respectively), "$(U_{0.62}Nd_{0.38})(PO_3)_4$" (c), and $Th(P_4O_{12})$ (d and e for Th1 and Th2, respectively).*

"**$(U_{0.62}Nd_{0.38})(PO_3)_4$**" crystallizes in the monoclinic *C*2/c space group. Both, U and Nd atoms share a common crystallographic site with 2-fold rotational symmetry. and form UO_8/NdO_8 coordination polyhedra with U/Nd–O bonds ranging from 2.342(3) to 2.432(3) Å (Fig. 6.4c). The R_{SD} of the U/Nd site is 1.396Å which is closer to the average VDP volume of U atoms in O environment (1.39(3) Å) rather than to that of Nd (1.46(3) Å) . The periodic unit of the $(PO_3)_n^{n-}$ chains in the crystal structure is only half of that of tt-$U(PO_3)_4$ and thus contains four PO_4 tetrahedra and has a length of ~ 7.11 Å (Fig. 6.4b). Terminal and bridging P–O bond distances range from 1.482(3) to 1.489(3) and from 1.581(3) to 1.596(3) Å, respectively. O – P – O angles in PO_4 tetrahedra range from 101.6(2)–119.8(2)° and P – O – P angles are equal to 129.2(2) and 135.1(2)°.

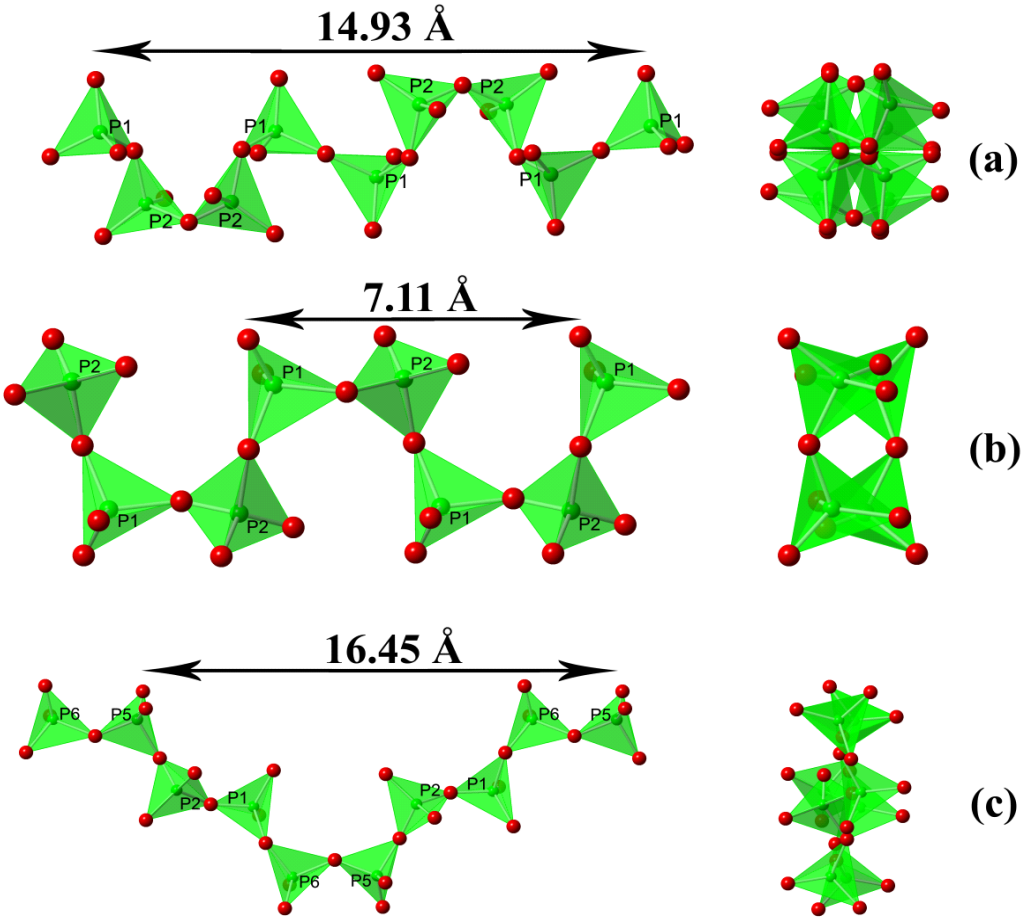

Figure 6.4: *Polyphosphate chains in crystal structures of the tetragonal $U(PO_3)_4$, "$(U_{0.62}Nd_{0.38})(PO_3)_4$", and β-$U(PO_3)_4$[12].*

Occupation of the same position by both, U^{4+} and Nd^{3+} obviously results in charge misbalance of the mixed U/Nd structure studied here and requires charge compensation. Various possible ways for charge balancing are conceivable, e.g. introduction of protons, partial substitution of non-reduced U^{6+} for U^{4+}, or presence of oxygen vacancies. All of these possible minor species or defects would be difficult to be detected by x-ray diffraction in the presence of heavy atoms like U. Appropriate spectroscopic methods, such as vibrational or UV/VIS spectroscopy, would require special microspectrometers running in laboratories which are equipped and licensed for work with radioactive material. At present, such a laboratory and the corresponding instruments are not at our disposal and shipping radioactive material to other laboratories is also difficult. Therefore, the answer to the question of how the charge compensation proceeds has to remain open. There are only few reports on crystal structures of compounds containing both U^{4+} and Ln^{3+} (particularly Nd) sharing one position with charge balance achieved by variation of outer sphere alkaline or ammonium cations site occupation factors [30-32].

Both tetraphosphates, **tr-Th(P_4O_{12})** and **tr-U(P_4O_{12}),** are isostructural and crystallize in space group $P\bar{1}$. Their crystal structures are based upon a 3D framework consisting of thorium/uranium atoms coordinated by tetraphosphate groups. There are two independent Th/U sites which are eightfold coordinated by O atoms in the form of a trigonal dodecahedron (Fig. 6.3d and e). Th–O and U–O bond distances are in ranges of 2.343(4)–2.453(3) and 2.276(8)–2.364(10) Å, respectively. Two of the three crystallographically independent tetraphosphate anions $(P_4O_{12})^{4-}$ possess a planar conformation, i.e. all phosphorus atoms lie within a single plane (Fig. 6.5a, shown in green). The third anion containing P1, P2, P3 and P4 atoms deviates from a plane (Fig. 6.5b, shown in purple) due to different arrangements of the bridging oxygen atoms as it is shown on Fig. 6.5. The bond distances between P and O atoms are in the ranges of 1.571(9)–1.610(9) and 1.438(9)–1.490(9) Å for bridging and terminal O atoms, respectively. The OPO angles in PO_4 tetrahedra vary from 100.3(5) to 120.6(5)°.

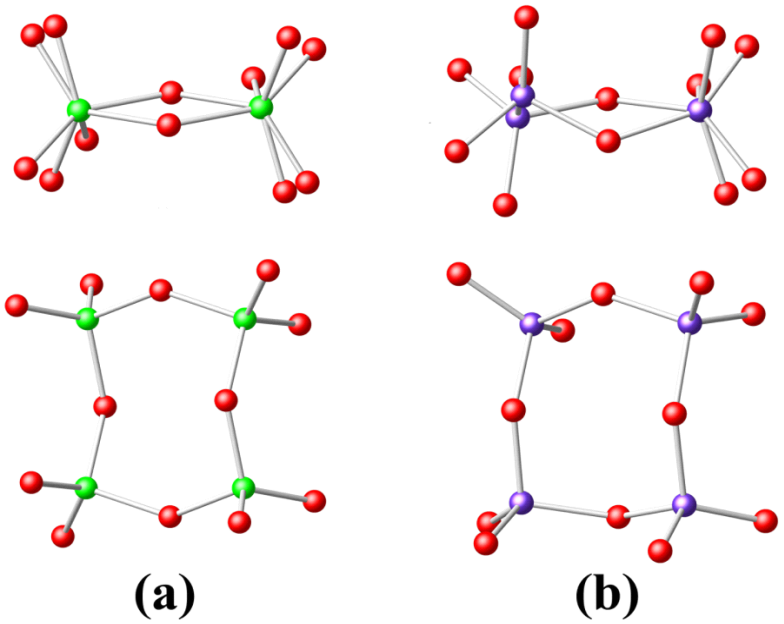

Figure 6.5: *View on two different conformational types of tetraphosphate anions in crystal structure of Th(P_4O_{12}). One of them contains two bridging O atoms above and two below plane of P atoms (a) and another one – three above and one below the plane built using any of three P atoms of this anion (b).*

6.7 Analysis of Structures and Systematization of the Polymorphs

Given that a triclinic unit cell can be chosen in different ways, the here reported Th(P_4O_{12}) has unit cell parameters which are comparable with those reported by Masse and Grenier [15] for Th(P_4O_{12}) and U(P_4O_{12}). Transformation matrices are given in Table 6.4. Thus, U^{4+} and Th^{4+} tetraphosphates should be isostructural. Previously, the crystal structure of U(P_4O_{12}) was reported with triclinic unit cell parameters a = 8.145, b = 8.272, c = 8.653 Å, α = 117.83, β = 117.24, γ = 91.02°, and V = 438.07 $Å^3$ [16]. The non-centrosymmetric space group *P*1 was chosen based on difference in R_1 values (0.068 for *P*1 against 0.087 for $P\bar{1}$) and intensity statistics. Despite rather low R_1 value, this model suffers from wide ranges of P–O bond lengths which are 1.32(3)–1.62(3) and 1.51(3)–1.70(3) Å for the terminal and bridging O atoms, respectively. Arguably, these deviations result from an inappropriately chosen unit cell and/or space group. Considering this together with the fact that the unit cell of our tr-Th(P_4O_{12}) was found to be approximately twice that of U(P_4O_{12}) we decided to reinvestigate the crystals of U(P_4O_{12}). All the picked crystals of tr-U(P_4O_{12}) were found to be non-merohedral twins which complicated the structure determination, but with tr-Th(P_4O_{12}) as a starting model and detwinned data we got a good fit with R_1 = 0.041 (see Supplementary for

cif). Taking into account the similar synthetic conditions, we assume that α-$U(PO_3)_4$ described in [14] is, in fact, tr-$U(P_4O_{12})$, despite the significantly different unit cell parameters.

Comparison of the crystal structures of tt-$U(PO_3)_4$, "$(U_{0.62}Nd_{0.38})(PO_3)_4$" and of the previously reported β-$U(PO_3)_4$ showed significant differences in the packing and topology of these compounds. As it was mentioned in [12], the U sites in β-$U(PO_3)_4$ are arranged in layers resembling the ...AB... stacking of a hexagonal closest packing of spheres. Accordingly, the U atoms in the U-sublattice (without taking P and O atoms under consideration) have VDP's with 12 faces which, in fact, represents the twelve nearest neighbors in a hexagonal closest packing [29], Fig. 6.6a and 6.7. At variance with β-$U(PO_3)_4$, the uranium atoms in the U-sublattice of tt-$U(PO_3)_4$, have VDP's in the shape of a truncated octahedron with 14 faces (Fig. 6.5b). This VDP is characteristic for a body-centered cubic lattice and more common for VDPs in sublattices [33]. The uranium/neodymium sublattice in "$(U_{0.62}Nd_{0.38})(PO_3)_4$" can be described as hexagonal layers in a ...AAA... arrangement, i.e. layers are almost unshifted against each other. Slight deviations of the U atoms from ideal positions makes the uranium atoms VDPs 18 faced.

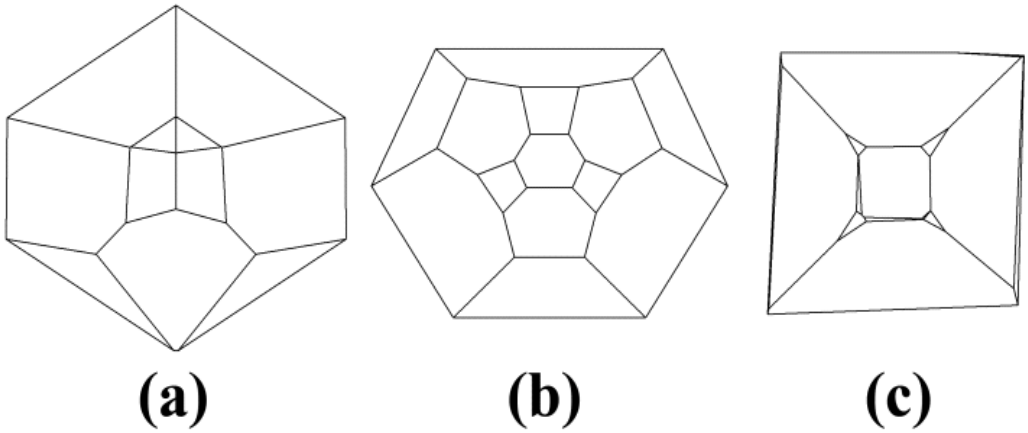

Figure 6.6: *Schloegel projections of metal atom Voronoi-Dirichlet polyhedra in metal sublattice in β-$U(PO_3)_4$ (a), tetragonal $U(PO_3)_4$ (b), "$(U_{0.62}Nd_{0.38})(PO_3)_4$" (c).*

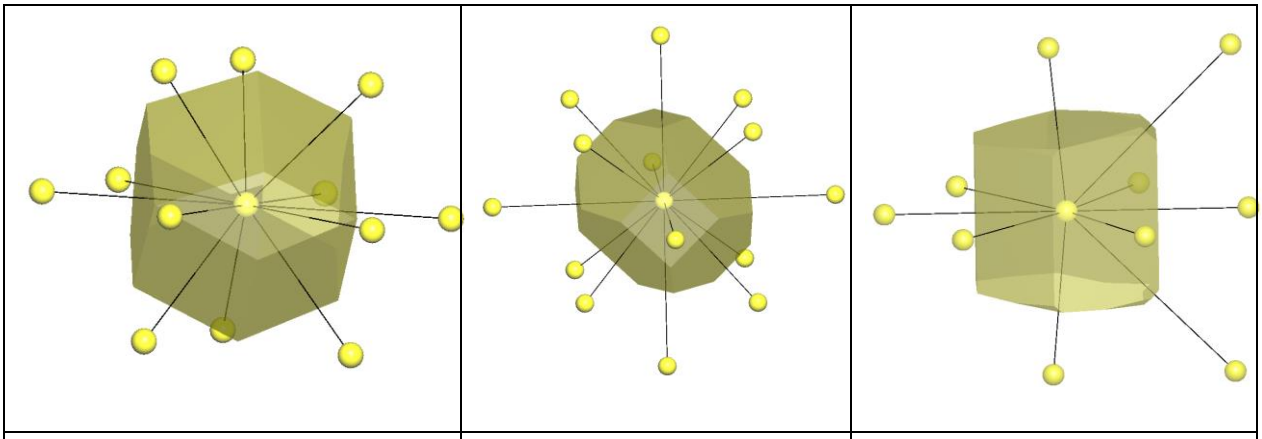

(a) (b) (c)

Figure 6.7*: The VDP of the U atoms in U-sublattice in the crystal structures of β -$U(PO_3)_4$ (a), tetragonal $U(PO_3)_4$ (b), $(U_{0.62}Nd_{0.38})H_{0.38}(PO_3)_4$ (c). In the latter, only U atoms that form direct contacts are shown.*

Variations in the U atoms arrangement in the considered crystal structures lead to different $(PO_3)_n^{n-}$ chain configurations (Fig. 6.4) and different spatial distribution with respect to U atoms. In tt-$U(PO_3)_4$ and "$(U_{0.62}Nd_{0.38})(PO_3)_4$", the phosphate chains are parallel to each other. U atoms in tt-$U(PO_3)_4$ are coordinated by four different $(PO_3)_n^{n-}$ chains and form eight-membered rings consisting of three phosphate groups with each of four chains. In "$(U_{0.62}Nd_{0.38})(PO_3)_4$", U atoms are also bound to four chains, but their coordination mode is different, in that U atoms form six-membered rings with the atoms of two chains and ten-membered rings with the atoms of two other chains. The crystal structure of β-$U(PO_3)_4$ contains crossing phosphate chains with an angle of 64.1° between them. Two of five chains connected with U atom are coordinated by a single oxygen atom and the other three form two six- and one ten-membered rings. Taking into account the flexibility of polyphosphate chains which possess rotational degrees of freedom about the P–O bonds, it can be concluded that the structure formation in the reported compounds is driven by the arrangement of metal sites.

All polymorphic modifications of thorium and uranium metaphosphates with general formula $(U/Th)P_4O_{12}$ known to date are listed in Table 6.4. There are three different polymorphic modifications. One contains tetraphosphate rings and the other two infinite polyphosphate chains. Tetragonal $An(PO_3)_4$ (*An* = Th, U) is the only modification for which the unit cell could be determined unambiguously, while the other two modifications were determined in various settings due to pseudosymmetry (Table 6.4). Besides tetragonal

polyphosphate, the best crystal models of thorium/uranium tetraphosphates *An*(P_4O_{12}) and polymetaphosphate *An*$(PO_3)_4$ with the lowest R_1 values and reasonable geometry were obtained in the triclinic and monoclinic [12] crystal systems, respectively.

Table 6.4: Polymorphic modifications of U(IV) and Th metaphosphates

	Compound	Sp. gr.	a, Å	b, Å	c, Å	α, °	β, °	γ, °	V, Å^3	Ref.
Triclinic tetraphosphate	Th(P_4O_{12})	$P\bar{1}$	8.2463(3)	8.7976(4)	14.6510(6)	78.545(3)	74.701(3)	62.268(4)	903.9	This work
		n. d. *	15.510(15)	8.251(7)	8.796(8)	117.80(7)	112.32(5)	89.14(5)[a]	902.9	[15]
	U(P_4O_{12})	$P\bar{1}$	8.1795(18)	8.7073(12)	14.474(3)	78.724(14)	74.14(2)	62.094(19)	873.5	This work
		n.d.	15.430(15)	8.147(6)	8.734(8)	117.64(7)	112.59(5)	89.08(5)[a]	880.2	[15]
		*P*1	8.145	8.272	8.653	117.83	117.24	91.02[b]	438.1	[16]
		n.d.	23.42	13.02	23.00	90	90	90[c]	7013.2	[14]
Tetragonal polyphosphate	Th$(PO_3)_4$	*I*4/mmm, I4mm, $I\bar{4}$m2, $I\bar{4}$2m, I422	11.440(10)	11.440(10)	14.978(20)	90	90	90	1960.5	[15]
	U$(PO_3)_4$	*I*422	11.30506(6)	11.30506(6)	14.92544(11)	90	90	90	1907.5	This work
Orthorhombic polyphosphate	Th$(PO_3)_4$	n.d.	14.35	15.11	9.05	90	90	90	1962.3	[36]
		*P*bcn	6.947(4)	15.120(20)	9.069(7)	90	90	90	952.6	[15]
	U$(PO_3)_4$	n.d.	14.33	14.96	9.05	90	90	90	1940.1	[36]
		*P*bca	13.80	14.92	9.00	90	90	90	1853.1	[14]
		*P*nab	8.95(1)	14.94(1)	6.89(1)	90	90	90	921	[37]
		*P*bcn	6.913(4)	14.967(20)	8.986(7)	90	90	90	929.8	[15]
		*P*bcn	6.907(1)	14.947(2)	8.986(1)	90	90	90	929.9	[17]
Monoclinic polyphosphate	U$(PO_3)_4$	*C*2/c	13.786(3)	29.843(6)	8.972(2)	90	90.01(3)	90	3691.3	[12]

*n.d.: not determined. E.s.d.'s (if any) are given according to a reference in the last column. Transformation matrices of a given cell to a cell reported in this work: [a] (0 1 0 0 0 -1 -1 0 -1) ; [b] (0 -1 0 0 0 1 -2 -1 -1); [c] (-0.25 0 -0.25 0 0.5 -0.25 0.25 -0.5 -0.5)

6.8 Raman Spectroscopy

Only single crystal of $Th(P_4O_{12})$ resulted a good Raman spectrum, while U(IV)-containing crystals give strong luminescence. Due to low symmetry of the crystal and presence of two configurations of the tetraphosphate groups mentioned above, the spectrum of $Th(P_4O_{12})$ (Fig. 6.8) contains large number of bands that belong to three main regions. The peak list was given in Table 6.5. The first one is in a range of 1100–1300 cm^{-1} and corresponding, according to literature data [34], to the symmetric and antisymmetric stretching vibrations of phosphate groups, $\nu_1(PO_4)$ and $\nu_3(PO_4)$, respectively. The second and third regions cannot be distinguished unambiguously without theoretical calculation of spectrum because of their overlap. Despite this, it is more likely that a border between these regions lies at ca. 415 cm^{-1}. The bands of the Raman shift region of 415–1100 cm^{-1} correspond to the symmetric and antisymmetric bending vibrations of phosphate groups, $\nu_2(PO_4)$ and $\nu_4(PO_4)$, respectively. The latter region of 50–415 cm^{-1} is due to lattice modes and Th-O vibrations.

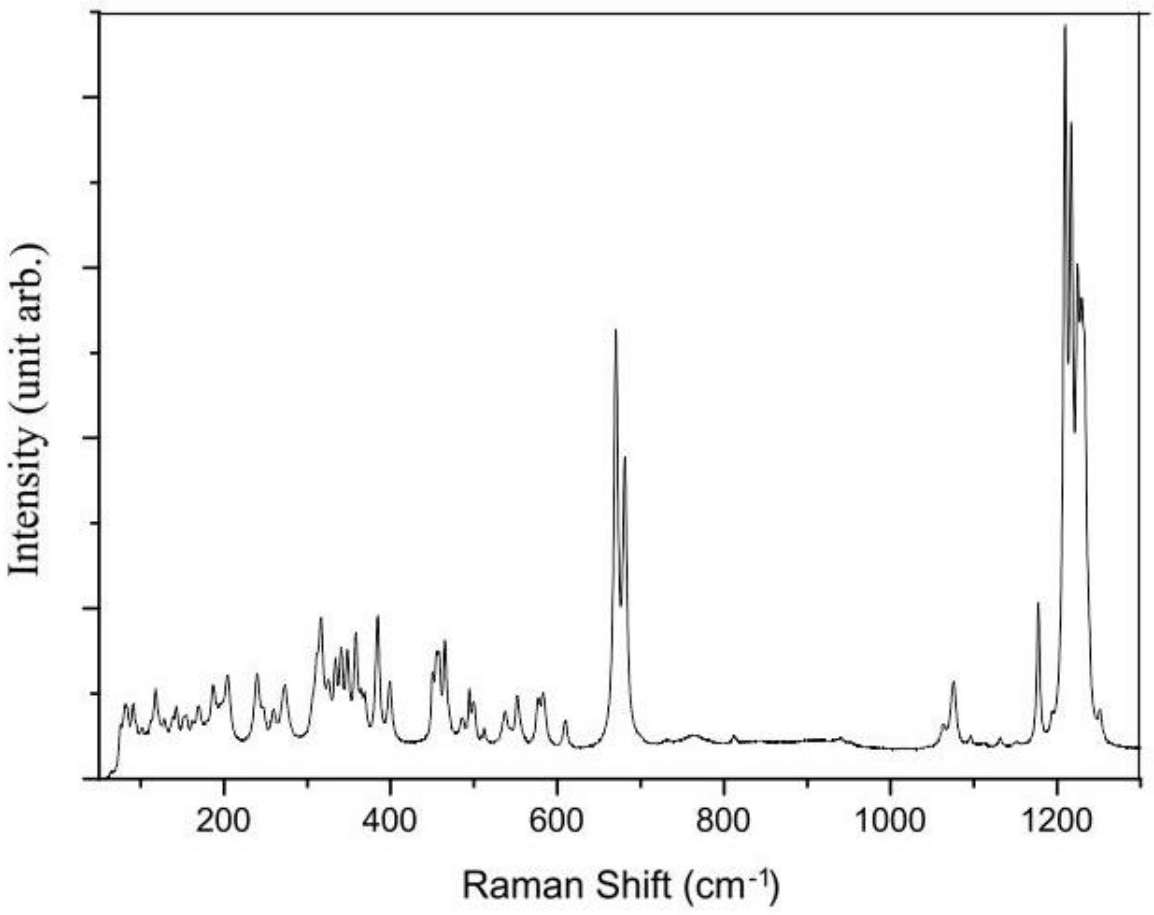

***Figure 6.8**: The Raman spectra of Raman spectrum of $Th(P_4O_{12})$.*

Table 6.5: Determined Raman Bands (cm^{-1}) for $Th(P_4O_{12})$

Intensity					
strong	medium		weak		shoulder
1224	1177	348	1251	153	1228
1217	1076	339	1130	142	451
1209	583	333	1095	129	
682	577	324	1063	101	
667	551	316	607	89	
	495	275	536	82	
	464	241	508		
	455	204	500		
	401	186	485		
	384	119	260		
	359		172		

6.9 Conclusions

A tetragonal modification of $U(PO_3)_4$, uranium metaphosphate with isomorphically incorporated neodymium cations, and thorium and uranium tetraphosphates were synthesized and structurally characterized. Comparison of the Voronoi-Dirichlet polyhedra of the metal atoms in tetragonal $U(PO_3)_4$ and the previously reported monoclinic modification showed metal sites arrangement to be in body centered cubic and hexagonal closest packing modes, respectively. Substitution of the about 10% larger Nd^{3+} for U^{4+} in the metaphosphate significantly changes the metal atom arrangement to a hexagonal ...**AAA...** packing mode. It would interesting to replace Nd^{3+} by heavier rare earth elements, for instance Ho^{3+} or Er^{3+}, because their ionic radii correspond closely to that of U^{4+}. The flexibility of the polyphosphate chains allows them to wrap around metal sites in all described cases to form eightfold coordination polyhedra which have a shape of either a cubic antiprisms or a trigonal dodecahedron. The crystal structure of tr-$Th(P_4O_{12})$ contains two conformational isomers of P_4O_{12} groups. Two of three crystallographic independent P_4O_{12} groups have all four P atoms lying within a plane, while the third one is slightly distorted. tr-$Th(P_4O_{12})$ was shown to be isostructural with tr-$U(P_4O_{12})$ which, in turn, was previously described as α-$U(PO_3)_4$.

6.10 References

1. S.V. Krivovichev; P.C. Burns; I.G. Tananaev; B.F. Myasoedov, *J. Alloys Compd.,* **2007**, 444-445, 457-463.
2. S.V. Krivovichev; V. Kahlenberg; I.G. Tananaev; R. Kaindl; E. Mersdorf; B.F. Myasoedov, *J. Am. Chem. Soc.,* **2005,** *127*, 1072-1073.
3. E.V. Alekseev; S.V. Krivovichev; W. Depmeier; O.I. Siidra; K. Knorr; E.V. Suleimanov; E.V. Chuprunov, *Angew. Chem. Int. Ed.,* **2006,** *45*, 7233-7235.
4. T.A. Sullens; R.A. Jensen; T.Y. Shvareva; T.E. Albrecht-Schmitt, *J. Am. Chem. Soc.,* **2004,** *126*, 2676-2677.
5. S. Wang; E.V. Alekseev; J. Diwu; W.H. Casey; B.L. Phillips; W. Depmeier; T.E. Albrecht-Schmitt, *Angew. Chem. Int. Ed.,* **2010,** *49*, 1057-1060.
6. P. Yu; S. Wang; E.V. Alekseev; W. Depmeier; D.T. Hobbs; T.E. Albrecht-Schmitt; B.L. Phillips; W.H. Casey, *Angew. Chem. Int. Ed.,* **2010,** *49*, 5975-5977.
7. P.O. Adelani; T.E. Albrecht-Schmitt, *Angew. Chem. Int. Ed.,* **2010,** *49*, 8909-8911.
8. S. Wang; E.V. Alekseev; J. Ling; G. Liu; W. Depmeier; T.E. Albrecht-Schmitt, *Chem. Mater.,* **2010,** *22*, 2155-2163.
9. S. Wang; E.V. Alekseev; J.T. Stritzinger; G. Liu; W. Depmeier; T.E. Albrecht-Schmitt, *Chem. Mater.,* **2010,** *22*, 5983-5991.
10. S.V. Krivovichev; P.C. Burns; I.G. Tananaev, *Structural Chemistry of Inorganic Actinide Compounds*. Elsevier: Amsterdam, 2007.
11. E.C. Buck; N.R. Brown; N.L. Dietz, *Environ. Sci. Technol.,* **1995,** *30*, 81-88.
12. H.A. Höppe; M. Daub, *Z. Kristall. -Cryst. Mater.* **2012,** *227*, 535-539.
13. V. Brandel; N. Dacheux, *J. Solid State Chem.,* **2004,** *177*, 4743-4754.
14. Y. Baskin, *J. Inorg. Nucl. Chem.,* **1967,** *29*, 383-391.
15. R. Masse, J.; .C. Grenier, *Bull. Soc. Fr. Miner. Cristal.,* **1972,** *95*, 136.
16. S.A. Linde; Y.E. Gorbunova; A.V. Lavrov, *Zh. Neorg. Khim.,* **1983,** *28*, 1391.
17. S.A. Linde; Y.E. Gorbunova; V.V. Ilyukhin; A.V. Lavrov; V.G. Kuznetsov, *Zh. Neorg. Khim.,* **1979,** *24*, 1786.
18. J. J. Katz; L. R. Morss; G. T. Seaborg, *The Chemistry of the Actinide and Transactinide Elements*. Springer Science+Business Media B.V: Dordrecht, 2011; Vol. 1-6.
19. N. Clavier; R. Podor; N. Dacheux, *J. Eur. Ceram. Soc.,* **2011,** *31*, 941-976.
20. D.B. Kitaev; Y.F. Volkov; A.I. Orlova, *Radiochem.,* **2004,** *46*, 211-217.
21. M.P. Orlova; A.I. Orlova; E.R. Gobechiya; Y.K. Kabalov; G.I. Dorokhova, *Crystallogr. Rep.,* **2005,** *50*, 48-51.
22. A. Tabuteau; M. Pagès; J. Livet; C. Musikas, *J. Mater. Sci. Lett.,* **1988,** *7*, 1315-1317.
23. J.W. Anthony, *Am. Mineral.,* **1965,** *50*, 1421.
24. N. Dacheux; N. Clavier; A.-C. Robisson; O. Terra; F. Audubert; J.-É. Lartigue; C. Guy, *Comptes Rendus Chim.,* **2004,** *7,*, 1141–1152.

25. A.I. Orlova; S.A. Khainakov; E.E. Loginova; T.A. Oleneva; S.G. Granda; V.S. Kurazhkovskaya, *Crystallogr. Rep.,* **2009,** *54*, 591-597.
26. D. Bregiroux; O. Terra; F. Audubert; N. Dacheux; V. Serin; R. Podor; D. Bernache-Assollant, *Inorg. Chem.,* **2007,** *46*, 10372-10382.
27. B.E. Scheetz; D.K. Agrawal; E. Breval; R. Roy, *Waste Manag.,* **1994,** *14*, 489-505.
28. B. Chapelet-Arab; G. Nowogrocki; F. Abraham; S. Grandjean, *J. Solid State Chem.,* **2005,** *178*, 3046-3054.
29. B. Chapelet-Arab; G. Nowogrocki; F. Abraham; S. Grandjean, *J. Solid State Chem.,* **2005,** *178*, 3055-3065.
30. B. Chapelet-Arab; L. Duvieubourg; G. Nowogrocki; F. Abraham; S. Grandjean, *J. Solid State Chem.,* **2006,** *179*, 4029-4036.
31. V.N. Serezhkin; D.V. Pushkin; L.B. Serezhkina, *J. Struct. Chem.,* **2009,** *50*, 14-21.
32. A. Burdese; M.L. Borlera, *Ann. Chim. Roma.,* **1963,** *53*, 344.
33. R. Douglass, *Acta Crystallogr.,* **1962,** *15*, 505-506.
34. N. Sánchez-Pastor; A.J. Pinto; J.M. Astilleros; L. Fernández-Díaz; M. A. Gonçalves, *Spectrochim. Acta A.,* **2013,** *113*, 196-202.

Chapter 7 SOME OTHER RESULTS FROM EXPLORING THE Th/U- A^{I}/ A^{II}- P/As SYSTEM

7.1 Th($As^{III}_4As^{V}_4O_{18}$): A Mixed- valent oxo- As(III)/As(V) Actinide Compound obtained under Extreme Conditions

7.1.1 Abstract

A high temperature/high pressure method was employed to investigate phase formation in the $Th(NO_3)_4{\cdot}5H_2O$–As_2O_3–$CsNO_3$ system. It was observed that an excess of As(III) in the starting system leads to the formation of Th($As^{III}_4As^{V}_4O_{18}$) which is a representative of a rare class of mixed-valent As^{III}/As^{V} compounds. This compound was studied with XRD, EDX, and Raman spectroscopy methods. Crystallographic data shows Th($As^{III}_4As^{V}_4O_{18}$) is built from $(As^{III}_4As^{V}_4O_{18})^{4-}$ layers connected through Th atoms. The arsenic layers are found to be isoreticular to those in previously reported As_2O_3 and $As_3O_5(OH)$, and the geometric differences between them are discussed. Bands in the Raman spectrum are assigned with respect to the presence of AsO_3 and AsO_4 groups.

7.1.2 Introduction

Interest in actinide chemistry has substantially expanded, especially in the last twenty years, because of its central role in nuclear energy and nuclear waste management, and of equal importance, because the 5f series represents an area of the periodic table where many questions remain unanswered. To date, many investigations have been devoted to understanding the behavior of thorium and uranium phosphate/arsenate compounds because both these elements have extremely long half-lives[1] and are present in far greater quantities than the heavier members of the series. It led, for example, to the investigation of a thorium phosphate/pyrophosphate which was shown to be suitable for actinides immobilization.[2-4] In addition, the compositional and structural diversity in this family is unparalleled.[5-10]

There are few examples of mixed-valent P^{III}/P^{V} actinide compounds.[11, 12] Although the phosphate compounds are generally better studied than arsenate analogs, examples of mixed-valent As^{III}/As^{V} minerals, such as dixenite $Cu^{I}Mn_{14}{}^{II}Fe^{III}(OH)_6(As^{III}O_3)_5(Si^{IV}O_4)_2(As^{V}O_4)$[13], hematolite $Mn_{10.39}Mg_{2.53}Al_{1.89}Fe_{0.19}(OH)_{23}(AsO_3)(AsO_4)_2$[14], and synadelphite $Mn_9(OH)_9(AsO_3)(AsO_4)_2(H_2O)_2$[15] have been reported. Synthetic mixed-valent As^{III}/As^{V} compounds are also known;[16-18] although the data are still very limited, and no examples exist from the actinide series.

7.1.3 Synthesis

The synthesis procedure was followed as described in section 2.3, and the information about the reactants is given in Table 7.1. The chemicals used were of analytical reagent grade

and were used without any other further purification. The reactants were thoroughly ground together with their appropriate ratios and loaded into a platinum crucible.

Table 7.1: The Experimental Reactants used in this chapter

Compound Name	**Purity**	**Company**
Thorium nitrate ($Th(NO_3)_4{\cdot}5H_2O$)	- -	Merck
Arsenite oxide (As_2O_3)	98%	Alfa-Aesar
Cesium nitrate ($CsNO_3$)	99.9%	Alfa-Aesar

Thorium nitrate $Th(NO_3)_4{\cdot}5H_2O$ (0.0700 g, 0.123 mmol), arsenic(III) oxide As_2O_3 (0.1947 g, 0.984 mmol), and $CsNO_3$ (0.0479 g, 0.246 mmol) in a molar ratio of 1: 8: 2 were mixed together and finely grounded. The experiment was performed at a pressure of 3 GPa and a temperature range from 1200 to 300°C. After heating the temperature was kept at 1200°C for 60 min. After that, the sample was slowly cooled down to 300°C in the rate of 0.234°C/min i.e. the cooling time was about 64 h. The capsule was then broken, and colourless crystals of $Th(As^{III}_4As^{V}_4O_{18})$ were isolated along with the amorphous phase and crystalline $CsAs_3O_8$.

Although analytical-grade As_2O_3 was used as an initial reagent, the resulting compound contains arsenic in both 3+ and 5+ oxidation states because of the presence of air and nitrate anions in the initial powdered mixture and in situ oxidation of As^{III} to As^{V}. Because no caesium is observed in the resulting compound, the role of caesium nitrate in the reaction mixture is to partially oxidize As_2O_3. This is accompanied by the fact that we have not observed any crystalline arsenic(III) compound after the reaction of the same reagents in a 1:3:2 ratio under similar conditions. Therefore, there should be a minimum amount of arsenic(III) with respect to the other reagents that provides formation of a mixed-valent arsenic(III)/arsenic(V) compound.

7.1.4 Single Crystal X-ray Diffraction

The data was collected and refined following the details mentioned in section 2.4. All the structures were checked for possible higher symmetry using the ADDSYM algorithm from the program PLATON, but none were found. Relevant crystallographic data and details of the experimental condition for this crystal were summarized in Table 7.2.

Table 7.2: Crystallographic data for $Th(As^{III}_4As^{V}_4O_{18})$

space group	*C2/c*
a, Å	18.2148(3)
b, Å	5.19792(7)
c, Å	17.3588(3)
β, °	99.1298(14)
V, $Å^3$	1622.70(4)
D_{calc}, g/cm^3	4.582
Z	4
λ, Å	0.71073
F(000)	1992
R_1	0.0160
wR_2	0.0423

7.1.5 Chemical Compositions

The electronic-microscopic image is shown in Fig. 7.1, and the experimental data as well as the calculated stoichiometry is shown inTable 7.3.

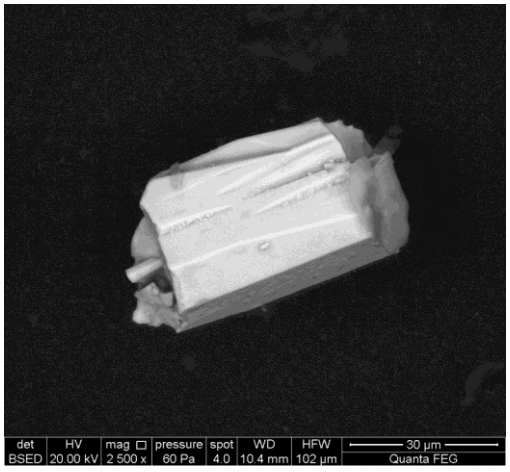

***Figure 7.1**: Electronic-microscopic image of a crystal of $Th(As^{III}_4As^{V}_4O_{18})$.*

Table 7.3: EDX elemental analysis and stoichiometry for $Th(As^{III}_4As^{V}_4O_{18})$

	Molar ratio, %		Total, %
	Th	As	
Measured	10.64	89.36	100
Calculated	11.11	88.89	100

The results of EDX elemental analysis are in good agreement with those of the single crystal X-ray diffraction studies. Proton positions could not be determined in the X-ray studies.

7.1.6 Structure Description

The crystal structure of $Th(As^{III}_4As^{V}_4O_{18})$ is based on a framework consisting of As^{III}/As^{V} layers and Th^{IV} centers (Fig. 7.2). Each Th atom lies on a two-fold rotational axis, and is connected to eight O atoms of eight different AsO_4 tetrahedra to form a coordination polyhedron in the shape of a slightly distorted square antiprism. The Th–O bond distances are normal and range from 2.3688(18) to 2.4724(18) Å.[19]

There are four crystallographic As sites. The As1 and As2 positions are occupied by trivalent arsenic ions, while As^{V} ions occupy As3 and As4 atomic sites. The As3–O and As4–O bond distances range from 1.6504(18)– 1.6624(18) and 1.7119(19)–1.7236(18) Å for terminal and bridging O atoms, respectively, and agree well with previously reported values. The O–As^{V}–O angles in AsO_4 tetrahedra vary from 102.96(10) to 118.35(9)°. As^{III} atoms form AsO_3 trigonal pyramids with As^{III}–O bond lengths in a range of 1.8068(19)–1.8218(19) Å for the O atoms bridging between As^{III} and As^{V}, and 1.7657(18) and 1.776(2) Å for those bridging between two As^{III} sites. The As^{III}–O bonds are influenced by the lone electron pairs of As^{III} atoms, and this is reflected in the strong deviation of the O–As^{III}–O angles, which lie in a range of 89.51(9)–98.32(9)°, from the tetrahedral As^{V} environments. To estimate the lone pair effect, the D_A values of the As^{III} atomic Voronoi-Dirichlet polyhedra (**VDP**)[20] were calculated. This value reflects the shift of an atom in a crystal structure from the center of its VDP. The values of calculated D_A are 0.583, 0.556, 0.023, and 0.046 Å for As1–As4, respectively, and agree well with previously reported average values of 0.63(7) and 0.05(3) for $As^{III}O_3$ and $As^{V}O_4$ VDP's[21], respectively.

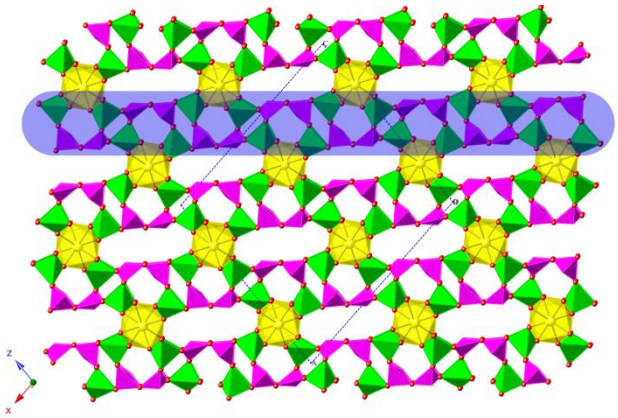

Figure 7.2: *A view of the crystal structure of $Th(As^{III}_4As^{V}_4O_{18})$. ThO_8, AsO_4, and AsO_3 coordination polyhedra are yellow, green, and magenta, respectively, and O atoms are red. $[As^{III}_4As^{V}_4O_{18}]^{4-}$ layer is marked with blue.*

Both As^{III} and As^{V} atoms form layers that are connected to Th sites by terminal O atoms of AsO_4 groups. To reveal the topology of the layer (i.e. in the crystal structure considered *without* Th–O bonds) we applied a standard simplification procedure using the ADS program of the TOPOS software package.[22, 23] The procedure applied to the $[As^{III}_4As^{V}_4O_{18}]^{4-}$ layer is shown in detail in Fig. 7.3. The first step is the building of a cation topology graph, and removal of the anions, i.e. O atoms (Fig. 7.3a, b). This graph consists of vertices (nodes) and edges which correspond to the cationic groups and connectivity between them, respectively (Fig. 7.3b). The second step is removal of bridging nodes (i.e. 2-coordinated) saving their connectivity (Fig. 7.3b, c). At this step one can see that due to removal of the As4 nodes, the As1 nodes also becomes bridging and are to be simplified (Fig. 7.3c). The resulting underlying net of the layer is built only of single As2 nodes and classified as the honeycomb (**hcb**) topological type (Fig. 7.3d). Nevertheless, an underlying net of the whole crystal structure *with* the Th–O bonds taken into account is significantly more complicated (Fig. 7.3b). To build this net, two thirds of the edges of the initial **hcb** net should be complemented with 4-coordinated As3 nodes, while the others – with $(As1As4)_2$ ring fragment. In this fragment, 3-coordinated As1 nodes form edges only with another As nodes, while 4-coordinated As4 nodes share edges with two As and two Th nodes. It is interesting to note, that such a step-by-step complementation could be seen in the crystal structures of [monoclinic-As_2O_3]–$[As^{III}_2As^{V}O_5(OH)]$–$[Th(As^{III}_4As^{V}_4O_{18})]$ series (Fig. 7.4). The structure of monoclinic-As_2O_3[26] is based on the layers with **hcb** underlying net, where the nodes correspond to As atoms. The same topological type is observed in the case of $As^{III}_2As^{V}O_5(OH)$, though there additional AsO_4 tetrahedra are complemented in one third of the **hcb** net edges (Fig. 7.4b,e, marked with blue). Finally, the four-membered rings of As nodes as well as AsO_4 tetrahedra are complemented in the 1 : 1 ratio to the rest of the edges to build a layer observed in $Th(As^{III}_4As^{V}_4O_{18})$ (Fig. 7.4c,f, marked with red).

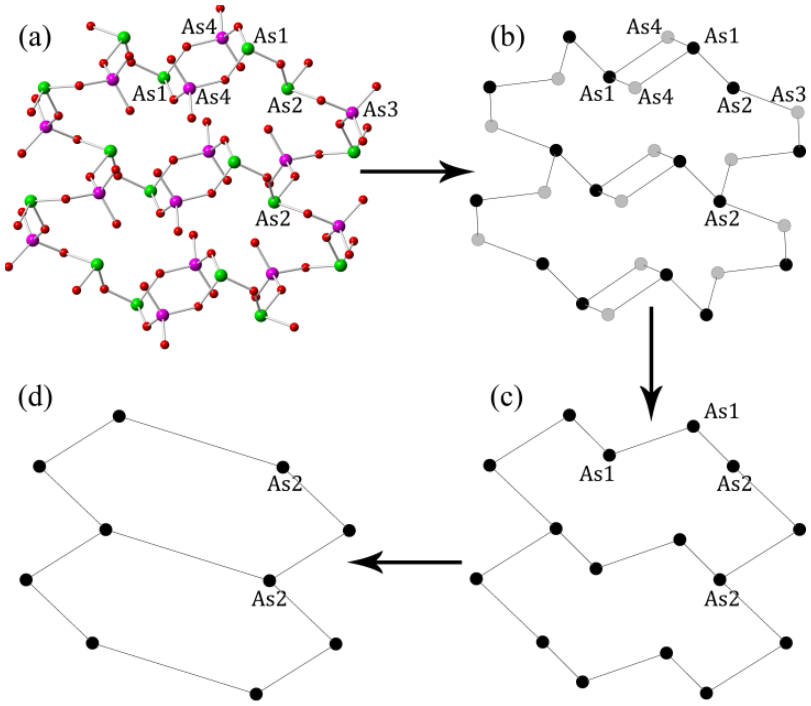

Figure 7.3: *The simplification procedure applied to the* $(As^{III}_4As^{V}_4O_{18})^{4-}$ *layers. O,* As^{III} *and* As^{V} *atoms are red, green, and magenta, respectively. In graph representation,* As^{III} *and* As^{V} *nodes are black and grey, respectively.*

Thus, the chemical evolution from purely As^{III} based 2D phases to mixed As^{III}/As^{V} compounds is followed by complication of the layered structure without changing the topologies.

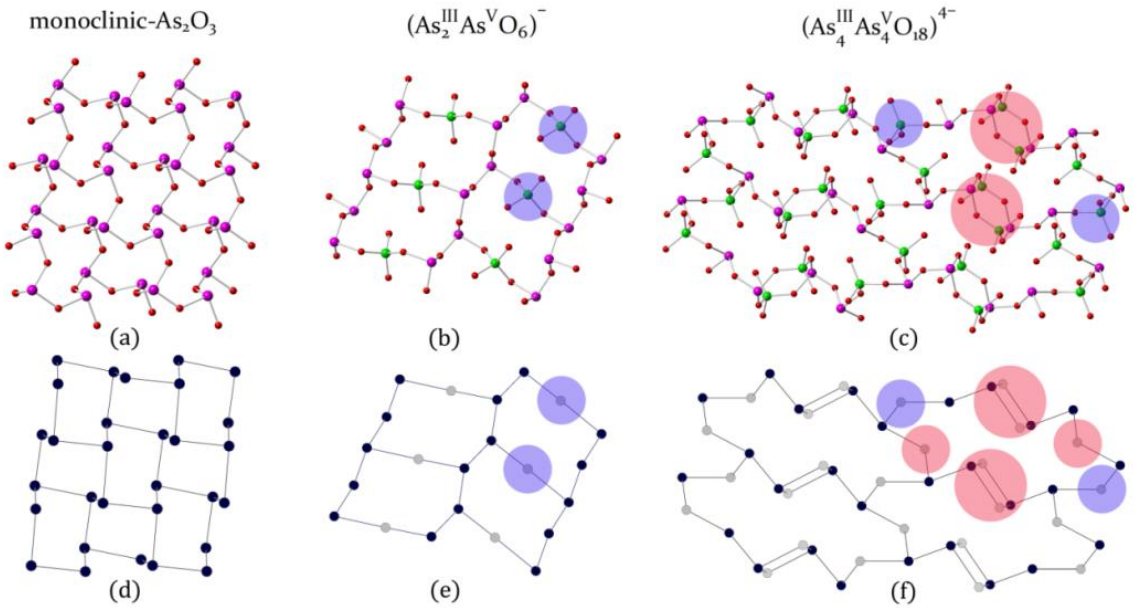

***Figure 7.4**: The arsenic layers (a–c) and their graph representation (d–f) in the crystal structures of monoclinic-As_2O_3, $As^{III}_2As^{V}O_5(OH)$, and $Th(As^{III}_4As^{V}_4O_{18})$. The color scheme is the same as in Fig. 7.3. Blue and red transparent circles marks nodes and corresponding AsO_4 tetrahedra and $As^{III}_2As^{V}_2O_9$ ring fragments that are implemented in the edges of initial As_2O_3 layer on each step in the (d) – (e) – (f) series.*

7.1.7 Raman Spectroscopy

The Raman spectrum (Fig. 7.5) was collected from the single crystal of $Th(As^{III}_4As^{V}_4O_{18})$. Band assignment shows presence of three groups of bands in the spectrum: low-frequency (100–300 cm^{-1}), medium-frequency (300–600 cm^{-1}), and high-frequency (700–950 cm^{-1}). Peaks of these groups were assigned as the crystal lattice, bending, and stretching vibrations for the low-, medium-, and high-frequency regions, respectively (Table 7.4).

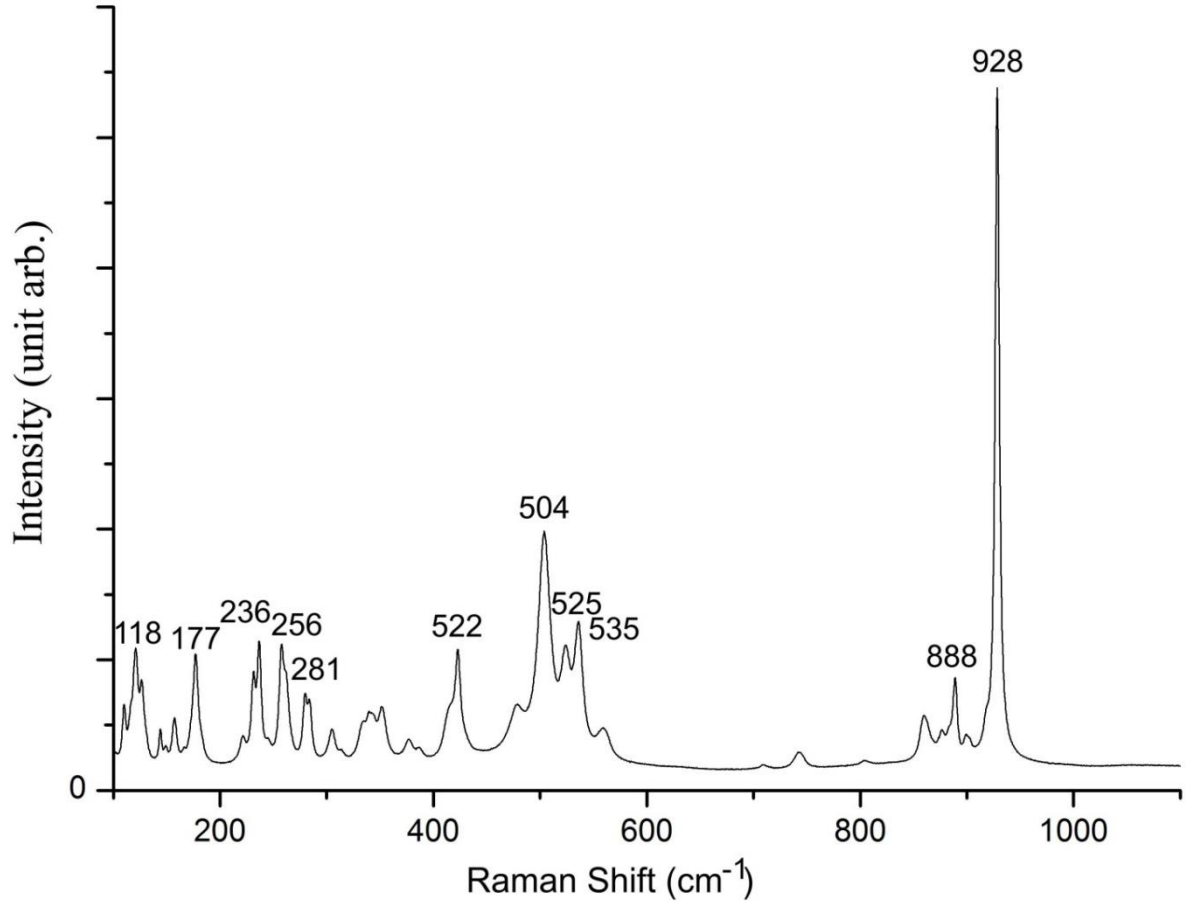

Figure 7.5: *The Raman spectra of Raman spectrum of* $Th(As^{III}_4As^{V}_4O_{18})$.

Table 7.4: Assignment of selected Raman bands corresponding to AsO_3 and AsO_4 vibrational modes

This study, cm^{-1}	AsO_3			AsO_4		
	Ref. data, cm^{-1}	Assignment	Ref.	Ref. data, cm^{-1}	Assignment	Ref.
928				915	υ_3	6
899	898	υ_3	5	902	υ_3	7
888	885	υ_3	5	888	υ_3	8
875	870	υ_1	5	877	υ_1 and υ_3	9
860				857	υ_1	10
745				763	υ_1 and υ_3	9
557	550	υ_4	5	556	υ_1	6
535				536	υ_4	9
525				525	υ_4	9
504				508	υ_4	9
480	483	υ_4	5	491	υ_2	10
422	418	υ_2	5	430	υ_2	10
367	369	υ_2	5	365	υ_2	10
353				348	υ_2	9
339				330	υ_2	10
305				308	υ_2	9
	Assignment				Ref.	
281, 256, 235, 232, 220, 157, 177, 143, 126, 118, 109	Lattice modes				8	
*υ_1 – symmetric stretching vibrations; υ_2 – symmetric bending vibrations; υ_3 – antisymmetric stretching vibrations; υ_4 – out-of-plane bending vibrations.						

7.1.8 Conclusions

To conclude, the first synthetic mixed-valent oxo-As(III)/As(V) Th compound using high temperature/high pressure conditions was obtained. The crystal structure of the compound is based on layers of AsO_4/AsO_3 polyhedra and Th cations. The underlying net of the layers has

hcb topological type and is isoreticular with those of previously reported monoclinic-As_2O_3 and $As^{III}_2As^{V}O_5(OH)$. The Raman spectrum of the compound consists of three regions corresponding to crystal lattice and bending and stretching vibrations of AsO_3/ AsO_4 groups.

7.2 $ATh_2(AsO_4)_3$(A= K, Rb, Cs, Ag), $LiTh_2(PO_4)_3$ and $BU^{IV}_2(PO_4)_3$ (B= Rb, Cs): Formation, Structures and Properties

7.2.1 Introduction

A series of alkaline thorium arsenates and phosphates, $ATh_2(AsO_4)_3$(A= K, Rb, Cs, Ag) and $LiTh_2(PO_4)_3$, have been synthesized by the high temperature solid state reaction. Other two alkaline uranium phosphate compounds $BU^{IV}_2(PO_4)_3$ (B= Rb, Cs) have been synthesized by the HT-HP solid state reaction. $ATh_2(AsO_4)_3$(A= K, Rb, Cs, Ag) and $BU^{IV}_2(PO_4)_3$ (B= Rb, Cs) phases are isostructural with the known thorium phosphate compounds, $ATh_2(PO_4)_3$(A= Na[24, 25], K[26], Rb[27], Cs[27]). The structure of $LiTh_2(PO_4)_3$ is quite similar to the others, but the analysis of the coordination environment of the anions phosphorus shows the difference.

7.2.2 Synthesis

All of the thorium bearing compounds obtained in this section have been synthesized by high temperature solid state reaction method. The synthesis followed the procedure depicted in Fig. 2.2 and the information about the reactants are given in Table 7.5. The chemicals used were of analytical reagent grade and without any other further purification. The reactants were thoroughly ground together with their appropriate ratios and loaded into a platinum crucible.

Table 7.5: The experimental reactants used in this chapter

Compound Name	**Purity**	**Company**
Thorium nitrate ($Th(NO_3)_4{\cdot}5H_2O$)	- -	Merck
Ammonium dihydrogen arsenate ($NH_4H_2AsO_4$)	98%	Alfa-Aesar
Lithium nitrate ($LiNO_3$)	99.9%	Alfa-Aesar
Sodium nitrate ($NaNO_3$)	99.9%	Alfa-Aesar
Potassium nitrate (KNO_3)	99.9%	Alfa-Aesar
Rubidium nitrate ($RbNO_3$)	99.9%	Alfa-Aesar
Cesium nitrate ($CsNO_3$)	99.9%	Alfa-Aesar

Table 7.6: Synthesis data and crystal profile of $ATh_2(AsO_4)_3$(A= K, Rb, Cs, Ag) and $LiTh_2(PO_4)_3$

Compound	**Formula**	**Th: As^V: A^I**	**Aimed temperature (K)**	**Colour/shape**
KThAsO-2	$KTh_2(AsO_4)_3$	1:10:3	1143	colorless block-like crystals
RbThAsO-2	$RbTh_2(AsO_4)_3$	1:10:1	1223	
CsThAsO-2	$CsTh_2(AsO_4)_3$	1:10:1	1273	
AgThAsO-1	$AgTh_2(AsO_4)_3$	1:10:1	1223	
Compound	**Formula**	**Th: P^V: Li**	**Aimed temperature (K)**	**Colour/shape**
LiThPO-2	$LiTh_2(PO_4)_3$	1:5:6	1273	strip-like crystal

After the reactants were thoroughly ground together with their appropriate ratios and loaded into a platinum crucible. The furnace was ramped up to the aimed temperature by the heating rate of 873 K/h, left there for 2 hours and then slowly cooled down to room temperature at a rate of 5 K/h. The titled crystals were isolated from the reaction product.

For the other two uranium phosphates (Table 7.7), which were obtained under HT-HP conditions, the synthesis procedure was as described in the section 2.1.3 . The chemicals used were of analytical reagent grade and without any other further purification, except of UO_3, which was taking as the initial reactant instead of $UO_2(NO_3)_2{\cdot}6H_2O$ and it was prepared by heating up the $UO_2(NO_3)_2{\cdot}6H_2O$ powder to 400 ^oC lasting for 4 hours. The experiment was performed at a pressure of 3 GPa, and the cooling rate is 0.25°C/min. The titled crystals were isolated from the reaction product.

Table 7.7: Synthesis data and crystal profile of $BU^{IV}_2(PO_4)_3$ (B= Rb, Cs)

Compound	**Formula**	**UO_3: P^V: A^I**	**Aimed temperature (K)**	**Colour/shape**
RbUPO-1	$RbU^{IV}_2(PO_4)_3$	1: 16: 2	1173	Green block like crystal
CsUPO-1	$CsU^{IV}_2(PO_4)_3$	1: 16: 2	1173	

7.2.3 Single Crystal X-ray Diffraction

The data was collected and refined following the details mentioned in section 2.4 . All the structures were checked for possible higher symmetry using the ADDSYM algorithm from the program PLATON[28], but none were found. Relevant crystallographic data and details of the experimental conditions for all the three crystals are summarized in Table 7.8.

Table 7.8: Crystallographic data for the titled structures

Compound	KThAsO-2	RbThAsO-2	CsThAsO-2	AgThAsO-2	LiThPO-2	RbUPO-1	CsUPO-1
space group	*C* 2/*c*	*C* 2/*c*	*C* 2/*c*	*C* 2/*c*	*C* 2/*c*	*C* 2/*c*	*C* 2/*c*
a /Å	18.2277(4)	18.3800(4)	18.5458(9)	18.0310(11)	17.3849(4)	17.5977(5)	17.5946(6)
b /Å	7.0590(2)	7.0925(2)	7.1489(3)	7.0223(5)	6.79667(17)	6.80599(18)	6.8052(3)
c /Å	8.2211(2)	8.2415(2)	8.2649(4)	8.2360(5)	8.13405(18)	8.0517(2)	8.0558(3)
β /°	100.364(2)	100.952(2)	101.677(4)	99.377(6)	101.086(2)	102.567(3)	102.517(4)
V /Å^3	1040.55(5)	1054.80(5)	1073.10(9)	1028.90(11)	943.18(4)	941.25(5)	941.64(6)
D_{calc} /g/cm^3	5.872	6.085	3.527	2.781	5.323	5.973	6.196
Z	4	4	5	4	4	4	4
λ /Å	0.71073	0.71073	0.71073	0.71073	0.71073	0.71073	0.71073
F(000)	1576	1648	930	712	1296	1448	1490
R1	0.0268	0.0235	0.0250	0.0470	0.0206	0.0453	0.0359
wR2	0.0548	0.0545	0.0883	0.1176	0.0660	0.1262	0.1129

$R(F) = \Sigma||F_o| - |F_c||/\Sigma|F_o|$. $wR(F_o^2) = [\Sigma w(F_o^2 - F_c^2)^2/\Sigma w(F_o^2)^2]^{1/2}$.

7.2.4 Bond Valence Analysis

Bond-valence sums (BVS) for all atom positions in $ATh_2(AsO_4)_3$(A= K, Rb, Cs, Ag), $LiTh_2(PO_4)_3$ and $BU^{IV}_2(PO_4)_3$ (B= Rb, Cs) phases were calculated, and the results are given in Table 7.9 -7.14.

Table 7.9: Bond-valence analysis for $KTh_2(AsO_4)_3$

	Th1	As1*	As2	K1*	Σ
O1	0.572		1.343	$0.194^{\times 2\downarrow}$	2.11
O2	0.454		1.205		2.06
	0.397				
O3	0.468		1.170		1.98
	0.342				
O4	0.427	$1.235^{\times 2\downarrow}$		$0.132^{\times 2\downarrow}$	2.03
	0.241				
O5	0.594		1.343		1.94
O6	0.441	$1.300^{\times 2\downarrow}$		$0.086^{\times 2\downarrow}$	1.90
				$0.077^{\times 2\downarrow}$	
Σ	3.93	5.07	5.07	0.65	

* stands for the atom site occupation is 50%.

Table 7.10: Bond-valence analysis for $RbTh_2(AsO_4)_3$

	Th1	As1*	As2	Rb1*	Σ
O1	0.579		1.346	$0.216^{\times 2\downarrow}$	2.14
O2	0.448	$1.208^{\times 2\downarrow}$	1.160		1.95
	0.346				
O3	0.405			$0.157^{\times 2\downarrow}$	2.01
	0.242				
O4	0.457		1.189		2.04
	0.396				
O5	0.448	$1.296^{\times 2\downarrow}$		$0.124^{\times 2\downarrow}$	1.97
				$0.097^{\times 2\downarrow}$	
O6	0.587		1.328	$0.026^{\times 2\downarrow}$	1.94
Σ	3.91	5.01	5.02	1.21	

* stands for the atom site occupation is 50%.

Table 7.11: Bond-valence analysis for $CsTh_2(AsO_4)_3$

	Th1	As1*	As2	Cs1*	Σ
O1	0.423		1.167		1.94
	0.346				
O2	0.587		1.325	$0.248^{\times 2\downarrow}$	2.16
O3	0.378	$1.189^{\times 2\downarrow}$		$0.192^{\times 2\downarrow}$	2.01
	0.249				
O4	0.494	$1.251^{\times 2\downarrow}$		$0.121^{\times 2\downarrow}$	2.05
				$0.180^{\times 2\downarrow}$	
O5	0.447		1.199		2.05
	0.401				
O6	0.573		1.339	$0.037^{\times 2\downarrow}$	1.95
Σ	3.90	4.88	5.03	1.48	

* stands for the atom site occupation is 50%.

Table 7.12: Bond-valence analysis for $AgTh_2(AsO_4)_3$

	Th1	Th2	As1	As2	As3	Ag1	Σ
O1		0.429		1.231			2.06
		0.396					
O2	0.465	0.250	1.199				2.07
	0.407						
O3	0.441	0.385		1.167			1.99
O4		0.491	1.300			0.123	1.91
O5	0.310	0.478	1.335				2.12
O6	0.594			1.300			1.89
O7	0.661			1.372			2.03
O8		0.578	1.335				1.91
O9	0.533				1.135		1.94
	0.271						
O10		0.385			1.529		2.16
O11*						0.870	0.87
O12		0.505			1.300	0.130	1.93
O13	0.407				1.410	0.185	2.00
Σ	4.09	3.90	5.17	5.07	5.37	1.31	

* stands for the atom site occupation is 20%.

Table 7.13: Bond-valence analysis for $RbU^{IV}_2(PO_4)_3$

	U1	P1*	P2	Rb1*	Σ
O1	0.573		1.317	$0.038^{\times 2\downarrow}$	1.93
O2	0.556		1.238	$0.232^{\times 2\downarrow}$	2.03
O3	0.442		1.114		1.94
	0.384				
O4	0.460	$1.279^{\times 2\downarrow}$		$0.085^{\times 2\downarrow}$	2.02
				$0.192^{\times 2\downarrow}$	
O5	0.366	$1.157^{\times 2\downarrow}$		$0.209^{\times 2\downarrow}$	1.99
	0.259				
O6	0.357		1.114		1.90
Σ	3.83	4.87	4.78	1.48	

* stands for the atom site occupation is 50%.

Table 7.14: Bond-valence analysis for $CsU^{IV}_2(PO_4)_3$

	U1	P1*	P2	Cs1*	Σ
O1	0.543		1.300	$0.339^{\times 2\downarrow}$	2.18
O2	0.408		1.173		1.94
	0.360				
O3	0.374	$1.151^{\times 2\downarrow}$		$0.232^{\times 2\downarrow}$	2.02
	0.258				
O4	0.430		1.099		1.92
	0.386				
O5	0.478	$1.225^{\times 2\downarrow}$		$0.112^{\times 2\downarrow}$	2.19
				$0.378^{\times 2\downarrow}$	
O6	0.576		1.289	$0.053^{\times 2\downarrow}$	1.92
Σ	3.81	4.75	4.86	2.12	

* stands for the atom site occupation is 50%.

7.2.3 Results and Discussion

All the titled compounds in this section adopted the same chemical formula. But they crystalized in two different space groups. When comparing their structures, three factors were taken into consideration, i.e. coordination environment of actinides; coordination environment of anions P or As; atom size of the cation. In this section, as shown in Fig.7.6, the bidentate $\boldsymbol{T}O_4$(***T***= As or P) are located at the transposition to the actinides(Th, U).

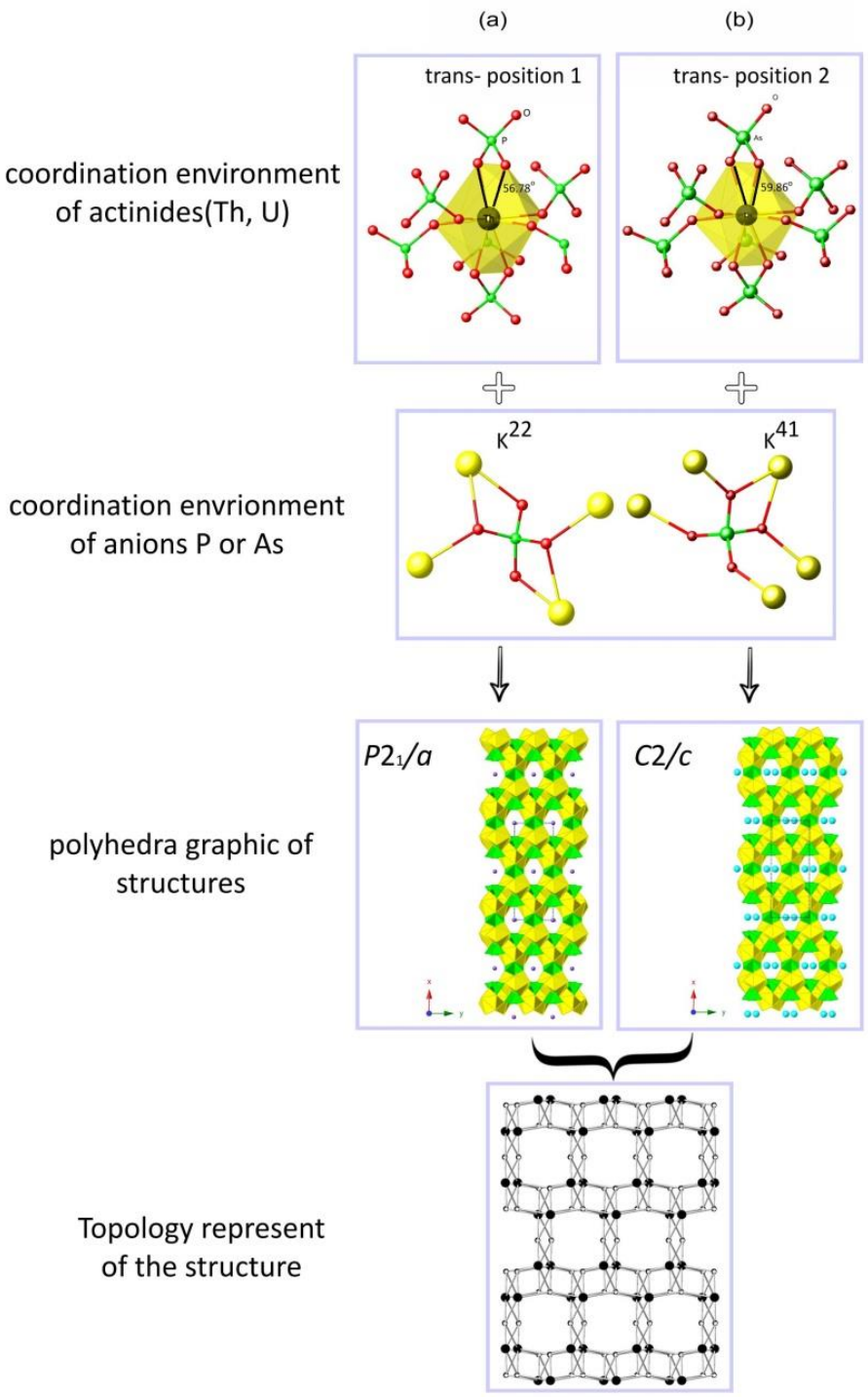

***Figure 7.6**: The comparison of the structure of (a) $LiTh_2(PO_4)_3$ (b) $ATh_2(AsO_4)_3$(A= K, Rb, Cs, Ag) and $BU^{IV}_2(PO_4)_3$ (B= Rb, Cs). ThO_8, $As(P)O_4$ coordination polyhedra are yellow and green, respectively, and O atoms are red; black dot is U atom, white dot is As(P) atom.*

The difference between the trans-position 1 and trans-position 2 is the angle of O-Th(U)- O, which is 56.78° and 59.86°, respectively. For the anions P(As), all of them adopted K^{22} and K^{41} geometry of the environment. While, the atom size of Li, compared to the other cations mentioned in this section, is obviously much smaller. So this resulted in the two different space groups, $P2_1/a$ and $C2/c$, while the topology of those two structures is same.

As $ATh_2(AsO_4)_3$(A= K, Rb, Cs, Ag) and $BU^{IV}_2(PO_4)_3$ (B= Rb, Cs) are isostructural, here only $CsTh_2(AsO_4)_3$ is discussed. For $CsTh_2(AsO_4)_3$, there are two independent crystallographic positions for the As atoms with site-symmetry C2 and C1 for As1 and As2, respectively. For $LiTh_2(PO_4)_3$, there are two independent crystallographic positions for the P atoms with site-symmetry C2 and C1 for P1 and P2, respectively. The crystallographic position for Th in both compounds is C1. The difference is the crystallographic position of the Cs and the Li cation, which is C2 and Ci, respectively.

7.2.4 Conclusions

All the titled compounds in this section adopted the same topology type. $ATh_2(PO_4)_3$ is a quite stable structural type, and the tetra- coordinated $\boldsymbol{T}O_4$(***T***= P or As) group (K^{22}, K^{41}) resulted in this 3D framework. Regarding the coordination chemistry, phosphate shows great similarity to arsenate, and Th^{IV} can be taken as the analogue of U^{IV}. The main driving force of the structural transformation in the $ATh_2(PO_4)_3$ family is the cation size, which makes this class behave very similar to that of $A_2Th(As/PO_4)_2$ (chapter 4 and 5).

7.3 $ATh(As_3O_{10})$ (A= Rb, Cs) and $RbTh(P_3O_{10})$: Formation, Structures

7.3.1 Introduction

Three alkaline thorium arsenates and phosphates with the same chemical formula, $ATh(As_3O_{10})$ (A= Rb, Cs) and $RbTh(P_3O_{10})$, have been synthesized. $CsTh(As_3O_{10})$ was synthesized from the HT-HP solid state reaction and the other two were obtained from the high temperature solid state reaction. There is only one known compound $KTh(P_3O_{10})$[28] possessing the same formula, which is isostructural to $RbTh(P_3O_{10})$. The arsenates $ATh(As_3O_{10})$ (A= Rb, Cs) crystalize in the same structural type which is different compared to the phosphates.

7.3.2 Synthesis

The information about the reactants was given in the Table 7.15 and the chemicals used were of analytical reagent grade and without any other further purification. For $RbTh(\boldsymbol{T}_3O_{10})$ (***T***= P, As), the synthesis following the Fig. 2.2 (**HT**) processes, the reactants were

thoroughly ground together with their appropriate ratios and loaded into a platinum crucible. (Table 7.16)

Table 7.15: The Experimental Reactants used in this chapter

Compound Name	**Purity**	**Company**
Thorium nitrate ($Th(NO_3)_4{\cdot}5H_2O$)	- -	Merck
Ammonium dihydrogen arsenate ($NH_4H_2AsO_4$)	98%	Alfa-Aesar
Ammonium dihydrogen phosphate ($NH_4H_2PO_4$)	98%	Alfa-Aesar
Rubidium nitrate ($RbNO_3$)	99.9%	Alfa-Aesar
Cesium nitrate ($CsNO_3$)	99.9%	Alfa-Aesar
Arsenic(3+) oxide (As_2O_3)	97%	Alfa-Aesar

Table 7.16: Synthesis data and crystal profile of $RbTh(\boldsymbol{T}_3O_{10})$ (***T***= P, As)

Compound	**Formula**	**Th: P^V: Rb**	**Aimed temperature (K)**	**Colour/shape**
RbThPO-2	$RbTh(P_3O_{10})$	1:10:8	1323	colorless block-like crystals
Compound	**Formula**	**Th: As^{III}: A^I**	**Aimed temperature (K)**	
RbThAsO-3	$RbTh(As_3O_{10})$	2:2:7	1023	

The platinum crucible then was transferred into the furnace. The furnace was ramped up to the aimed temperature by the heating rate of 873 K/h, left there for 2 hours and then slowly cooled down to room temperature at a rate of 5 K/h. The titled crystals were isolated from the reaction product.

For $CsTh(As_3O_{10})$, which was obtained under HT-HP conditions, the synthesis procedure following section 2.1.3. The used chemicals were of analytical reagent grade and without any other further purification. The experiment was performed at a pressure of 3 GPa, and the cooling rate is 0.435°C/min. The titled crystals will be isolated from the reaction product. (Table 7.10)

Table 7.17: Synthesis data and crystal profile of $CsTh(As_3O_{10})$

Compound	**Formula**	**Th: As^V: Cs**	**Aimed temperature (K)**	**Colour/shape**
CsThAsO-3	$CsTh(As_3O_{10})$	1: 6: 2	1173	colorless block-like crystals

7.3.3 Single Crystal X-ray Diffraction

The data was collected and refined following the details mentioned in section 2.4. All the structures were checked for possible higher symmetry using the ADDSYM algorithm from the program PLATON[28], but none were found. Relevant crystallographic data and details of the experimental conditions for all the three crystals are summarized in Table 7.18.

Table 7.18: Crystallographic data for the titled structures

Compound	$RbTh(P_3O_{10})$	$RbTh(As_3O_{10})$	$CsTh(As_3O_{10})$
space group	$P2_12_12_1$	*Fddd*	*Fddd*
a /Å	8.2973(3)	9.3250(6)	9.3874(4)
b /Å	10.0070(3)	19.8087(16)	19.9149(9)
c /Å	10.3128(3)	20.3153(15)	20.4069(9)
V /Å^3	856.29(4)	3752.6(5)	1073.10(9)
D_{calc} /g/cm^3	4.425	4.972	5.221
Z	4	16	16
λ /Å	0.71073	0.71073	0.71073
F(000)	1008	4896	5184
R1	0.0416	0.0444	0.0264
wR2	0.1201	0.0820	0.0668

$R(F) = \Sigma||F_o| - |F_c||/\Sigma|F_o|$. $wR(F_o^2) = [\Sigma w(F_o^2 - F_c^2)^2/\Sigma w(F_o^2)^2]^{1/2}$.

7.3.4 Bond Valence Analysis

Bond-valence sums (BVS) for all atom positions in $ATh_2(AsO_4)_3$(A= K, Rb, Cs, Ag), $LiTh_2(PO_4)_3$ and $BU^{IV}_2(PO_4)_3$ (B= Rb, Cs) phases were calculated, and the results are given in Table 7.19 -7.21.

Table 7.19: Bond-valence analysis for $RbTh(P_3O_{10})$

	Th1	P1	P2	P3	Rb1	Σ
O1	0.595	1.303			0.163	2.06
O2	0.505		1.300		0.099	1.97
					0.062	
O3	0.561		1.300		0.154	2.02
O4	0.513	1.321			0.090	1.92
O5			0.920	0.995		1.91
O6	0.489			1.357	0.115	1.96
O7	0.382			1.346	0.096	1.86
O8		0.955		1.093	0.086	2.14
O9	0.592	1.303			0.102	2.00
O10	0.610		1.255		0.028	1.89
Σ	4.25	4.88	4.78	4.79	0.97	

Table 7.20: Bond-valence analysis for $RbTh_2(AsO_4)_3$

	Th1	As1*	As2	Rb1*	Σ
O1	$0.422^{\times 2\downarrow}$	$1.413^{\times 2\downarrow}$		$0.114^{\times 2\downarrow}$	1.95
O2		$1.099^{\times 2\downarrow}$	0.965	$0.093^{\times 2\downarrow}$	2.16
O3	$0.546^{\times 2\downarrow}$		1.372		1.92
O4	$0.528^{\times 2\downarrow}$		1.339	$0.082^{\times 2\downarrow}$	1.87
O5	$0.598^{\times 2\downarrow}$		1.325	$0.051^{\times 2\downarrow}$	1.92
Σ	4.19	5.03	5.00	0.68	

* stands for the atom site occupation is 50%.

Table 7.21: Bond-valence analysis for $CsTh_2(AsO_4)_3$

	Th1*	As1*	As2	Cs1*	Σ
O1		$1.096^{\times 2\downarrow}$	0.932	$0.024^{\times 2\downarrow}$	2.18
				$0.128^{\times 2\downarrow}$	
O2	$0.550^{\times 2\downarrow}$		1.321	$0.111^{\times 2\downarrow}$	1.98
O3	$0.600^{\times 2\downarrow}$		1.321	$0.061^{\times 2\downarrow}$	1.98
O4	$0.516^{\times 2\downarrow}$		1.368		1.88
O5	$0.428^{\times 2\downarrow}$	$1.391^{\times 2\downarrow}$		$0.157^{\times 2\downarrow}$	1.98
Σ	4.19	4.97	4.94	0.96	

* stands for the atom site occupation is 50%.

7.3.5 Results and Discussion

All the titled compounds in this section adopted the same chemical formula, but $ATh(As_3O_{10})$ (A= Rb, Cs) and $RbTh(P_3O_{10})$ have different topology types. In this section, as shown in Fig. 7.7, two bidentate $\boldsymbol{T}O_4$(***T***= As or P) are located at the cis- position to the Th atom. The difference between the cis-position 1 and cis-position 2 is shown in the Fig. 7.7, the geometry of the marked circle parts are different.

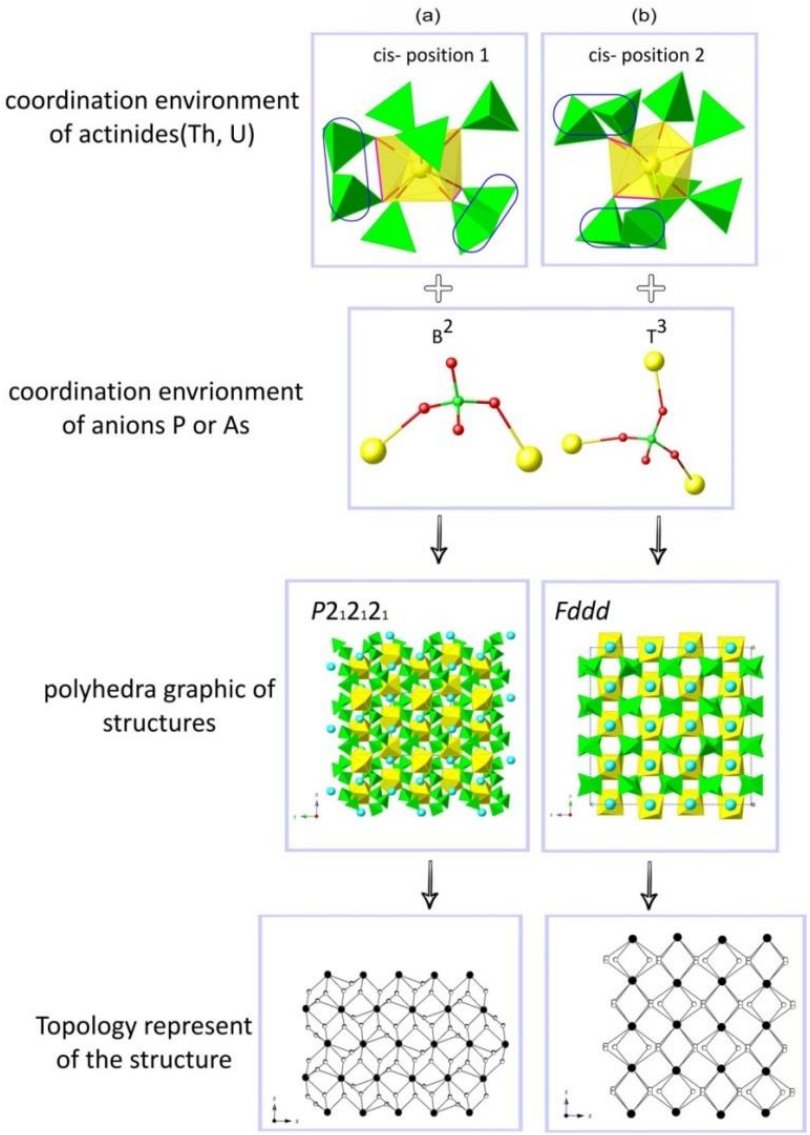

Figure 7.7: The comparison of the structure of (a) $RbTh(P_3O_{10})$ (b) $ATh(As_3O_{10})$ (A= Rb, Cs). ThO_8, $As(P)O_4$ coordination polyhedra are yellow and green, respectively, and O atoms are red; black dot is U atom, white dot is As(P) atom.

Besides, the coordination types of the P(As) anions adopted B^2 and T^3 geometries. As $RbTh(As_3O_{10})$ and $CsTh(As_3O_{10})$ are isostructural, here only $CsTh(As_3O_{10})$ is discussed. For $CsTh(As_3O_{10})$, there are two independent crystallographic positions for the As atoms with site-symmetry C2 and C1 for As1 and As2, respectively. For $RbTh(P_3O_{10})$, the As atoms only adopt one independent crystallographic position with site-symmetry C1. The bond length of As-O in $CsTh(As_3O_{10})$ ranges from 1.645(4) to 1.664(4) Å and 1.733(5) to 1.793(5) Å for terminal and bridging O atoms, respectively. Meanwhile, the bond lengths of P-O in $RbTh(P_3O_{10})$ range from 1.491(8) to 1.525(9) Å and from 1.571(9) to 1.635(8) Å for terminal and bridging O atoms, respectively. Owing to the As1 atom with C2 site- symmetry, the As_3O_{10} chain has a higher symmetry compared to the P_3O_{10} chain. For the Cs and Th in $CsTh(As_3O_{10})$, all of them adopted the C2 site-symmetry, while for that in $RbTh(P_3O_{10})$, all of the Cs and Th adopted the C1 site-symmetry. So $CsTh(As_3O_{10})$ crystalized in a higher symmetry space group *C*2/*c*, and $RbTh(P_3O_{10})$ crystalized in a lower symmetry space group $P2_1/a$.

7.3.6 Conclusions

The main driving force of structural transformation of this class is the coordination environment of P(As) anions. The combination of tetra-coordinated $\boldsymbol{T}O_4$(***T***= P or As) group (B^2, T^3) with cis-position 1 and cis-position 2 resulted in space group $P2_12_12_1$ and *Fddd*, respectively. The symmetry of cis-position 2 is higher than that of cis-position 2. This makes the structure of $ATh(As_3O_{10})$ (A= Rb, Cs) own a higher symmetry compared to $RbTh(P_3O_{10})$.

7.4 References

1. D. R. Lide, *CRC handbook of chemistry and physics: a ready-reference book of chemical and physical data*. CRC Press: Boca Raton, 2005.
2. P. Bénard; V. Brandel; N. Dacheux; S. Jaulmes; S. Launay; C. Lindecker; M. Genet; D. Louër; M. Quarton, *Chem. Mater.,* **1996,** *8*, 181-188.
3. N. Dacheux; R. Podor; B. Chassigneux; V. Brandel; M. Genet, *J. Alloys Compd.,* **1998**, 271-273, 236-239.
4. N. Dacheux; N. Clavier; G. Wallez; V. Brandel; J. Emery; M. Quarton; M. Genet, *Mater. Res. Bull.,* **2005,** *40*, 2225-2242.
5. E.V. Alekseev; S.V. Krivovichev; T. Malcherek; W. Depmeier, *J. Solid State Chem.,* **2008,** *181*, 3010-3015.
6. E.V. Alekseev ; S.V. Krivovichev ; W. Depmeier, *J. Solid State Chem.,* **2009,** *182*, 2977-2984.
7. E. M. Villa; S. Wang; E. V. Alekseev; W. Depmeier; T. E. Albrecht-Schmitt, *Eur. J. Inorg. Chem.,* **2011,** *2011*, 3749-3754.
8. S.V. Krivovichev; P.C. Burns; I.G. Tananaev, *Structural Chemistry of Inorganic Actinide Compounds*. Elsevier: Amsterdam, 2007.
9. V. Brandel; N. J. Dacheux, *Solid State Chem.,* **2004,** *177*, 4755-4767.
10. V. Brandel; N. Dacheux, *J. Solid State Chem.,* **2004,** *177*, 4743-4754.
11. E.M. Villa; C.J. Marr; D. Juan; E.V. Alekseev; W. Depmeier; T.E. Albrecht-Schmitt, *Inorg. Chem.,* **2013,** *52*, 965-973.
12. E.M. Villa; C.J. Marr; L.J. Jouffret; E.V. Alekseev; W. Depmeier; T.E. Albrecht-Schmitt, *Inorg. Chem.,* **2012,** *51*, 6548-6558.
13. T. Araki; P. B. Moore, *Am. Mineral.,* **1981,** *66*, 1263-1273.
14. P. B. Moore; T. Araki, *Am. Mineral.,* **1978,** *63*, 150-159.
15. P. B. Moore, *Am. Mineral.,* **1970,** *55*, 2023-2037.
16. H. Effenberger; F. Pertlik, *J. Solid State Chem.,* **1987,** *70*, 219-224.
17. D. Bodenstein; A. Brehm; P.G. Jones; E. Schwarzmann; G.M.Z. Sheldrick, *Naturforsch. B Chem. Sci.,* **1982,** *37*, 138-140.
18. P.G. Jones; W. Beesk; G.M. Sheldrick; E. Sharman, *Acta Crystallogr. Sect. B,* **1980,** *36*, 439-440.
19. B. Xiao; T.M. Gesing; P. Kegler; G. Modolo; D. Bosbach; H. Schlenz; E.V. Suleimanov; E.V. Alekseev, *Inorg. Chem.,* **2014,** *53*, 3088-3098.
20. V.A. Blatov; V.N. Serezhkin, *Russ. J. Inorg. Chem.,* **2000,** *45*, S105-S222.
21. D.V. Pushkin; V.N. Serezhkin; Y.A. Buslaev, *Russ. J. Inorg. Chem.,* **2000,** *45*, 483-488.
22. V.A. Blatov; A. P. Shevchenko; V.N. Serezhkin, *J. Appl. Crystallogr.,* **2000,** *33*, 1193-1193.

23. E. V. Alexandrov; V. A. Blatov; A. V. Kochetkov; D. M. Proserpio, *CrystEngComm,* **2011,** *13*, 3947.
24. V.B. Kalinin; A.M. Golubev; V.A. Tafeenko; S.Yu. Stefanovich, *Kristallografiya,* **1992,** *37*, 1220-1226.
25. B. Matkovic; B. Kojic-Prodic; M. Sljukic; M. Topic; R.D. Willett; F. Pullen, *Inorg. Chim. Acta,* **1970,** *4*, 571-576.
26. B. Matkovic; B. Prodic; M. Sljukic, *Croat. Chem. Acta* **1968,** *40*, 147-161.
27. K. Krishnan; S.K. Sali; K.D. Singh Mudher, *J. Alloy. Compd.,* **2006,** *414*, 310-316.
28. Z. Ruzic Toros; B. Kojic-Prodic; R. Liminga; S. Popovic, *Inorganica Chimica Acta* **1974,** *8*, 273-278.

Chapter 8 CONCLUSIONS AND OUTLOOK

In this work, the chemical and structural behaviour of U and Th in phosphorus(V) and arsenic(III/V) oxo-systems was studied. Using hydrothermal reactions, high temperature solid state reactions and high temperature high pressure solid state reactions, a large family of novel Th and U arsenates, arsenites and phosphates have been synthesized and studied. Obtained phases were analyzed structurally, spectroscopically and characterized by SEM/EDX, HT PXRD and DSC.

The results of performed research significantly improved the understanding of An(IV) oxo-phosphate and oxo-arsenate formation, their structural properties and thermal behavior. Based on the results of the study, transuranic(IV) elements behavior in similar conditions including technological and natural processes involving phosphorus and arsenic can be predicted. Of course, additional experiments with Np(IV) and Pu(IV) are necessary to confirm this assumption. Generally, based on the obtained results, two main reasons of structural evolution and structure type stability fields for the family of Th and U phosphates and arsenates can be proposed. These are firstly the size of the alkali cations and secondly the local environment of the $\boldsymbol{T}O_4$ tetrahedra and the nature of **T** element. The analysis of the data shows that the first aspect has the most influence. According to the each chapter, the following points were summarized:

1. **RbUAs-1**, **2**, and **3** have been synthesized, and all of those three structures are based up on the 2D layer motif, owing to the insufficient valence unit of the uranyl ion UO_2^{2+}. By analysing the layers, it is supposed that the geometric diversity rises from the re-orientable $(AsO_2(OH)_2)^-$ groups in the layers. The presence of the U and Rb is a second factor in fine topology orientation in this group of compounds.
2. The novel $A^I_2Th(\boldsymbol{T}O_4)_2$ (A^I= Li, Na, K, Rb, Cs; ***T***= As, P) family have been synthesized. According to the analysis of structural evolution in this family, it is supposed that the cation (A^I) size is the main driving force in structures formation and evolution. The coordination environment of the anionic groups ($\boldsymbol{T}O_4$) and Th also play an important role. The relationship between those factors and the structure evolution was graphically concluded.
3. The single crystals of $ATh_2(AsO_4)_3$(A= K, Rb, Cs, Ag), $LiTh_2(PO_4)_3$ and $BU^{IV}_2(PO_4)_3$ (B= Rb, Cs) have been synthesized and studied. The structures of these compounds adopted a similar $ATh_2(PO_4)_3$ topology type which is a well-known and very stable structure type. The coordination chemistry of phosphate is similar to that of arsenate, and here Th(IV)

and U(IV) have same coordination environment. Similarly to $A^{I}_2Th(\boldsymbol{T}O_4)_2$ (A^{I}= Li, Na, K, Rb, Cs; ***T***= As, P) family, a size of the alkali cation plays a crucial role in symmetry change in $ATh_2(AsO_4)_3$ group of compounds.

4. Single crystals of $U(PO_3)_4$, of a mixed U^{4+}/Nd^{3+} polymetaphosphate "$(U_{0.62}Nd_{0.38})(PO_3)_4$", and of two new tetraphosphates, $Th(P_4O_{12})$ and $U(P_4O_{12})$, have been synthesized and studied. The periodicity of polymeric $(PO_3)_n^{n-}$ chains in $U(PO_3)_4$ and "$(U_{0.62}Nd_{0.38})(PO_3)_4$" is different. Interestingly, the incorporation of the Nd^{3+} into the U^{4+} in the metaphosphate significantly changes the coordination of the metal atom. A structural classification of the family of U and Th polyphosphates was also given.
5. The polyarsenates and polyphosphates $ATh(As_3O_{10})$ (A= Rb, Cs) and $RbTh(P_3O_{10})$ have been obtained and studied. The difference of the space group of these compounds arises from the varities of the coordination environment of the Th atom.
6. The chemistry of actinides under high pressures and temperatures has not yet been investigated. Under high pressure, the first synthetic mixed-valent oxo-As(III)/As(V) Th compound has been obtained. The key factor to get this compound is that a minimum amount of arsenic(III) must be guaranteed, owing to the presence of air and nitrate anions which will oxidize the As^{III} to As^{V}.

Appendix: PAPERS AND CONFERENCES

1. Journal papers:

1. Na Yu, Vladislav V. Klepov, Eric M. Villab, Dirk Bosbach, Evgeny V. Suleimanov, Wulf Depmeier, Thomas E. Albrecht-Schmitt, Evgeny V. Alekseev. (**2014**) Topologically identical, but geometrically isomeric layers in hydrous α-, β- $Rb[UO_2(AsO_3OH)(AsO_2(OH)_2)]\cdot H_2O$ and anhydrous $Rb[UO_2(AsO_3OH)(AsO_2(OH)_2)]\cdot H_2O$. ***Journal of Solid State Chemistry***. 215, 152–159.

2. Shijun Wu, Piotr M.Kowalski, Na Yu, Thomas Malcherek, Wulf Depmeier, Dirk Bosbach, Shuao Wang, Evgeny V. Suleimanov, Thomas E. Albrecht-Schmitt, and Evgeny V. Alekseev. (**2014**) Highly Distorted Uranyl Ion Coordination and One/Two-Dimensional Structural Relationship in the $Ba_2[UO_2(\boldsymbol{T}O_4)_2]$ (***T*** = P, As) System: An Experimental and Computational Study. ***Inorganic Chemistry***. 53(14), 7650– 7660.

3. Na Yu, Vladislav V. Klepov, Philip Kegler, Dirk Bosbach, Thomas E. Albrecht-Schmitt, and Evgeny V. Alekseev. (**2014**) $Th(As^{III}_4As^{V}_4O_{18})$: a Mixed-Valent Oxoarsenic(III)/arsenic(V) Actinide Compound Obtained under Extreme Conditions. ***Inorganic Chemistry***. 53(16), 8194– 8196.

4. Na Yu, Vladislav V. Klepov, Giuseppe Modolo, Dirk Bosbach, Evgeny V. Suleimanov, Thorsten M. Gesing, Lars Robben, and Evgeny V. Alekseev. (**2014**) Morphotropy and Temperature-Driven Polymorphism in $A_2Th(AsO_4)_2$ (A = Li, Na, K, Rb, Cs) Series. ***Inorganic Chemistry***. 53 (20), 11231– 11241.

5. Na Yu, Vladislav V. Klepov, Stefan Neumeier, Wulf Depmeier, Dirk Bosbach, Evgeny V. Suleimanov andEvgeny V. Alekseev.(**2015**) Further Insight into Uranium and Thorium Metaphosphate Chemistry and the Effect of Nd^{3+} Incorporation into Uranium(IV) Metaphosphate. ***European Journal of Inorganic Chemistry***. 2015(9), 1562– 1568.

2. Conference Presentations and Lectures

1. 2013.02.28-2013.03.01 Aachen, Germany (BMBF)

As one member of the research project “Conditioning” funded by the Federal Ministry of Education and Research (BMBF), I attend this first project meeting.

A talk was presented: “*Single-crystal X-ray Diffractometers*”. Na Yu, Evgeny V. Alekseev

2. 2013.05.27- 2013.05. Strasburg, France(EMRS)

A poster was presented: “*Thorium arsenates from high temperature solid state reactions*”. Na Yu, Evgeny V. Alekseev

Ps: I was invited by Prof. Degueldre Claude to be the Chair assistant, and my work performance was excellent by the feedback of the conference organization.

3. 2013.08.15- 2013.08.16 Hannover, Germany (BMBF)

A talk was presented: "*Synthesis, structure and spectroscopy of novel actinide (U^{6+}, Th^{4+}) arsenates*". Na Yu, Evgeny V. Alekseev

4. 2014.02.26-2014.02.28 Grenoble, France (BMBF)

A talk was presented: "*U^{4+}/U^{6+} and Th^{4+} phosphates and arsenates*". Na Yu, Klepov Vladislav, Alekseev Evgeny

5. 2014.03.17-2014.03.21 Berlin, Germany (DGK)

22nd Annual Conference of the German Crystallographic Society (DGK)

A poster was presented: "*Thorium Arsenates from High Temperature Solid State Reactions*". Na Yu, Klepov Vladislav, Alekseev Evgeny

Ps: This poster won the second award. (Top 3 from 220)

6. 2014.07.07-2014.07.09 Bonn, Germany

8th European Summer School

A poster was presented: "*Single Crystal X-ray Diffraction and its Application in Actinide Studies*". Vladislav Klepov, Na Yu, Evgeny Alekseev

7. 2014.09.27-2014.10.01 Bremen, Germany

1st Meeting of the Young Crystallographers

8. 2014.10.07-2014.10.09 Frankfurt, Germany (BMBF)

A talk will be presented: "*Thorium Compounds containing Group V elements (N, P, As)*". Na Yu

9. 2015.03.16-2015.03.19 Goettingen, Germany (DGK)

23nd Annual Conference of the German Crystallographic Society (DGK)

A poster was presented: "*Further Insight into Uranium and Thorium Metaphosphate Chemistry and the Effect of Nd^{3+} Incorporation into Uranium(IV) Metaphosphate*". Na Yu, Klepov Vladislav, Alekseev Evgeny